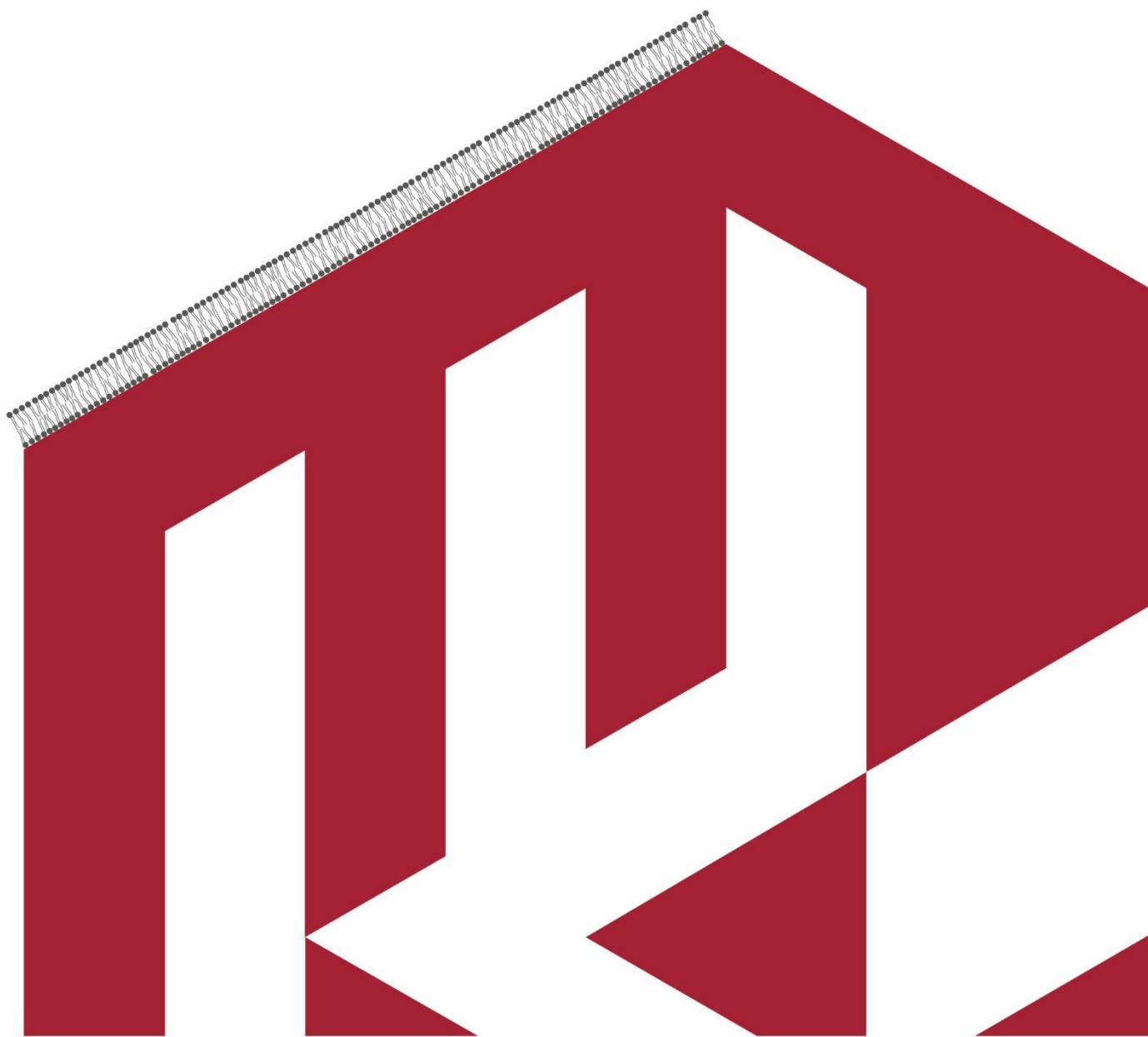


# Ph.D. Thesis

Electrochemical, spectroscopic  
and atomic force microscopy studies  
of mechanisms of antimicrobial peptides  
interactions with model biological membranes

---

Marta Majewska







Institute of Physical Chemistry  
Polish Academy of Sciences  
Kasprzaka 44/52  
01-224 Warsaw, Poland

**Ph.D. Thesis**

**Electrochemical, spectroscopic  
and atomic force microscopy studies  
of mechanisms of antimicrobial peptides  
interactions with model biological membranes**

Marta Majewska

Supervisor: Prof. Włodzimierz Kutner, Ph.D., D.Sc.  
Auxiliary supervisor: Dr Piotr Pięta, Ph.D.

The thesis was prepared within the International Doctoral Studies  
at the Institute of Physical Chemistry, Polish Academy of Sciences, Warsaw, Poland

Warsaw, August 2021



## Statement of originality

I, Marta Majewska, confirm that the research included within the present thesis was carried out by myself or in collaboration with and supported by others, as described in acknowledgments. Moreover, the previously published material is listed below.

I attest that I have exercised reasonable care to ensure that the work is original, and does not, to the best of my knowledge, violate any Polish law, infringe any third party's copyright or other Intellectual Property Right, or contains any confidential material.

I accept that the Polish Academy of Sciences has the right to use plagiarism detection software to check the electronic version of the thesis.

I confirm that my thesis has previously not been submitted for the award of a degree by IPC PAS or any other institute or university.

The copyright of this thesis rests with the author, and no quotation from it or information derived from it may be published without the author's prior written consent.

Signature:

*Marta Majewska*

Date:

*02.08.2021*



## Acknowledgments

I would like to thank:

**Prof. Włodzimierz Kutner** for accepting me in his research group of Molecular Films where I had the opportunity to learn electrochemical techniques and their applications in different fields, such as molecularly imprinted polymers for sensors application, as well as, besides science research, crediting me for engaged participation in the responsible task of co-organizing the International Workshop on Surface Modification for Chemical and Biochemical Sensing, SMCBS, since 2015, through 2017, 2019, up to 2021 edition.

**Dr. Piotr Pięta** for a friendly yet professional work atmosphere and loads of forbearance and trust, making this demanding time of Ph.D. research remain a still good memory. Moreover, Dr. Pięta significantly contributed to the results obtained with the PM-IRRAS.

**Dr. Vlad Zamlynniy** for invaluable help during the installation and optimization of the PM-IRRAS setup in our laboratory at the IPC PAS and further analysis of the data acquired.

**Prof. Jacek Lipkowski** for introducing me to the PM-IRRAS technique.

**Dr. Michael Grossutti** for ATR-IR measurements of BacSp222 in a dry multibilayer film.

**M.Sc. Faria Khan** and **Prof. Rafał Szmigielski** for fruitful cooperation on, initially, a side project that finally became an important part of my research and thesis. Especially, M.Sc. Faria Khan for phase-contrast microscopy imaging of BEAS-2B and A549 epithelial cell lines.

**Prof. Robert Nowakowski** for sharing his expertise in atomic force microscopy and sharing access to his microscope devices.

**Dr. Dusan Mrdenovic** for his help and support as a laboratory buddy.

**Dr. Kamila Łepicka** for supporting me since the very beginning of my Master's studies at the IPC PAS and throughout my Ph.D. studies. I am glad that we had an opportunity to work together on a side project, which became a part of Kamila's thesis, resulting in high-quality publications.

Finally, I owe gratitude to Piotr Karpiński for his patience and help, which helped me get through this demanding time.



## Funding



The Polish National Science Centre financially supported the present research, through the OPUS 12 project, entitled: „Interaction of membrane-active peptides with the model cell membrane and their role in a drug delivery system. Electrochemical, PM-IRRAS as well as STM, and AFM studies”. Grant no. 2016/23/B/ST4/02791 to Dr. Piotr Pięta.



# List of publications

## Publications selected for the thesis

1. **M. Majewska**, V. Zamlynny, I. S. Pieta, R. Nowakowski, P. Pieta, Interaction of LL-37 human cathelicidin peptide with a model microbial-like lipid membrane, *Bioelectrochemistry* 2021, 141, 107842. (IF = 4.72)
2. **M. Majewska**, F. Khan, I. S. Pieta, A. Wróblewska, R. Szmigielski, P. Pieta, Toxicity of selected airborne nitrophenols on eukaryotic cell membrane models, *Chemosphere* 2021, 266, 128996. (IF = 5.78)
3. **M. Majewska**, D. Mrdenovic, I. S. Pieta, R. Nowakowski, P. Pieta, Nanomechanical characterization of a single phospholipid bilayer in ripple phase with PF-QNM AFM, *Biochim. Biophys. Acta – Biomembr.* 2020, 1862, 9, 183347. (IF = 3.79)
4. P. Pieta, **M. Majewska**, Z. Su, M. Grossutti, B. Wladyka, M. Piejko, J. Lipkowski, P. Mak, Physicochemical Studies on Orientation and Conformation of a New Bacteriocin BacSp222 in a Planar Phospholipid Bilayer, *Langmuir* 2016, 32, 5653-5662. (IF = 3.83)

## Other publications

5. D. Mrdenovic, P. Zarzycki, **M. Majewska**, I. S. Pieta, R. Nowakowski, W. Kutner, J. Lipkowski, P. Pieta, Inhibition of Amyloid  $\beta$ -Induced Lipid Membrane Permeation and Amyloid  $\beta$  Aggregation by K162, *ACS Chem. Neurosci.* 2021, 12, 3, 531-541. (IF = 4.49)
6. H. Munawar, A. Garcia-Cruz, **M. Majewska**, K. Karim, W. Kutner, S. A. Piletsky, Electrochemical determination of fumonisin B1 using a chemosensor with a recognition unit comprising molecularly imprinted polymer nanoparticles, *Sens. Actuators B Chem.* 2020, 128552. (IF = 7.10)
7. D. Mrdenovic, **M. Majewska**, I. S. Pieta, P. Bernatowicz, R. Nowakowski, W. Kutner, J. Lipkowski, P. Pieta, Size-Dependent Interaction of Amyloid  $\beta$  Oligomers with Brain Total Lipid Extract Bilayer–Fibrillation Versus Membrane Destruction, *Langmuir* 2019, 35, 36, 11940-11949. (IF = 3.68)
8. P. Lach, M. Cieplak, **M. Majewska**, K. R. Noworyta, P. S. Sharma, W. Kutner, “Gate Effect” in *p*-Synephrine Electrochemical Sensing with a Molecularly Imprinted Polymer and Redox Probes, *Anal. Chem.* 2019, 91, 12, 7546-7553. (IF = 6.35)
9. K. Łępicka, **M. Majewska**, R. Nowakowski, W. Kutner, P. Pieta, High electrochemical stability of *meso*-Ni-salen based conducting polymer manifested by potential-driven reversible

changes in viscoelastic and nanomechanical properties, *Electrochim. Acta* 2019, 297, 94-100. (IF = 5.12)

10. K. Łępicka, P. Pieta, A. Shkurenko, P. Borowicz, **M. Majewska**, M. Rosenkranz, S. Avdo-shenko, A. A. Popov, W. Kutner, Spectroelectrochemical Approaches to Mechanistic Aspects of Charge Transport in *meso*-Nickel(II) Schiff Base Electrochromic Polymer, *J. Phys. Chem. C* 2017, 121, 16710-16720. (IF = 4.54)

## List of patent applications

1. K. Łępicka, P. Pięta, R. Rybakiewicz, M. Zagórska, **M. Majewska**, W. Kutner, „Nowy monomer, bisimid naftalenowy sfunkcjonalizowany w rdzeniu ditieno[3,2-b:2',3'-d]pirolem o sekwencji D-A-D i sposób jego otrzymywania oraz polimer przewodzący wytworzony przez polimeryzację tego monomeru, sposób jego wytwarzania i zastosowanie jako materiału elektrodowego do superkondensatorów” (“New monomer of naphthalene bisimide, functionalized in the core by dithieno[3,2-b:2',3'-d]-pyrrole with D-A-D sequence and method for obtaining it and the conductive polymer produced through polymerization of this monomer, method for producing it and its application as the electrode material for supercapacitors”). Pol. Pat. Appl. No. P.418333, 18.08.2016, patent granted on 20.12.2019, PAT.234733.
2. A. Garcia-Cruz, A. Pietrzyk-Le, K. Bartoń, K. Pasierbiewicz, **M. Majewska**, P. Borowicz, G. Spólnik, P.S. Sharma, M. Cieplak, K. Nikiforow, K. Noworyta, P. Pięta, W. Danikiewicz, P. Lisowski, F. D'Souza, W. Kutner, “Syntetyczny polimer nukleotydowy z warstwą rozpoznającą, jego wytwarzanie i zastosowanie do selektywnego oznaczania rakotwórczej heterocyklicznej aminy aromatycznej za pomocą czujnika chemicznego” (“Synthetic nucleotide polymer with the recognizing layer, production of such a polymer and application for selective determination of carcinogenic heterocyclic aromatic amine by means of the chemical sensor”). Pol Pat. Appl. No. P.423557, 24.11.2017
3. **M. Majewska**, M. Michalak, W. Nogala, P. Pieta. „Sposób izolacji sondy do skaningowej mikroskopii tunelowej (STM) w środowisku przewodzącym, sonda otrzymana takim sposobem oraz jej zastosowanie” (“Method for insulation of the probe for scanning tunneling microscopy (STM) in the conducting environment, the probe obtained by this method and its application”). Pol. Pat. Appl. No. P.421719, 26.05.2017.



## Poster presentations at international conferences

1. **M. Majewska**, K. Łępicka, R. Nowakowski, W. Kutner, P. Pięta, Erasmus+ Mobility training, International Workshop on Supercapacitors and Energy Storage (Bologna, Italy), 27 – 28 Jun 2019, “High electrochemical stability of *meso*-Ni-salen based conducting polymer manifested by potential-driven reversible changes in viscoelastic and nanomechanical properties.”
2. **M. Majewska**, D. Mrdenovic, R. Nowakowski, P. Pięta, The 8<sup>th</sup> International Workshop on Surface Modification for Chemical and Biochemical Sensing – SMCBS’2017 (Żelechów, Poland), 3 – 7 Nov 2017, “Nanomechanical characterization of the biomimetic membrane after antimicrobial peptide adsorption studied with PeakForce QNM atomic force microscopy mode.” (Best Poster Award by the Institute of Physical Chemistry PAS Microsymposium, 16 – 18 Jan 2018).
3. **M. Majewska**, D. Mrdenovic, P. Pięta, R. Nowakowski, XIV Warszawskie Seminarium Doktorantów Chemików (XIV Warsaw Seminar of Chemistry PhD students) (Warsaw, Poland), 9 Jun 2017, “Characterization of phospholipid bilayer surface structures by AFM” („Charakteryzacja struktur powierzchniowych dwuwarstw fosfolipidowych za pomocą mikroskopii sił atomowych”).
4. **M. Majewska**, K. Łępicka, P. Pięta, W. Kutner, The 9<sup>th</sup> Workshop on Applications of Scanning Probe Microscopy (IX Seminarium. Badania prowadzone metodami skaningowej mikroskopii bliskich oddziaływań) – STM/AFM 2016 (Zakopane, Poland), 30 Nov – 4 Dec 2016, “Nanomechanical properties of redox conducting polymers imaged in electrochemical conditions by AFM.”
5. **M. Majewska**, P. Pięta, Z. Su, M. Grossutti, B. Władyka, M. Piejko, J. Lipkowski, P. Mak, The 7<sup>th</sup> International Workshop on Surface Modification for Chemical and Biochemical Sensing – SMCBS’2015 (Pultusk, Poland), 6 – 10 Nov 2015, “Determination of the influence of a new bacteriocin-like peptide BacSp222 on a model biological membrane by chronocoulometry, AFM and PM-IRRAS.”



## Oral presentations at international conferences

1. **M. Majewska**, D. Mrdenovic, P. Pieta, The 9<sup>th</sup> AFM BioMed Conference (Münster, Germany), 2 – 6 Sep 2019, “Nanomechanical characterization of phospholipid bilayers in macro-ripple phase with Peak Force QNM atomic force microscopy mode.”

2. **M. Majewska**, R. Nowakowski, P. Pięta, The 15<sup>th</sup> International Congress of Young Chemists – YoungChem 2017 (Lublin, Poland), 11 – 15 Oct 2017, “Spectroelectrochemical and microscopic approaches to study interactions between antimicrobial peptides and model biological membranes.”



## List of abbreviations

Abbreviation	Full name
AFM	Atomic force microscopy
Alm	Alamethicin
AMP	Antimicrobial peptide
ATR	Attenuation total reflectance
BLM	Bilayer lipid membrane
$\beta$ -Tg	1-Thio- $\beta$ -D-glucose
CD	Circular dichroism
CE	Counter electrode
CMC	Critical micellar concentration
CPE	Constant phase element
CPE <sub>m</sub>	Constant phase element of the membrane
CPE <sub>sp</sub>	Constant phase element of the spacer
CV	Cyclic voltammetry
2D-COS	Two-dimensional correlation spectroscopy
DeflSens	Deflection sensitivity
DMPC	1,2-Dimyristoyl- <i>sn</i> -glycero-3-phosphocholine
DMPG	1,2-Dimyristoyl- <i>sn</i> -glycero-3-phospho-(1'- <i>rac</i> -glycerol)
DPPC	1,2-Dipalmitoyl- <i>sn</i> -glycero-3-phosphocholine
DPPG	1,2-Dipalmitoyl- <i>sn</i> -glycero-3-phospho-(1'- <i>rac</i> -glycerol)
EC-PFQNM	Electrochemical PeakForce Quantitative Nanomechanical Mapping
EEC	Equivalent electric circuit
EIS	Electrochemical impedance spectroscopy
EDL	Electric double layer
fBLM	Floating bilayer lipid membrane
F-D curve	Force-distance curve
FM	Flat mirror
FSD	Fourier self-deconvolution

FTIR	Fourier-transform infrared (spectroscopy)
gA	Gramicidin
hBLM	Hybrid bilayer lipid membrane
LB	Langmuir-Blodgett
LS	Langmuir-Schaefer
LUV	Large unilamellar vesicle
MIC	Minimum inhibitory concentration
MLV	Multilamellar vesicle
MSEFS	Mean squared electric field strength
NMR	Nuclear magnetic resonance
OCP	Open circuit potential
OHP	Outer Helmholtz plane
OW	Optical window
PBS	Phosphate buffered saline
PC	Phosphatidylcholine
PEM	Photoelastic modulator
PF-QNM	PeakForce Quantitative Nanomechanical Mapping
PG	Phosphatidylglycerol
P/L	Peptide-to-lipid (molar ratio)
PM	Parabolic mirror
PM-IRRAS	Polarization-modulation infrared reflection-absorption spectroscopy
POPC	1-Palmitoyl-2-oleoyl- <i>sn</i> -glycero-3-phosphocholine
POPG	1-Palmitoyl-2-oleoyl- <i>sn</i> -glycero-3-phospho-(1'- <i>rac</i> -glycerol)
PZC	Potential of zero charge
PZFC	Potential of zero free charge
PZTC	Potential of zero total charge
QCM-D	Quartz crystal microbalance with dissipation monitoring
RE	Reference electrode
SAM	Self-assembled monolayer
SCE	Saturated calomel electrode

sLM	Supported lipid monolayer
sBLM	Supported bilayer lipid membrane
SD	Second derivative (method)
SSD	Synchronous sampling detector
ST	Static polarizer
SUV	Small unilamellar vesicle
tBLM	Tethered bilayer lipid membrane
TOM	Tabletop optical mount
VF	Vesicle fusion
W	Gold wire
WE	Working electrode

## List of symbols

$A$  – intensity of the IR absorption band

$C_{dl}$  – electric double-layer capacitance,  $\mu\text{F cm}^{-2}$

$C_H$  – capacitance of the interface between the metal and water reservoir,  $\mu\text{F cm}^{-2}$

$C_m$  – membrane capacitance,  $\mu\text{F cm}^{-2}$

$C_s$  – capacitance of the diffuse layer,  $\mu\text{F cm}^{-2}$

$C_{sp}$  – spacer capacitance,  $\mu\text{F cm}^{-2}$

$c_M$  – molar concentration,  $\text{mol dm}^{-3}$  [M]

$d$  – thickness, nm

$d_{sub}$  – thickness of the submembrane region, nm

$E$  – Young's modulus, MPa

$E^*$  – reduced elastic modulus, MPa

$\vec{E}$  – electric field of the photon,  $\text{V m}^{-1}$

$E_{pzc}$  – the potential of zero charge, V

$f$  – frequency, Hz

$f_0$  – resonance frequency, Hz

$F_{adh}$  – adhesion force, nN

$h$  – thickness of the bilayer, nm

$h_m$  – thickness of the bilayer hydrophobic core, nm

$H_I, H_{II}$  – hexagonal normal (I) and inverted (II) phase

$I$  – current,  $\mu\text{A}$

$I_0$  – current amplitude,  $\mu\text{A}$

$I_p$  – the intensity of  $p$ -polarized light

$I_s$  – the intensity of  $s$ -polarized light

$I_{SSD}^{diff}$  – the intensity difference signal at the SSD terminal

$I_{SSD}^{ave}$  – the intensity average signal at the SSD terminal

$j$  – imaginary unit

$J_0$  – zero-order Bessel function

$J_2$  – second-order Bessel function

$k$  – spring constant,  $\text{N m}^{-1}$

$L_\alpha$  – lamellar liquid-crystalline phase

$L_\beta$  – lamellar gel phase

$L_{\beta'}$  – lamellar gel with tilted acyl chains phase  
 $L_c$  – lamellar crystalline phase  
 $L_o$  – lamellar liquid-ordered phase  
 $M_I, M_{II}$  – micellar normal (I) and inverted (II) phase  
 $m$  – mass, g  
 $M_w$  – molecular weight, Da ( $\text{g mol}^{-1}$ )  
 $n$  – refractive index  
 $\Delta N$  – number of fringes  
 $P_{\beta'}$  – ripple phase  
 $q$  – charge, C  
 $Q$  – constant phase element coefficient  
 $Q_m$  – membrane constant phase element coefficient  
 $Q_{sp}$  – spacer constant phase element coefficient  
 $Q_{II}^M, Q_{II}^B$  – cubic micellar (M) inverted and bilayer (B) inverted phase  
 $r_0$  – the radius of a (circular) defect, nm  
 $R_a$  – arithmetic roughness, nm  
 $R_{ad}$  – critical adsorption radius, nm  
 $R_s$  – equivalent supporting electrolyte resistance,  $\Omega$   
 $R_{def}$  – equivalent defects resistance,  $\Omega$   
 $R_p$  – reflectivity of the  $p$ -polarized light  
 $R_q$  – quadratic roughness, nm  
 $R_r$  – minimum rupture radius, nm  
 $R_s$  – reflectivity of the  $s$ -polarized light  
 $R_{tip}$  – AFM tip radius, nm  
 $\Delta S$  – reflection-absorption spectrum  
 $t$  – time, s  
 $V$  – voltage, V  
 $V_0$  – alternating voltage amplitude in EIS, mV  
 $Y_{def}$  – the submembrane impedance (admittance), pS  
 $Z$  – total impedance,  $\Omega$   
 $Z_0$  – the magnitude of total impedance,  $\Omega$   
 $Z'$  – real component of impedance,  $\Omega$   
 $Z''$  – imaginary component of impedance,  $\Omega$

$\alpha$  – frequency dispersion constant  
 $\Gamma$  – analyte surface concentration, mol cm<sup>-2</sup>  
 $\delta$  – elastic deformation (indentation), nm  
 $\epsilon$  – relative electric permittivity  
 $\epsilon_0$  – vacuum permittivity, 8.85 × 10<sup>-14</sup> F cm<sup>-1</sup>  
 $\epsilon_m$  – bilayer lipid membrane relative electric permittivity, ~2.0  
 $\epsilon_s$  – aqueous electrolyte solution relative electric permittivity, ~80.0  
 $\theta$  – the angle between the electric field of the photon and the transition dipole of vibration in the analyte molecule, °  
 $\theta_{C=O}$  – the angle between the transition dipole moment of the amide I group and the surface normal, °  
 $\theta_{helix}$  – tilt angle of the  $\alpha$ -helix against the surface normal, °  
 $\theta_{ref}$  – the angle between the  $\alpha$ -helix long axis and the transition moment of the amide I vibration, which serves as a reference angle, °  
 $\theta_{tilt}$  – tilt angle of the *trans* fragment of phospholipid acyl chains against the surface normal, °  
 $\kappa$  – attenuation coefficient  
 $\lambda_0$  – the wavelength at which the PEM is optimized  
 $\vec{\mu}$  – transition dipole moment, C m  
 $\nu$  – Poisson's ratio  
 $\rho_{sub}$  – specific resistance of submembrane region,  $\Omega$  cm  
 $\sigma$  – charge density,  $\mu$ C cm<sup>-2</sup>  
 $\sigma_M$  – metal surface charge density,  $\mu$ C cm<sup>-2</sup>  
 $v$  – potential or voltage scan rate, V s<sup>-1</sup>  
 $\Phi$  – phase angle, °  
 $\varphi$  – volume fraction of the analyte  
 $\varphi_0$  – maximum phase shift introduced by the PEM  
 $\chi_m$  – membrane dipole potential, V  
 $\psi_s$  – surface Volta potential, V  
 $\Delta\psi$  – potential drop across the membrane, V  
 $\Delta\psi_m$  – the transmembrane potential, V  
 $\omega$  – angular frequency, rad s<sup>-1</sup>

## Abstract (Eng.)

The present thesis aims to resolve mechanisms underlying the antimicrobial activity of membrane-active peptides towards model biological membranes under biologically relevant conditions. The motivation for the research originates from the problem of antibiotic resistance in bacteria, one of the biggest threats to global health and food safety nowadays. Potential alternatives to conventionally available antibiotics are antimicrobial peptides (AMPs). It was initially hypothesized that their mode of action is membrane disruption through pore formation. However, with time, more complicated mechanisms have been proposed, and the mode of action of various AMPs remains unrecognized.

Knowledge of AMPs structure and its correlation with the mechanism of action is utilized to design novel antimicrobial agents for clinical applications. In the present study, two peptides were investigated, a newly isolated BacSp222 bacteriocin produced by *S. pseudintermedius* strain 222 and LL-37 human cathelicidin. Experiments were performed using a model biological membrane comprised of a phospholipid bilayer deposited on a solid substrate, either gold electrode or mica. The goal was to find the secondary structure, orientation, and localization of AMPs in the phospholipid bilayer. Simultaneously, the effects of the AMP on phospholipid conformation and orientation were unraveled. Three complementary experimental techniques were used, including atomic force microscopy (AFM) for direct visualization of the membrane surface, electrochemical impedance spectroscopy (EIS) to characterize changes in membrane electrical parameters, e.g., capacitance and resistance, and polarization-modulation infrared reflection-absorption spectroscopy (PM-IRRAS) performed on electrode-supported phospholipid bilayer for determination of conformational and orientational changes of analyzed molecules. These surface-sensitive techniques operate under an electrochemical setting, which provides biologically relevant conditions by mimicking transmembrane potential. The present research provides a novel insight into understanding the relations between LL-37 and BacSp222 and multicomponent model membranes.

Moreover, an attempt to screen the toxicity of nitrophenols, airborne pollutants hypothesized to interact with biological membranes, is presented. Similarly as for AMPs, surface-sensitive techniques were involved in revealing the activity of these pollutants on model biological membranes. Finally, the mechanical study of the model membrane in a ripple phase is discussed. Apparently, the formation and mechanical properties of the ripple phase in a supported single bilayer lipid membrane have uniquely been described.



## Abstract (Pol.)

Celem niniejszej rozprawy jest wyjaśnienie mechanizmów leżących u podstaw aktywności przeciwdrobnoustrojowej membrano-aktywnych peptydów względem modelowych błon biologicznych w warunkach zbliżonych do warunków fizjologicznych. Motywacja badań wynika z problemu antybiotykooporności bakterii, jednego z najpoważniejszych zagrożeń dla zdrowia człowieka i bezpieczeństwa żywności. Alternatywą dla konwencjonalnych antybiotyków są peptydy przeciwdrobnoustrojowe (ang. antimicrobial peptides, AMPs). Początkowo postawiono hipotezę, że ich mechanizm działania polega na uszkodzeniu błony bakteryjnej poprzez tworzenie porów. Jednak z czasem zaproponowano bardziej skomplikowane mechanizmy, a sposób działania różnych AMP-ów pozostaje nierozpoznany.

Znajomość struktury AMP-ów i jej wpływu na mechanizm działania jest wykorzystywana do projektowania nowych AMP-ów do zastosowań klinicznych. W niniejszej pracy zbadano dwa peptydy, tj. nowo wyizolowany BacSp222 i jedyną ludzką katelicydynę, LL-37. Eksperymenty przeprowadzono posługując się modelową błoną biologiczną zbudowaną z dwuwarstwy fosfolipidowej osadzonej na złotej elektrodzie lub mice. Cel badań obejmował ustalenie struktury drugorzędowej oraz orientacji i lokalizacji cząsteczek tych AMP-ów w dwuwarstwie fosfolipidowej. Zbadano również wpływ tych peptydów na konformację i orientację fosfolipidów w dwuwarstwie. Zastosowano trzy wzajemnie uzupełniające się techniki eksperymentalne, tj. mikroskopię sił atomowych (AFM) do wizualizacji powierzchni membrany, elektrochemiczną spektroskopię impedancyjną (EIS) w celu scharakteryzowania zmian parametrów elektrycznych błony, np. pojemności i oporności, oraz spektroskopię odbiciowo-absorpcyjną z modulacją polaryzacji w podczerwieni (PM-IRRAS) aby określić zmiany konformacji i orientacji analizowanych cząsteczek. Te powierzchniowo czułe techniki zastosowano w warunkach elektrochemicznych, które zapewniają warunki istotne z biologicznego punktu widzenia poprzez naśladowanie potencjału transbłonowego. Niniejsze badania przyczyniają się do pogłębionego zrozumienia zależności między strukturą i aktywnością LL-37 i BacSp222 a modelowymi membranami wieloskładnikowymi.

Ponadto, w pracy podjęto próbę weryfikacji toksyczności nitrofenoli będących składnikami zanieczyszczeń powietrza. Podejrzewa się, że nitrofenole oddziałują z błonami komórkowymi płuc. Podobnie jak w przypadku AMP-ów, w badaniach zastosowano techniki powierzchniowo czułe, aby wyjaśnić wpływ tych zanieczyszczeń na modelowe błony biologiczne. Przeprowadzono również badania mechaniczne modelowej błony w fazie zmarszczkowej. Po raz pierwszy pokazano powstawanie i właściwości mechaniczne tej fazy w pojedynczej dwuwarstwie fosfolipidowej osadzonej na podłożu stałym.



## List of tables

Table 1-1. Comparison of proposed mechanisms of activity for selected membrane-active peptides studied by complementary EIS, PM-IRRAS, AFM techniques.

Table 2-1. Physicochemical properties of the phospholipids used.<sup>182</sup>

Table 3-1. The conditions used to acquire PM-IRRA spectra in the indicated spectral regions for the DMPC-d<sub>54</sub>/BacSp222 membrane.

Table 3-2. The calculated values of the order parameter ( $S$ ), the tilt angle ( $\theta_{\text{tilt}}$ ) of transition dipole moment vs. electrode surface normal, and tilt angle ( $\theta_{\text{helix}}$ ) of the  $\alpha$ -helix long axis vs. transition moment of the amide I vibration (reference angle,  $\theta_{\text{ref}}$ ), at each applied potential.

Table 3-3. Values of the equivalent electrical circuit elements for the 3×PC bilayer.  $R_s$  and  $R_{\text{def}}$  are resistances of a supporting electrolyte solution and membrane defects, respectively;  $Q_m$  and  $Q_{\text{sp}}$  are constant phase elements of a membrane and a spacer, respectively;  $\alpha_m$  and  $\alpha_{\text{sp}}$  are constant-phase-element dimensionless parameters.

Table 3-4. Values of the equivalent electrical circuit components for the DMPC bilayer.  $R_s$  and  $R_{\text{def}}$  are resistances of a supporting electrolyte solution and a membrane defects, respectively;  $Q_m$  and  $Q_{\text{sp}}$  are constant phase elements of a membrane and a spacer, respectively;  $\alpha_m$  and  $\alpha_{\text{sp}}$  are constant-phase-element dimensionless parameters.

Table 3-5. Values calculated for each component of the equivalent electrical circuit applied to model the 3×PC/3×PG bilayer in the absence and presence of LL-37.

Table 3-6. An average breakthrough force, jump width, elastic deformation, and corrected layer thickness for the 3×PC/3×PG membrane in the LL-37 absence and presence, calculated based on the averaged F-D curves-derived parameters.  $A$  and  $A'$ , and  $B$  and  $B'$  denote the breakthrough force distributions shown in Figure 3.4-5b and 5c.

Table 3-7. Summary of the conditions used to obtain the PM-IRRA spectra for the 3×PC/3×PG bilayer supported on an Au(111)| $\beta$ -Tg electrode in the absence and presence of LL-37 in the C–H stretching region.

Table 3-8. Order parameters of the lipid acyl chain and corresponding tilt angles for the 3×PC/3×PG bilayer in the absence and presence of LL-37.



## List of figures

Figure 1.3-1. Examples of natural phospholipids isolated from (a) porcine brain and chicken egg and (b) *E. coli*, representing main components of eukaryotic and prokaryotic cell membranes, respectively.

Figure 1.3-2. Structure of a glycerophospholipid, phosphatidylcholine (PC).

Figure 1.3-3. Schematic structures of lipid phases. I. Lamellar phase: (a) subgel,  $L_c$ ; (b) gel,  $L_\beta$ ; (c) gel tilted,  $L_\beta$ ; (d) rippled gel,  $P_\beta$ ; (e) fully interdigitated gel,  $L_\beta^{int}$ ; (f) partially interdigitated gel; mixed interdigitated gel; (h) liquid crystalline,  $L_\alpha$ . II. Lipid micellar aggregates: (i) spherical micelles,  $M_I$ ; (j) cylindrical micelles (tubules); (k) disks; (l) inverted micelles,  $M_{II}$ ; (m) liposomes. III. Non-lamellar mesomorphic liquid crystalline phases: (n) hexagonal,  $H_I$ ; (o) inverted hexagonal,  $H_{II}$ ; (p) inverted micellar cubic,  $Q_{II}^M$ ; (q) bilayer cubic,  $Q_{II}^B$ ,  $Im3m$  topology; (r) bilayer cubic,  $Pn3m$  topology; (s) bilayer cubic,  $Ia3d$  topology. Adapted from Ref.<sup>35</sup>

Figure 1.3-4. (a) A detailed diagram of a lipid bilayer cell membrane, reproduced from Ref.<sup>47</sup> Schemes of different metal-supported biomimetic membranes: (b) supported lipid monolayer, sLM; (c) supported BLM, sBLM; (d) hybrid BLM, hBLM; (e) polymer-cushioned BLM; (f) tethered BLM, tBLM; (g) floating BLM, fBLM. Adapted from Ref.<sup>21</sup>

Figure 1.3-5. A schematic representation of an electric potential profile across (a) a bilayer lipid membrane, (b) electrode-supported BLM, (c) electrode-supported BLM with omitted surface potentials. Three contributions to electric potential profile ( $\Delta\psi$ ) are shown, the transmembrane potential ( $\psi_m$ ), the surface charges potential ( $\psi_s$ ), and the membrane dipole potential ( $\chi_m$ ). Superscripts 1 and 2 denote the inner and outer leaflet of the bilayer. Subscripts M, m, s, and S denote metal, membrane, surface, and solution, respectively. The electric permittivities  $\epsilon_m$  and  $\epsilon_s$  for the bilayer core and the aqueous phase are 2 and 80, respectively. Adapted from Ref.<sup>41</sup>

Figure 1.3-6. A schematic illustration of a force-distance curve representing a tip-sample separation distance during atomic force spectroscopy measurement. The tip approaches the sample's surface and, first, makes contact, then indents the sample, and when reaching a breakthrough force, it breaks through the lipid bilayer, which is represented by a jump in a force-distance curve.

Figure 1.4-1. A schematic representation of the preparation of an asymmetric lipid bilayer on a solid substrate (gold) from the air-water interface (blue). (a) Langmuir-Blodgett vertical

withdrawing, (b) Langmuir-Schaefer transfer by horizontal touching, (c) resulting Y-type bilayer. Different colors mark different lipids in the two leaflets.

Figure 1.5-1. Electrochemical STM images of AMP interactions with a lipid monolayer. (a) DMPC/gA (9:1 lipid-to-peptide molar ratio) at the Au(111) electrode, acquired at 0.20 V vs. Ag|AgCl in 0.1 M NaF, using a tunneling current of 0.35 nA and a bias voltage of -0.45 V. (b) Enlarged image with individual gA channel and proposed peptide model based on structure from PDB databank under the access code of 1MAG. (c) DMPC/eggPC with alamethicin incorporated at the 15:1 lipid-to-peptide molar ratio, deposited at the Au(111) surface. Image acquired at tunneling current of 0.78 nA. (d) Structural model of alamethicin assembly proposed and superimposed on an STM image. Reproduced from Ref.<sup>129, 130</sup>

Figure 1.5-2. AFM topography image,  $100 \times 100 \text{ nm}^2$ , of the DMPC/DMPG/Alm (9:9:2) bilayer deposited at the Au(111)| $\beta$ -Tg electrode. The images on the right are zoomed fragments from the white boxes. Their size is  $20 \times 20 \text{ nm}^2$ . Reproduced from Ref.<sup>54</sup>

Figure 1.5-3. The fast-scanning AFM topography images of a DOPC/DOPG (1:1) sBLM in the presence of  $1 \mu\text{M}$  Smp43, injected into the fluid cell at  $t = 0 \text{ s}$ . Scan size is  $1 \times 1 \mu\text{m}^2$ . Reproduced from Ref.<sup>131</sup>

Figure 1.6-1. The structure of human LL-37, shown as (a) a ribbon diagram color-coded from N-terminus (blue) to C-terminus (red), (b) hydrophobic surfaces are marked red and hydrophilic are blue. Structure available from PDB databank under the access code of 2K60.

Figure 2.1-1. Single-crystal Au(111) electrode in a glass capillary.

Figure 2.1-2. (a) The experimental CV curve of a bare Au(111) electrode in 0.01 M KClO<sub>4</sub>, at a scan rate of  $20 \text{ mV s}^{-1}$ , after electrode electropolishing and then flame annealing. (b) The Au(111) electrode under the same conditions, in the double-layer potential range of the CV curve. Reconstruction is lifted at potentials above +0.4 V vs. SCE.

Figure 2.1-3. The double-layer capacitance vs. potential curve for a bare Au(111) electrode in 0.01 M KClO<sub>4</sub> with data acquisition starting from the negative potential edge.

Figure 2.1-4. Structural formula of 1-thio- $\beta$ -D-glucose ( $\beta$ -Tg) sodium salt.

Figure 2.1-5. The surface pressure vs. area compression isotherm of DMPC spread on an aqueous subphase at 21 °C. Compression was stopped at  $35 \text{ mN m}^{-1}$ , and at this surface pressure, the monolayer was transferred onto the mica substrate using first the LB and then

the LS technique (curve not shown). The 20- and 2-(mm min<sup>-1</sup>) speed was applied for the barriers and dipper, respectively.

Figure 2.2-1. Schematic representation of the force-distance curve acquired for every pixel of the AFM PF-QNM image. Features of the curve used for calculating adhesion, dissipation, deformation, peak force, and modulus are marked. The  $d_0$  parameter corresponds to the tip position at the sample surface (contact point).

Figure 2.2-2. CV curves for POPC:POPG (3:2) (curve 1, solid) and POPC:POPG (3:2) + LL-37 (40:1 lipid-to-peptide molar ratio) (curve 2, dash) bilayers at 20 mV s<sup>-1</sup>, in 0.01 M PBS. Current density increased in the presence of membrane-active peptide, indicating membrane disruption.

Figure 2.2-3. Bode plots of the (a), (c) magnitude and (b), (d) phase of the electrochemical impedance in the case of (a), (b) homogenous and (c), (d) heterogeneous distribution of defects, schematically shown as insets in Panels a and c, calculated for several defects at defect density of (1) 3, (2) 7, (3) 19, (4) 61, (5) 169, (6) 331, (7) 1519  $\mu\text{m}^{-2}$ . Other model parameters include  $C_H$ , 10  $\mu\text{F cm}^{-2}$ ;  $d_{\text{sub}}$ , 1.5 nm;  $\rho_{\text{sub}}$ , 10<sup>5</sup>  $\Omega \text{ cm}$ ;  $Y_{\text{def}}$ , 70 pS;  $\epsilon$ , 2.9;  $h_m$ , 3.0 nm;  $r_0$ , 1 nm;  $R_s$ , 0.1  $\Omega$ . Adapted from Ref.<sup>121</sup>

Figure 2.2-4. Equivalent electric circuits, modeled to correspond to BLM components, proposed for (a) a perfectly insulating bilayer and (b) a bilayer in the presence of defects when the transport of ions into the submembrane region is enhanced (schematically marked by arrows).

Figure 2.2-5. The surface selection rule of IRRAS. The incident beam,  $h\nu_i$ , (a)  $p$ -polarized or (b)  $s$ -polarized, is reflected from a smooth metal surface, resulting in the electric field enhancing or attenuating, respectively. Adapted from Ref.<sup>60</sup>

Figure 2.2-6. A schematic of (a) a thin-layer cell configuration, (b) the experimental PM-IRRAS set-up (FM, flat mirror; PM, parabolic mirror; SP, static polarizer; PEM, photoelastic modulator; OW, optical window; L, lens; D, detector) showing details of the glass spectroelectrochemical cell (WE, working electrode; CE, counter electrode; RE, reference electrode; W, gold wire). Adapted from Ref.<sup>105</sup>

Figure 2.2-7. Photographs of spectroelectrochemical laboratory setup. (a) TOM box, FTIR spectrometer, potentiostat, and PEM controller. (b) Insight of the TOM box, including mirrors, PEM, spectroelectrochemical cell, and detector, with IR beam path marked with red arrows.

Figure 2.2-8. The mean squared electric field strength for a *p*-polarized light at the metal surface for CaF<sub>2</sub>|D<sub>2</sub>O|Au(111) stratified medium, calculated for a convergent ( $\pm 5^\circ$ ) beam of the wavenumber of (a) 2900 cm<sup>-1</sup> and (b) 1600 cm<sup>-1</sup>.

Figure 2.2-9. Reflectance spectra of a thin-layer spectroelectrochemical cell composed of CaF<sub>2</sub>|D<sub>2</sub>O|Au(111). The solid curve indicates the experimental spectrum, the dashed curve is a theoretical spectrum for the thin cavity thickness of 5  $\mu\text{m}$ , and the angle of incidence of  $57^\circ$ , the correction coefficient is 0.95.

Figure 2.2-10. The theoretical response functions of the PEM calculated by Bessel software<sup>200</sup> and the (a) second-order and (b) zero-order calibration spectra. Solid curves indicate empirical calibration spectra for  $J_2$  and  $J_0$  functions, dotted curves are the theoretical Bessel functions, and dashed curves are the theoretical cosine terms. The PEM was optimized for 2900 cm<sup>-1</sup>.

Figure 2.2-11. The PM-IRRA spectra of the 3 $\times$ PC:3 $\times$ PG (3:2) membrane deposited on Au(111)| $\beta$ -Tg in the presence of LL-37 in the 40:1 lipid-to-peptide molar ratio, in the C–H stretching region, acquired in 10 mM NaF<sub>2</sub> in D<sub>2</sub>O at 100 mV, (a) after *J*-function correction and before background subtraction (solid curve), with spline function (dashed curve) and template points (circles), (b) after background subtraction.

Figure 2.2-12. Scheme of a thin-cavity transmission flow cell used for the determination of analyte optical constants. The design of the cell was adapted from Zamlynny,<sup>200</sup> and the cell was custom machined.

Figure 2.2-13 The transmission IR spectrum of the interference fringes between two CaF<sub>2</sub> windows in the air (without purging, CO<sub>2</sub> and H<sub>2</sub>O bands are visible in the spectra), used to calculate the thickness of a thin layer between the windows.

Figure 2.2-14. (a) Optical constants for DMPC:DMPG (3:2) vesicles (0.125% volume concentration) in D<sub>2</sub>O for 2900 cm<sup>-1</sup> region. The dashed curve indicates a refractive index ( $n$ ), and the solid curve indicates an attenuation coefficient ( $\kappa$ ). (b) Screenshot of OptCo software.

Figure 2.2-15. The simulated spectrum for randomly oriented 3 $\times$ PC:3 $\times$ PG (3:2) molecules in D<sub>2</sub>O, calculated for 5- $\mu\text{m}$  gap thickness and  $57^\circ$  incident angle for the 2900 cm<sup>-1</sup> region.

Figure 2.2-16. PM-IRRA spectra of the DMPC film acquired at  $-800$  mV vs. Ag|AgCl. (a) 7-Point Savitsky-Golay second derivative with the 3<sup>rd</sup> order polynomial function. (b) The PeakFit result; the solid black curve is an original spectrum, dashed black curve is a cumulative peak fit result, with  $R^2 = 0.996$ .

Figure 2.2-17. Schematic representation of the direction of the transition dipoles for (a) symmetric and (b) asymmetric stretches for a lipid acyl chain. (c) Schematic of the tilt angle ( $\theta_{\text{tilt}}$ ) of a lipid acyl chain. Adapted from Ref.<sup>60</sup>

Figure 2.3-1. Schematic of an all-glass three-electrode V-shaped electrochemical cell (a) front and (b) side view. Argon inlets are marked, where the bottom one allows passing the gas through the electrolyte before the experiment and is switched to the top one that maintains gas flow above the solution during the experiment. The supporting electrolyte solution is marked in violet, Teflon™ parts are marked in blue, gas molecules are depicted as green dots.

Figure 3.1-1. The  $3 \times 3 \mu\text{m}^2$  AFM topography images of the DMPC single bilayer supported on mica, acquired at 21 °C in a buffer solution (a) with and (b) without Tris component, pH = 7.6 and 7.4, respectively. (c) The cross-sectional profiles were taken along the straight lines displayed in Panels a and b.

Figure 3.1-2. (a)  $5 \times 5 \mu\text{m}^2$  and (b)  $1 \times 1 \mu\text{m}^2$  AFM image of DMPC bilayer acquired at 21 °C in 20 mM Tris, 150 mM NaCl, 5 mM EDTA buffer, pH = 7.6. (c) Cross-sectional profile taken along the straight line displayed in Panel b.

Figure 3.1-3. The AFM topography images of the DMPC single bilayer acquired at (a) 115, (b) 285, and (c) 378 min of continuous scanning at 21 °C in 20 mM Tris, 150 mM NaCl, 5 mM EDTA buffer, pH = 7.6. (d) Cross-sectional height profiles were taken along the lines indicated in Panels b and c.

Figure 3.1-4. AFM topography images of the DMPC bilayer deposited on mica acquired at different timespans during continuous scanning at 21 °C in 20 mM Tris, 150 mM NaCl, 5 mM EDTA buffer, pH = 7.6. Arrows indicate areas of increased height and lateral size, suggesting sites of phase transitions. All images are  $3 \times 3 \mu\text{m}^2$  in size and 0 to 15.5 nm in z-scale. The scale bar corresponds to a 400-nm distance.

Figure 3.1-5. AFM maps of the (a) topography and (b) corresponding Young's modulus of the DMPC single bilayer deposited on mica. The bilayer was imaged at 21 °C in 20 mM Tris, 150 mM NaCl, 5 mM EDTA buffer, pH = 7.6.

Figure 3.1-6. (a) Topography and (b) Young's modulus map of a DMPC single bilayer deposited on mica. (c) Corresponding cross-sectional profiles of the topography (solid red curve) and Young's modulus (dashed green curve) from Panels a and b, respectively. Imaging was performed at 21 °C in 20 mM Tris, 150 mM NaCl, 5 mM EDTA buffer, pH = 7.6.

Figure 3.1-7. (a) The AFM topography image and (b, c, d) Young's modulus histograms calculated for the (b) higher and (c) lower stripe of the ripples as well as (d) smooth bilayer schematically indicated as rectangles on the AFM topography image. The Young's modulus was calculated by analyzing ~10 000 F-D curves acquired during the AFM imaging.

Figure 3.1-8. (a) The AFM topography image and (b, c) Young's modulus map of the DMPC single bilayer deposited on mica determined (b) without and (c) with solid substrate correction. (d, e, f) Young's modulus histograms, corresponding to Young's modulus map shown in Panel c, calculated for the (d) higher and (e) lower stripes of the ripples as well as (f) smooth bilayer.

Figure 3.2-1. The structure of BacSp222, shown as (a, b) a ribbon diagram, color-coded from N-terminus (blue) to C-terminus (red). (c, d) Surfaces are marked blue for the most hydrophilic, through white to orange for the most hydrophobic. (e, f) Coulombic potential generated in Chimera for pH = 5.0. Positively charged surfaces are colored blue, through white to red for negatively charged. BacSp222 structures can be found in the PDB under accession code 5LWC. Adapted from Ref.<sup>241</sup>

Figure 3.2-2. Charge density curves for the bare Au(111) electrode (black) and the Au(111) electrode coated with DMPC (blue) and DMPC/BacSp222 (9:1 molar ratio) (red) in a 0.1 M KClO<sub>4</sub> supporting electrolyte solution. The bottom abscissa plots the potential applied to the Au(111) electrode vs. the reference electrode. The top abscissa plots values of  $(E - E_{pzc})$ , which is a measure of the potential drop across the membrane, equivalent of the transmembrane potential.

Figure 3.2-3. PM-IRRAS spectra in the C-D stretching region corresponding to (a) DMPC-d<sub>54</sub> and (b) DMPC-d<sub>54</sub>/BacSp222 (9:1 molar ratio), for potentials from 200 to -800 mV. The spectra simulated for randomly oriented DMPC-d<sub>54</sub> and DMPC-d<sub>54</sub>/BacSp222 molecules are marked in blue.

Figure 3.2-4. Spectra deconvolution by Lorentzian fit of the (a) simulated spectra of randomly oriented DMPC-d<sub>54</sub>/BacSp222 molecules and (b) experimental spectra of DMPC-d<sub>54</sub>/BacSp222 bilayer measured at 0 V. The deconvoluted spectra are marked as black squares, and the cumulative result of deconvolution is marked as a red curve.

Figure 3.2-5. (a) Peak center position vs. the potential for the (top)  $\nu_{as}(CD_2)$  and (bottom)  $\nu_s(CD_2)$  in the BacSp222 (●) presence and (■) absence.

Figure 3.2-6. The average tilt angle of the *trans* fragment of the phospholipid acyl chains vs. the potential for DMPC-d<sub>54</sub> in the BacSp222 (●) presence and (■) absence.

Figure 3.2-7. PM-IRRA spectra in the amide I region corresponding to the BacSp222 C=O stretching vibrations at selected potentials from 300 to -800 mV vs. Ag|AgCl. The spectrum simulated for randomly oriented BacSp222 molecules is marked in blue.

Figure 3.2-8. (a) Deconvolution of the amide I band of the randomly oriented BacSp222 molecules. The positions of sub-bands were determined using (b) the Fourier self-deconvolution and (c) the second-derivative method.

Figure 3.2-9. Deconvolution of the amide I band of the BacSp222 incorporated in the DMPC bilayer recorded at the potential of (a) 100 mV, (b) -600 mV, and (c) -800 mV vs. Ag|AgCl. The black curve is the experimental spectra. The red dotted curve is the cumulative result of band deconvolution.

Figure 3.2-10. The average tilt angle of (a) the transition dipole moments ( $\theta_{C=O}$ ) and (b) the major axis of the  $\alpha$ -helical components ( $\theta_{helix}$ ) of BacSp222 as a function of the electrode potential vs. Ag|AgCl. The tilt angle of  $\alpha$ -helices was calculated for reference angles of (●) 34° and (●) 38°.

Figure 3.2-11. Polarized ATR-IR spectra of the dry multibilayer DMPC/BacSp222 film acquired in collaboration with Michael Grossutti and Prof. Jacek Lipkowski. Bands characteristic for amide I and amide II vibrations of BacSp222 and two bands associated with the C=O stretching and C-H bending of DMPC are visible.

Figure 3.2-12. The AFM images of a DMPC bilayer deposited on mica, (a) in the absence and (c - h) in the presence of BacSp222. (b) Cross-sectional profiles of (curve 1) DMPC and (curve 2) DMPC/BacSp222, as shown on images a and c. Three samples of DMPC/BacSp222 bilayer deposited on mica are shown, at concentrations of (c, d) 90:1 lipid-to-peptide molar ratio, and (e - h) 10:1 lipid-to-peptide molar ratio. Inset in Panel e shows an enlarged and processed area of possible pores cluster, with the scale bar indicating a 20-nm distance.

Figure 3.3-1. Phase-contrast optical microscopy images of (top) BEAS-2B and (bottom) A549 cell lines incubated for (a-c) 24 h and (d-f) 48 h in the (a and d) 0  $\mu\text{g mL}^{-1}$  (control cells), (b and e) 0.1  $\text{mg mL}^{-1}$ , (c and f) 0.2  $\text{mg mL}^{-1}$  nitrophenols mixture solution. Images scale bars refer to 50  $\mu\text{m}$  distance. Images were acquired in collaboration with M.Sc. Faria Khan and Prof. Rafał Szmigielski.

Figure 3.3-2. Cyclic voltammetry curves for the (a) 3×PC and (b) DMPC model membranes, deposited on Au(111)|β-Tg electrode, before (curve 1 and 3, solid) and after (curve 2 and 4, dashed red) 20-h incubation in the 200-μg mL<sup>-1</sup> mixed nitrophenols 0.01 M PBS solution. The scan rate was 20 mV s<sup>-1</sup>.

Figure 3.3-3. The phase angle of impedance vs. frequency curves for the 3×PC membrane, deposited on the Au(111)|β-Tg electrode, (a) before and (b) after 20-h incubation in the 200-μg mL<sup>-1</sup> nitrophenols mixture in 0.01 M PBS (pH = 7.4). Symbols and curves of the same colors represent experimental data and fitting the equivalent electrical circuits, respectively.

Figure 3.3-4. The phase angle of impedance vs. frequency curves for the DMPC membrane, deposited on the Au(111)|β-Tg electrode (a) before and (b) after 20-h incubation in the 200-μg mL<sup>-1</sup> nitrophenols mixture in 0.01 M PBS (pH = 7.4). Symbols and curves of the same colors represent experimental data and fitting the equivalent electrical circuits, respectively.

Figure 3.3-5. The modulus of impedance vs. frequency curves for the (a) 3×PC and (b) DMPC membrane, deposited on the Au(111)|β-Tg electrode, before (solid curves) and after (dashed curves) 20-h incubation in the 200-μg mL<sup>-1</sup> nitrophenols mixture in 0.01 M PBS (pH = 7.4). Symbols and curves of the same colors represent experimental data and results of fitting the equivalent electrical circuits, respectively.

Figure 3.3-6. Membrane (a) capacitance and (b) resistance calculated for the 3×PC bilayer before (curves 1 and 1', blue) and after (curves 2 and 2', red) 20-h incubation in the 200-μg mL<sup>-1</sup> nitrophenols mixture in 0.01 M PBS (pH = 7.4).

Figure 3.3-7. Membrane (a) capacitance and (b) resistance calculated for the DMPC bilayer before (curves 1 and 1', blue) and after (curves 2 and 2', red) 20-h incubation in the 200-μg mL<sup>-1</sup> nitrophenols mixture in the 0.01 M PBS solution. The inset shows enlarged values of resistance for the DMPC bilayer after incubation in the nitrophenols mixture solution.

Figure 3.3-8. AFM images of the 3×PC bilayer deposited on mica, acquired in Milli-Q water (a) before and (b) after 1-h incubation in the 2 mg mL<sup>-1</sup> nitrophenols mixture in 0.01 M PBS (pH = 7.4).

Figure 3.3-9. AFM images of the 3×PC bilayer deposited on mica, acquired in Milli-Q water (a, e) before and after incubation in the 200-μg mL<sup>-1</sup> nitrophenols mixture solution for (b, c) 15 min, (f) 18 h, and (g) 24 h. All images are of the same sample; Panel g was captured in a different sample area. Image (c) shows an enlarged area marked in Panel b, and graph (d) shows the cross-sectional height profile taken along the line indicated in Panel c.

Figure 3.3-10. AFM images of (a, b) topography and (d, e) corresponding Young's modulus maps of the DMPC bilayer deposited on mica, acquired in Milli-Q water, (a, d) before and (b, e) after 1-h incubation in the 200- $\mu\text{g mL}^{-1}$  nitrophenol mixture in 0.01 M PBS (pH = 7.4). (c) Cross-sectional height profile and edge fit (dashed curve), and (f) Young's modulus histograms of the DMPC bilayer before (curve  $d'$ , blue) and after (curve  $e'$ , red) incubation in the nitrophenols mixture.

Figure 3.3-11. The AFM topography images of the DMPC bilayer deposited on mica (a) before and (b) 24 h after DMPC incubation in 200  $\mu\text{g mL}^{-1}$  nitrophenols mixture in 0.01 M PBS (pH = 7.4). (c) Cross-sectional height profiles, taken along the lines indicated in Panels a and b and corresponding edge fits (dashed curves).

Figure 3.4-1. The phase angle as a function of frequency curves for the Au(111)| $\beta$ -Tg|3 $\times$ PC/3 $\times$ PG membrane (a) in the absence and the presence of LL-37 at the (b) 1:500 and (c) 1:60 peptide-to-lipid molar ratio at different potentials in 10 mM PBS (pH = 7.4). Symbols and curves of the same colors represent experimental data and results of fitting the equivalent electrical circuits, respectively. Inset in Panel b shows the low-frequency range of the phase angle changes with frequency, magnified.

Figure 3.4-2. The modulus of impedance vs. frequency curves for the Au(111)| $\beta$ -Tg|3 $\times$ PC/3 $\times$ PG model microbial membrane (a) in the absence and presence of the LL-37 at the (b) 1:500 and (c) 1:60 peptide-to-lipid molar ratio, at different potentials in 10 mM PBS (pH = 7.4). Symbols and curves of the same colors represent experimental data and results of fitting the equivalent electrical circuits, respectively.

Figure 3.4-3. (a) Defects resistance ( $R_{\text{def}}$ ) and (b) membrane capacitance ( $Q_m$ ) calculated at different potentials for the Au(111)| $\beta$ -Tg|3 $\times$ PC/3 $\times$ PG membrane in the absence (curve 1 and 1') and in the presence of LL-37 (curves 2 and 2' as well as 3 and 3'). Curves 2 and 2', and 3 and 3' refer to the 1:500 and 1:60 peptide-to-lipid molar ratio, respectively.

Figure 3.4-4. The AFM images of the 3 $\times$ PC/3 $\times$ PG membrane deposited on mica, in the LL-37 (a) absence and (b, c) presence, at (b) 1:500 and (c) 1:60 peptide-to-lipid molar ratio. Insets in Panels b and c show higher resolution images exhibiting the membrane morphology in more detail. (d) Corresponding cross-sectional profile along the dashed line in Panel a. Measured heights indicated in panel (d) are  $h_1 \approx 5.71$  nm,  $h_2 \approx 4.07$  nm, and  $h_3 \approx 3.38$  nm.

Figure 3.4-5. (a) Exemplary force-distance curves for the 3 $\times$ PC/3 $\times$ PG membrane in the LL-37 absence (curve 1) and presence (curve 2). (b-f) Histograms of the jump width and breakthrough forces of the F-D curves acquired for the 3 $\times$ PC/3 $\times$ PG membrane deposited on

mica in the LL-37 (b, c, e) absence and (d, f) presence at the 1:60 peptide-to-lipid molar ratio. For the intact bilayer, breakthrough force distributions are bimodal as shown in Panels b, the 1<sup>st</sup> jump (*A* and *B* distribution), and c, the 2<sup>nd</sup> jump (*A'* and *B'* distributions).

Figure 3.4-6. The AFM images of the 3×PC/3×PG membrane deposited on mica, (a) before and (b) 15 min, and (c) 65 min after 1-μg LL-37 injection into the AFM cell, which corresponds to the 1:500 peptide-to-lipid molar ratio. Corresponding cross-sectional profiles along dashed lines in the image (a), (b), and (c) are shown in (d), (e), and (f), respectively. Measured height differences indicated in panel (f) are  $\Delta h_1 \approx 1.3$  nm,  $\Delta h_2 \approx 1.0$  nm, and  $\Delta h_3 \approx 3.0$  nm.

Figure 3.4-7. (a) and (b) PM-IRRA spectra for the C–H stretching region of the 3×PC/3×PG acyl chains, in the absence and presence of LL-37 at the 1:500 peptide-to-lipid molar ratio, respectively, for selected potentials vs. Ag|AgCl in 0.1 M NaF in D<sub>2</sub>O. Corresponding spectra for randomly oriented molecules that mimic experimental conditions are shown in Panel c and d, respectively. They were calculated using the optical constants of cell materials.

Figure 3.4-8. The optical constants for the C–H stretching region, determined from 3×PC/3×PG vesicles in D<sub>2</sub>O. The dashed curve indicates a refractive index, and the solid curve indicates an attenuation coefficient.

Figure 3.4-9. Changes in the (a)  $\nu_s(\text{CH}_2)$  band center position, (b)  $\nu_s(\text{CH}_2)$  band FWHM, and (c) lipid acyl chains average tilt angle (with respect to membrane normal) as a function of potential for the 3×PC/3×PG bilayer deposited on the Au(111)|β-Tg electrode, in the (■) LL-37 absence and (●) presence, in the 0.1 M NaF in D<sub>2</sub>O solution.

# Table of contents

Statement of originality.....	iii
Acknowledgments.....	v
Funding.....	vii
List of publications.....	ix
List of patent applications.....	xi
Poster presentations at international conferences.....	xiii
Oral presentations at international conferences.....	xv
List of abbreviations.....	xvii
List of symbols.....	xx
Abstract (Eng.).....	xxiii
Abstract (Pol.).....	xxv
List of tables.....	xxvii
List of figures.....	xxix
Table of contents.....	xxxix
CHAPTER 1: Literature review.....	1
1.1. Introduction.....	1
1.2. Antimicrobial peptides as a possible solution to antibiotic resistance.....	1
1.3. Biological membranes and model membranes.....	5
1.3.1. Biological membranes, their structure, and function.....	5
1.3.2. Biomimetic membrane models.....	9
1.3.3. The electric potential across a bilayer lipid membrane.....	12
1.3.4. Mechanical properties of a bilayer lipid membrane.....	14
1.4. Lipid bilayer fabrication methods.....	16
1.4.1. Langmuir films.....	16
1.4.2. Small unilamellar vesicles fusion.....	17
1.4.3. A multicomponent phospholipid bilayer.....	20
1.5. Physicochemical studies of model biological membranes.....	21
1.6. Peptide-lipid interaction studies on the example of LL-37 human cathelicidin.....	28
1.7. Objectives of the thesis.....	32
CHAPTER 2: Materials and methods.....	34
2.1. Materials.....	34

2.1.1. Reagents and solutions.....	34
2.1.1.1. Phospholipids stock solutions.....	34
2.1.1.2. Peptides stock solutions.....	35
2.1.1.3. Supporting electrolyte solutions.....	36
2.1.2. Cleaning procedures.....	36
2.1.3. Sample preparation.....	37
2.1.3.1. Gold(111) electrode handling.....	37
2.1.3.2. Hydrophilic modification of gold(111) electrode.....	38
2.1.3.3. Small unilamellar vesicles deposition.....	39
2.1.3.4. Langmuir films formation.....	39
2.2. Instrumentation and techniques.....	41
2.2.1. Atomic force microscopy.....	41
2.2.1.1. PeakForce Quantitative Nanomechanical Mapping.....	41
2.2.2. Electrochemical techniques.....	42
2.2.2.1. Cyclic voltammetry.....	42
2.2.2.2. Metal-solution interface and the electric double layer.....	43
2.2.2.3. Differential capacitance and the potential of zero charge.....	44
2.2.2.4. Electrochemical impedance spectroscopy.....	46
2.2.2.5. Equivalent electric circuits.....	48
2.2.3. Polarization-modulation infrared reflection-absorption spectroscopy.....	49
2.2.3.1. Introduction and fundamental theory.....	50
2.2.3.2. PM-IRRAS setup.....	51
2.2.3.3. Optimization of the PM-IRRAS experimental conditions.....	52
2.2.3.4. Corrections of the PM-IRRAS experimental spectra.....	54
2.2.3.5. Transmission IR spectroscopy.....	56
2.2.3.6. Optical constants.....	57
2.2.3.7. Simulation of the PM-IRRA spectra.....	58
2.2.3.8. PM-IRRA spectra band deconvolution.....	59
2.2.3.9. Determination of the orientation of organic molecules adsorbed at the metal electrode surface.....	60
2.3. Experimental procedures.....	63
2.3.1. Atomic force microscopy imaging.....	63
2.3.1.1. Calibration procedure.....	63

2.3.1.2. AFM nanomechanical data analysis.....	64
2.3.1.3. Finite thickness correction.....	65
2.3.2. Electrochemical measurements.....	66
2.3.2.1. Electrochemical impedance spectroscopy measurements and data analysis.....	67
2.3.2.2. Chronocoulometry measurements.....	67
2.3.3. PM-IRRAS measurements.....	67
2.3.3.1. PM-IRRAS experiment.....	67
CHAPTER 3: Results and discussion.....	70
3.1. Nanomechanical characterization of a DMPC single bilayer in a ripple phase.....	70
3.1.1. Phospholipid bilayer and its phase transitions.....	70
3.1.2. Ripple phase in a single DMPC bilayer.....	71
3.1.3. Nanomechanical mapping of a single DMPC bilayer in a ripple phase.....	76
3.1.4. Conclusions.....	80
3.2. Orientational and conformational studies of BacSp222 activity towards a DMPC bilayer.....	81
3.2.1. Bacteriocin BacSp222.....	81
3.2.2. Electrochemical properties of the DMPC bilayer in the presence of BacSp222.....	82
3.2.3. Conformational and orientational changes of the DMPC bilayer in the presence of BacSp222.....	84
3.2.4. Change of orientation and secondary structure of BacSp222 in the presence of the DMPC bilayer in the electric field.....	88
3.2.4.1. ATR-IR study of the BacSp222 orientation in a dehydrated DMPC multibilayer.....	92
3.2.5. AFM imaging of the DMPC bilayer disruption upon BacSp222 activity.....	94
3.2.6. Conclusions.....	96
3.3. Toxicity of selected airborne nitrophenols on a model lung-like lipid membrane.....	97
3.3.1. Nitrophenols – environmental pollutants and screening of their toxicity effects.....	97
3.3.1.1. Preparation of nitrophenols mixture.....	98
3.3.1.2. Model lung-like lipid membrane.....	99

3.3.2. Cytotoxic activity of the nitrophenols mixture towards BEAS-2B and A549 epithelial cells.....	99
3.3.3. Electrochemical study of defect formation in a model membrane.....	101
3.3.4. Phospholipids rearrangement and model membrane disintegration upon nitrophenols activity.....	107
3.3.5. Conclusions.....	111
3.4. Interaction of LL-37 human cathelicidin peptide with model microbial-like lipid membrane.....	112
3.4.1. LL-37 cathelicidin peptide.....	112
3.4.2. Electrochemical study of defects formation in a model membrane.....	112
3.4.3. AFM imaging of model membrane disintegration upon LL-37 activity.....	117
3.4.4. Changes in orientation and conformation of the phospholipid acyl chains in the presence of LL-37.....	123
3.4.5. Conclusions.....	127
CHAPTER 4: Research summary and future prospective.....	128
References.....	130

# CHAPTER 1: Literature review

## 1.1. Introduction

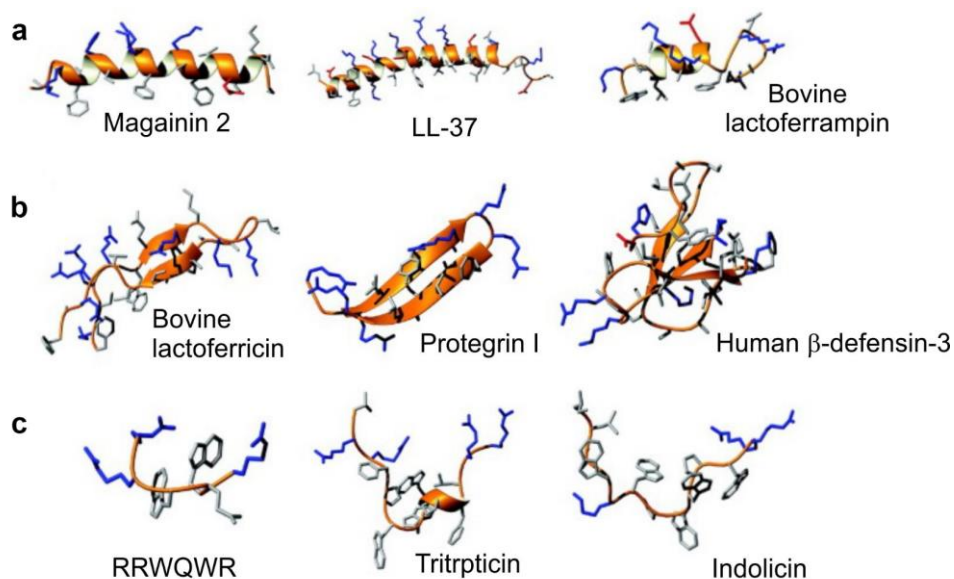
This chapter is conceived as a general introduction to model biological membranes and antimicrobial peptides (AMPs). It is organized as follows. It begins with a brief overview of the antibiotic resistance problem, which became a motivation for the research presented herein. Then, the current possibilities for developing AMPs as new antibiotics and their mechanisms of activity are discussed. The structure of the biological cell membrane is very briefly presented to broaden the understanding of biomimetic membrane studies and then compared to model membranes and their design. Next, techniques used to study lipid-protein interactions are described, and it is discussed why surface-sensitive techniques applied to biomimetic membranes are useful and complementary to other studies. Finally, the current knowledge of the LL-37 peptide interactions with biological and model membrane systems is discussed.

## 1.2. Antimicrobial peptides as a possible solution to antibiotic resistance

The motivation for the research undertaken in the present work is the problem of antibiotic resistance in bacteria. Antibiotics are used to prevent and treat bacterial infections in humans and animals. Antibiotic resistance occurs in bacteria when activating a self-defense resistance mechanism in response to antibiotic exposure. Medicine faces a huge challenge as bacterial resistance to conventional antibiotics is overgrowing. Moreover, bacteria fast adapt to new threats and develop various new mechanisms preventing any antibiotic from working effectively. Diseases that used to be easily curable, such as pneumonia, tuberculosis, gonorrhea, salmonella, may soon become, or already are, difficult or impossible to cure. In the U.S.A. alone, above 2.8 million antibiotic-resistant infections occur, and more than 35 000 people die each year because of ineffective antibiotics, as reported by the CDC.<sup>1</sup> World Health Organization states that antibiotic resistance is one of the biggest threats to global health and food safety nowadays, as it can affect anyone in any part of the world.<sup>2</sup> One of the actions undertaken by the healthcare and pharmaceutical industries is to research and develop entirely new classes of antibiotics or other antimicrobial agents.

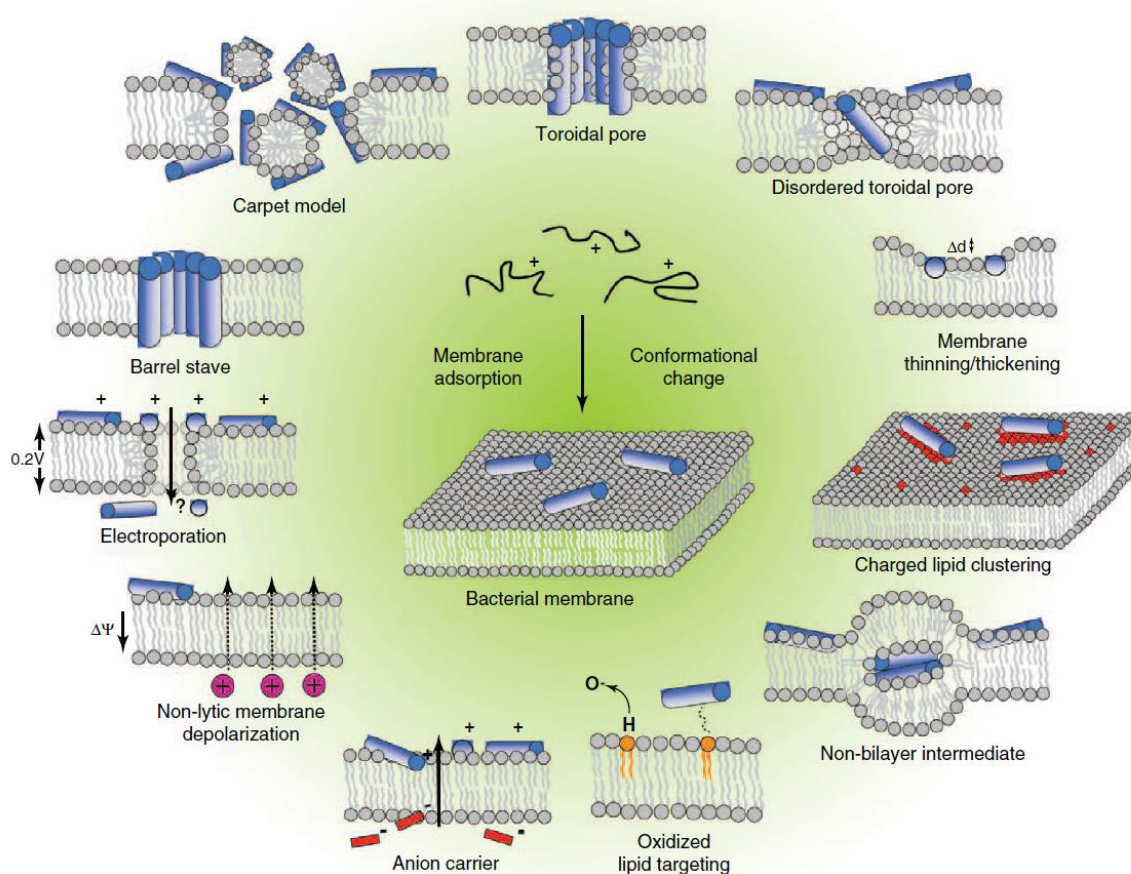
Membrane-active peptides are in abundance in nature. Considering their initial activity, they can be classified into three major classes, i.e., AMPs acting through membrane disruption, amyloid peptides binding and permeabilizing cell membrane, and cell-penetrating peptides able to translocate across a membrane.<sup>3</sup> AMPs are produced by almost all organisms and are a part of the innate immune response.<sup>4</sup> Animals and plants produce AMPs in tissues where the infection occurred, exhibiting a range of antibacterial, antiviral, antifungal, and antiparasitic activities<sup>5</sup> mainly through membrane disruption.<sup>6</sup> Moreover, some modulate immune response.<sup>7,8</sup> They are promising as therapeutic alternatives to conventional antibiotics, capable of effectively killing multi-drug-resistant bacteria.<sup>9</sup>

There have been above 50 families of AMPs recognized so far, among them aureins, bacteriocins, cathelicidins, cecropins, magainins, dermaseptins, defensins, mellitins, and many others.<sup>10</sup> Physicochemical properties also categorize AMPs. One class of AMPs that gained particular attention as a novel type of antibiotics is cationic AMPs.<sup>7</sup> Preferably, alternatives to antibiotics should exhibit selectivity towards pathogens' membrane while being non-toxic to host cells and not inducing resistance mechanisms in target pathogens. The former is perfectly accomplished by cationic AMPs, which, due to their structure, interact selectively, and at the same time, non-specifically (without specific mediating membrane species)<sup>11</sup> involving hydrophobic and electrostatic interactions with negatively charged bacterial membranes. They are usually small, 10-50 amino acid amphipathic peptides, comprised of up to 50% hydrophobic amino acid residues, and characterized by a positive net charge generated mainly by basic residues of lysine and arginine.<sup>7</sup> They exhibit different secondary structures, including  $\alpha$ -helices,  $\beta$ -sheets,  $\beta$ -turns (Scheme 1.2-1). It was initially hypothesized that their mode of action is membrane disruption through pore formation. However, the reality turned out to be much more complicated, and the mode of action of various AMPs remains unrevealed.<sup>12, 13</sup> Several models were proposed to describe possible modes of membrane activity of various AMPs (Scheme 1.2-2), including, among others, pore formation, "carpet" model, and membrane thinning.<sup>14</sup> Moreover, proposed mechanisms of interaction are not excluding each other.



Scheme 1.2-1. Secondary structures of most commonly occurring AMPs classes: (a)  $\alpha$ -helical, (b)  $\beta$ -sheet, and (c) extended peptides, resolved by solution NMR spectroscopy in the presence of detergent micelles, except  $\beta$ -sheet peptides, whose structures were determined in aqueous solutions. Positively charged side chains are colored in blue, negatively charged in red, and remaining side chains in grey. Reproduced from Ref.<sup>14</sup>

Following Scheme 1.2-2, first, AMPs adsorb on the membrane surface in a flat-lying orientation through hydrophobic and electrostatic interactions. Then, usually, when a particular surface concentration is reached, AMPs can insert into the membrane to form a barrel-stave or toroidal pores. In the toroidal model, the lipid bilayer leaflets bend in the vicinity of a pore so that both AMPs and lipid headgroups surround the water inside the pore. AMPs form a compact structure in the barrel-stave model, similar to a barrel stave, with a channel opening. In the “carpet” model, AMPs may interact with lipids via peptide-lipid complexes formation and solubilize the membrane similarly to micellar dissolution instead of pore formation. After AMPs adsorption at the membrane surface, membrane thinning or thickening may occur. Moreover, lipid domains may be introduced through membrane reorganization leading to surrounding AMPs by anionic lipids. Non-bilayer intermediates can be induced in some specific cases, or AMPs may specifically target oxidized phospholipids. AMPs may become coupled with small anions across the bilayer, causing their efflux. In non-lytic membrane depolarization, the membrane potential can be influenced without structural damage. In the molecular electroporation model, the accumulation of AMPs on the outer leaflet increases the membrane potential so that membrane becomes permeable to various molecules, including AMPs themselves.



Scheme 1.2-2. A schematic representation of possible mechanisms of initial AMPs activity on the cytoplasmic bacterial membrane. The proposed mechanisms may occur combined. Reproduced from Ref.<sup>14</sup>

Knowledge of AMPs structure and its correlation with the mechanism of action is applied in designing novel antimicrobial agents used in clinical applications.<sup>8</sup> For example, in the recent five years, belonging to the lipopeptide class of AMPs murepavidin (called POL7080, NCT03409679) and surotomycin (called NCT01597505, NCT01598311), synthetic AMPs have entered phase 3 clinical trials.<sup>12</sup>

Worth mentioning, there is a significant number of AMPs databases containing structural and functional information, e.g., the Antimicrobial Peptide Database (ADP),<sup>15</sup> Database of Antimicrobial Activity and Structure of Peptides (DBAASP),<sup>16</sup> Data Repository of Antimicrobial Peptides (DRAMP),<sup>17</sup> Linking Antimicrobial Peptides (LAMP),<sup>18</sup> and many other. They are useful in finding structural information and target pathogens. However, molecular-level details of lipid-membrane interactions are usually not included or simply missing.

In the long journey from peptide sequence proposal, synthesis, through assigning activity mechanism, cytotoxicity, to clinical trials, various experimental techniques are employed to elucidate the mechanism of AMPs activity, e.g., X-ray diffraction, neutron scattering, solution nuclear magnetic resonance spectroscopy, circular dichroism spectroscopy, fluorescent

microscopy, atomic force, and electron microscopy, applied for the phospholipid vesicles, live cells, detergent micelles, and in native environments.<sup>12</sup> In overall, the conformational and physicochemical properties of AMPs are considered most important in determining an anti-microbial mode of activity,<sup>12</sup> along with the influence of membrane composition.<sup>19, 20</sup>

Although the techniques mentioned above are beneficial, they lack information regarding peptide-lipid interactions under electrochemical conditions, which provide biologically relevant conditions by mimicking transmembrane potential. That can be achieved by employing electrochemical and spectroelectrochemical measurements performed on electrode-supported planar biomimetic membranes.<sup>21</sup> Electrode-supported, similarly to the solid-supported bilayer, allows for applying surface sensitive techniques, such as imaging and spectroscopy, additionally introducing transmembrane potential. These issues are discussed below.

### **1.3. Biological membranes and model membranes**

Detailed understanding of peptide-lipid interactions first requires knowledge of the biological membrane structure and function. Biological membranes gained interest early on as essential components of all living organisms. They constitute a protective shell envelope around the cells as well as the cell nucleus. Thorough understanding of the membrane role in the organism, cell permeation, and signaling, further applications in drug delivery or sensing platforms were found, not to recall the most recent application in mRNA vaccines (however, with the use of cationic lipids, which do not occur in nature).

This section aims to draw the basic ideas behind biomimetic membranes, which is impossible without understanding biological membrane features. Therefore, biological membrane structure and functionalities are briefly discussed, together with its building blocks, lipids. Then, the possibilities in manufacturing biomembrane mimics and their principles are presented, followed by a short description of membrane electrical and mechanical properties.

#### **1.3.1. Biological membranes, their structure, and function**

Biological membranes play a key role as a base structure of all living organisms. It is exciting to track the versatility of cell membrane functions. It could be postulated that membranes are the most critical structural and functional components of the cell, providing the structural, barrier, contact, receptor, and transport functions. The biological membrane constitutes a cell envelope, a barrier that protects the cell from external conditions and maintains cell shape. It allows compartmentalization and modular design of the cell. Biomembrane is a carrier for

a vast range of proteins, peripheral and integral, responsible for cell signaling, thus playing an active role in information transfer between the cells. The membrane is selectively permeable to particular ions and enables controlled transportation of various molecules in and out of the cell. Selective permeability keeps ion concentration difference between the outside and inside of the cell, thus maintaining transmembrane potential. Once the non-equilibrium ion distribution is canceled because of cell membrane damage, cell apoptosis occurs. In other words, the presence of a membrane with such architecture and capabilities allows keeping the cell out of equilibrium with the environment, which is the key to maintain life processes.

The first idea of a cell membrane comprised of a phospholipid bilayer was experimentally deduced by comparing areas of monolayers of lipids extracted from red blood cells to calculated cell surface area.<sup>22</sup> Many years later, high-resolution electron microscopy helped develop, back in 1972, a fluid-mosaic membrane model,<sup>23</sup> which is still a relevant way to understand the structure of biological membranes.<sup>24</sup> It assumes that phospholipids arrange into a bilayer in which the proteins are anchored in various ways, including peripheral and integral orientation, forming fluid-mosaic structure, keeping both lipids and proteins mobile. The updated model accentuates the significance of lipids specialized clusters and protein complexes aggregates and emphasizes the role of non-random “mosaic” distribution of membrane surface assemblies<sup>25</sup> and specialized lipid rafts in cell signaling pathways.<sup>26</sup> Both proteins and lipids remain mobile within the bilayer, dynamically rearranging via Brownian motion. Lipids translational motion in the plane of the membrane occurs with a lateral diffusion coefficient of  $10^{-13}$  to  $10^{-8}$   $\text{cm}^2 \text{ s}^{-1}$ , its rotation around axes normal to the membrane surface is 0.1-100 ns, and motion of acyl chains is 0.01-1 ns.<sup>27</sup> There were other models proposed to describe biological membrane structure, e.g., it was postulated that the phospholipids are incorporated into a polymerized membrane protein structure.<sup>28</sup> However, they did not withstand the test of time and experimental results.

Lipid bilayers are self-organized structures. Lipids are amphiphilic molecules that self-assemble into bilayer structures driven by hydrophobic interactions. Three types of lipids are distinguished: phospholipids, glycolipids, and sterols, from which phospholipids are most abundant in biological cells. For instance, the predominant components of the eukaryotic cell membrane are the zwitterionic phospholipids (zero net charge), such as phosphatidylcholine (PC), phosphatidylethanolamine (PE), phosphatidylserine (PS), phosphatidylinositol (PI), and phosphatidic acid (PA). In contrast, prokaryotic cell membranes are enriched in negatively charged phospholipids like phosphatidylglycerol (PG), phosphatidylethanolamine (PE), or cardiolipin (CL) (Figure 1.3-1).<sup>29,30</sup> Additionally, cholesterol is only present in eukaryotic cells.

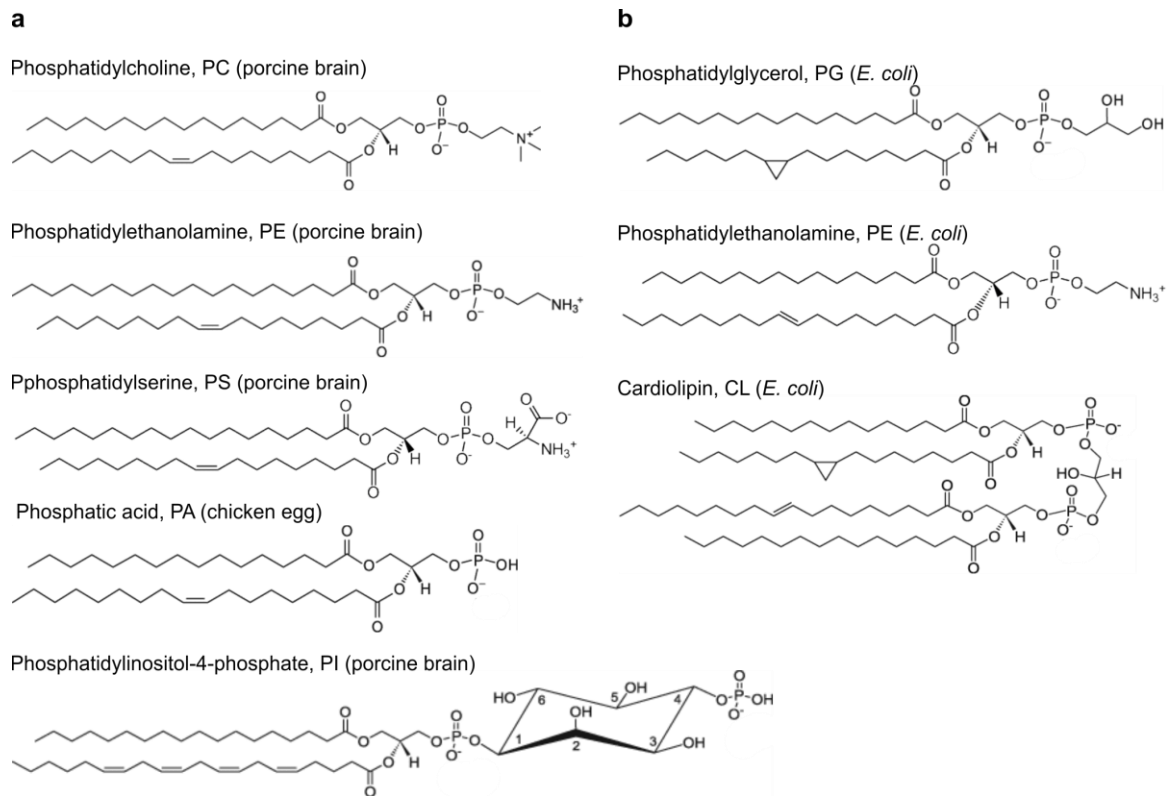


Figure 1.3-1. Examples of natural phospholipids isolated from (a) porcine brain and chicken egg and (b) *E. coli*, representing main components of eukaryotic and prokaryotic cell membranes, respectively.

Phospholipids are divided into two main classes, i.e., glycerophospholipids and sphingolipids (for instance, sphingomyelin). The glycerophospholipid polar headgroup contains choline connected through phosphate to glycerol. Glycerol is connected via ester links to two hydrocarbon fatty acid chains that constitute the hydrophobic part of the molecule. Acyl chains may contain a double bond (Figure 1.3-2). Such unsaturated acyl chains with the *cis* double bond will exhibit a kink which makes part of the chain tilted against the major phospholipid axis.

Structurally, biomembrane is anisotropic and inhomogeneous, with physical properties similar to liquid crystals. Such features make it more challenging to study the physical and electrochemical properties of the membrane, not to mention

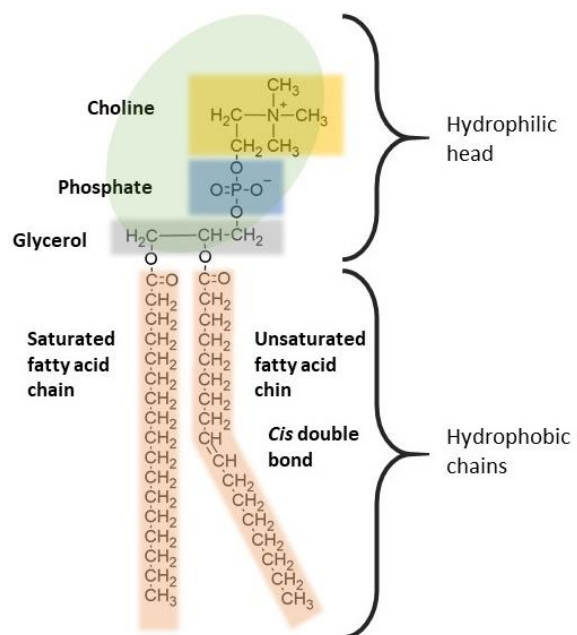


Figure 1.3-2. Structure of a glycerophospholipid, phosphatidylcholine (PC).

a small size of the cell of the order of several  $\mu\text{m}$ , and the abundance of a variety of membrane proteins (Figure 1.3-4a). Therefore, simplified models were introduced, such as micelles, liposomes, lipid bilayers, and solid-supported lipid films. Stable bilayer lipid membranes (BLMs) were first reported in 1962,<sup>31</sup> several years later, liposomes were discovered,<sup>32</sup> and solid-supported BLMs were introduced in 1986.<sup>33</sup> To understand how the physical properties of the phospholipid bilayer affect the biological functionality of a cell membrane, simplified membrane models are investigated.<sup>19, 34</sup>

Biological membrane exists in liquid-crystalline, lamellar phase. However, lipids' assemblies are polymorphic and mesomorphic, which means they form several solid phases and also intermediate phases between liquid and crystal phases (Figure 1.3-3).<sup>35</sup> They may form structurally and geometrically different phases, such as micellar aggregates and non-lamellar phases. Examples of polymorphic transitions are the subtransition from lamellar crystalline (subgel) ( $L_c$ ) to lamellar gel tilted ( $L_{\beta'}$ ) and pretransition from ( $L_{\beta'}$ ) to rippled gel ( $P_{\beta'}$ ). Thermotropic phase transitions proceed with increasing temperature from lamellar crystalline ( $L_c$ ), through the lamellar gel ( $L_{\beta}$ ), lamellar liquid-crystalline ( $L_{\alpha}$ ), and further mesomorphic phases, bilayer cubic ( $Q_{II}^B$ ), inverted hexagonal ( $H_{II}$ ), inverted micellar cubic ( $Q_{II}^M$ ), to inverted micellar ( $M_{II}$ ).<sup>35</sup> Moreover, the gel phase may be exhibited by different structures (interdigitated, rippled), and cubic phases may have different topologies ( $Im3m$ ,  $Pn3m$ ,  $Ia3d$ ). The intermediate liquid-ordered ( $L_o$ ) state (between  $L_{\beta}$  and  $L_{\alpha}$ ) is relevant to the lipid rafts in biological membranes.<sup>36</sup> Generally, double-chain lipids, like phospholipids, form  $L_{\alpha}$  and inverted phases (denoted II). The mesomorphic lipid phases proceed with an increase of water content from "water in oil" inverted phases ( $M_{II}$ ,  $Q_{II}^M$ ,  $H_{II}$ ,  $Q_{II}^B$ ), through  $L_{\alpha}$ , then normal "oil in water" phases ( $Q_I^B$ ,  $H_I$ ,  $Q_I^M$ ), to micellar solution ( $M_I$ ) and finally, monomers.<sup>35</sup> Inverted phases occur at low water content, which forces negative surface curvature by increasing the packing of lipid headgroups. In contrast, very high water content results in micellar and monomer solutions. Phase transition from lamellar gel to lamellar liquid-crystalline (solid-fluid), or chain-melting transition, occurs with large enthalpy change and results in a significant increase in lipid surface area ( $\sim 25\%$ ) and specific volume ( $\sim 4\%$ ),<sup>35</sup> which is reflected by the change in mechanical properties of the bilayer.

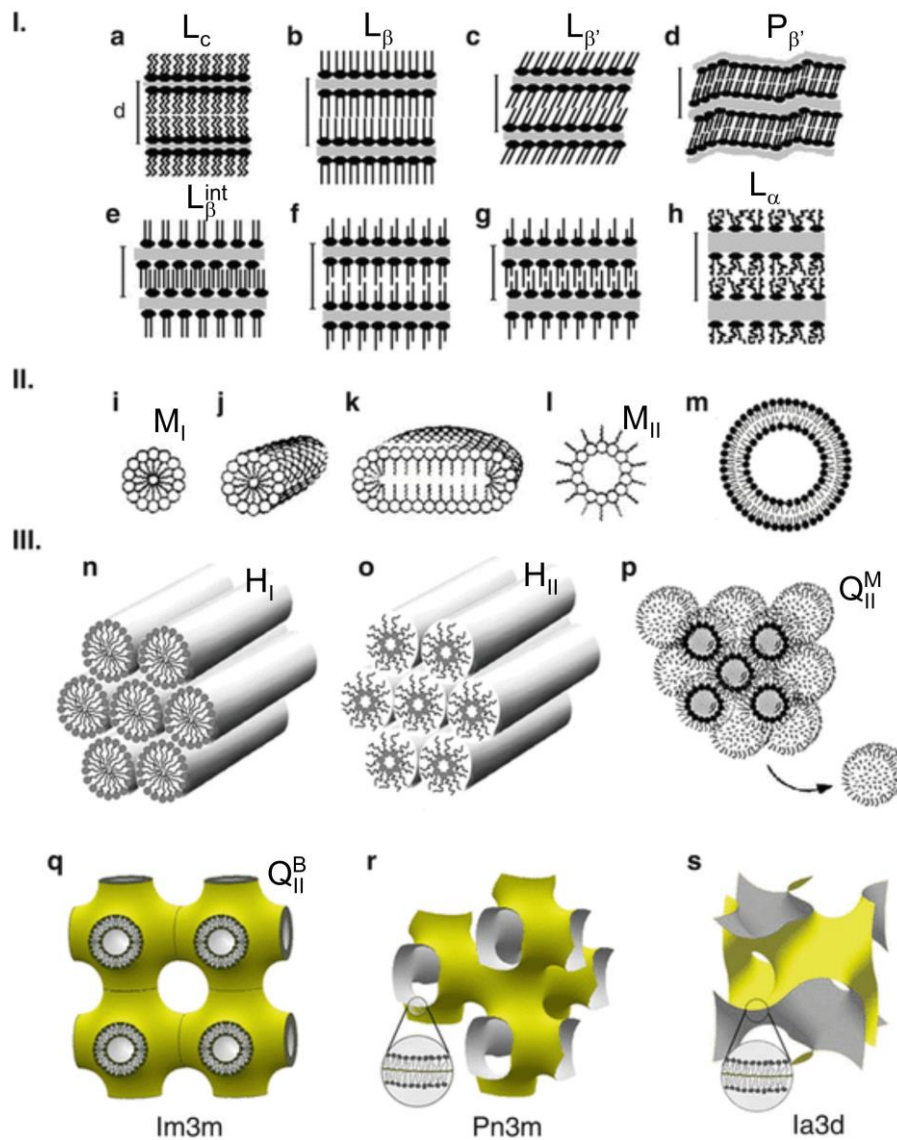


Figure 1.3-3. Schematic structures of lipid phases. I. Lamellar phase: (a) subgel,  $L_c$ ; (b) gel,  $L_\beta$ ; (c) gel tilted,  $L_{\beta'}$ ; (d) rippled gel,  $P_{\beta'}$ ; (e) fully interdigitated gel,  $L_{\beta}^{int}$ ; (f) partially interdigitated gel; (g) mixed interdigitated gel; (h) liquid crystalline,  $L_\alpha$ . II. Lipid micellar aggregates: (i) spherical micelles,  $M_I$ ; (j) cylindrical micelles (tubules); (k) disks; (l) inverted micelles,  $M_{II}$ ; (m) liposomes. III. Non-lamellar mesomorphic liquid crystalline phases: (n) hexagonal,  $H_I$ ; (o) inverted hexagonal,  $H_{II}$ ; (p) inverted micellar cubic,  $Q_{II}^M$ ; (q) bilayer cubic,  $Q_{II}^B$ ,  $Im3m$  topology; (r) bilayer cubic,  $Pn3m$  topology; (s) bilayer cubic,  $Ia3d$  topology. Adapted from Ref.<sup>35</sup>

### 1.3.2. Biomimetic membrane models

Model biological membranes mimic the structure and properties of biological membranes. They allow incorporating various macromolecules, e.g., enzymes, antibodies, receptors, nucleic acids, and pharmacological compounds, like drugs or antimicrobial peptides.

Solid-supported BLMs have planar geometry, so they take advantage of having no curvature. That scales better to the size of bacteria or other cells than the liposomes, which have a very high surface curvature. The resulting geometry of a solid-supported, planar lipid membrane allows for applying surface analytical techniques, such as scanning probe microscopy,

thermodynamic analysis, or scattering techniques.<sup>37</sup> The literature agrees that the supported BLMs are models that significantly contribute to fundamental studies on biological cell membranes,<sup>38</sup> and provide a sensing platform for protein studies,<sup>39-41</sup> allowing the application of electrochemical techniques.<sup>21, 42</sup>

For a phospholipid bilayer's solid support, hydrophilic and flat surfaces are favored. They allow the lipids to assemble readily on the surface via physisorption. Glass, silica, freshly cleaved mica, flame-annealed gold are often used. When immersed in neutral aqueous solutions, they exhibit negative surface charge densities.

Figure 1.3-4b-g shows several examples of solid- or metal- (gold) supported BLMs that differ in their architecture. Supported lipid monolayer (sLM) (Figure 1.3-4b) can be obtained using the Langmuir-Blodgett technique (Section 1.4.1 and 2.1.3). Bilayer lipid membrane (Figure 1.3-4c) can be deposited directly on solid support if it is sufficiently hydrophilic. A thin layer of water is present between the BLM and the gold electrode surface.<sup>43</sup> Supported BLM (sBLM) can be deposited by Langmuir-Blodgett – Langmuir-Schaeffer, or vesicle fusion methods (Sections 1.4.2 and 2.1.3). More sophisticated architectures of model membranes were introduced to reduce the negative impact of solid support. The solid support presence in proximity to the bilayer influences phospholipids' mobility and impacts peptide insertion. Therefore, it is preferable to provide a spacer between the bilayer and the substrate. Hybrid BLMs (hBLM), tethered BLMs<sup>40, 44, 45</sup> (tBLM), and polymer-cushioned BLMs (Figure 1.3-4e),<sup>46</sup> were introduced. Hybrid BLM is a lipid monolayer deposited on, e.g., alkylthiol monolayer, which acts as an inner bilayer leaflet and a spacer between the solid surface and the monolayer (Figure 1.3-4d). In tBLMs, specially synthesized thiolipids can anchor the bilayer and serve as a hydrophilic spacer. They can provide support for a BLM, forming a tethered BLM (Figure 1.3-4f). Gold support can be modified by self-assembly of a hydrophilic monolayer spacer containing thiol groups. It provides a highly hydrophilic and hydrated spacer allowing the bilayer to “float” on top of it (Figure 1.3-g).

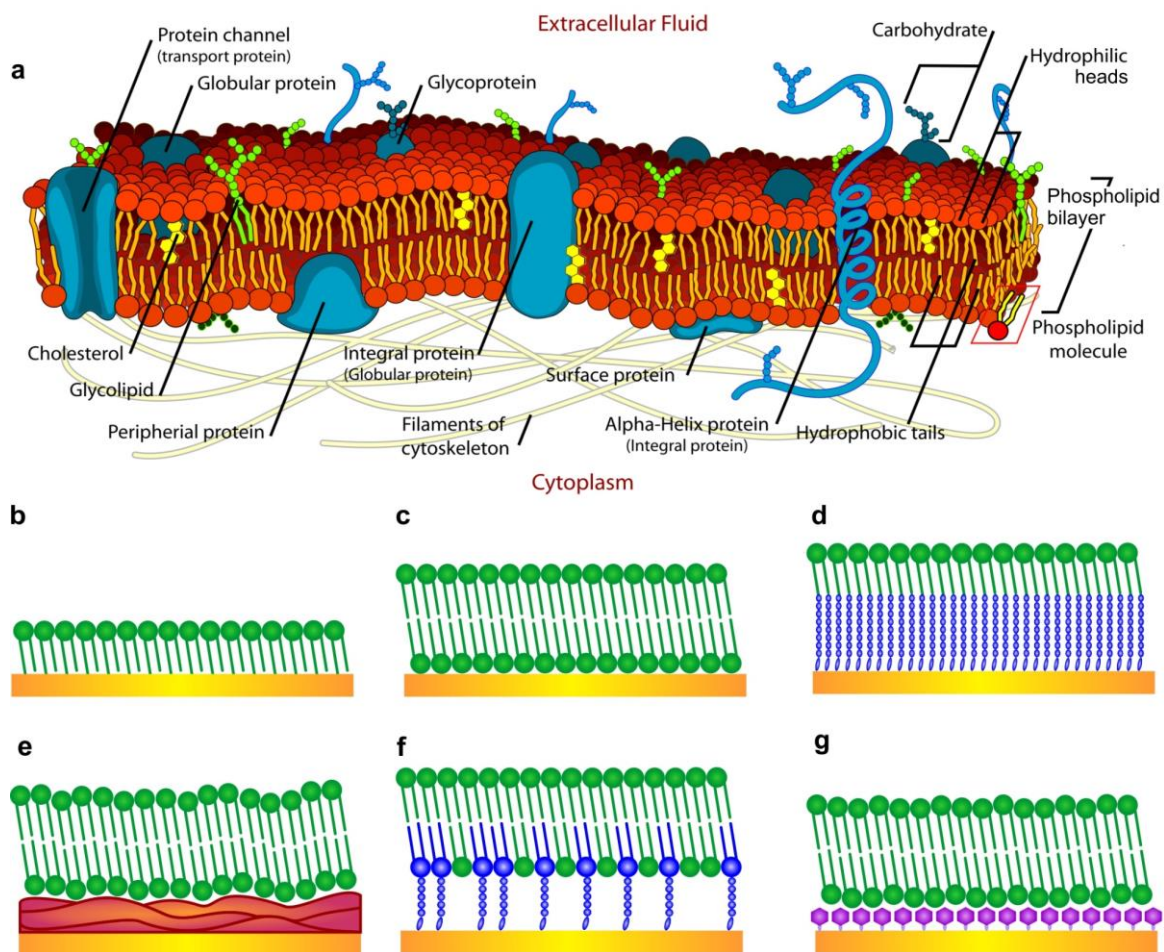


Figure 1.3-4. (a) A detailed diagram of a lipid bilayer cell membrane, reproduced from Ref.<sup>47</sup> Schemes of different metal-supported biomimetic membranes: (b) supported lipid monolayer, sLM; (c) supported BLM, sBLM; (d) hybrid BLM, hBLM; (e) polymer-cushioned BLM; (f) tethered BLM, tBLM; (g) floating BLM, fBLM. Adapted from Ref.<sup>21</sup>

A well-studied example of a hydrophilic spacer is a self-assembled monolayer of 1-thio- $\beta$ -D-glucose (SAM-Tg). It was characterized by atomic force microscopy (AFM),<sup>48</sup> electrochemical techniques, and electrochemical scanning tunneling microscopy (EC-STM).<sup>49</sup> SAM-Tg is easily spread on an Au(111) surface from methanol or an aqueous solution. It provides a water-rich spacer between the BLM and Au(111) electrode, improving phospholipid mobility and preventing peptides from substrate-induced denaturation. The presence of  $\beta$ -Tg improves hydration of lipid headgroups in the inner leaflet (leaflet in the proximity to the metal substrate). The water in the spacer region is structured as a strong hydrogen network, more ordered than that in bulk.<sup>50</sup> SAM-Tg is stable in a broad potential range; it is desorbed below  $\sim -600$  mV vs. SCE, and it oxidizes at positive electrode potentials.<sup>51</sup>

Floating BLM with SAM-Tg spacer was successfully applied in physicochemical studies of membrane-active peptides revealing, e.g., ionophore properties of valinomycin,<sup>52</sup> and

gramicidin A,<sup>53</sup> pore formation by alamethicin,<sup>54, 55</sup> and colicin E1,<sup>56</sup> BLM disruption by amyloid  $\beta$  peptides<sup>57</sup> and its inhibition.<sup>58</sup> This membrane model was also adapted to the present research due to its simplicity and effectiveness in producing stable BLMs.

### 1.3.3. The electric potential across a bilayer lipid membrane

The application of electrode-supported BLMs allows using sophisticated surface-sensitive techniques to study bilayer properties with molecular resolution. The electrode potential influences the metal surface reconstruction and phase transition of adsorbed layers directly or by influencing electrode charges.<sup>59</sup> Understanding the origin of electric potential profile across biomembrane is essential in interpreting experimental results acquired under electrochemical conditions.

According to the discussion in Ref.<sup>41</sup>, three components contribute to the potential drop across the membrane ( $\Delta\psi$ ), i.e., the transmembrane potential ( $\Delta\psi_m$ ), the potential generated by surface charges ( $\psi_s$ ), and the membrane dipole potential ( $\chi_m$ ).

The transmembrane potential,  $\Delta\psi_m$ , is the potential drop across the membrane caused by differences in ionic concentrations on both sides of the membrane and selective permeation of ions through the membrane (Donnan potential). The transmembrane potential of a 5-7-nm thick membrane is typically from  $-250$  to  $-10$  mV and results in electric field strength of  $-5 \times 10^7$  to  $-2 \times 10^6$  V m<sup>-1</sup>.<sup>60, 61</sup>

Charged or dipolar species present at the membrane surface, such as lipid headgroups and water dipoles, generate an outer (Volta) potential,  $\psi_s$ . The presence of fixed surface charges generates this potential. For negatively charged phospholipid headgroups, generating a diffuse double layer with a potential drop of approximately 60 mV, corresponding electric field strength, at a distance of 1 nm from the surface is  $2 \times 10^7$  V m<sup>-1</sup>.<sup>61</sup>

The orientation of dipolar residues of the lipids and water dipoles between the aqueous phases and the hydrophobic core of the membrane generates the membrane dipole potential,  $\chi_m$ .<sup>62</sup> The value of  $\chi_m$  cannot be measured directly in an experiment and can only be theoretically calculated<sup>63</sup> or deduced indirectly from an independent experiment. A  $\chi_m$  was determined to be between 220 and 280 mV for phosphatidylcholine, with a positive side inside the membrane.<sup>62</sup> The  $\chi_m$  potential drop across the small headgroup region produces a relatively large electric field of the order of  $10^8$ - $10^9$  V m<sup>-1</sup>.<sup>60</sup>

Surface charges are compensated by the ions present in the solution, resulting in a long-range  $\Delta\psi_s$  potential drop. In combination with a short-range  $\chi_m$  potential, a complex electric potential profile occurs across a membrane (Figure 1.3-5).

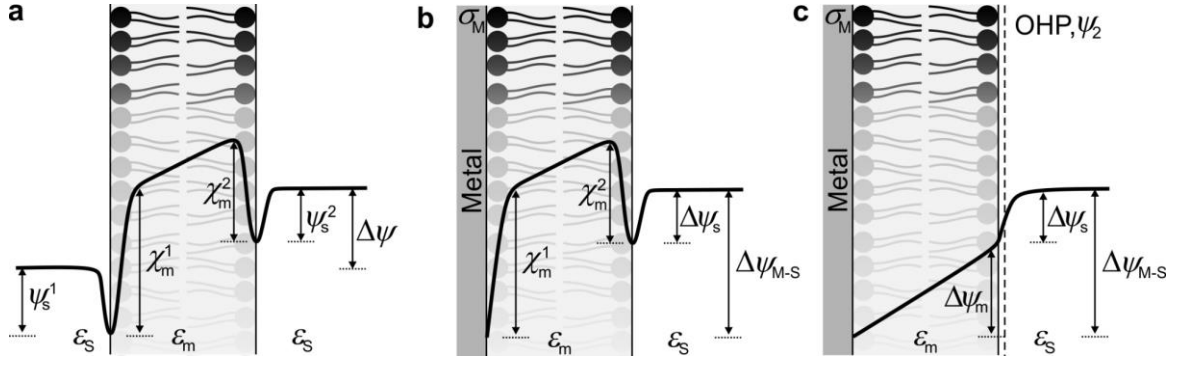


Figure 1.3-5. A schematic representation of an electric potential profile across (a) a bilayer lipid membrane, (b) electrode-supported BLM, (c) electrode-supported BLM with omitted surface potentials. Three contributions to electric potential profile ( $\Delta\psi$ ) are shown, the transmembrane potential ( $\psi_m$ ), the surface charges potential ( $\psi_s$ ), and the membrane dipole potential ( $\chi_m$ ). Superscripts 1 and 2 denote the inner and outer leaflet of the bilayer. Subscripts M, m, s, and S denote metal, membrane, surface, and solution, respectively. The electric permittivities  $\epsilon_m$  and  $\epsilon_s$  for the bilayer core and the aqueous phase are 2 and 80, respectively. Adapted from Ref.<sup>41</sup>

A lipid bilayer can be represented by a capacitor, with capacitance equal to  $C_m = \epsilon\epsilon_0 h^{-1}$  where  $\epsilon$  and  $\epsilon_0$  are the electric permittivities of the bilayer and vacuum, respectively, and  $h$  is a bilayer thickness. The specific capacitance of biological membranes is  $\sim 1 \mu\text{F cm}^{-2}$ .<sup>61, 62</sup>

For a lipid bilayer deposited on a metal electrode surface (Figure 1.3-5b), an influence from the metal charge ( $\sigma_M$ ) results in an outer (Volta) potential drop across the membrane (between the metal (M) and the bulk electrolyte (S),  $\Delta\psi_{M-S} \equiv \Delta\psi$ , Eq. 1.3.3-1)<sup>41</sup>, where  $C$  is the total capacitance of the interface. The total capacitance of the lipid bilayer in contact with a solution can be represented by two capacitors connected in series, the membrane capacitance ( $C_m$ ) and capacitance of the diffuse layer ( $C_s$ ). Often, for high electrolyte concentrations,  $C_m \approx C$ .

$$\Delta\psi_{M-S} = \frac{\sigma_M}{C} = \frac{\sigma_M}{C_m} + \frac{\sigma_M}{C_s} \quad 1.3.3-1$$

The inner (Galvani) potential is a sum of an outer (Volta) and surface dipole potential,  $\phi = \psi + \chi$ . Therefore, the inner potential drop between the metal electrode and the electrolyte solution can be expressed as a sum of the potential drop across the membrane (between the metal (M) and the outer membrane leaflet (2),  $\Delta\psi_{M-2} = \Delta\psi_m$ ) deposited on a metal electrode and the potential drop across the diffuse layer (between the outer membrane leaflet (2) and the bulk electrolyte (S),  $\Delta\psi_{2-S} = \Delta\psi_s$ ) or simply the outer Helmholtz plane potential (OHP,  $\Delta\psi_{2-S} \equiv \psi_2$ ) (Eq. 1.3.3-3).<sup>41</sup>

$$\Delta\psi_m = \frac{\sigma_M}{C_m} \quad 1.3.3-2$$

$$\Delta\phi_{M-S} = \frac{\sigma_M}{C_m} + \frac{\sigma_M}{C_s} + \chi_m = \Delta\psi_m + \Delta\psi_s + \chi_m \quad 1.3.3-3$$

The potential drop across the membrane can also be expressed as a difference between the potential applied to the electrode ( $E$ ) and the potential of zero charge ( $E_{pzc}$ ) (1.3.3-4).<sup>41</sup>

$$\Delta\psi_m = E - E_{pzc} - \psi_2 \quad 1.3.3-4$$

Thus, the value of the inner membrane potential drop can be expressed as follows.

$$\Delta\phi_m = E - E_{pzc} - \psi_2 + \chi_m \quad 1.3.3-5$$

The OHP potential can be calculated using the Gouy-Chapman theory of the diffuse layer, and the  $E_{pzc}$  can be determined in an independent experiment where free charge density can be determined from the differential capacity.<sup>64</sup> The inner potential drop across the membrane cannot be precisely experimentally determined because it requires knowledge of the dipole potential,  $\chi_m$ .<sup>41</sup> Therefore, an approximation is often used,<sup>41</sup> neglecting the membrane dipole potentials, resulting in a simplified electric potential profile (Figure 1.3-5c). Then, the  $\Delta\psi_m$  is treated as an approximate measure of  $\Delta\phi_m$ . The estimated transmembrane potential agrees with experimental values for a DMPC bilayer at the Au(111).<sup>41</sup> According to Equations 1.3.3-2 and 1.3.3-4, the potential drop across the membrane can be estimated using  $\sigma_M/C_m$  or  $E - E_{pzc} - \psi_2$ . The membrane potential drop analysis is important because it reassures that the experimentally determined transmembrane electric fields for a model system are biologically relevant.

### 1.3.4. Mechanical properties of a bilayer lipid membrane

Significant insights into understanding the nanomechanical characteristics of BLM can be found in studies where the AFM measurements are employed. Physicochemical properties of a lipid bilayer can be described in terms of mechanical stability, and any disruption in a bilayer structure may be recognized by changes in these properties. For a comparative study, detailed knowledge of intact bilayer's properties is required. In other words, BLM is characterized before and after interaction with membrane-active peptides.

Ion-binding, phospholipid structure,<sup>65</sup> and temperature<sup>66</sup> influence nanomechanics of a phospholipid bilayer. Therefore, the AFM membrane studies must be performed in an optimized and repeatable environment.

The influence of phospholipid chemical composition on the nanomechanical behavior was investigated using AFM (Figure 1.3-6). Upon plastic deformation, a jump occurs in the approaching part of the force-distance (F-D) curve, which is interpreted as a fingerprint of a bilayer mechanical stability.<sup>67</sup> The breakthrough force is the force needed to puncture the bilayer. It is a force at which elastically compressed molecules jump out from their initial positions in the bilayer at equilibrium, and as a result, form a cavity for the AFM tip penetrating the bilayer.<sup>68, 69</sup> Calcium ions increase the model lipid membranes rigidity, thickness, lipid

packing, and ordering while decrease lipid mobility.<sup>70</sup> The effects of pH and ionic strength of the aqueous environment, from which the phospholipid bilayer was deposited, and its nano-mechanics was studied, indicating that higher ionic strengths imply higher breakthrough forces.<sup>71</sup> Some studies also demonstrate that sample deformation below 20% of its thickness results in negligible mechanical contribution from the solid substrate at indentation forces of  $\sim 200$  pN,<sup>72</sup> and different substrates, i.e., hydrophilic mica, SiO<sub>2</sub>, gold, and hydrophobic APTES-functionalized mica, do not influence the bilayer properties.<sup>71</sup> On the contrary, other studies suggest that finite sample thickness approximation must be considered to account appropriately for the solid substrate's influence on BLM mechanical properties.<sup>73, 74</sup>

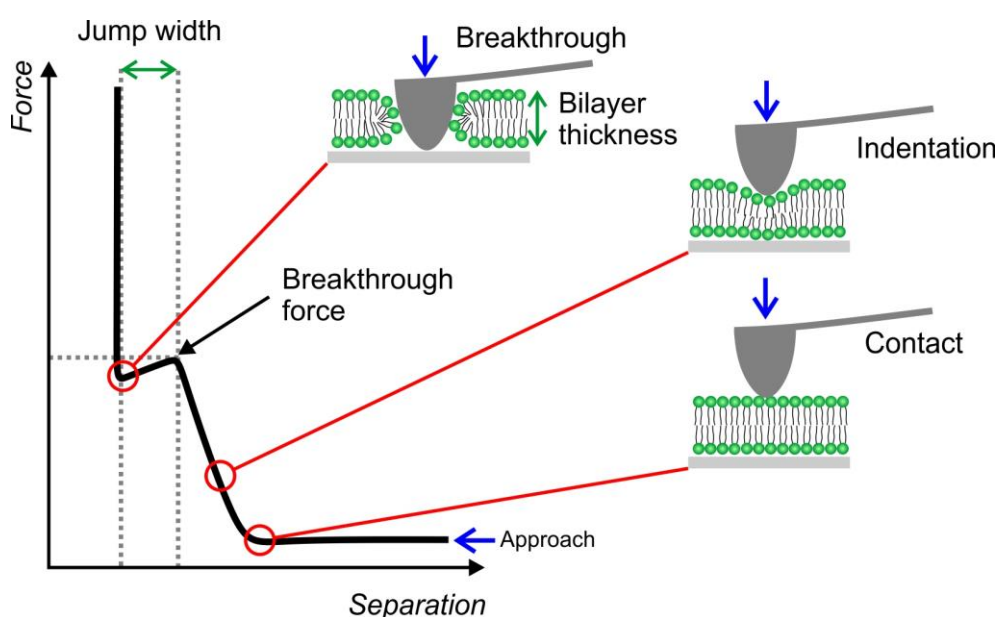


Figure 1.3-6. A schematic illustration of a force-distance curve representing a tip-sample separation distance during atomic force spectroscopy measurement. The tip approaches the sample's surface and, first, makes contact, then indents the sample, and when reaching a breakthrough force, it breaks through the lipid bilayer, which is represented by a jump in a force-distance curve.

Moreover, the nanomechanical stability of the bilayer increases with the increase of the length of the acyl chain of phospholipids. The force required to push the probe through the bilayer (for a jump to occur) linearly increases for each additional methylene group in the acyl chain.<sup>67</sup> Furthermore, the breakthrough force varies significantly between different lipid headgroups.<sup>67</sup> The presence of cholesterol linearly increases the mechanical stability of a bilayer in both liquid and gel phases.<sup>67</sup>

In phase transition, chain melting is connected with rotation around the carbon bonds of the phospholipid hydrocarbon chains.<sup>27</sup> The lowest energy holds for *trans* and the highest for *cis* conformations of the chains. In the gel state, mobility is restricted, and the saturated chains

are in the *trans* conformation. In the vicinity of transition temperature probability of rotation increases. Rotation by  $120^\circ$  relative to the *trans* results in  $+/-$  *gauche* conformations. As a result, a kink-like conformation appears in the lipid chain, and the chain becomes shorter by  $\sim 0.127$  nm, while the cross-sectional area increases.<sup>27</sup> Therefore, phase transition in a lipid bilayer from gel to the liquid phase is accompanied by a decrease in the thickness and increase in the area per molecule.<sup>75</sup> The shift of the kink is of the order of small molecules' diffusion rates through a lipid bilayer (like water or oxygen). Thus, it can be assumed that the transport of molecules through the lipid bilayer can be due to the appearance of free volume in a membrane, formed by kinks.<sup>27</sup>

As discussed above, the nanomechanical stability of a phospholipid bilayer depends on many factors, thus implying meticulous selection and maintenance of experimental conditions. Detailed understanding of a phospholipid bilayer behavior allows interpreting interaction mechanisms between membrane-active molecules and a phospholipid bilayer.

## 1.4. Lipid bilayer fabrication methods

The ability to produce stable biomimetic membranes in a planar geometry opened possibilities to apply surface characterization techniques to study BLMs' properties and directly observe membrane-active species interacting with BLMs. In this section, I will briefly present methods most commonly used for planar bilayer lipid membranes fabrication.

### 1.4.1. Langmuir films

Langmuir-Blodgett – Langmuir-Schaefer (LB/LS) transfers are commonly used to fabricate realistic models of supported lipid bilayers on solid substrates, especially if asymmetry between the leaflets' composition is needed. For the first time, the LB vertical transfer was used to deposit the dipalmitoylphosphatidylcholine (DPPC) films on a hydrophilic surface<sup>76</sup> to mimic a biological membrane. The LB/LS transfer allows preparing well-organized, asymmetric, Y-type planar lipid bilayers on solid surfaces.<sup>77</sup> In the Y-type bilayer, the hydrocarbon chains are turned to each other, and the polar head groups are directed outside of the membrane corresponding to biological membrane structure. The LB/LS transfer controls the lateral packing of lipid molecules in the supported lipid bilayer. Before the transfer, a lipid monolayer at the air|water interface is compressed to a selected surface pressure ( $\pi$ ). Usually, lipid monolayers are transferred at  $25 < \pi < 42$  mN m<sup>-1</sup>, mimicking the packing, orientation, and physical state of lipids in natural cell membranes.<sup>78</sup> The lipid composition, area per lipid

molecule, lateral packing, surface coverage, and the physical state of lipid molecules transferred onto a solid surface are controlled. It is possible to introduce membrane-active peptides to the water bulk and allow interacting with a lipid monolayer at the air|water interface. The resulting layer may be further transferred on a solid substrate. However, this approach requires a high amount of peptide, which is often unavailable, and the interaction occurs with a single leaflet only instead of a fully formed bilayer.

Figure 1.4-1 illustrates the LB/LS transfer resulting in the fabrication of an asymmetric supported lipid bilayer on a solid surface.<sup>79</sup> LB/LS method was successfully used in the fabrication of, e.g., POPE/POPG and POPC/Chol bilayers for studies of lipopeptide activity,<sup>80</sup> and an asymmetric h-DMPC/d-DMPC for layer-by-layer characterization studies of DMPC.<sup>81</sup>

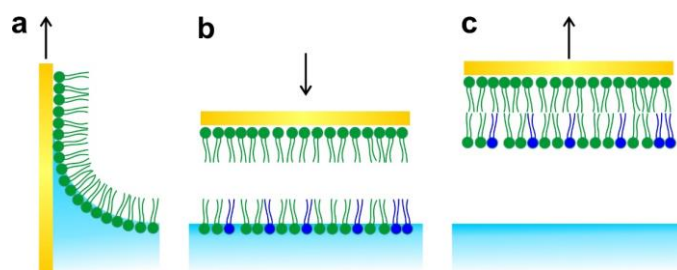


Figure 1.4-1. A schematic representation of the preparation of an asymmetric lipid bilayer on a solid substrate (gold) from the air-water interface (blue). (a) Langmuir-Blodgett vertical withdrawing, (b) Langmuir-Schaefer transfer by horizontal touching, (c) resulting Y-type bilayer. Different colors mark different lipids in the two leaflets.

### 1.4.2. Small unilamellar vesicles fusion

The amphiphilic nature of lipids allows them to form liposomes in aqueous solutions. Then, when in contact with a hydrophilic substrate, liposomes can spread on a solid surface by self-assembly. One of the first methods to prepare liposomes, herein referred to as phospholipid vesicles, was described by Barenholz.<sup>82</sup> This work showed the method of preparation of homogeneously sized small unilamellar vesicles (SUVs). With some minor modifications and improvements, it has been widely used to produce solid-supported, floating, or tethered BLMs.

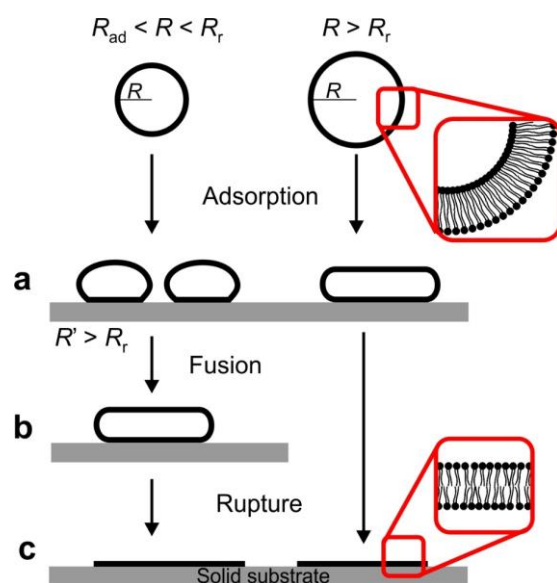
The vesicle fusion (VF) method is simple and highly effective, making it sufficient in many applications. Besides, it does not provide strict control over the composition of the phospholipid bilayer when it comes to phospholipid mixtures. The LB/LS method produces bilayers of higher packing density than VF, and phospholipids in a bilayer obtained by VF are less ordered,<sup>83</sup> which may be perceived as an advantage, facilitating peptide insertion. Finally, VF gives an advantage over LB/LS by allowing membrane-active peptides, even if available in

small quantities, to easily incorporate into vesicles under biologically relevant conditions and then be fused in the form of a bilayer.

Lipid vesicles formation requires a dry lipid film that undergoes hydration. As a result, stacks of bilayers become fluid and swell. During agitation, hydrated lipid sheets detach from the film, self-close, and form multilamellar vesicles (MLVs). Energy input is necessary to reduce the vesicles' size, so the solution is sonicated, and small unilamellar vesicles (SUVs) are formed. Another option to reduce multilamellar vesicles to unilamellar vesicles is extrusion. Lipid suspension is forced through a filter with a defined pore size to yield particles of a diameter near the pore size of the filter used. Extrusion through filters with 100 nm pores typically yields large unilamellar vesicles (LUVs) with a mean diameter of 120-140 nm.

The stages of BLM formation via vesicles fusion consist of the adhesion and fusion of SUVs at a solid substrate followed by their rupture, unrolling, and spreading onto the substrate. The theory of vesicles adhesion, fusion, and rupture has been experimentally confirmed.<sup>84</sup> The theory assumes that vesicles fusion stages depend on their size. Scheme 1.4-1 shows stages of lipid bilayer formation by vesicles fusion. Vesicles with a radius smaller than the critical adsorption radius ( $R < R_{ad}$ ) do not adsorb at the solid substrate. Vesicles with radius between  $R_a$  and  $R_r$  firstly need to fuse to form larger vesicles, which may flatten and then, rupture. Vesicles with a radius greater than minimum rupture radius ( $R > R_r$ ) directly adsorb as flattened vesicles and then rupture to lipid bilayer patches at the solid substrate. Mechanism of vesicle rupture is driven by its support-induced deformation. Moreover, vesicles initially adsorbed at the surface need to reach a critical surface density to initiate rupture into bilayer patches further.<sup>85</sup>

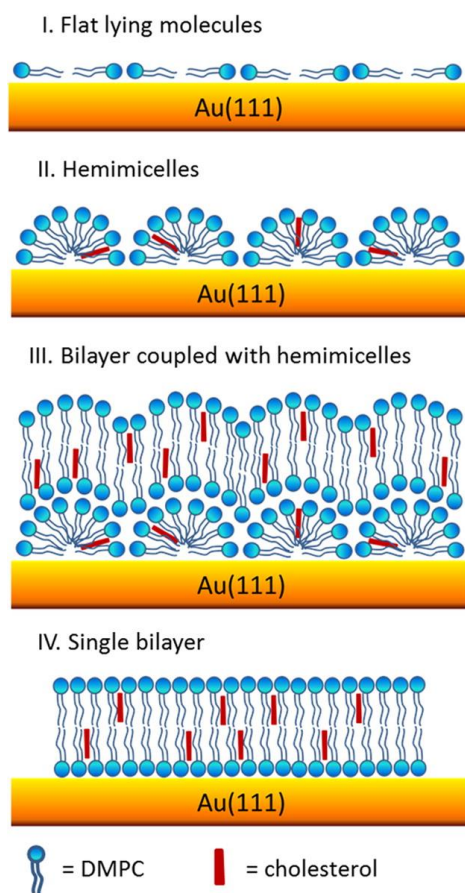
Furthermore, it has been demonstrated that the rupture efficiency of surface-adsorbed vesicles is improved in the presence of divalent and trivalent cations, such as  $Ca^{2+}$ ,  $Tb^{3+}$ .<sup>84</sup> Additionally, both vesicle adhesion to the surface and its rupture are enhanced at lipid bilayer edges.<sup>86</sup> For multicomponent lipid mixtures, the kinetics of substrate-lipid interactions and interactions between lipids are suggested to be different than for a single-component vesicle, resulting in different rupture times.<sup>87</sup> Also, the vesicle and the resulting bilayer composition may not be the same. For example, a POPC/DPPC mixture results in the bilayer enriched in POPC compared to the original vesicle composition.<sup>88</sup> Finally, it was shown in plasmon resonance and crystal quartz microbalance studies<sup>89</sup> that VF is only possible at atomically smooth surfaces, e.g., freshly cleaved mica.



Scheme 1.4-1. Schematic of vesicles fusion and subsequent stages of lipid bilayer formation on a solid substrate. (a) Adsorption of the vesicles with  $R > R_{ad}$  on the substrate. Vesicles with  $R > R_r$  flatten just after adsorption. (b) Fusion of the vesicles with  $R_{ad} < R < R_r$  already bound to the surface. After fusion, the radius enlarges to  $R' > R_r$ , sufficient for vesicle flattening. (c) Rupture of surface-bound vesicles with  $R > R_r$  and formation of lipid bilayer patches. Insets show structural details of schematically presented liposomes and bilayers. Adapted from Ref.[84](#)

The mechanism of SUVs spreading on gold electrodes was recently described.[90](#) DMPC phospholipids mixed with cholesterol were studied (Scheme 1.4-2). First, SUVs adsorb at the gold surface and then rupture, releasing phospholipid molecules that adopt a flat-lying orientation, with a head-to-head and tail-to-tail organization. These stripes promote the accumulation of lipid molecules in the form of hemimicelles. Hydrophilic and highly curved hemimicellar surface enhances the rupture of SUVs and the formation of a bilayer on top of hemimicelles. Coupled layers slowly transform into the single phospholipid bilayer by reorganization of phospholipids within the structure. Excess lipids are removed from the bilayer.

Fusion of SUVs was successfully applied in the deposition of DMPC/egg-PC<sup>55</sup> and DMPC/DMPG<sup>54</sup> fBLMs to study pore-forming alamethicin.



Scheme 1.4-2. A scheme of BLM formation at the Au(111) surface. Reproduced from Ref.<sup>90</sup>

### 1.4.3. A multicomponent phospholipid bilayer

Multicomponent BLMs are gaining interest as sufficient models for protein binding study.<sup>91</sup> A multicomponent lipid membrane applied in this study refers to a bilayer comprised of several kinds of phospholipids. Properties of this system are not a sum of properties of individual components, but they usually are more dynamic structures, with decreased bending modulus, area compressibility modulus, and viscosity.<sup>92</sup> The bilayer thickness of saturated lipids in the fluid phase is known to increase by  $\approx 0.19$  nm for each additional methylene in the lipid tail.<sup>93-95</sup> However, in binary lipid mixtures, the resulting thickness of the bilayer is lower than expected from single components. Examined lipid mixtures are by  $\sim 3$  to 8% thinner than expected if the single-component membrane thicknesses were additive.<sup>92</sup>

For multicomponent lipid mixtures, the kinetics of substrate-lipid interactions and interactions between lipids are different than for a single-component vesicle, resulting in different rupture times.<sup>87</sup> Moreover, the vesicle and the resulting bilayer composition may not be the same. For example, for POPC/DPPC mixtures, the resulting bilayer was enriched in POPC compared to the original vesicle composition.<sup>88</sup>

Application of a multicomponent system was a challenge and, simultaneously, a compromise between control over the composition of a resulting bilayer, which is not available via vesicle fusion, and enhanced access of peptides to the bilayer surface achieved in vesicles. The composition of a multicomponent bilayer was verified in the present study via AFM imaging by visualizing phospholipid domains. It allowed concluding on bilayer quality sufficient for further study.

## 1.5. Physicochemical studies of model biological membranes

The research presented in this thesis exploits the surface-sensitive physicochemical techniques to characterize model biological membranes influenced by the presence of membrane-active peptides or other toxic molecules. Therefore, this section is conceived to review current research in peptide-lipid interaction studies, including visualization techniques, such as scanning tunneling microscopy (STM), atomic force microscopy (AFM), electrochemical impedance spectroscopy (EIS), and polarization-modulation infrared reflection-absorption spectroscopy (PM-IRRAS) studies. Different techniques that were applied to gain knowledge regarding biological membranes and model membrane systems are described.

In biology, structure and function are inextricably related. A given AMP is regarded safe and efficient as a potential therapeutic when the minimum inhibitory concentration (minimum concentration necessary to inhibit bacterial growth) is low and maximum peptide concentration not yet inducing hemolysis is high.<sup>29</sup> In other words, it is beneficial to improve antimicrobial activity or decrease hemolytic activity, or both. These characteristics are related to physicochemical parameters of AMP, such as length, amino acid sequence, charge, hydrophobicity, amphipathicity, self-association, and secondary structure, which are also interconnected.<sup>29</sup> By manipulating these parameters, one can alter the resulting antimicrobial activity or hemotoxicity, which is one of the key interests among peptide scientists working on AMPs.

Physicochemical studies of AMPs offer those peptide scientists a helpful hand by digging into details of the relation between AMPs structure and its influence on model biological membranes of different compositions.

AMP activity can be tracked on bacteria *in vivo*, e.g., the activity of LL-37 was monitored on *E. coli* using fluorescence microscopy.<sup>96</sup> This allows localizing peptides while they translocate through the outer and inner membrane and correlate their location with the time of inhibition of cell growth. Freeze-fracture electron microscopy was applied to study changes in

the membrane structure of *E. coli* and *C. albicans* induced by the activity of bovine lactoferrin.<sup>97</sup> Regarding membrane models, liposomes were postulated to serve as a promising model of a biological cell<sup>98</sup> because they provide a platform helpful in elucidating the binding affinity of AMPs towards liposomes varying in, e.g., lipid composition. That can be achieved in fluorescence or titration calorimetry studies. However, such studies cannot provide information on the mechanism by which peptides destruct membranes. Moreover, peptide labeling is required for fluorescence studies, and freeze-fracture microscopy does not provide biologically relevant conditions.

Nuclear magnetic resonance (NMR) spectroscopy in a solid- and liquid-state are powerful in biological membranes studies, especially solid-state NMR spectroscopy provides high-resolution spectra. This spectroscopy provides information on the structure, orientation, and dynamics of peptides and lipids in spatially oriented samples.<sup>99</sup> For studying membrane properties, <sup>31</sup>P substitution is useful because each lipid molecule has one phosphate in a head-group. It was used to determine domain formation in bilayers comprised of anionic lipids induced by some AMPs. For example, cateslytin caused the segregation of lipid mixture into anionic and zwitterionic lipid domains.<sup>20</sup> <sup>2</sup>H NMR spectroscopy was applied to determine membrane order parameter, which depends on the extent to which lipid molecules are mobile in the membrane.<sup>20</sup> However, NMR spectroscopy requires high amounts of specially labeled molecules and highly ordered samples to produce high-resolution spectra.

Other studies informative on phospholipid bilayers' physicochemical characteristics were X-ray and neutron scattering, which brings vast information on phase behavior, structural and mechanical properties of bilayer lipid membranes by analyzing the sample electron (neutron) density patterns.<sup>95, 100</sup> Film thickness, hydration of the lipid bilayer, arrangement of the hydrophilic and hydrophobic parts can be determined. X-rays have mainly been used to determine the structure of crystalline materials. However, several techniques were developed that allowed for the successful characterization of liquid materials such as lipid bilayers.<sup>101</sup> For example, the ends of acyl chains of opposing bilayer leaflets in a DPPC gel phase were shown to be interdigitated, making both leaflets strongly coupled and their tilt angle interconnected,<sup>102</sup> which is highly detailed structural information. Also, the analysis of scattering patterns allows deriving membrane's elastic properties, such as bending modulus and bulk compression modulus, e.g., a study showed that the bending rigidity of DOPC bilayers decreases with increasing alamethicin peptide concentration.<sup>101</sup> However, these techniques have numerous limitations, e.g., measurements are usually performed on bilayer stacks instead of a single bilayer, samples are not always hydrated but in a crystalline state (it depends on the technique applied), and finally, like many other techniques, they require tedious structural modeling to extract sample properties.

As briefly described above, there are many excellent techniques available for studying the structural properties of lipid membranes. However, it is usually difficult to introduce biologically relevant conditions to these techniques. Nonetheless, it is achievable by using planar lipid membranes comprised of a single lipid bilayer under physiological buffer conditions and, finally, mimicking transmembrane potential. That is possible in the following techniques.

Possibly, vibrational spectroscopy is most often used in organic molecules study. Infrared (IR) spectroscopy can give detailed information on the sample's composition. Moreover, in anisotropic samples adsorbed on either a prism surface or solid reflective surface, data on the orientation and conformation of the molecules can be retrieved by applying attenuated total reflection IR (ATR-IR) or polarization-modulation infrared reflection-absorption spectroscopy (PM-IRRAS), respectively. Supramolecular assemblies can be characterized at the level of molecule fragments. Orientation and conformation of these fragments can be determined. In detail, the physical state of lipid acyl chains, hydration of lipid headgroups, and peptides secondary structure can be determined for a single lipid bilayer in PM-IRRAS.<sup>103</sup> Moreover, PM-IRRAS measurements can be performed under electrochemical conditions because reflective metal surfaces can serve as electrodes.<sup>104</sup> The principles of this method were already described in Ref.<sup>105</sup> PM-IRRAS under electrochemical conditions was successfully used to study physicochemical properties of phospholipid bilayers deposited at the Au(111) electrode<sup>60, 81, 106-111</sup> and then in peptide/lipid interaction studies.<sup>56, 112-115</sup> Au(111) was a sufficient substrate for applications in biomimetic studies.<sup>116</sup>

EIS well complements electrochemical PM-IRRAS. EIS is a kind of spectroscopy measuring the dielectric properties of a material. It can be used to extract information on the capacitance and permeability of a BLM and their changes when proteins are incorporated into BLM. EIS requires an equivalent electric circuit (EEC) model to extract the sample's structural information from the impedance spectrum. As discussed in Section 1.3.3 above, a lipid bilayer deposited on a metal surface can be regarded as a capacitor. Therefore, the simplest EEC that can describe this system is a supporting electrolyte resistance connected in series with membrane capacitance, an *RC* circuit. However, real systems deviate from this model. Many EEC models, some highly complex, have been proposed to analyze the EIS response of BLMs.<sup>117-120</sup> In general, EEC models for lipid membranes are heuristic.

An attempt to interpret the EIS response for tBLMs, accounting for defect formation, concluded that the response is too complex to be modeled by a finite number of conventional EEC elements and can only be derived by analytical calculations.<sup>120</sup> However, mathematical analysis has shown that this complicated response can be modeled by reducing it to a finite number of EEC elements in special cases.<sup>120</sup> The EEC model for tBLMs was proposed and described in detail by Valincius.<sup>121</sup> It was recently successfully applied in several studies of

BLMs not only in tethered but also floating BLM models, i.e., studies of ion transport mechanisms of gramicidin A channels in fBLM,<sup>53</sup> ionophore properties of valinomycin in fBLM<sup>52</sup> and tBLM,<sup>122</sup> daptomycin lipopeptide,<sup>123</sup> potential-controlled colicin E1 ion channels,<sup>56</sup> alamethicin channel formation in fBLM<sup>55, 124</sup> and tBLM<sup>114</sup> and inhibition by amiloride in tBLMs.<sup>125</sup> It is especially informative to compare similar studies on fBLM and tBLM because it verifies the applicability of the Valincius approach to analyze the EIS response of fBLMs. fBLMs may produce different EIS responses because the fBLM and tBLM spacers have different properties, such as thickness, hydration, and structure of the water layer.<sup>49, 50, 126, 127</sup>

Valinomycin was first studied in tBLM in different supporting electrolytes, showing selectivity towards K<sup>+</sup> cation.<sup>122</sup> However, peptides have restricted mobility in tBLMs, which may prevent potential-dependent reorganization of the peptide. Thus, valinomycin was again studied in fBLM. The obtained values of membrane capacitance for fBLM were much higher than for tBLM reported previously, and it was suggested that higher water content in the spacer region accounts for that increase. Similarly, membrane resistance values were much higher than obtained for a similar model system on tBLM. These data show that fBLMs are much more insulating and have fewer defects than tBLMs. The Valincius approach seems good enough for comparative studies, as performed in the present thesis. However, precise determination of BLM properties through this, or other, EEC model seems to seek further scrutiny.

Quartz crystal microbalance with dissipation monitoring (QCM-D) can be used to track in situ real-time peptide-lipid dynamics by monitoring changes in resonant frequency and energy dissipation of a quartz resonator. Simultaneously, the lipid bilayer deposited on top of it undergoes changes in mass (lipid extraction) or viscoelastic properties. Moreover, it can be determined if these changes occur near the bilayer|solution or bilayer|quartz interface, giving spatial information on peptide activity.<sup>128</sup>

Surface-sensitive or structure analyzing techniques are usually very demanding in terms of a proper interpretation of data. Very often, data analysis requires the application of various models assuming some properties of the system. Only visualization techniques, especially STM and AFM, can provide direct information on topographical changes induced by peptides.

Molecular-resolution images were provided by STM, e.g., in gramicidin A (gA) and alamethicin (Alm) studies at lipid monolayers (Figure 1.5-1).<sup>129, 130</sup> Pore structures were resolved, and direct information on peptide aggregation and the peptide assembly structure were obtained. For gA and Alm, the radiuses of AMPs assemblies were estimated as ~0.9 and ~1.0 nm, respectively.

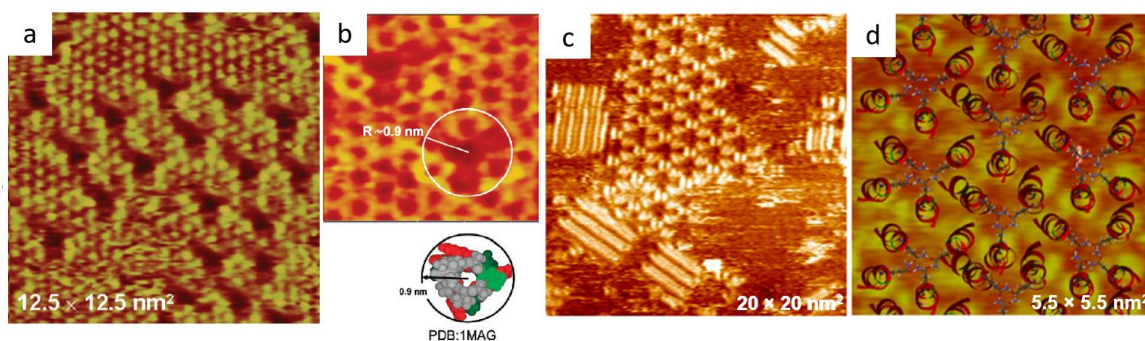


Figure 1.5-1. Electrochemical STM images of AMP interactions with a lipid monolayer. (a) DMPC/gA (9:1 lipid-to-peptide molar ratio) at the Au(111) electrode, acquired at 0.20 V vs. Ag|AgCl in 0.1 M NaF, using a tunneling current of 0.35 nA and a bias voltage of -0.45 V. (b) Enlarged image with individual gA channel and proposed peptide model based on structure from PDB databank under the access code of 1MAG. (c) DMPC/eggPC with alamethicin incorporated at the 15:1 lipid-to-peptide molar ratio, deposited at the Au(111) surface. Image acquired at tunneling current of 0.78 nA. (d) Structural model of alamethicin assembly proposed and superimposed on an STM image. Reproduced from Ref.[129](#),[130](#)

Moreover, Alm in a BLM was imaged (Figure 1.5-2).[54](#),[55](#) Unfortunately, bilayers are too thick to be imaged by STM. High-resolution AFM allowed resolving the detailed structure of the transmembrane pore-forming Alm assemblies.

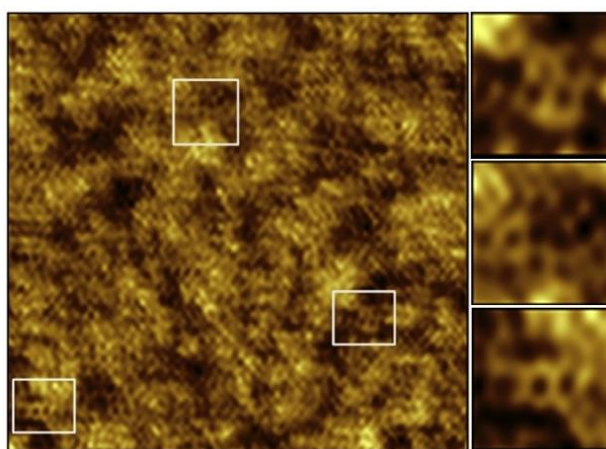


Figure 1.5-2. AFM topography image,  $100 \times 100 \text{ nm}^2$ , of the DMPC/DMPG/Alm (9:9:2) bilayer deposited at the Au(111)| $\beta$ -Tg electrode. The images on the right are zoomed fragments from the white boxes. Their size is  $20 \times 20 \text{ nm}^2$ . Reproduced from Ref.[54](#)

Many AMPs exhibit complex behavior, and their interaction with BLM includes several steps. AFM allows to in situ visualize consecutive stages of peptide-lipid interactions, e.g., shown for Smp43 peptide, which exhibited membrane defect formation via a carpet model combined with expanding poration.[131](#)

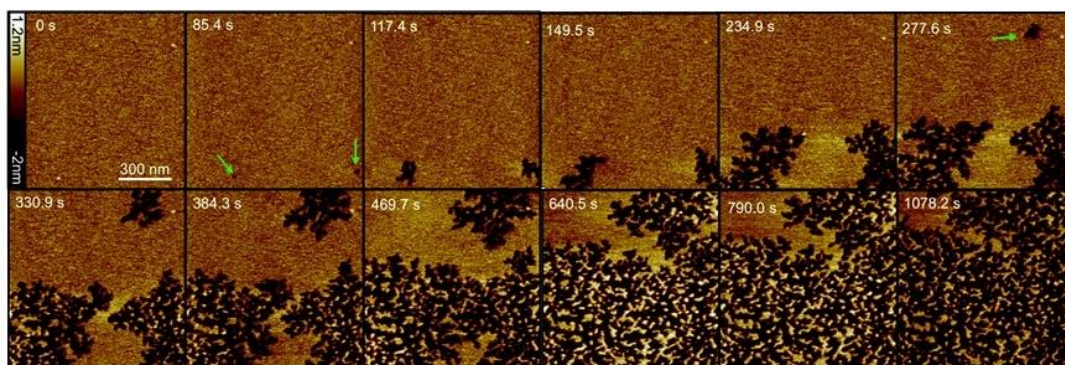


Figure 1.5-3. The fast-scanning AFM topography images of a DOPC/DOPG (1:1) sBLM in the presence of 1  $\mu\text{M}$  Smp43, injected into the fluid cell at  $t = 0$  s. Scan size is  $1 \times 1 \mu\text{m}^2$ . Reproduced from Ref.[131](#)

AFM allows visualizing any real-time AMPs effect on membrane topography, e.g., thinning or thickening, defect forming, clustering of phospholipids, changing packing of lipids resulting in changing of lipids phase, lipid extracting, forming nano-domains, peptide aggregating, all described in Ref.[132](#) and references cited therein. Moreover, membrane surface can be nanomechanically characterized, as shown for lipopeptides,[80](#), [133](#) and melittin.[134](#) The latter study exhibited that the mechanical properties of a model membrane influenced the mechanism of melittin interaction, even though both membranes were negatively charged. In less stiff DMPG, melittin reorients into the bilayer resulting in membrane micellization and lipid removal. For more stiff DMPS, it was not observed, so the peptide remained in surface-adsorbed, parallel orientation.

In summary, AFM, EIS, and PM-IRRAS studies have already been shown as powerful and complementary techniques to study peptide-lipid interactions. They complement each other well because all measurements can be performed under exactly the same conditions. This approach of complementary measurements performed for comparative purposes was adapted in studies described in the present thesis. Table 1-1 summarizes the application of these techniques combined to elucidate mechanisms of activity of several chosen membrane-active peptides.

Table 1-1. Comparison of proposed mechanisms of activity for selected membrane-active peptides studied by complementary EIS, PM-IRRAS, AFM techniques.

AMP	Secondary structure	Net charge at pH = 7.4	Water solubility	Proposed mechanism of action	Model membrane	Applied techniques	References
Daptomycin lipopeptide	Cyclic	-3	Soluble	Complex interaction including membrane depolarization	DPPG/POPG/CL (1:1:2) fBLM	AFM, QCM, SEIRAS	<a href="#">123</a>
Alamethicin	$\alpha$ -helical	-1	Insoluble	Barrel-stave pore formation	DPhPC fBLM, DPhPC sBLM, DPhPC/DPTL tBLM, DMPC/DMPG (1:1), DMPC/egg-PC (1:1) fBLMs	EIS, PM-IRRAS, AFM	<a href="#">54, 55, 113, 114, 124</a>
Valinomycin	Cyclic	0	Insoluble	Pore-forming, ionophore	DPhPC fBLM, DPhPC/DPTL tBLM	EIS, PM-IRRAS	<a href="#">52, 122</a>
Gramicidin A	$\alpha$ -helical	0	Insoluble	Pore-forming	DPhPC fBLM, DPhPC/DPTL tBLM	EIS, PM-IRRAS	<a href="#">53, 117</a>
Cecropin B	$\alpha$ -helical	+6	Soluble	Complex interaction including detergent-like mechanism and peptide-lipid aggregates	POPC/Chol (7:3), <i>E. coli</i> PE/PG (8:2) sBLMs	EIS, AFM, QCM	<a href="#">128</a>
Melittin	$\alpha$ -helical	+6	Soluble	Complex interaction including detergent-like mechanism and defect formation	DMPG, DMPS, DMPC, DMPC/Chol (7:3) sBLMs	EIS, AFM	<a href="#">134, 135</a>

## 1.6. Peptide-lipid interaction studies on the example of LL-37 human cathelicidin

The purpose of exploring all the information discussed in previous chapters is to apply them to peptide-lipid studies. Herein, I would like to focus on peptide-lipid interaction studies on the example of the LL-37 human cathelicidin peptide. Although the number of research studies regarding LL-37 activity is extensive, many of these studies reported contradictory results. Therefore the following section elucidates why different mechanisms are reported and what details regarding the LL-37 mechanism of activity have already been found.

The LL-37 is a 37-amino acid AMP representing one of the major AMPs families, cathelicidins. It is a cationic polypeptide with a net charge of +6 at pH = 7.4 of the following sequence: NH<sub>2</sub>-LLGDFFRKSKEKIGKEFKRIVQRIKDFLRNLPRTES-COOH. It adopts an  $\alpha$ -helical structure from residues 11-32 in both aqueous solution and the presence of lipids.<sup>136, 137</sup> This structure may change depending on membrane composition, including lipid saturation.<sup>138</sup> The  $\alpha$ -helix has a characteristic bend between Gly-14 and Glu-15.<sup>139</sup> The amino acids' sequence decides on hydrophobic and hydrophilic sites spatially separated (Figure 1.6-1). The LL-37 peptide is the only representative of cathelicidins found in humans. A highly conserved N-terminal signal peptide called a cathelin domain and a structurally varied C-terminus, an antimicrobial peptide component, characterize cathelicidins.<sup>140</sup> In other words, the antibacterial activity of LL-37 resides mainly in its C-terminal region, the LL-17-37 fragment.

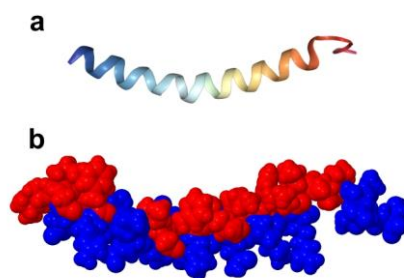


Figure 1.6-1. The structure of human LL-37, shown as (a) a ribbon diagram color-coded from N-terminus (blue) to C-terminus (red), (b) hydrophobic surfaces are marked red and hydrophilic are blue. Structure available from PDB databank under the access code of 2K60.

LL-37 was first identified in 1995 by three groups independently,<sup>141-143</sup> and first isolated from neutrophils.<sup>142</sup> However, it is expressed by many innate immune cells. Therefore, it is an essential component of an innate immune response,<sup>7</sup> exhibiting multifunctional activities.<sup>144</sup> For instance, it exhibits a broad spectrum of activity against Gram-negative<sup>96</sup> and Gram-positive<sup>145-148</sup> bacteria, tumor cells,<sup>149</sup> some viruses,<sup>150, 151</sup> and fungi,<sup>152, 153</sup> by disrupting

their membranes. It neutralizes the activity of bacterial endotoxins.<sup>148, 154, 155</sup> The LL-37 revealed promising results in studies related to drug-resistant bacteria.<sup>156, 157</sup> Furthermore, it acts as an immunomodulatory agent<sup>8, 152, 154, 158, 159</sup> and is considered essential for epithelial defense.<sup>160</sup> Interestingly, being both a pro- and anti-inflammatory agent, LL-37 is engaged in autoimmune diseases.<sup>161</sup> It is cytotoxic<sup>137</sup> and hemolytic.<sup>145</sup> However, the antibacterial and the cytotoxic activities of LL-37 are inhibited in the presence of human serum.<sup>137, 162</sup> Moreover, the host cell membranes are rich in sterols, which may be another factor preventing the LL-37 attack.<sup>140, 152</sup> Nevertheless, numerous studies indicate that LL-37 is an appropriate candidate for research, development, and production of novel AMPs-derived antimicrobial drugs.<sup>157</sup> Therefore, a detailed understanding of the physicochemical processes accompanying the LL-37 antimicrobial activity is fascinating.

LL-37 was found to be effective against different bacteria strains in a broad range of concentrations, from 0.5 up to 1000  $\mu\text{g mL}^{-1}$  of minimum inhibitory concentration (MIC),<sup>157</sup> or, e.g., in *Bacillus* species, 1 up to 66  $\mu\text{g mL}^{-1}$  GI<sub>50</sub> (the concentrations resulting in a 50% growth inhibition).<sup>163</sup> The peptide alters bacteria's membrane integrity at critical concentrations, leading to bacteria lysis,<sup>164, 165</sup> even within minutes.<sup>166</sup> Numerous studies reporting a broad range of LL-37 concentrations pose a challenge in study design on model biological membranes because it is difficult to elucidate what concentrations should be assessed regarding model BLM. Moreover, LL-37 localization in the membrane is concentration-dependent,<sup>167</sup> and the mechanism of LL-37 activity on bacteria changes with the peptide concentration.<sup>96, 146, 167</sup>

It is widely agreed that the composition and physicochemical properties of the model membrane impact the LL-37 activity and influence the results of peptide/lipid interaction studies.<sup>136, 165, 168-170</sup> AMP activity can switch based on the acyl chains structure and length<sup>169</sup> but not the lipid headgroups.<sup>138</sup> However, lipid headgroups composition seems to play a significant role in the LL-37 selectivity.<sup>171</sup> The peptide insertion is favored for the saturated lipid tail, such as DPPG, at high surface pressures, as shown by external reflection FTIR spectroscopy and neutron reflection at the air-water interface.<sup>172</sup> Pores are formed in bilayers composed of unsaturated phospholipids (DOPC/DOPG, 4:1), while fibril-like peptide-lipid superstructures modulate membranes in bilayers comprising saturated phospholipids (DMPC/DMPG, 4:1 and 3:2) at LL-37 concentrations between 1 to 20  $\mu\text{M}$ .<sup>138</sup> LL-37 preference towards specific lipids depends on chain packing density, which is the highest for least packed PG (PE<PS<PC<PG).<sup>169</sup> The choice of a model system can influence the results of peptide-lipid interactions because packing density, ability to form intermolecular H-bonds, and lipids molecular shape influence peptide behavior. Moreover, the lipid net charge might not be the decisive factor in determining the membrane disruption mechanism.<sup>169</sup> In overall, the

physicochemical properties of the target membrane are one of the key factors for the LL-37 mode of activity.

LL-37 molecules' orientation in the membrane may depend on the sample hydration state. These molecules orient in parallel in a non-swollen state of DMPC (1:50 P:L molar ratio)<sup>173</sup> and PC/Chol and PC/PG (1:70 P:L molar ratio),<sup>174</sup> while for swollen stacked DOPC bilayers (in P:L = 1:100, 1:80, 1:50 molar ratios) transmembrane pores with water channel of 2.3-3.3 nm diameter were formed in a two-stage mechanism, aligning almost normal to the lipid membrane surface, as shown by circular dichroism (CD), neutron in-plane scattering, XRD, grazing angle X-ray scattering, and fluorescence microscopy.<sup>175</sup>

Two main pathways of LL-37 activity are membrane attack,<sup>176</sup> and regulation of innate immune response<sup>177</sup>. Model membrane studies focus on details of membrane attack mechanisms. However, the literature does not indicate a single mechanism of the LL-37 membrane attack.<sup>7</sup> The activity of the LL-37 involves insertion into the membrane, interaction with negatively charged lipids, change of lipids organization, packing and cooperativity, pore formation, and membrane disintegration. Instead, several different mechanisms emerge from numerous studies. Often mentioned is the "carpet" model ("carpet" membrane dissolution).<sup>173, 178, 179</sup> According to this mechanism, peptides primarily interact with lipid headgroups, followed by transmembrane defect formation<sup>136, 175, 180</sup> or the detergent-like mechanism.<sup>174</sup> Several studies suspect pore formation mechanism, but the applied techniques cannot resolve the nature of pore-like defects.<sup>146, 173</sup> In some studies, undefined defects described as transient lesions causing transmembrane current fluctuations were reported.<sup>165</sup> What the literature is more agreeable about is that the peptide oligomerizes in solution and then adsorbs on the membrane surface in the form of monomers or oligomers.<sup>174</sup> Specifically, it keeps an oligomeric form when adsorbed to zwitterionic phospholipids (e.g., PC) but dissociates into monomers when adsorbed to negatively charged phospholipids (e.g., PG).<sup>164, 174</sup>

The transition of LL-37 from disordered to helical structure depends on solution pH, concentration, and presence of anions.<sup>137</sup> LL-37 undergoes  $\alpha$ -helix formation upon membrane insertion,<sup>167</sup> and its  $\alpha$ -helicity in PBS varies depending on the membrane composition, being higher in the presence of PC/PG phospholipids vs. PC alone.<sup>138</sup> Structural changes and oligomerization suggest further fibril-like structures formation. LL-37 exhibits the potential to form peptide-lipid complexes in vivo.<sup>171</sup> Oligomerization and then the formation of fibril-like structures by peptide dimers in the presence of lipids was confirmed by electron microscopy, using lipid vesicles (DOPC/DOPG, 3:7; 1:250 P/L molar ratio) incubated with gold-labeled S37C mutant peptides, which are modified LL-37 equivalent.<sup>171</sup> When the LL-37 peptide adsorbs on the membrane surface, it can polymerize and selectively extract bacterial lipids, de-

stabilizing the membrane. Two lipids can be extracted from a membrane per one LL-37 monomer.<sup>171</sup> The fibers may be necessary to increase the local peptide concentration and then extract lipids from the cytoplasmic membrane after peptide interactions.<sup>181</sup> The LL-37 mechanism of action involves the formation of cytotoxic oligomers in the presence of acidic/negatively charged phospholipids (SOPC/POPG, 4:1 and 3:2)<sup>178</sup> or the formation of fibril-like structures in the presence of saturated phospholipids (DMPC/DMPG, 4:1),<sup>138</sup> however not involving refolding from  $\alpha$ -helix to  $\beta$ -sheet (the fibers are not amyloid-like).<sup>175</sup> Supposedly, LL-37 exhibits a hitherto unknown mechanism at sites of injury, based on a "dual-offensive protective" role. That is, LL-37 locally increases its concentration, which is promoted by fiber-like structures, and then inserts into the membrane and forms a protective shield against bacteria.<sup>138</sup> The channel was formed in the POPE/POPG 3:1 model membrane, and it was tilted by 20° against the membrane normal.<sup>181</sup> The mode of LL-37 activity depends on the lipid hydrocarbon chain length.<sup>169</sup> Presumably, the amount of anionic lipid in the membrane does not influence the binding affinity. Rather, the viscoelastic properties of the hydrophobic core affect the LL-37 action. Moreover, the peptides promoted liposome aggregation and fusion into tubular superstructures in saturated lipids (DMPC/DMPG), not observed for unsaturated lipids (DOPC/DOPG).<sup>138</sup>

Solid-state NMR spectroscopy and differential scanning calorimetry performed on DMPC/DMPG 4:1, POPC/POPG 4:1, POPE/POPG 4:1 bilayers suggested that LL-37 is oriented parallel to the membrane surface and must initially interact with the membrane via "carpet" mechanism and then induce membrane damage by formation of toroidal pores or other membrane defects which are less well-defined. The study excluded a detergent-like mechanism due to lack of signal characteristic for micelles and suggested a toroidal-pore model because of positive curvature strain in lipid bilayers in the presence of the peptide.<sup>173</sup> Besides, a change in membrane curvature does not necessarily indicate pore formation.<sup>168</sup> The tilt of DMPC and DMPC/DMPG headgroups increased with the LL-37 concentration increase, and in the presence of anionic phospholipids, it was pronounced more than for the zwitterionic ones. Studies on DMPG bilayers suggested that LL-37 induces dynamically changing toroidal pores, and LL-37 monomers dynamically change their positions within the pore, moving between the surface of an upper leaflet to the bottom of a lower leaflet, with the possibility of peptide slipping entirely out of the bilayer, back on the surface.<sup>128</sup> The LL-37 C-terminus stays at the bilayer surface, while N-terminus buries deeply in the bilayer,<sup>128</sup> as it contains 30% of the hydrophobic amino acids of the peptide.<sup>137</sup>

The LL-37 mode of action with negatively charged membranes suggests a detergent-like effect via the so-called "carpet" model, as mentioned before. A non-pore carpet mechanism has been suggested based on ATR-FTIR and <sup>31</sup>P NMR spectroscopy experiments performed

on oriented PC, PC/Chol, and PC/PG multilayers. The data indicated that LL-37 (up to 5 mol %) was oriented parallel to the bilayer surface and did not penetrate deeply into the membrane hydrophobic core.<sup>173, 174</sup> Therefore, presumably, LL-37 interacts with the membrane by a detergent-like mechanism rather than transmembrane poration. CV, EIS, and AFM experiments on recombinant (18 kDa) LL-37 interacting with DOPC/DPPG sBLMs also suggested a "carpet" model followed by a detergent-like mode of activity towards PG-containing membranes, with peptides initially interacting with the lipid headgroups.<sup>179</sup>

Reviewing the available literature on LL-37, one can find many studies yet not leading to consistent outcomes. Conceivably, this is growing evidence of AMPs activity enormously depending on the physicochemical properties of the target membrane itself.<sup>19</sup> That would possibly explain the multifunctionality of some peptides, including LL-37. Therefore, a simple approach to validating the peptide activity in a single-component model membrane might be insufficient. Perhaps, the mechanisms of multifunctional membrane-active peptides should only be provided concerning the composition and physicochemical properties of the target membrane.

## 1.7. Objectives of the thesis

The overall aim of the present thesis was to unravel the properties of model biological membranes exposed to membrane-active molecules such as antimicrobial peptides and toxic components of air pollution. Moreover, nanomechanical properties of a model biological membrane in the ripple phase were characterized.

In the first part of the thesis, Tris-induced formation of ripple phase in a supported single DMPC bilayer lipid membrane was monitored. The conformation of phospholipids in the ripple phase was previously studied by, e.g., X-ray diffraction. However, the majority of ripple phase studies were performed on multibilayer. The present research aimed to investigate the nanomechanical properties of the single DMPC bilayer in a ripple phase and to understand corrugations' formation for this phase by utilizing an AFM direct visualization technique. To the best of my knowledge, these were attempted for the first time.

Next, the activity of membrane-active molecules towards model cell membranes was studied. First, BacSp222 in a DMPC bilayer was investigated. BacSp222 is a recently isolated bacteriocin whose structure and properties were unknown. The goal was to reveal BacSp222 secondary structure in the presence of lipids and then to find its orientation in the membrane and its influence on phospholipid molecules.

Then, the toxicity of the nitrophenols mixture on model cell lines was monitored. The goal was to verify whether the nitrophenols mixture interacts with a bilayer lipid membrane or not. If it interacts, then what is the nature of these interactions. The goal was to check if there was any affinity towards chosen phospholipids and what was the response of nitrophenols in a lung-like multicomponent model membrane. This research was proposed to complement the toxicity assays performed on cell lines.

Finally, the last project aimed to investigate the activity of LL-37. In the literature, there is no agreement on the mode of LL-37 activity. Moreover, it is widely agreed that the bilayer composition influences behavior of peptides, and usually, only single or two-component membranes were studied. Therefore, this project aimed to study the LL-37 behavior in a multicomponent microbial-like bilayer lipid membrane. The goal was to reveal changes induced in a phospholipid bilayer by the LL-37 presence.

Three complementary experimental techniques were used to achieve these goals, including AFM for direct visualization of the membrane surface, EIS to characterize changes in membrane electrical parameters, and PM-IRRAS to determine conformation and orientation of analyzed molecules. The experiments were performed under electrochemical conditions, mimicking transmembrane potential.

## CHAPTER 2: Materials and methods

### 2.1. Materials

#### 2.1.1. Reagents and solutions

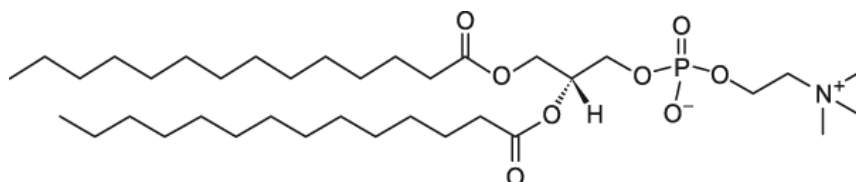
All aqueous solutions were prepared using a freshly filtered Milli-Q UV-Plus 18.2 M $\Omega$  cm resistivity water (Millipore®) or deuterated water (99.90%, Eurisotopes, Cambridge Isotope Laboratories, Inc).

Sulphuric acid (98%, Chempur), nitric acid (65%, Chempur), hydrogen peroxide (30%, Sigma-Aldrich), ethyl alcohol (Line-Antybakteria 96%, Lineal Chemicals), isopropyl alcohol (ACS reagent,  $\geq$ 99.5%, Sigma-Aldrich) and RBS™ 25 solution (concentrate, Sigma-Aldrich) were used for cleaning.

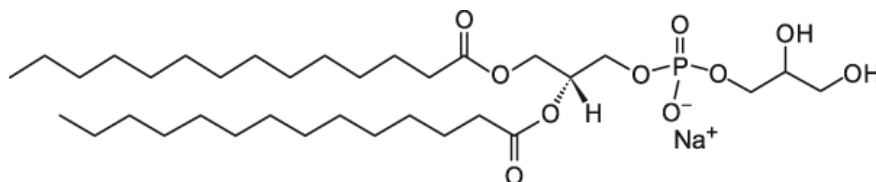
##### 2.1.1.1. Phospholipids stock solutions

Chloroform (anhydrous,  $\geq$ 99%, 0.5-1.0% ethanol as the stabilizer, Sigma-Aldrich) and methanol (99.9% for HPLC, POCH) were used to prepare phospholipid stock solutions. The following six phospholipids of three different acyl chain lengths (in terms of the number of carbon atoms) were used.

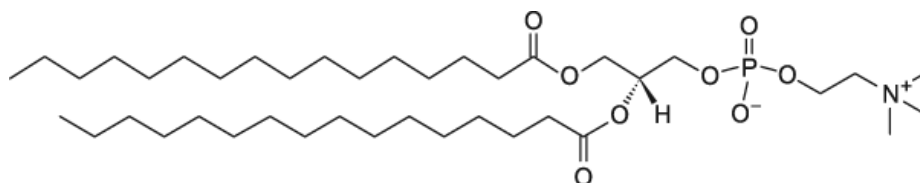
- 1,2-Dimyristoyl-*sn*-glycero-3-phosphocholine, DMPC (14:0-14:0)



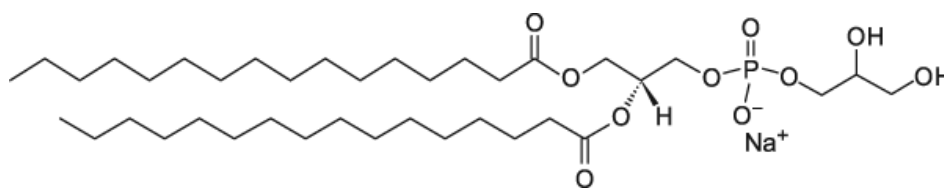
- 1,2-Dimyristoyl-*sn*-glycero-3-phospho-(1'-*rac*-glycerol), DMPG (14:0-14:0)



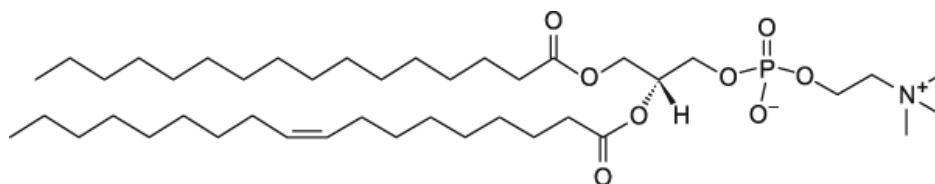
- 1,2-Dipalmitoyl-*sn*-glycero-3-phosphocholine, DPPC (16:0-16:0)



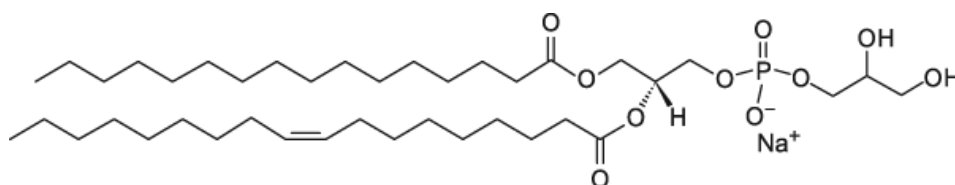
- 1,2-Dipalmitoyl-*sn*-glycero-3-phospho-(1'-*rac*-glycerol), DPPG (16:0-16:0)



- 1-Palmitoyl-2-oleoyl-*sn*-glycero-3-phosphocholine, POPC (16:0-18:1)



- 1-Palmitoyl-2-oleoyl-*sn*-glycero-3-phospho-(1'-*rac*-glycerol), POPG (16:0-18:1).



Phospholipids were purchased from Sigma-Aldrich and used without further purification. Chloroform and the chloroform:methanol (3:1, *v/v*) solution were used to dissolve PC and PG phospholipids, respectively. The final concentration of the stock solution was 1 mg mL<sup>-1</sup> or 10 mg mL<sup>-1</sup>. The physicochemical properties of the phospholipids are summarized in Table 2-1.

Table 2-1. Physicochemical properties of the phospholipids used.<sup>182</sup>

Phospholipid	Main transition temperature, $T_m$ , °C	Chain lengths, no. of C atoms	Net charge	Molecular weight, g mol <sup>-1</sup>
DMPC	24	14:0-14:0	0	677.93
DMPG	23	14:0-14:0	-1	688.85
DPPC	41	16:0-16:0	0	760.08
DPPG	41	16:0-16:0	-1	770.99
POPC	-2	16:0-18:1	0	734.04
POPG	-2	16:0-18:1	-1	744.95

### 2.1.1.2. Peptides stock solutions

Freshly filtered Milli-Q water (1 mL) was added to LL-37 (human) trifluoroacetate salt ( $\geq 95\%$  (HPLC) from Sigma-Aldrich or Bachem (1 mg), and then the resulting solution was vortexed

for ~40 s. The stock solution prepared that way was divided into ten 100- $\mu$ L aliquots in Eppendorf tubes, each containing LL-37 (100  $\mu$ g). Aliquots were stored as prepared at  $-20$  °C and used within a month or lyophilized if more extended storage was needed.

Bacteriocin BacSp222 was obtained in a powder form from collaborators (Department of Analytical Biochemistry, Faculty of Biochemistry, Biophysics and Biotechnology, Jagiellonian University, Cracow, Poland). BacSp222 was purified from the *Staphylococcus pseudintermedius* 222 culture supernatant, as described in detail elsewhere.<sup>183</sup> The BacSp222 powder was stored at  $-20$  °C before use.

### 2.1.1.3. Supporting electrolyte solutions

Phosphate buffered saline (PBS) was prepared by dissolving a PBS tablet (Sigma-Aldrich) in freshly filtered Milli-Q water (200 mL), yielding 0.01 M PBS (0.0027 M potassium chloride and 0.137 M sodium chloride, pH = 7.4). PBS was used as the supporting electrolyte solution in electrochemical and microscopic experiments.

Sodium fluoride ( $\geq 99\%$  BioReagent, Sigma-Aldrich) was treated in UV ozone cleaner (Nano BioAnalytics, UVC-1014) for 20 min before dissolving in D<sub>2</sub>O (99.9%, Eurisotop). 0.1 M NaF was used as the supporting electrolyte solution in spectroscopic experiments.

In some experiments, the KCl, KClO<sub>4</sub> ( $\geq 99\%$ , Sigma-Aldrich), or CaCl<sub>2</sub> (97%, POCH basic) supporting electrolytes were used.

Ethylenediaminetetraacetic acid, EDTA, (BioUltra, anhydrous,  $\geq 99\%$  (titration), Sigma-Aldrich), 4-(2-hydroxyethyl)piperazine-1-ethanesulfonic acid, HEPES, (BioPerformance Certified,  $\geq 99.5\%$  (titration), cell culture tested, Sigma-Aldrich), and tris(hydroxymethyl)amino-methane, Tris, (ACS reagent  $\geq 99.8\%$ , Sigma-Aldrich) buffers were used for AFM imaging of the bilayer in the ripple phase.

### 2.1.2. Cleaning procedures

All glassware was cleaned consecutively with water and ethanol beforehand, then thoroughly dried, and then soaked in a hot (80 °C) mixture of H<sub>2</sub>SO<sub>4</sub>:HNO<sub>3</sub> (3:1, v/v) for 1 h. Next, it was left until the acid cooled down before the glassware was removed from the acid bath. Subsequently, it was rinsed with copious distilled water several times and then left overnight to soak in water to dissolve any residues of the adsorbed acid. Finally, glassware was rinsed again with fresh Milli-Q water and dried in the oven for several hours at 60 °C. Glassware was stored in dust-free, sealed containers. All Teflon™ parts and some glassware were cleaned by soaking in a freshly prepared “piranha” solution (H<sub>2</sub>SO<sub>4</sub>:H<sub>2</sub>O<sub>2</sub>; 3:1, v/v) for 20 min, instead of an acid bath. (Warning. “Piranha” solution is dangerous if contacting skin or eyes.)

If any other parts were not suitable for acid cleaning, like plastic cups, those were sonicated in a 2% RBS™ 25 solution for 20 min, then rinsed with water, and then sonicated in Milli-Q water for 20 min, next rinsed with the water again, and finally left to dry.

Atomic force microscopy (AFM) fluid cell and its compartments were soaked in a mild detergent solution for several hours, then rinsed with copious water, and then dried with a nitrogen stream.

AFM probes were cleaned before use and if reused. This cleaning consisted of 5-min consecutive soaking of the probe in a mild detergent, ethanol, isopropanol, and Milli-Q water. Then it was UV-cleaned for 10 min. Finally, the cleaned probes were stored in a desiccator.

### 2.1.3. Sample preparation

#### 2.1.3.1. Gold(111) electrode handling

Gold(111) single-crystal disk electrodes (Figure 2.1-1) (MaTeck) of 10-, 12-, and 15-mm diameters were electropolished after purchase (before the first use). The procedure of electropolishing was described earlier<sup>184</sup> and adapted herein for handling gold electrodes. In brief, in the two-electrode open-air cell, with a gold wire serving as the counter electrode, first, 0.1 A cm<sup>-1</sup> current was galvanostatically applied to the working electrode, Au(111), in 1 M HClO<sub>4</sub> for 5 min. Then, the formed brownish layer was removed by dipping the electrode in 10% HCl for 60 s. The electrode was rinsed with



Figure 2.1-1. Single-crystal Au(111) electrode in a glass capillary.

Milli-Q water before transferring between solutions. The procedure was repeated five times. The electrode was then flame annealed<sup>185</sup> in the dark. For that, the crystal was heated up by propane/butane neutral flame until dark orange, then left to cool down only until glowing has vanished, which was repeated ten times. Then the crystal was left to cool down for 1 min, quenched in Milli-Q water, and the flame annealing was repeated three times. The crystal was not quenched in water after last flame annealing, but left to cool down for 3-5 min under cover, then a Milli-Q water drop was dispensed on the crystal surface and left to cool down completely for several minutes. The CV measurement was performed using 0.1 M H<sub>2</sub>SO<sub>4</sub> and 0.1 M KClO<sub>4</sub> supporting electrolyte solutions to confirm the gold surface reconstruction. Potential of transition from reconstructed Au(111)-(22 × √3) to unreconstructed Au(111)-(1 × 1) surface (Figure 2.1-2) was identified beyond 0.4 V vs. SCE. Pronounced differences in the current response for anodic and cathodic potentials could be safely attributed to reconstruction phenomena. Peak positions were compared with those of the reference found in

literature.<sup>186, 187</sup> This transition is also manifested as the double-layer capacitance change of the electrode (Figure 2.1-3).

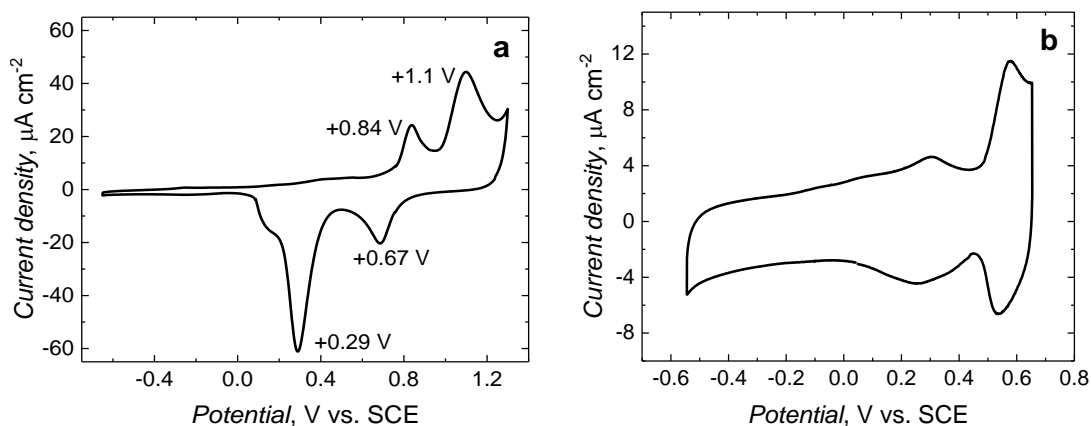


Figure 2.1-2. (a) The experimental CV curve of a bare Au(111) electrode in 0.01 M KClO<sub>4</sub>, at a scan rate of 20 mV s<sup>-1</sup>, after electrode electropolishing and then flame annealing. (b) The Au(111) electrode under the same conditions, in the double-layer potential range of the CV curve. Reconstruction is lifted at potentials above +0.4 V vs. SCE.

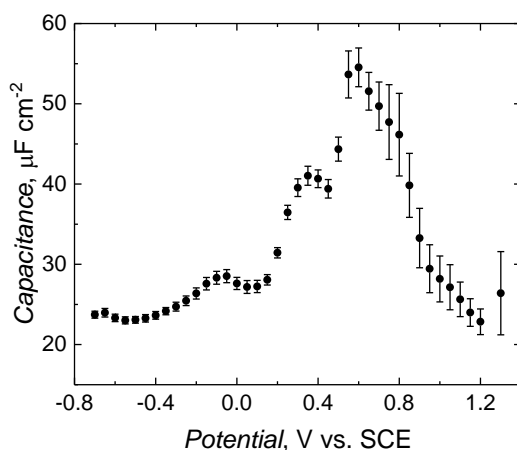


Figure 2.1-3. The double-layer capacitance vs. potential curve for a bare Au(111) electrode in 0.01 M KClO<sub>4</sub> with data acquisition starting from the negative potential edge.

### 2.1.3.2. Hydrophilic modification of gold(111) electrode

The gold(111) electrode surface was modified by a hydrophilic and conductive self-assembled monolayer of 1-thio-β-D-glucose (β-Tg, SAM-Tg).<sup>48, 49, 188</sup> For that purpose, the 1-thio-β-D-glucose sodium salt (99%, Sigma-Aldrich) (Figure 2.1-4) was dissolved in Milli-Q water, yielding a 1 mg mL<sup>-1</sup> stock solution. This solution was stored at -20 °C. It was used to prepare 2 mL (0.4 mg mL<sup>-1</sup>) of 2 mM β-Tg aqueous solution for electrode modification. The annealed and then cooled down electrode was immersed in this solution for 20 h (or 5 h in some cases). Afterward, the modified Au(111) was rinsed with copious Milli-Q water. The SAM-Tg coated

electrode was dried in air. The latter experiments show that a 5-h deposition of  $\beta$ -Tg suffices to produce a high-quality hydrophilic spacer.<sup>57</sup>

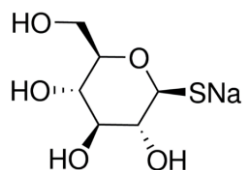


Figure 2.1-4. Structural formula of 1-thio- $\beta$ -D-glucose ( $\beta$ -Tg) sodium salt.

### 2.1.3.3. Small unilamellar vesicles deposition

Sufficient volumes of stock solutions in a total amount of 1 mg phospholipids were combined in a test tube. First, the solution was vortexed under the argon flow for 30-45 min until a dry phospholipid film was formed on the test tube walls. This film was stored in a desiccator for at least 24 h before use. Then, 1 mL of Milli-Q water, deuterated water, or PBS solution was added to the dry phospholipid film, and the resulting solution was sonicated at 45 °C for 30 min. As a result, spheres of 25 to 100 nm in diameter, enveloped by a single lipid bilayer, were formed, called small unilamellar vesicles (SUVs).<sup>82, 189</sup> The that way prepared SUVs solution was used for the model biological cell membrane deposition.<sup>84, 90</sup> For that, this solution was drop-cast onto freshly cleaved muscovite mica surface (V-1 grade 12-mm diameter disks, TedPella, or Electron Microscopy Sciences) and self-assembled for approximately 1 h. In the case of the gold(111) electrode, the electrode was immersed in the SUVs solution from the top in a hanging meniscus configuration and allowed for self-assembling for 20 h.

### 2.1.3.4. Langmuir films formation

The DMPC bilayer for ripple phase investigation was immobilized onto a mica disk by LB/LS deposition. Briefly, DMPC was dissolved in chloroform ( $\geq 99.0\%$ , Sigma-Aldrich) to form a 1 mg mL<sup>-1</sup> stock solution. This solution was stored at -20 °C. Before deposition, a 32  $\mu$ L of the DMPC stock solution was left at ambient temperature to warm up and equilibrate. Then, the solution was spread dropwise at the surface of Milli-Q water filling the Langmuir trough (601BAM trough of Nima Technology, Ltd) and left for 20 min to allow chloroform to evaporate. Then, barriers were brought together with a constant 20-(mm min<sup>-1</sup>) speed to compress the monolayer spread between them until the target pressure of 35 N m<sup>-1</sup> was reached. At this pressure, the monolayer was left to stabilize for 20 min before deposition. Surface pressure was measured with an accuracy of  $\sim 0.1$  mN m<sup>-1</sup> with a PS4 sensor of Nima Technology of a Wilhelmy plate type. The first leaflet of DMPC was transferred from the Langmuir trough at a surface pressure of 35 mN m<sup>-1</sup> by the LB technique (Figure 2.1-5). The monolayer was transferred onto a solid substrate with the D1L linear dipper of Nima Technology with a

speed of  $2 \text{ mm min}^{-1}$ . After the monolayer deposition, the supported DMPC monolayer was dried for 60 min under ambient conditions, and then a second leaflet was deposited with the LS technique. During the deposition, both the aqueous subphase and environment temperature were kept at  $21 \text{ }^\circ\text{C}$ . After deposition, the sample was stored at  $4 \text{ }^\circ\text{C}$  overnight with a buffer drop on top. The buffer was composed of either 20 mM TRIS, 150 mM NaCl, 5 mM EDTA (pH = 7.6) or 10 mM HEPES, 150 mM NaCl, 5 mM  $\text{CaCl}_2$  (pH = 7.4). These buffer solutions were further used for AFM imaging. Before this imaging, samples were conditioned for 1 h at  $21 \text{ }^\circ\text{C}$ , i.e., below the main transition temperature for supported DMPC bilayers, which is  $24 \text{ }^\circ\text{C}$ .<sup>190</sup> The precaution was taken to avoid bilayer exposure to the air.

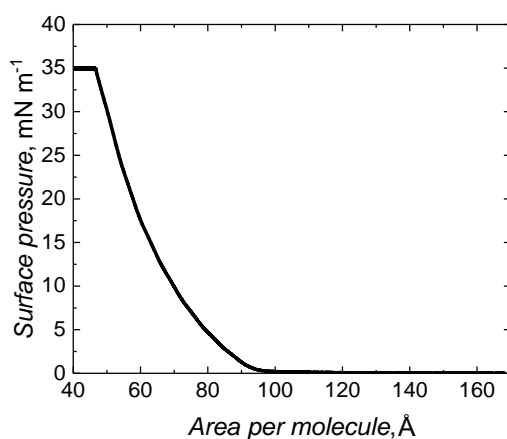


Figure 2.1-5. The surface pressure vs. area compression isotherm of DMPC spread on an aqueous subphase at  $21 \text{ }^\circ\text{C}$ . Compression was stopped at  $35 \text{ mN m}^{-1}$ , and at this surface pressure, the monolayer was transferred onto the mica substrate using first the LB and then the LS technique (curve not shown). The 20- and  $2\text{-}(\text{mm min}^{-1})$  speed was applied for the barriers and dipper, respectively.

## 2.2. Instrumentation and techniques

Metal-supported bilayer lipid membranes allow applying numerous surface techniques, including spectroscopy, microscopy, and electrochemistry, to investigate the electric-field-driven changes in properties of biomolecular compounds at the molecular level and investigate membrane processes. In this section, AFM, polarization-modulation infrared reflection-absorption spectroscopy (PM-IRRAS), and electrochemical techniques, including cyclic voltammetry (CV) and electrochemical impedance spectroscopy (EIS), are briefly introduced.

### 2.2.1. Atomic force microscopy

AFM imaging allows measuring fragile biological samples at nanometer resolution without damaging them by minimizing the lateral forces. Moreover, local mechanical properties in the nanometer scale can be investigated using the PeakForce Quantitative Nanomechanical Mapping (PF-QNM) mode of AFM, which was applied in the present research.

#### 2.2.1.1. PeakForce Quantitative Nanomechanical Mapping

PeakForce Quantitative Nanomechanical Mapping is based on Bruker's core technology, called Tapping Mode™.<sup>191</sup> In Tapping Mode™, the feedback loop keeps the cantilever vibration amplitude constant, while PF-QNM keeps the maximum force applied to the tip (Peak Force) at a constant level. As a result, the contact area between the tip and the sample is minimized; thus, the deformation depth and lateral forces are decreased. In PF-QNM, the probe oscillates at ~1-2 kHz, i.e., far below the cantilever resonant frequency, usually being between 1 kHz and 2 MHz.<sup>192</sup> This modulation frequency is intentionally chosen to be significantly lower than the cantilever resonant frequency. Therefore, the force measurement bandwidth of a cantilever is approximately equal to the resonant frequency of the fundamental bending mode used for force detection. In effect, during PF-QNM imaging, an adequately selected cantilever deflects immediately in response to instantaneous changes in interaction force. Measurement of the instantaneous force on the tip is necessary to separate the contributions from different mechanical properties of the sample such as modulus, adhesion, dissipation and deformation. To do so, a force sensor with significantly higher bandwidth than the frequency of the periodic interactions is required.

A force vs. distance (F-D) curve indicates the probe's approach and withdrawal towards the sample surface (Figure 2.2-1). This movement comprises approaching the sample surface, contacting the sample surface at  $d_0$ , applying peak force, and reaching the given force set-point, work of adhesion, and withdrawal of the probe. The F-D curve is acquired for every pixel of the image and then analyzed to produce maps of the sample's mechanical properties.

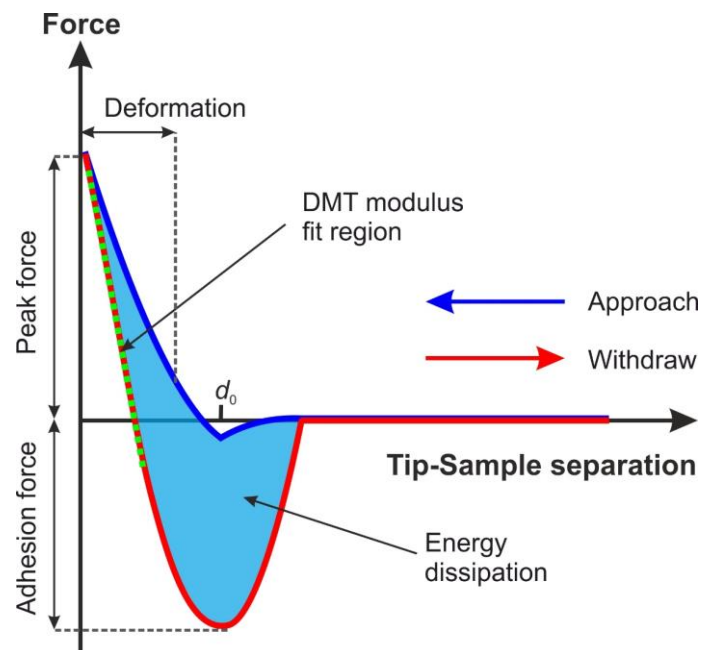


Figure 2.2-1. Schematic representation of the force-distance curve acquired for every pixel of the AFM PF-QNM image. Features of the curve used for calculating adhesion, dissipation, deformation, peak force, and modulus are marked. The  $d_0$  parameter corresponds to the tip position at the sample surface (contact point).

## 2.2.2. Electrochemical techniques

Electrochemical techniques allow transducing chemical changes in the biomimetic membrane to electric signals such as current, capacitance, or resistance. It provides a tool for studying interactions of membrane-active molecules and electric-field driven changes in the phospholipid bilayer that can be characterized by electrochemical measurements.<sup>42</sup>

### 2.2.2.1. Cyclic voltammetry

Cyclic voltammetry (CV) is the voltammetric, or volt-amperometric technique where the current ( $I$ ) is recorded through the working electrode as a function of time ( $t$ ) while the potential ( $E$ ) applied to the working electrode is changed linearly as a function of  $t$  ( $dE = v dt$ ), at a constant potential scan rate ( $v$ ) between two chosen potential limits. As a result, a cyclic voltammogram, a CV curve, is obtained as the current vs. potential relation,  $I = f(E)$ . The shape of a CV curve depends on the nature of the electrode processes. In the case of faradaic processes, the peak-shaped curve is obtained. In the case of non-faradaic processes, a rectangular-shaped curve is recorded, characteristic of capacitive behavior. The present dissertation is focused on the non-faradaic electrode processes occurring within lipid bilayer membranes. Based on CV measurements, a potential range is determined in which the Au(111)| $\beta$ -Tg|BLM electrode exhibits capacitive behavior. That is, the electrode can be characterized by charging and discharging of the electric double layer that is always formed at the electrode-solution

interface. A current change in the CV curve is a measure of the change in the electrode capacitance. Therefore, it might be an initial indicator of model membrane disruption (Figure 2.2-2) or a change in its dielectric properties. Specific membrane capacitance ( $C_m$ ), which is a ratio of membrane capacitance to electrode area coated with the membrane, depends on the relative electric permittivity ( $\epsilon_m$ ) of the hydrophobic core, the thickness of the hydrophobic core ( $h_m$ ), and the vacuum permittivity  $\epsilon_0 = 8.85 \times 10^{-14} \text{ F cm}^{-1}$  (Eq. 2.2.2-1).<sup>121</sup>

$$C_m = \frac{\epsilon_m \epsilon_0}{h_m} \quad 2.2.2-1$$

The relative electric permittivity of the hydrophobic core is usually reported to be  $\sim 2.1$ .<sup>63</sup> However, it was experimentally shown, that taking into account permittivity of polar head-groups, the relative electric permittivity of the whole bilayer is estimated to be  $\sim 3.2$ .<sup>193</sup> Nevertheless, direct calculations are not trivial, and it was not intended to estimate bilayer thickness based on CV or EIS results. AFM was relied on in this matter, and present relation was used for assessment purposes only.

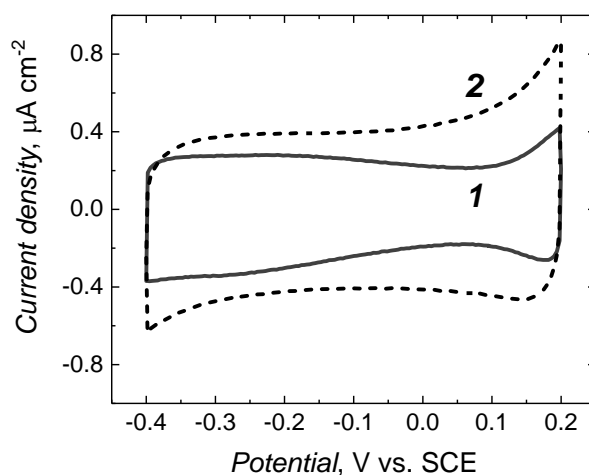


Figure 2.2-2. CV curves for POPC:POPG (3:2) (curve 1, solid) and POPC:POPG (3:2) + LL-37 (40:1 lipid-to-peptide molar ratio) (curve 2, dash) bilayers at  $20 \text{ mV s}^{-1}$ , in  $0.01 \text{ M PBS}$ . Current density increased in the presence of membrane-active peptide, indicating membrane disruption.

### 2.2.2.2. Metal-solution interface and the electric double layer

Suppose a metal electrode (electronic conductor) is connected with an electrolyte solution (ionic conductor). In that case, an equilibrium state will be established by balancing the charge on the metal surface by the ions in the electrolyte solution. The initial electron distribution at the electrode surface depends on the electrode material, its crystalline structure, and the crystallographic face exposed.<sup>194</sup> The surface charge on the metal electrode results from a change in electron density at the surface. An external voltage applied to the electrode's metal or electrostatic interaction with ions in the solution, or charge transfer processes of redox species present in the solution give rise to this excess or deficiency of electrons.

Charged species and dipoles present at the metal-solution interface form the electric double layer (EDL). At a given potential, the electrode-solution interface is characterized by a double-layer capacitance,  $C_{dl}$ . This capacitance often depends on potential applied, unlike in real capacitors, in which capacitance is independent of the voltage across their plates.

Since the first introduction of the EDL model by Helmholtz in 1879, the Gouy-Chapman-Stern model has been commonly used to describe the EDL structure, with Grahame and Bockris-Devanathan-Müller models also applied to account for other accompanying physical phenomena, such as specific anion adsorption or a shear plane presence.<sup>194</sup> This plane limits the area where the electrode charge rigidly holds the ions. This plane potential is the zeta or electrokinetic potential.

### 2.2.2.3. Differential capacitance and the potential of zero charge

Analysis of experimental results of capacitance vs. electrode potential behavior under different conditions that led to the expansion of subsequent versions of double-layer models also accounted for defining the potential of zero charge (PZC or  $E_{pzc}$ ). It was observed that the total capacitance decreases with the decrease of the (non-adsorbing) supporting electrolyte concentration at PZC characteristic of the given electrode material and electrolyte.

The surface charge density of a metal electrode ( $\sigma_M$ ) is a function of the electrode potential ( $E$ ) and surface Gibbs excess (surface coverage,  $\Gamma$ ),  $\sigma_M = f(\Gamma, E)$ . Therefore charge density can be differentiated as following.<sup>64</sup>

$$d\sigma_M = \left(\frac{\partial\sigma_M}{\partial\Gamma}\right)_E d\Gamma + \left(\frac{\partial\sigma_M}{\partial E}\right)_\Gamma dE \quad 2.2.2-2$$

When the surface concentration of adsorbed molecules does not change during the measurement ( $\Gamma = const.$ ), the first component of Eq. 2.2.2-2 becomes zero,  $\left(\frac{\partial\sigma_M}{\partial\Gamma}\right)_E = 0$ . As a result, change in electrode potential (charging of the interface) induces the following change in charge density.<sup>64</sup>

$$\sigma_M = \int_{E_{pzfc}}^E \left(\frac{\partial\sigma_M}{\partial E}\right)_\Gamma dE = \int_{E_{pzfc}}^E C_\Gamma dE \quad 2.2.2-3$$

The  $C_\Gamma$  is the differential capacitance at a constant surface coverage. Charge density,  $\sigma_M$ , expressed by Eq. 2.2.2-3, is the so-called free charge density responsible for the EDL capacitance. The potential at which the free charge equals zero is called the potential of zero free charge (PZFC or  $E_{pzfc}$ ).

On the other hand, when the surface charge is measured by stepping the potential between adsorption ( $E_{ads}$ ) and desorption ( $E_{des}$ ) potentials of surface molecules, by applying for example chronocoulometric technique, the surface concentration changes, and  $\left(\frac{\partial\sigma_M}{\partial\Gamma}\right)_E \neq 0$ .

In this case, a change in electrode potential and surface concentration induces the following change in charge density.<sup>64</sup>

$$\sigma_M = \int_{E_{\text{ads}}}^{E_{\text{des}}} \left( \frac{\partial \sigma_M}{\partial E} \right)_\Gamma dE + \int_\Gamma^0 \left( \frac{\partial \sigma_M}{\partial \Gamma} \right)_E d\Gamma = \int_{E_{\text{ads}}}^{E_{\text{des}}} C_\Gamma dE + \int_\Gamma^0 \left( \frac{\partial \sigma_M}{\partial \Gamma} \right)_E d\Gamma \quad 2.2.2-4$$

The charge measured with the reductive desorption method is called the total charge. The total charge includes the charge of the EDL and the charge density at the desorption potential. The potential at which the total charge equals zero is called the potential of zero total charge (PZTC or  $E_{\text{pztc}}$ ).

In many cases,  $E_{\text{pztc}} \approx E_{\text{pzfc}}$  and this potential, at which all charges vanish, is the  $E_{\text{pzc}}$ . However, this is not always the case, as shown for the SAM-Tg deposited at the Au(111).<sup>64</sup> The  $E_{\text{pzc}}$  value can be estimated from the position of the diffuse layer minimum on a differential capacitance vs. potential curve obtained for a dilute solution of the pure non-adsorbing supporting electrolyte.<sup>195</sup> Another methods used for the exact determination of  $E_{\text{pzfc}}$  and  $E_{\text{pztc}}$  are the immersion and chronocoulometric method, described in Ref.<sup>64</sup> The  $E_{\text{pzc}}$  is widely applied in various electrochemical issues, such as electrocapillary and electrokinetic phenomena, and electric double-layer structure.<sup>195</sup> In the context of this thesis, the knowledge of the  $E_{\text{pzc}}$  value for a given system can be used to measure the potential drop across the BLM.<sup>64</sup>

The differential capacitance at a constant surface coverage, found in 2.2.2-3, can also be rewritten in the following way.

$$C_\Gamma = \left( \frac{\partial \sigma_M}{\partial E} \right)_\Gamma + \left( \frac{\partial \sigma_M}{\partial \Gamma} \right)_E \frac{d\Gamma}{dE} \quad 2.2.2-5$$

Eq. 2.2.2-5 describes the differential capacitance of an electrode covered with specifically adsorbed ions or molecules. It has two components, the true capacitance, and the pseudocapacitance.

$$C_{\text{true}} = \left( \frac{\partial \sigma_M}{\partial E} \right)_\Gamma \quad C_{\text{pseudo}} = \left( \frac{\partial \sigma_M}{\partial \Gamma} \right)_E \frac{d\Gamma}{dE} \quad 2.2.2-6$$

When the surface coverage is constant, the pseudocapacitive component vanishes and  $C_\Gamma = C_{\text{true}}$ . Pseudocapacitive peaks only arise when a change in surface Gibbs excess of adsorbed molecules take place. It happens during phase transition or adsorption or desorption of molecules at the electrode surface.<sup>60</sup> Therefore, differential capacitance measurements help elucidate the potential range in which the adsorbed molecules form a stable film, and the desorption potential. The minimum capacitance can be used to assess bilayer quality.<sup>60</sup>

#### 2.2.2.4. Electrochemical impedance spectroscopy

Electrochemical impedance spectroscopy, EIS, is a non-invasive spectroscopic technique exploring relaxation phenomena with time constants ranging from minutes down to nanoseconds. EIS is based on perturbing the electrochemical system with an alternating, small-amplitude voltage which keeps the system at equilibrium or steady state. EIS is a type of dielectric spectroscopy that allows studying dielectric properties of the electrode material as a function of the frequency and amplitude of the external alternating electric field applied. Dielectric relaxation is a dipole movement (dipole relaxation) and electrical charge (ionic relaxation) responding to the external electric field. Usually, EIS experiments are performed at amplitudes of several mV and in a frequency range of 10 mHz to 100 MHz, which corresponds to 100 s to 10 ns relaxation time. Thus, EIS allows observing slow processes (at low frequencies), e.g., diffusion and adsorption, and fast processes (at high frequencies), e.g., charge transfer and double-layer charging/discharging. Moreover, EIS allows characterizing the electrochemical system by assigning properties responsible for energy storage (capacitor) and energy dissipation (resistor). EIS measurements are conducted by applying a (usually) sinusoidal perturbing voltage,  $V(t)$ , of small amplitude,  $V_0$ , and angular frequency,  $\omega$ , equal to  $2\pi f$  where  $f$  is the frequency (Hz). The current response,  $I(t)$ , will be a sinusoid at the same angular frequency  $\omega$ , current amplitude  $I_0$ , but shifted in phase  $\Phi$ . The system's impedance,  $Z(\omega)$ , is then defined as the ratio of alternating voltage to current.

$$Z(\omega) = \frac{V(t)}{I(t)} = \frac{V_0 \sin \omega t}{I_0 \sin(\omega t + \Phi)} \quad 2.2.2-7$$

Impedance is therefore characterized by  $Z_0 = \frac{V_0}{I_0}$  and phase  $\Phi$  is thus a vector quantity. As such, it can be expressed in a complex notation and presented as a Nyquist plot using a complex plane diagram.

$$Z = Z_0(\cos \Phi + j \sin \Phi) = Z' + j Z'' \quad 2.2.2-8$$

Where  $Z' = Z_0 \cos \theta$  and  $Z'' = Z_0 \sin \theta$  are the real and imaginary components of impedance, respectively, and  $j = \sqrt{-1}$  is the imaginary number.

The impedance at a given frequency is related to the process occurring at the corresponding timescale. Another way to present EIS data involves constructing a Bode plot. This plot includes all information collected during impedance measurement. It is a representation of the phase angle,  $\Phi$ , and the logarithm of the magnitude of the impedance,  $\log Z_0$ , versus the logarithm of the frequency,  $\log f$ .

Changes in the dielectric and insulating properties of a membrane reflect the activity of a particular toxin. EIS measurements are widely applied to study interactions between cationic antimicrobial peptides and model biological membranes.<sup>21</sup> Analysis of the Bode plots

allows recognizing defect formation within the lipid bilayer.<sup>121</sup> For pore-forming peptides, EIS spectra exhibit a characteristic minimum in the phase angle.<sup>56, 113, 114, 124</sup> The magnitude and frequency of the minimum of the phase and modulus of impedance indicate membrane damage and might be used to estimate the extent of this damage in terms of defect density in the case of homogenous defect distribution (Figure 2.2-3a and 3b).<sup>121, 196</sup> For non-homogeneous defect distribution, the EIS response is qualitatively similar to homogenous defect distribution (Figure 2.2-3c and 3d); however, quantitative estimation is not that straightforward and requires additional analysis described in details in Ref.<sup>197</sup>

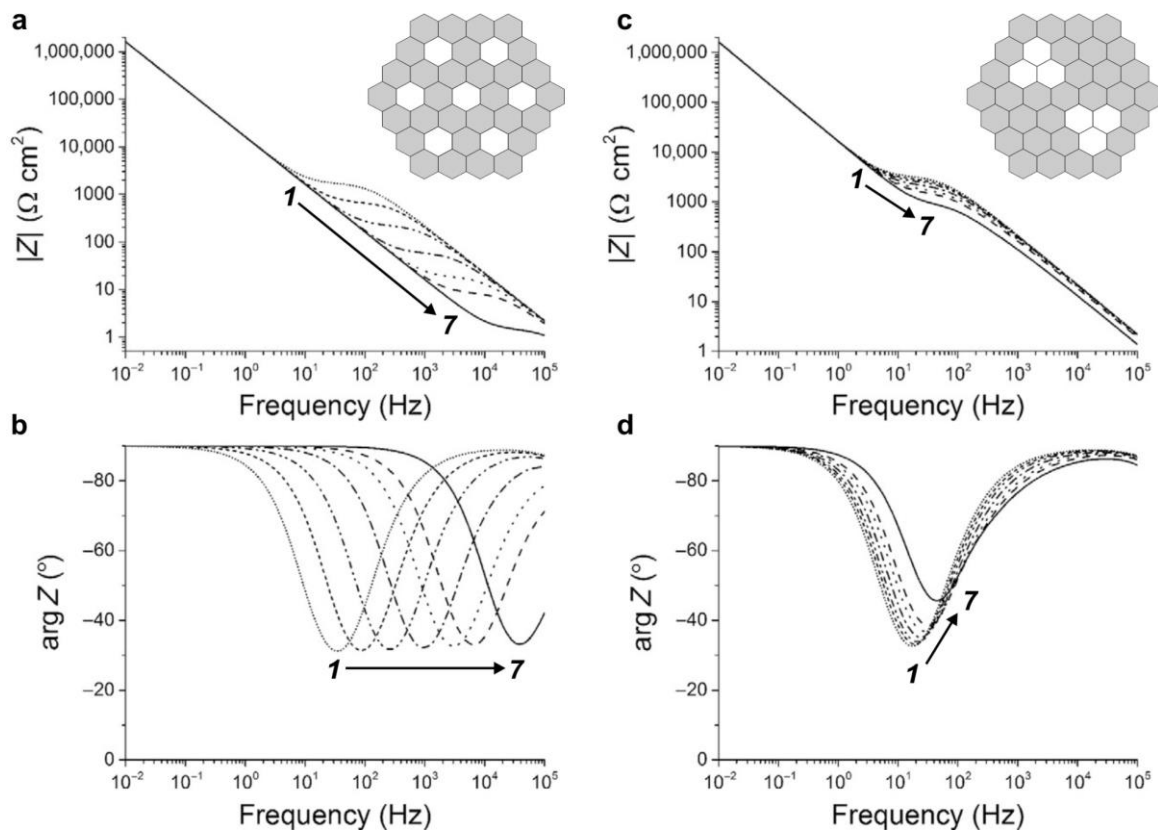


Figure 2.2-3. Bode plots of the (a), (c) magnitude and (b), (d) phase of the electrochemical impedance in the case of (a), (b) homogenous and (c), (d) heterogeneous distribution of defects, schematically shown as insets in Panels a and c, calculated for several defects at defect density of (1) 3, (2) 7, (3) 19, (4) 61, (5) 169, (6) 331, (7) 1519  $\mu\text{m}^{-2}$ . Other model parameters include  $C_H$ , 10  $\mu\text{F cm}^{-2}$ ;  $d_{\text{sub}}$ , 1.5 nm;  $\rho_{\text{sub}}$ ,  $10^5 \Omega \text{ cm}$ ;  $Y_{\text{def}}$ , 70 pS;  $\epsilon$ , 2.9;  $h_m$ , 3.0 nm;  $r_0$ , 1 nm;  $R_s$ , 0.1  $\Omega$ . Adapted from Ref.<sup>121</sup>

### 2.2.2.5. Equivalent electric circuits

The equivalent electric circuit (EEC) is designed so that the electrochemical response of a real physical system corresponds to the simulated response of the EEC (Figure 2.2-4). In other words, every EEC element should have a physical meaning corresponding to the studied system structure. EECs were used to fit impedance spectra obtained and calculate membrane capacitance and resistance.

A perfect defect-free bilayer resembles a perfect insulator and thus can be described as a series  $RC$  circuit (Figure 2.2-4a). However, naturally occurring defects are present in real systems, and ions are exchanged throughout the bilayer (Figure 2.2-4b). Therefore, an additional  $R_{\text{def}}$  element in parallel to the capacitor accounts for that. Moreover, a constant phase element (CPE) is utilized, which is an equivalent electrical circuit component applied to model an EDL that exhibits the behavior of an imperfect capacitor.<sup>59</sup> The CPE impedance ( $Z_{\text{CPE}}$ ) is defined as:

$$Z_{\text{CPE}} = \frac{1}{Q(j\omega)^\alpha} [\Omega] \quad 2.2.2-9$$

where  $Q$  is the constant phase element coefficient, measured in [ $\mu\text{F cm}^{-2} \text{s}^{\alpha-1}$ ] units, where  $\alpha$  is the frequency dispersion constant (empirically related to frequency dispersion) or constant phase defined as  $(-90 \cdot \alpha)^\circ$ ;  $\alpha$  is a number between 0 and 1. It is close to 1 if the impedance is dominated by capacitive behavior.<sup>198</sup> Therefore,  $Q$  can be considered as a capacitance for  $\alpha \approx 1$ . If  $\alpha$  is close to 0, the impedance is dominated by resistance. Values close to 0.5 might be interpreted as characteristic for Warburg impedance and suggest that the rate of ions diffusion through defects controls the impedance.

For a bilayer whose structure is affected by transmembrane defects or pores, an additional circuit element is introduced to EEC to account for an impedance decrease because of ion transport. This transport is now allowed through the defects to the submembrane region and metal surface (Figure 2.2-4b).<sup>121</sup> This region, uncovered by the presence of defects, is described by the  $\text{CPE}_{\text{sp}}$  ( $Q_{\text{sp}}$ ) element, the equivalent of the submembrane spacer impedance. For the floating bilayer lipid membrane (fBLM), this refers to the SAM-Tg.

After transmembrane defects formation because of the activity of membrane-active species, the distribution of defects is rather heterogeneous. Therefore, the ions that penetrate the membrane and eventually reach the SAM-Tg are not uniformly distributed in this layer. That implies that its inner leaflet is not equipotential. On the other hand, for an intact bilayer, the layer can be regarded as equipotential.<sup>124</sup> The bilayer and SAM-Tg are electrically coupled, so the model in Figure 2.2-4a could be used to fit the EIS data of the intact bilayer. However, throughout the experiments, we found that it was more accurate to compare EIS data of intact bilayer to a bilayer altered by membrane-active species if both sets of spectra are fitted, if

possible, to the same EEC model shown in Figure 2.2-4b. The reason is that the real intact bilayer is never defect-free, and the stochastic nature of bilayer self-assembly results in varying distribution and density of natural defects between samples. Therefore, it is more accurate to compare the system before and after the action of membrane-active molecules by taking into account the  $CPE_{sp}$  in both cases. For a bilayer low in defects, experimental values of  $\alpha_{sp}$  may be close to zero, which means that the impedance of a submembrane region becomes resistive and cannot be distinguished from the  $R_{def}$ . In that case, an EEC model can be reduced to that in Figure 2.2-4c.

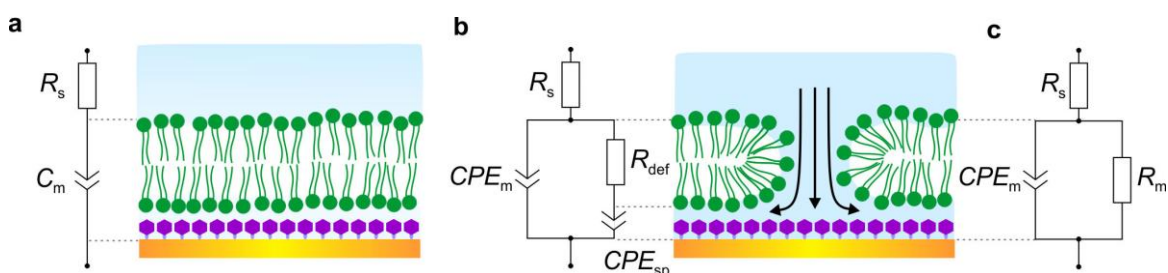


Figure 2.2-4. Equivalent electric circuits, modeled to correspond to BLM components, proposed for (a) a perfectly insulating bilayer and (b) a bilayer in the presence of defects when the transport of ions into the submembrane region is enhanced (schematically marked by arrows).

The model in Figure 2.2-4b was developed for tethered BLMs (tBLMs),<sup>120, 121</sup> but it was successfully applied for fBLMs as well.<sup>52</sup> The main difference between the two BLMs is the water content in the spacer region of the model membrane, which is small for tBLM,<sup>126, 127</sup> and high in fBLM.<sup>48, 50</sup> A submembrane region of the fBLM can be regarded as a water-rich layer characterized by an ordered network of hydrogen bonds (more ordered than that in bulk).<sup>50</sup> Some data suggests that the intact fBLMs result in fewer defects than the corresponding tBLMs,<sup>52</sup> which seems advantageous in distinguishing bilayer properties from AMPs-induced defects.

### 2.2.3. Polarization-modulation infrared reflection-absorption spectroscopy

PM-IRRAS measurements are applied to study thin organic molecular films adsorbed at the metal electrode surface. The PM-IRRAS setup allows determining the orientation and conformation of the adsorbed species quantitatively. The fundamental theory of the technique is described in detail in the literature.<sup>60, 105, 199</sup> In this section, the most fundamental and vital aspects of the PM-IRRAS measurements conducted during the present studies are recalled.

### 2.2.3.1. Introduction and fundamental theory

A thin-layer configuration cell of infrared reflection-absorption spectroscopy (IRRAS) allows placing the metal electrode at the optical window separated only by an electrolyte solution layer several micrometer-thick (Figure 2.2-6a). The IR beam is transmitted through the window-solution interface, a thin layer of the electrolyte, and then is reflected from the metal electrode surface. Thus, the optical path relies on the external reflection of the beam. In this configuration, it is almost impossible to remove the background spectrum. The background correction is made possible by polarization modulation (PM). Fast modulation of the incident beam occurs between parallel (*p*-polarization) and perpendicular (*s*-polarization) directions to the plane of incidence of the IR beam. An adsorbed on the metal electrode thin molecular film characterization relies on the surface selection rule (Figure 2.2-5). Thanks to the surface selection rule, the quantitative analysis of orientation and conformation of adsorbed on reflecting surface molecules is possible.

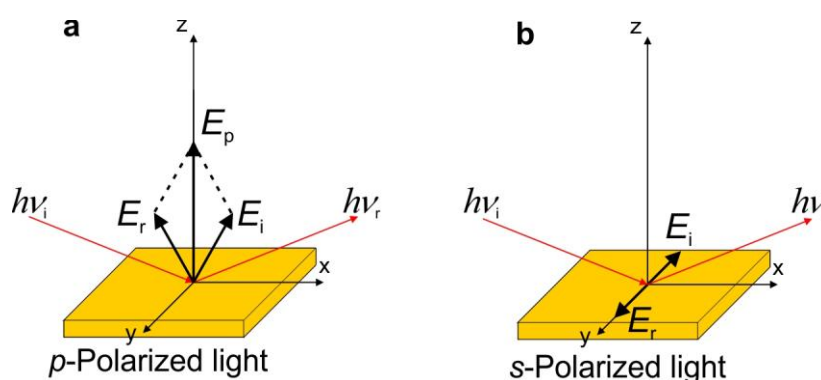


Figure 2.2-5. The surface selection rule of IRRAS. The incident beam,  $h\nu_i$ , (a) *p*-polarized or (b) *s*-polarized, is reflected from a smooth metal surface, resulting in the electric field enhancing or attenuating, respectively. Adapted from Ref.<sup>60</sup>

Upon illuminating a smooth metal electrode with the *p*-polarized light at a grazing angle of incidence, the electric field component perpendicular to the substrate surface is enhanced. In the case of illumination with the *s*-polarized light, the electric field component parallel to the substrate surface almost vanishes in the vicinity of a metal surface. Therefore, *s*-polarized light reflectivity ( $R_s$ ) is insensitive to surface adsorbed molecules and carries information from the bulk of the electrolyte solution. On the other hand, the reflectivity of the *p*-polarized light ( $R_p$ ) is sensitive to the molecules adsorbed at the surface through enhanced interference with their transition dipole component perpendicular to the electrode surface and thus is used to obtain a spectrum of the adsorbed molecules. That way, adsorbed molecules can be distinguished from the background signal from the molecules present in the bulk of the electrolyte solution. First, the background signal is acquired using *s*-polarized light. Then, the

*p*-polarized spectrum, which contains information from both background and surface molecules, is collected. Finally, the reflection-absorption spectrum  $\Delta S$  of the adsorbed film is obtained by subtracting reflectance of the *s*- from *p*-polarized light normalized by their average (2.2.3-1).

$$\Delta S = \frac{\Delta R}{\langle R \rangle} = \frac{|R_p - R_s|}{(R_p + R_s)/2} \quad 2.2.3-1$$

Still, PM-IRRAS is sensitive to molecules present on both the surface and in the vicinity of the metal electrode if these are at a distance of the  $\frac{1}{4}$  wavelength of the incident radiation (below 1  $\mu\text{m}$ ). Therefore, the background from the electrolyte cannot entirely be removed from the  $\Delta S$  spectrum. That implies certain restrictions in selecting aqueous electrolyte solution ( $\text{H}_2\text{O}$  or  $\text{D}_2\text{O}$ ) or analyte molecules (deuterated or non-deuterated) for the experiment to reduce the overlapping of the absorption bands.

### 2.2.3.2. PM-IRRAS setup

The PM-IRRAS basics of operation lie in the thin cavity cell configuration (Figure 2.2-6a) and the incident beam polarization modulation. Radiation beam from the Fourier-transform infrared (FTIR) spectrometer travels outside the device into the specially designed and custom machined setup that is placed in an external tabletop optical mount (TOM) box (Figure 2.2-6b and Figure 2.2-7). The TOM box can be continuously purged with a nitrogen stream to ensure the  $\text{CO}_2$  and water vapor removal during the experiment.

A convergent IR beam enters the TOM box and is deflected by flat and parabolic mirrors into the static polarizer. The beam travels through the photoelastic modulator (PEM) and reaches the spectroelectrochemical cell. The spectroelectrochemical cell is custom machined, all-glass, and connected to the optical window ( $\text{CaF}_2$  1" equilateral prism, Janos Technology) via Teflon™ flange. The beam is focused onto the working electrode, a 15-mm Au(111) single-crystal disk held in a glass capillary, which is used to approach the electrode towards the optical window in a precise and controllable way. The electrode is connected with the potentiostat clamp via a gold wire. A Pt foil cylinder is used as the counter electrode, and a saturated Ag|AgCl reference electrode is connected to the cell through a glass capillary. The reflected IR beam enters the MCT-A (mercury-cadmium-telluride, TRS 50 MHz bandwidth, Nicolet) detector through the ZnSe lens (1" focal length, 1.5" diameter with an anti-reflective coating, Janos Technology). Both the spectroelectrochemical cell and the detector are movable so that the incident angle can be adjusted according to the desired band that is to be analyzed, and the detected signal can be maximized.

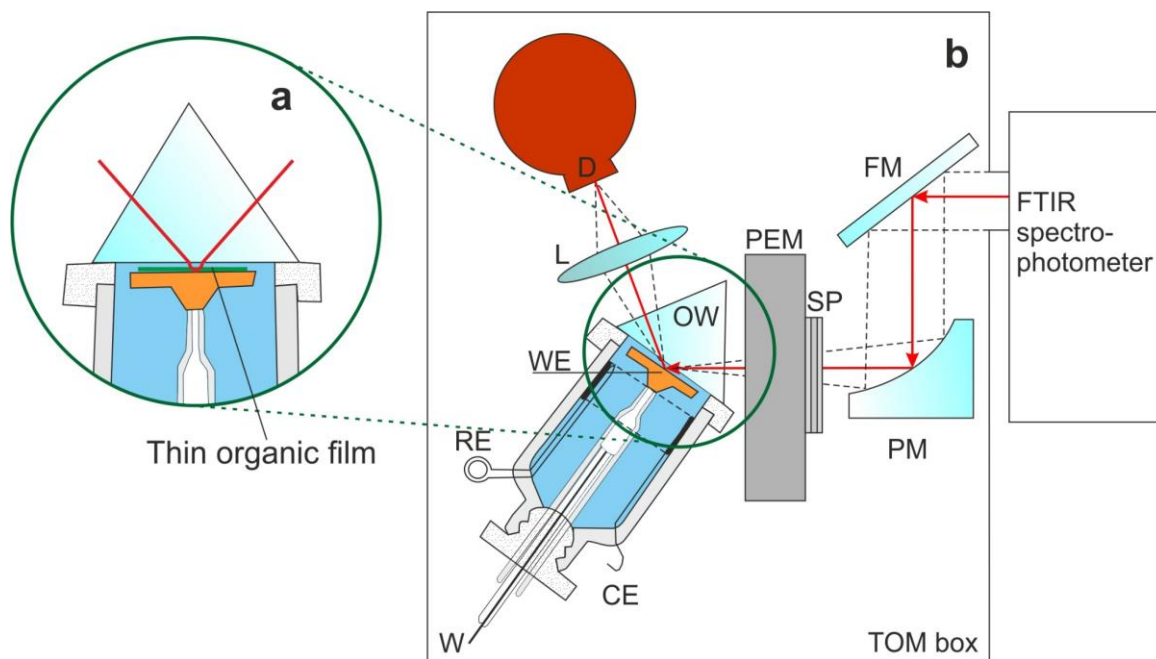


Figure 2.2-6. A schematic of (a) a thin-layer cell configuration, (b) the experimental PM-IRRAS set-up (FM, flat mirror; PM, parabolic mirror; SP, static polarizer; PEM, photoelastic modulator; OW, optical window; L, lens; D, detector) showing details of the glass spectroelectrochemical cell (WE, working electrode; CE, counter electrode; RE, reference electrode; W, gold wire). Adapted from Ref.<sup>105</sup>

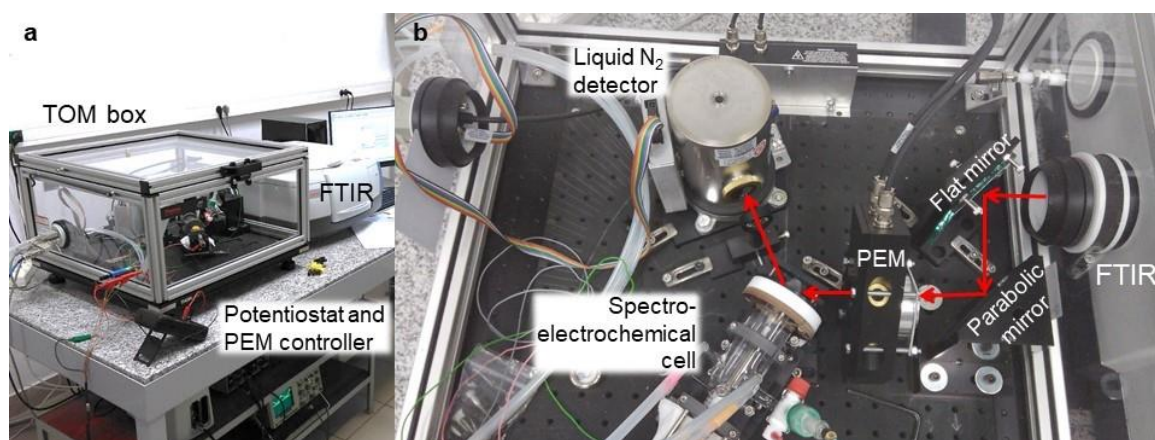


Figure 2.2-7. Photographs of spectroelectrochemical laboratory setup. (a) TOM box, FTIR spectrometer, potentiostat, and PEM controller. (b) Insight of the TOM box, including mirrors, PEM, spectroelectrochemical cell, and detector, with IR beam path marked with red arrows.

### 2.2.3.3. Optimization of the PM-IRRAS experimental conditions

The absorbance of organic molecules at the metallic mirror surface is proportional to a mean squared electric field strength (MSEFS) of the  $p$ -polarized light. Therefore, optimizing experimental conditions is equivalent to finding a global maximum of an MSEFS of the  $p$ -polarized light at the metal electrode surface.<sup>105, 200, 201</sup> Figure 2.2-8 presents a graph of an MSEFS as a function of the angle of incidence and the thin cavity gap thickness that was calculated for

a thin layer cell comprised of CaF<sub>2</sub> optical window, D<sub>2</sub>O electrolyte solution, and an Au(111) electrode, for convergent ( $\pm 5^\circ$ ) radiation of 2900 and 1600 cm<sup>-1</sup>. Calculations were performed using the Fresnel software.<sup>200</sup> The resulting optimal experimental conditions that maximize MSEFS value are 2.5  $\mu\text{m}$  at 56.3° and 3.4  $\mu\text{m}$  at 66° for 2900 cm<sup>-1</sup> and 1600 cm<sup>-1</sup> region, respectively.

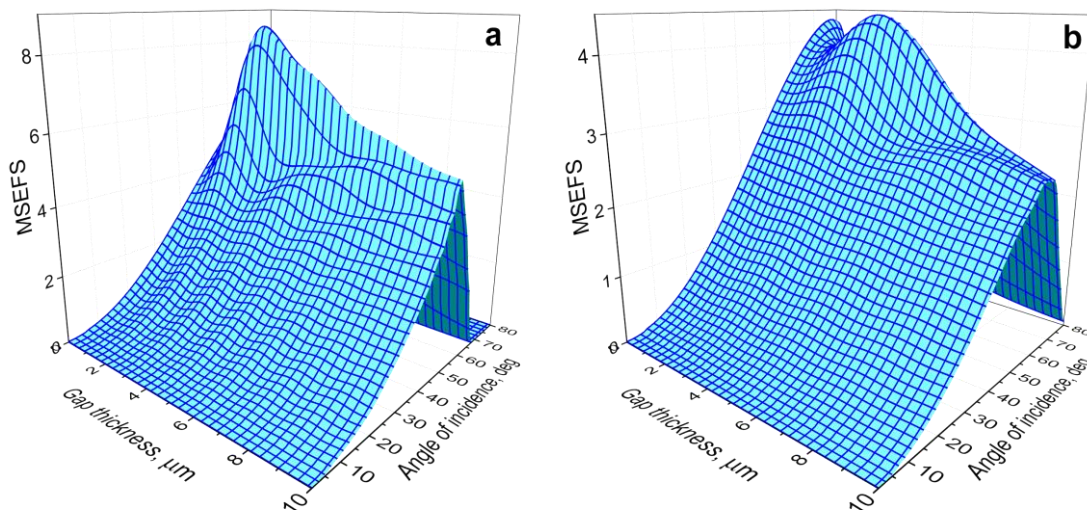


Figure 2.2-8. The mean squared electric field strength for a *p*-polarized light at the metal surface for CaF<sub>2</sub>|D<sub>2</sub>O|Au(111) stratified medium, calculated for a convergent ( $\pm 5^\circ$ ) beam of the wavenumber of (a) 2900 cm<sup>-1</sup> and (b) 1600 cm<sup>-1</sup>.

The experimental conditions, including an incidence angle and thin cavity gap thickness, are established before the experiment. For example, the incidence angle is readily set by moving the detector in the TOM box.

Thin-layer gap thickness is determined experimentally by measuring the reflectivity of the thin-layer cell. The procedure, described in detail elsewhere,<sup>105, 200</sup> compares the cell's theoretical reflectivity simulated using Fresnel equations in Fresnel software<sup>200</sup> and the experimental reflectivity of the corresponding cell setup (Figure 2.2-9). The thin cavity calculations are corrected by the multiplication coefficient, which accounts for the reflectivity decrease. That is because the electrode area is smaller than the IR beam spot size. Thus, gap thickness is optimal when the multiplication coefficient is close to 1.0.

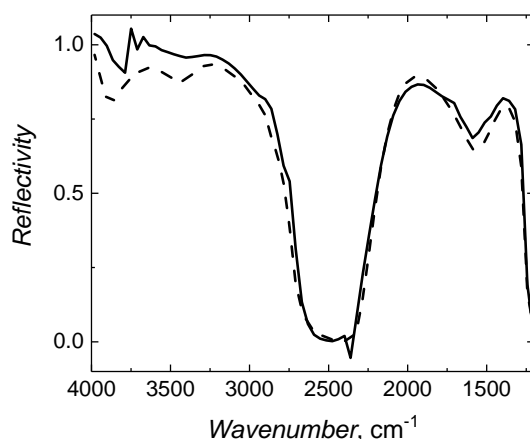


Figure 2.2-9. Reflectance spectra of a thin-layer spectroelectrochemical cell composed of  $\text{CaF}_2|\text{D}_2\text{O}|\text{Au}(111)$ . The solid curve indicates the experimental spectrum, the dashed curve is a theoretical spectrum for the thin cavity thickness of  $5\ \mu\text{m}$ , and the angle of incidence of  $57^\circ$ , the correction coefficient is 0.95.

#### 2.2.3.4. Corrections of the PM-IRRAS experimental spectra

The PM-IRRAS experiment can fully be optimized for a single wavelength only. That is a direct consequence of the PEM operation, in detail described elsewhere.<sup>105</sup> In brief, at  $\lambda_0$ , a wavelength at which the PEM is optimized, the polarization of the incident beam is periodically changed between  $p$ - and  $s$ -polarization, and every  $90^\circ$ , either  $I_s$  or  $I_p$  is incident at the detector. If the wavelength of the incident beam deviates from the  $\lambda_0$ , the polarization of the incident beam becomes circular (has both  $p$ - and  $s$ - components).

The signal from the detector must be demodulated, and a synchronous sampling detector (SSD) is utilized in our PM-IRRAS setup for this purpose. As a result, the experimental spectrum is the ratio of the intensity difference signal  $I_{\text{SSD}}^{\text{diff}}(2\omega)$  at the second harmonic frequency to the intensity average signal  $I_{\text{SSD}}^{\text{ave}}(2\omega)$  at the SSD terminal (Eq. 2.2.3-2).

$$\left(\frac{\Delta I}{\langle I \rangle}\right)_{\text{Exp}} = \frac{I_{\text{SSD}}^{\text{diff}}(2\omega)}{I_{\text{SSD}}^{\text{ave}}(2\omega)} = \frac{\Delta I \cdot J_2(\varphi_0)}{\langle I \rangle + \frac{1}{2}\Delta I \cdot J_0(\varphi_0)} \quad 2.2.3-2$$

In this equation,  $\varphi_0$  is the maximum phase shift introduced by the PEM, and  $J_2$  and  $J_0$  are the second-order and zero-order Bessel functions of  $\varphi_0$ , respectively. The following equations express  $J_2$  and  $J_0$ .

$$J_2(\varphi_0) = \frac{1 - \cos \varphi_0}{2}; \quad J_0(\varphi_0) = \frac{1 + \cos \varphi_0}{2} \quad 2.2.3-3$$

To calculate  $\frac{\Delta I}{\langle I \rangle}$  (or  $\frac{\Delta R}{\langle R \rangle}$ ) from the experimental PM-IRRAS spectra, the  $J_2$  and  $J_0$  functions must be determined in an independent experiment, in detail described elsewhere.<sup>200</sup> The determined calibration spectra for  $J_2$  and  $J_0$  functions are then used to correct experimental spectra (Figure 2.2-10). Thanks to this procedure, the PEM response artifacts are removed

from the experimental data. However, every two or three months, the PEM calibration procedure should be repeated because its response changes with time.

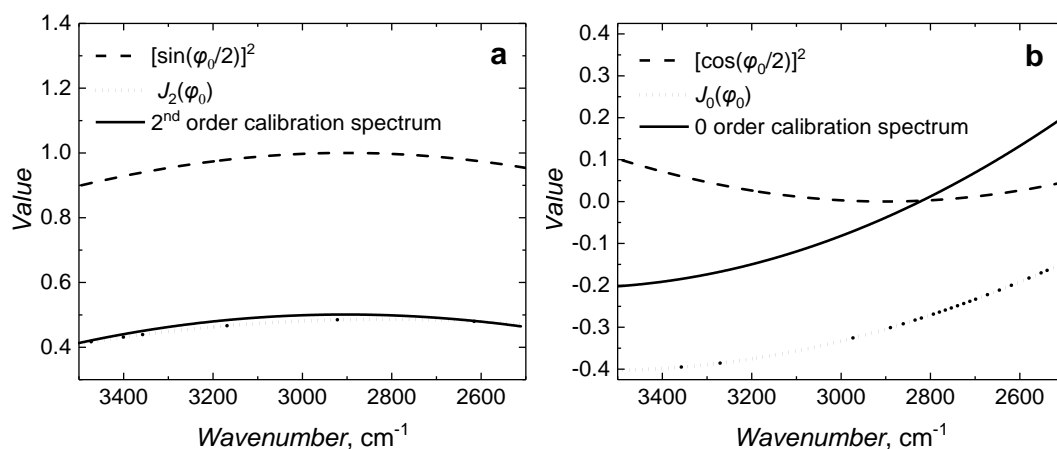


Figure 2.2-10. The theoretical response functions of the PEM calculated by Bessel software<sup>200</sup> and the (a) second-order and (b) zero-order calibration spectra. Solid curves indicate empirical calibration spectra for  $J_2$  and  $J_0$  functions, dotted curves are the theoretical Bessel functions, and dashed curves are the theoretical cosine terms. The PEM was optimized for  $2900\text{ cm}^{-1}$ .

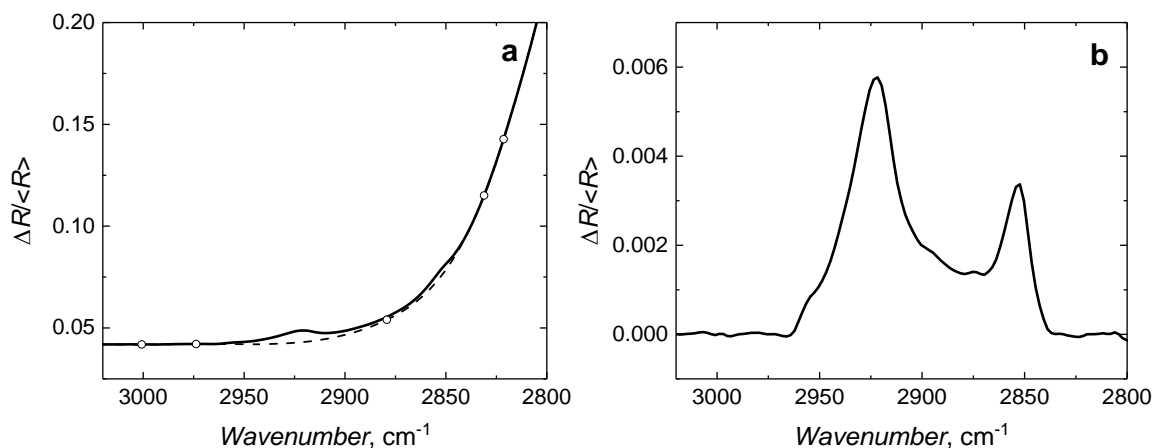


Figure 2.2-11. The PM-IRRA spectra of the 3×PC:3×PG (3:2) membrane deposited on Au(111)|β-Tg in the presence of LL-37 in the 40:1 lipid-to-peptide molar ratio, in the C-H stretching region, acquired in 10 mM NaF<sub>2</sub> in D<sub>2</sub>O at 100 mV, (a) after  $J$ -function correction and before background subtraction (solid curve), with spline function (dashed curve) and template points (circles), (b) after background subtraction.

The  $J$ -functions correction of the experimental spectra is accomplished using the Spline software, an updated version of Fresnel software.<sup>200</sup> The last step of the PM-IRRA spectra corrections is background subtraction. This step requires establishing the template for building the spline function to remove the background from the experimental spectra. The Spline program builds an interpolated spline, which models the IR absorbance of the background species for

the entire frequency range at the given electrode potential. The spline is then subtracted from the experimental spectrum. An example of a result of this background correction is presented in Figure 2.2-11.

### 2.2.3.5. Transmission IR spectroscopy

The IR absorbance spectrum of randomly oriented molecules is necessary to accurately determine the average angle of the transition dipole moment for a chosen IR vibrational mode of those molecules. Transmission spectroscopy was used to determine the optical constants of the molecules used in this study. A scheme of the transmission cell is presented in Figure 2.2-12. Two CaF<sub>2</sub> windows (32-mm diameter, 3-mm thick) are separated by a Teflon™ gasket of 25 μm nominal thickness and pressed together with aluminum plates. Teflon™ tubing was inserted as the inlet and outlet to the Teflon™ body, and a 1-mL plastic syringe was attached to fill the cell with the analyte solution. The empty cell was inserted into the FTIR spectrometer (Thermo Fisher Scientific) in the focal point center. The spectrum of the empty cell in the air (Figure 2.2-13) was used to calculate the real thickness, *d*, of the transmission cell cavity using the following equation.

$$d = \frac{\Delta N}{2n(\bar{\nu}_2 - \bar{\nu}_1)} \quad 2.2.3-4$$

In this equation, *n* is the refractive index of the medium inside the cell (for empty cell in the air *n* = 1), and Δ*N* is the number of fringes between  $\bar{\nu}_2$  and  $\bar{\nu}_1$ . For the situation presented in Figure 2.2-13, Δ*N* = 6 and Δ $\bar{\nu}_N$  = 1021, thus *d* = 29.38 μm.

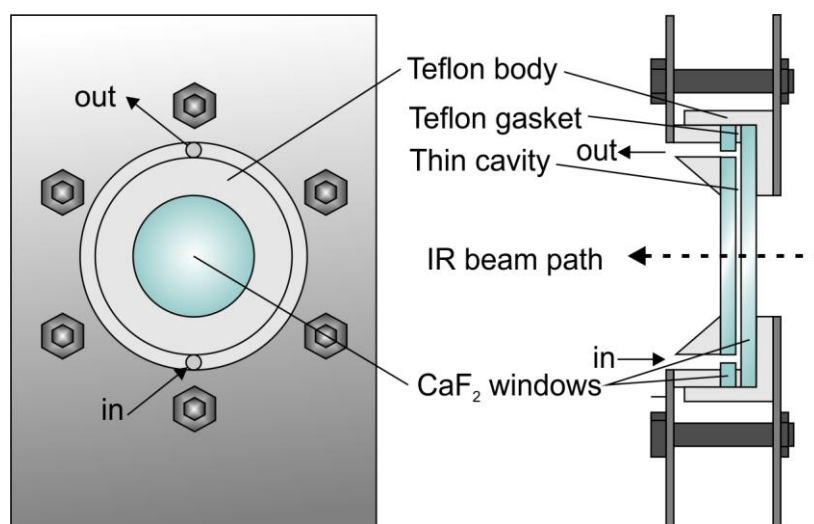


Figure 2.2-12. Scheme of a thin-cavity transmission flow cell used for the determination of analyte optical constants. The design of the cell was adapted from Zamlynyy,<sup>200</sup> and the cell was custom machined.

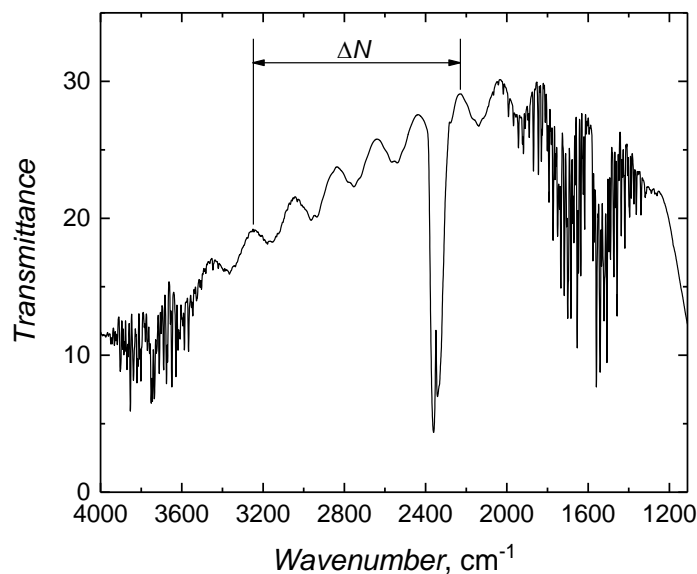


Figure 2.2-13 The transmission IR spectrum of the interference fringes between two  $\text{CaF}_2$  windows in the air (without purging,  $\text{CO}_2$  and  $\text{H}_2\text{O}$  bands are visible in the spectra), used to calculate the thickness of a thin layer between the windows.

Once the cavity thickness was established, the cell was filled by placing the inlet tube in the solution and withdrawing the syringe piston at the outlet tube. This sequence was applied to minimize air bubbles forming inside the transmission cell. Next, the background spectrum was acquired with 200 scans. Then, the transmission cell was filled with an analyte solution of a 0.125 or 0.5% volume concentration, and the background spectrum was acquired again. The ratio of the intensity of the analyte spectrum to that of the blank is the transmittance of the analyte.

### 2.2.3.6. Optical constants

The Optical Constants program, named OptCo,<sup>200</sup> was used to calculate optical constants of the analyte, namely, refractive index,  $n$ , and attenuation coefficient,  $\kappa$ . An example of optical constants calculated for DMPC:DMPG (3:2) is presented in Figure 2.2-14.

OptCo software requires an input of experimental transmission spectra, analyte concentration (volume fraction of the analyte), electrolyte composition, cell cavity thickness, optical window material, and an initial estimate for the analyte average refractive index (the value of 1.3 was used). First, the attenuation coefficient for the analyte,  $\kappa_i$ , is calculated by the software using the Beer-Lambert law, which takes into account the dilution of the analyte.<sup>200</sup> A volume fraction is used to calculate the attenuation coefficients because it allows preserving information on interactions between the analyte and the electrolyte solution. Then, the obtained approximate attenuation coefficient  $\kappa_i$  values are used to calculate the  $\kappa$  value for analyte solutions of other concentrations. The Kramers-Krönig transformation is then applied to

determine the refractive index of the analyte,  $n_i$ , using the  $\kappa_i$  value as an initial estimate.<sup>200</sup> A detailed incremental calculation procedure can be found in Ref.<sup>200</sup> Calculations are repeated incrementally until the theoretical transmittance spectra deviated from those experimental spectra by no more than a specified value of precision, set to 1%.

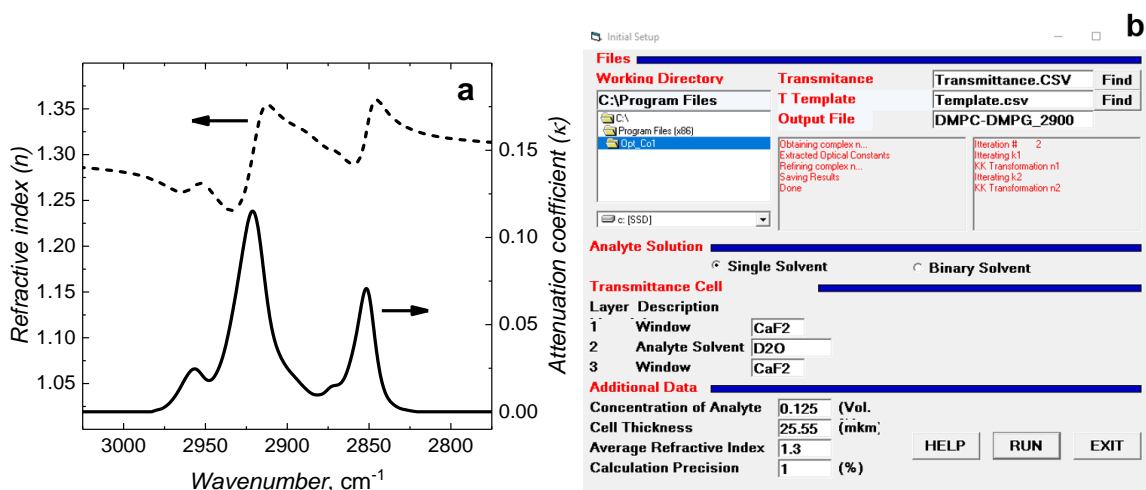


Figure 2.2-14. (a) Optical constants for DMPC:DMPG (3:2) vesicles (0.125% volume concentration) in  $\text{D}_2\text{O}$  for 2900  $\text{cm}^{-1}$  region. The dashed curve indicates a refractive index ( $n$ ), and the solid curve indicates an attenuation coefficient ( $\kappa$ ). (b) Screenshot of OptCo software.

### 2.2.3.7. Simulation of the PM-IRRA spectra

Optical constants obtained for the isotropic solution of the analyte assume no preferential orientation of transition dipoles of analyte molecules. Therefore, these constants can be used for simulating the spectrum of randomly oriented molecules of the analyte deposited on the metal electrode surface with Fresnel software.<sup>200</sup> The values of the incidence angle and the thin-cavity thickness used to acquire the experimental data are input to the software. Optical constants of the optical window, electrolyte, and metal electrode are taken from the literature and already implemented into the software. The simulated spectrum is obtained from the reflectivities of the model cell using Eq. 2.2.3-1. The simulated theoretical spectrum, calculated for each experimental setup, is then utilized to determine the orientation of organic molecules adsorbed on the metal electrode. An example of simulated spectrum calculated for 3×PC:3×PG (3:2) molecules in  $\text{D}_2\text{O}$ , for 5- $\mu\text{m}$  gap thickness and 57° incident angle for the 2900  $\text{cm}^{-1}$  region, is shown in Figure 2.2-15.

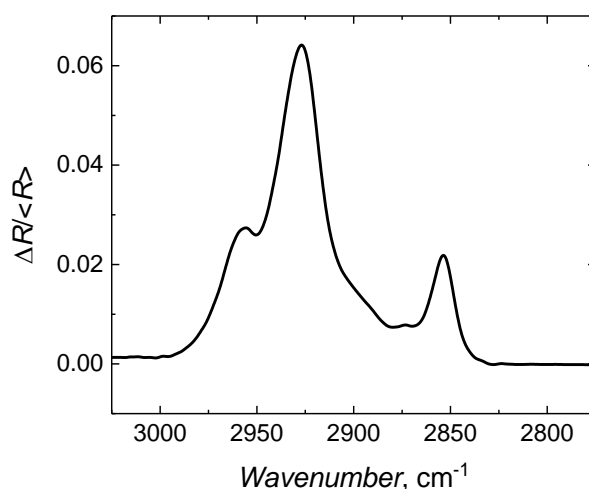


Figure 2.2-15. The simulated spectrum for randomly oriented 3×PC:3×PG (3:2) molecules in D<sub>2</sub>O, calculated for 5- $\mu$ m gap thickness and 57° incident angle for the 2900 cm<sup>-1</sup> region.

### 2.2.3.8. PM-IRRA spectra band deconvolution

Band deconvolution is a crucial step in attaining proper values of the integrated intensities of the absorption bands,  $A$ , required for precise tilt angle calculations of studied molecules. For resolving overlapping bands in PM-IRRA spectra, the second derivative (SD) and Fourier self-deconvolution (FSD) are applied.

The SD method is initially used to identify band positions (Figure 2.2-16a). That can be done with either Origin or Omnic software v. 9.8 (Thermo Fisher Scientific Inc.). Then, at least 7-Point Savitsky-Golay SD with the 3<sup>rd</sup> order polynomial function was applied to the analyzed band. Local minima in the SD denote peak positions. If the signal-to-noise ratio is low, the SD method will overestimate the number of vibrational bands in the case of broad spectral bands. In such a case, the FSD method should be applied to identify the peaks. First, the FSD was performed in Omnic to confirm peak positions. Then, a triangular apodization was applied. The bandwidth and the enhancement factor were optimized for a given band to ensure that an accurate number of peaks was resolved. The values were usually  $\sim 15.0$  and  $\sim 2.5$  bandwidth and enhancement factor, respectively, for the phospholipid C–H stretching region. Then, PeakFit v. 4.12 software (SeaSolve Software Inc.) was used to perform thorough peak fitting (Figure 2.2-16b). A Lorentz peak type was used for the C–H stretching band of the phospholipid acyl chain, while the Gauss peak type was used for the amide I band of peptides. First, the analyzed spectra were baseline corrected, and then the “Auto FitPeaks II Second Derivative” option was chosen to perform band deconvolution. The fitting was iterated several times until the optimal fit, with  $R^2 > 0.97$  value, was obtained.

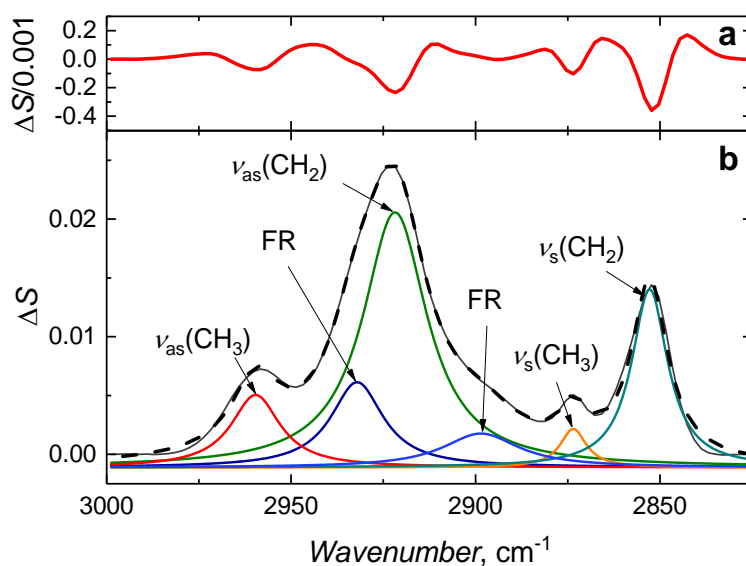


Figure 2.2-16. PM-IRRA spectra of the DMPC film acquired at  $-800$  mV vs. Ag|AgCl. (a) 7-Point Savitsky-Golay second derivative with the 3<sup>rd</sup> order polynomial function. (b) The PeakFit result; the solid black curve is an original spectrum, dashed black curve is a cumulative peak fit result, with  $R^2 = 0.996$ .

### 2.2.3.9. Determination of the orientation of organic molecules adsorbed at the metal electrode surface

Processed experimental PM-IRRA spectra are ready for quantitative analysis. Information that can be extracted from these spectra is the orientation of the molecules adsorbed at the metal electrode surface. That is, it is possible to calculate tilt angles of, for example, phospholipid acyl chains vs. electrode surface normal. A procedure implemented in this study utilizes isotropic optical constants to extract the molecular orientation of the anisotropic film comprised of molecules of this analyte. The integrated intensity of the absorption band,  $A$ , of the analyte molecule film adsorbed at the metal electrode is, therefore, proportional to the square dot product of the transition dipole moment,  $\vec{\mu}$ , and the electric field of the photon,  $\vec{E}$ , as given by the following equation.<sup>200, 201</sup>

$$\int A dv \propto \Gamma |\vec{\mu} \cdot \vec{E}|^2 = \Gamma |\mu|^2 \langle E^2 \rangle \cos^2 \theta \quad 2.2.3-5$$

In this equation,  $\Gamma$  is the analyte surface concentration,  $|\mu|$  is the absolute value of the transition dipole moment,  $\langle E^2 \rangle$  is the mean squared electric field strength (MSEFS) of the photon, which was discussed in Section 2.2.3.3, above, of this Chapter, and  $\theta$  is the angle between the electric field of the photon, which is always normal to the metal surface,<sup>201</sup> and the transition dipole of vibration in the analyte molecule.

To determine from Eq. 2.2.3-5 the molecular orientation as a direct absolute value of  $\theta$ , one needs to compare the experimental reflectance-absorbance spectra,  $A_{\text{exp}}$ , with the theoretical simulated spectra for randomly oriented molecules,  $A_{\text{sim}}$ . The theoretical spectrum is

simulated for the same surface concentration, the angle of incidence, the thin-cavity thickness, and the absolute value of the transition dipole moment (assuming that the absolute value of the transition dipole moment is the same during transmission measurement and reflection-absorption measurement), as in the experiment. The theoretical spectra calculation procedure was described in Sections 2.2.3.5 and 2.2.3.6 above. In the case of absorption of a linearly polarized light by randomly oriented molecules,  $\cos^2 \theta = \frac{1}{3}$ .<sup>60, 200</sup> Then, the following equation can be used to calculate  $\theta$ .

$$\cos^2 \theta = \frac{1 \int A_{\text{exp}} d\nu}{3 \int A_{\text{sim}} d\nu} \quad 2.2.3-6$$

Once the angle between the surface normal and the transition dipole moment of the analyte molecule is calculated, tilt angles of specific molecule's vibrations can be calculated, given the geometry between those vibrations is known. Usually, the directions of the transition dipoles are available in the literature. Intensities of the bands corresponding to the symmetric,  $\nu_s(\text{CH}_2)$ , and asymmetric,  $\nu_{\text{as}}(\text{CH}_2)$ , vibrational mode of methylene stretches are used to calculate the hydrocarbon tilt angle of lipid acyl chains (Figure 2.2-17). The vectors of the transition dipoles of the symmetric and asymmetric methylene stretches are perpendicular to each other and are perpendicular to the fully extended all-*trans* fragment of the acyl chain. Therefore, the tilt angle ( $\theta_{\text{tilt}}$ ) of the *trans* fragments of acyl chains can be calculated using the following relationship.<sup>60, 202</sup>

$$\cos^2 \theta_{\text{as}} + \cos^2 \theta_s + \cos^2 \theta_{\text{tilt}} = 1 \quad 2.2.3-7$$

This equation gives the average orientation,  $\theta_{\text{tilt}}$ , of the hydrocarbon chain in the *trans* conformation. Another parameter used to describe the orientation of acyl chains is the order parameter,  $S$ , for the transition dipole moment, which is defined as<sup>60, 104</sup>

$$S_{\text{CH}_2} = \frac{1}{2}(3\langle \cos^2 \theta \rangle - 1) \quad 2.2.3-8$$

where  $\theta$  is calculated from Eq. 2.2.3-6. The order parameter can assume values between  $-0.5$  and  $1$ . The average tilt of transition dipole of molecules is oriented perpendicular or parallel to the surface normal if  $S = -0.5$  or  $S = 1$ , respectively. If  $S = 0$ , the system is disordered with randomly oriented molecules, whose average tilt angle is  $54.7^\circ$  (i.e., magic angle).

In amide I band analysis, the average tilt angle of the  $\alpha$ -helices,  $\theta_{\text{helix}}$ , with respect to the surface normal was calculated according to the following equation.

$$\theta_{\text{helix}} = \cos^{-1} \sqrt{\frac{2}{3}(S_{\text{helix}} + 1)} \quad 2.2.3-9$$

In this equation,  $S_{\text{helix}}$  is the order parameter of the helical axis calculated using the equation<sup>104, 203-205</sup>

$$S_{\text{helix}} = \frac{2}{3} \frac{S_{\text{C=O}}}{\cos^2 \theta_{\text{ref}} - 1} \quad 2.2.3-10$$

where  $\theta_{\text{ref}}$  denotes the angle between the  $\alpha$ -helix long axis and the transition moment of the amide I vibration, which serves as a reference angle;  $S_{\text{C=O}}$  is the order parameter associated with the angle between the transition dipole moment of the amide I group and the surface normal, calculated by the following equation.<sup>104</sup>

$$S_{\text{C=O}} = \frac{3}{2} (\cos^2 \theta_{\text{C=O}} - 1) \quad 2.2.3-11$$

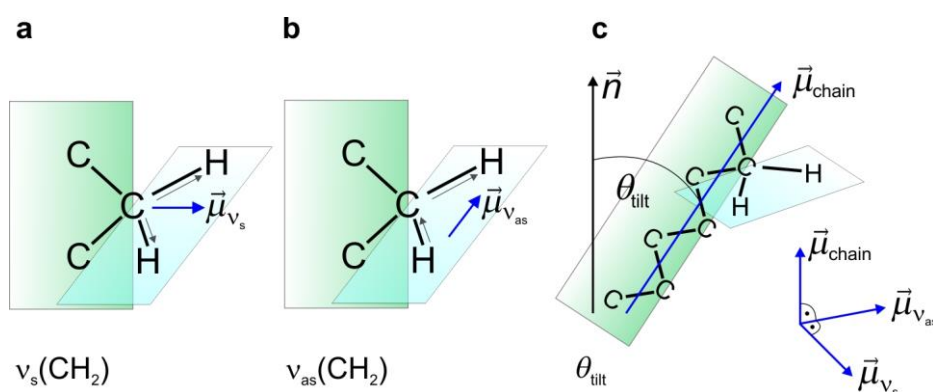


Figure 2.2-17. Schematic representation of the direction of the transition dipoles for (a) symmetric and (b) asymmetric stretches for a lipid acyl chain. (c) Schematic of the tilt angle ( $\theta_{\text{tilt}}$ ) of a lipid acyl chain. Adapted from Ref.<sup>60</sup>

## 2.3. Experimental procedures

### 2.3.1. Atomic force microscopy imaging

MultiMode 8 microscope with NanoScope V controller from Bruker (Bruker Corporation, Santa Barbara, CA) was used for atomic force microscopy imaging of the phospholipid bilayers. Moreover, the PF-QNM mode was used for imaging. AFM experiments were performed using an aqueous environment. Therefore, a fluid cell (MMTMEC, Bruker) with a silicone O-ring was used, together with plastic 1-mL syringes for cell filling and fluid withdrawal. Imaging was conducted with an “E” piezoelectric scanner, with a maximum imaging area of  $10 \times 10 \mu\text{m}^2$ .

AFM tips, made of quartz-like material, with Cr/Au reflective coating were used (qp-BioAC, Nanosensors, NanoWorld AG, Switzerland). The shape of the cantilever was a circular symmetric hyperboloid with a nominal tip end radius  $R_{\text{tip}} < 10 \text{ nm}$ , nominal spring constant  $k = 0.1 \text{ N m}^{-1}$  ( $0.06 - 0.18 \text{ N m}^{-1}$ ), 50 kHz resonance frequency, and 60- $\mu\text{m}$  length.

Other probes included the silicon nitride BioLever Mini BL-AC40TS-C2 (Olympus) probe, with Cr/Au reflective coating,  $k = 0.09 \text{ N m}^{-1}$  ( $0.02 - 0.14 \text{ N m}^{-1}$ ), and  $f_0 = 110 \text{ kHz}$  (20 - 30 kHz in water) with silicone tetrahedral tip of nominal  $R_{\text{tip}} = 8 \text{ nm}$ . ScanAsyst Fluid+ ( $k = 0.7 \text{ N m}^{-1}$ ), and the ScanAsyst Air ( $k = 0.4 \text{ N m}^{-1}$ ) probe from Bruker.

#### 2.3.1.1. Calibration procedure

For quantitative AFM measurements, probe calibration is required. The  $R_{\text{tip}}$  was determined by imaging titanium roughness sample (RS-12M, Bruker) in the air and performing Tip Qualification procedure in NanoScope Analysis software.<sup>206</sup> Special attention was paid to image the sample with similar deflection values from the probe to probe (<2 nm at most flat surfaces). The value of the average deformation of the roughness sample was used as input for tip qualification and radius estimation (“Height 1 from Apex”). It is essential to determine  $R_{\text{tip}}$  at a low deformation depth and then, during imaging, select a setpoint value that allows maintaining deformation at a constant level, the same level as that during the calibration. The rest of the calibration was performed before each experiment in Milli-Q water. Deflection sensitivity, DeflSens, was determined at the freshly cleaved muscovite mica surface (V-1 grade 12-mm diameter disks, TedPella or Electron Microscopy Sciences), and the spring constant,  $k$ , was calculated using the thermal tune method.<sup>207</sup>

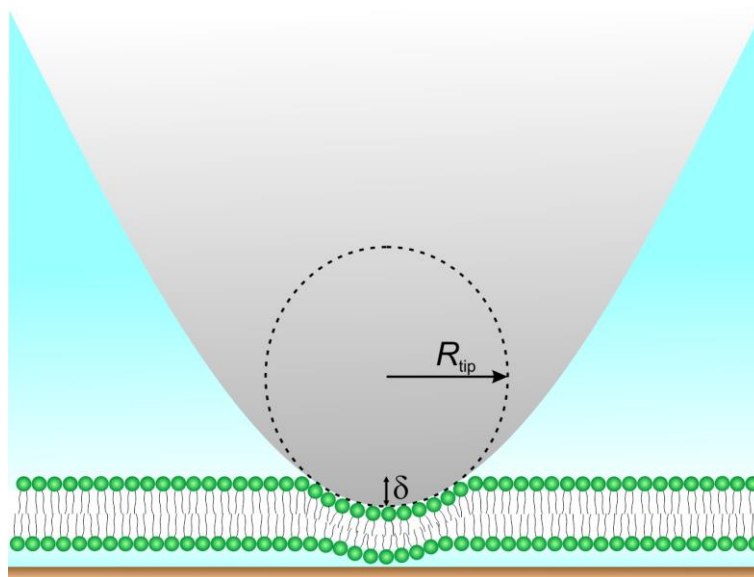
### 2.3.1.2. AFM nanomechanical data analysis

Data were analyzed with the use of NanoScope Analysis v. 1.7 (Bruker Corporation), Gwyddion v. 2.54-2.58, and AtomicJ v. 2.1-2.2.<sup>208</sup> Basic operations, such as background removal, step line correction (tilt removal), horizontal strokes correction, or cross-sectional profiles and roughness analysis, were performed using Gwyddion. The quantitative nanomechanical analysis was run in AtomicJ.

Young's modulus was determined by fitting the Hertz model to the retraction part of the force curve.<sup>74</sup> In this model, the relation between indentation and force assumes a spherical indenter and is described by the following equation:

$$F = \frac{4E}{3(1-\nu^2)} \sqrt{R_{\text{tip}}} \delta^{\frac{3}{2}} \quad 2.3.1-1$$

where  $F$  is the applied force load,  $E$  is Young's modulus of the sample,  $\nu$  is Poisson's ratio of the sample,  $\delta$  is indentation depth, and  $R_{\text{tip}}$  is the AFM tip end radius. Even though several indentation models are available, I assumed this approach as correct because the tip end radius compared to the bilayer thickness is large enough to assume spherical tip geometry in contact with the sample. Therefore, the contact radius remains smaller than the sphere radius. For example, for an 8-nm tip end radius, the contact radius is 5.3 or 3.9 nm at an indentation depth of 2 or 1 nm, respectively. Moreover, the tip-sample adhesion force is negligible in comparison with the loading force. Regarding material properties, the bilayer is assumed to be isotropic and linearly elastic. Last, the Hertz approach resulted in quality higher, or similar, in terms of  $R^2$ , to that of other models. Scheme 2.3-1 shows a paraboloidal tip with a sphere-approximated end radius indenting a thin bilayer. Values of the Poisson's ratio should be obtained experimentally (in an independent experiment) to calculate the sample modulus of elasticity (referred to as Young's modulus). For biological samples, it is assumed that they are incompressible. Thus, Poisson's ratio of 0.5 is used for modulus calculations. Overestimation of Poisson's ratio leads to underestimation of Young's modulus. According to the Monte Carlo simulations,<sup>209</sup> fluid and interdigitated phases exhibit comparable Poisson's ratio in both  $x$  and  $y$  directions, 0.5 and 0.4, respectively, which is characteristic of isotropic materials, while for the gel phase, Poisson's ratio is significantly different for both directions, being 0.11 and 0.54, showing that bilayers in the gel phase behave as an anisotropic material.



Scheme 2.3-1. Schematic representation of the tip-surface contact and indentation, scaled up remaining real proportions corresponding to a 5-nm thick bilayer with 1-nm diameter phospholipid headgroups, paraboloid tip end radius approximated by an 8-nm radius sphere and 2 nm indentation depth,  $\delta$ . The bilayer is separated from the mica by a 1-nm thick water layer.

In most cases, the F-D curves were pre-processed by cropping the domain to 80-100 nm, the contact estimator was chosen to be robust exhaustive, the estimation method was based on the contact model with the 3<sup>rd</sup> degree baseline estimation, and the contact point was found on the extended curve. Finally, the model was fitted to the curve's withdrawal part by applying an algorithm utilizing robust estimators. Those estimators reject the parts of force-distance data that grossly deviate from the model, which usually means deviation from a linear elastic deformation.

### 2.3.1.3. Finite thickness correction

Finite sample thickness correction was applied to consider the rigid substrate effect. Although some works state that membrane properties are not influenced by the supporting material when the indentation depth is below 20% of the sample thickness,<sup>72</sup> Young's modulus values were herein corrected by utilizing equations based on the Lebedev-Ufliand (1958) exact numerical solution to the problem of a thin sample indented with a spherical or conical tip. This approach was approximated using a Lebedev-Chebyshev method and implemented in AtomicJ software. Hence the effect of a rigid substrate for a loose layer indented by a small paraboloidal probe is much lower than for bounded layers or conical probes. The Lebedev-Chebyshev correction for non-adherent samples and the paraboloidal tip (Hertz model) was applied to our data. The sample thickness was determined based on the topography image containing both areas of the sample and the substrate.

### 2.3.2. Electrochemical measurements

All electrochemical measurements were conducted with a BioLogic VSP potentiostat/galvanostat with a low-current (LC) option (it lowers the base current to 1 nA) (BioLogic Sciences Instruments) unless otherwise stated. Measurements were performed at a controlled room temperature of 21 °C.

All electrochemical measurements were performed in an all-glass three-electrode cell with a hanging meniscus configuration, Teflon™ caps, and Nylon gas tubing. (Figure 2.3-1). A hanging meniscus is obtained by a working electrode approaching the electrolyte solution surface until it is touched, and then the electrode is withdrawn until it stays in contact with the electrolyte solution joined only with a meniscus between them. This way, only the Au(111) surface is in contact with the solution, and the active area of the electrode (which possesses exposed, and therefore, electrochemically active edge) is kept constant throughout all experiments. A 10-mm diameter disk Au(111) single-crystal was used as the working electrode. Moreover, a saturated calomel electrode, SCE, connected to the cell through a salt bridge, and a 0.5-mm diameter gold wire, spirally coiled into a flat 10-mm diameter disk, were used as the reference and counter electrode, respectively.

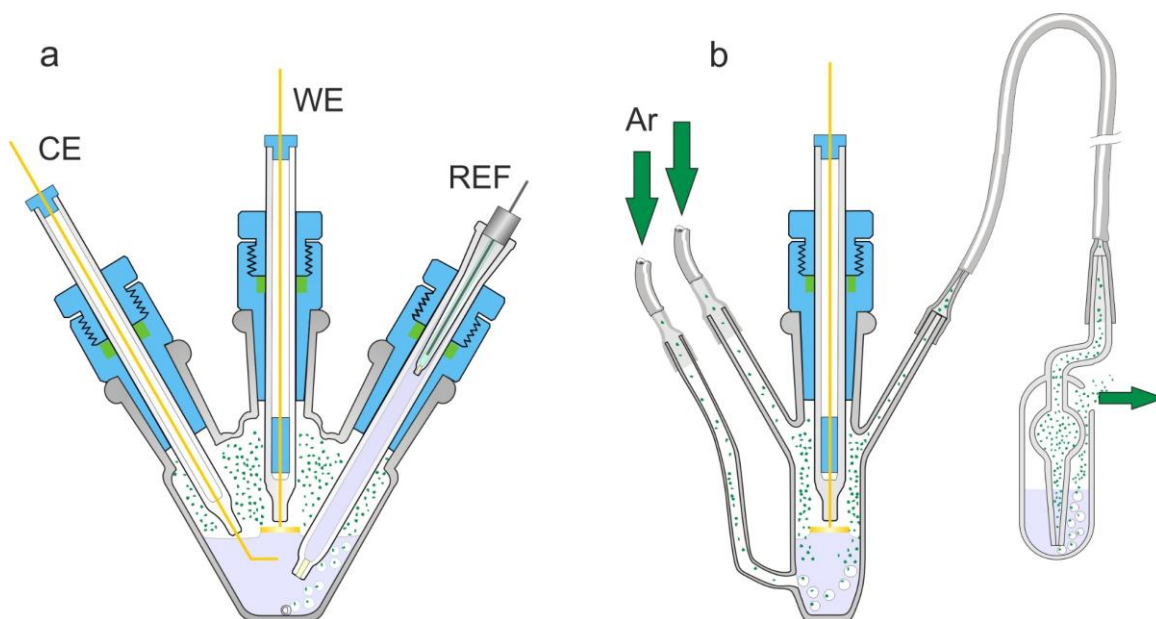


Figure 2.3-1. Schematic of an all-glass three-electrode V-shaped electrochemical cell (a) front and (b) side view. Argon inlets are marked, where the bottom one allows passing the gas through the electrolyte before the experiment and is switched to the top one that maintains gas flow above the solution during the experiment. The supporting electrolyte solution is marked in violet, Teflon™ parts are marked in blue, gas molecules are depicted as green dots.

Before each electrochemical experiment, the electrochemical cell was deaerated with argon passing through the solution for 30 min, while the WE was withdrawn from the solution to

avoid model membrane damage. Then, the Ar flow was maintained above the solution during the whole experiment.

CV experiments were performed at a scan rate of 20 mV s<sup>-1</sup>. The electrode was conditioned by running 20 CV cycles before EIS measurements. A potential range in which the Au(111)|β-Tg|fBLM electrode exhibited the capacitive behavior was 100 to -400 mV vs. SCE.

### 2.3.2.1. Electrochemical impedance spectroscopy measurements and data analysis

EIS measurements were performed every 100 mV, from 100 to -400 mV, at a 5-mV sinusoidal amplitude, with an average of 3 measurements per frequency and 10 points per decade, in the frequency range of 10 kHz to 10 mHz (or 10 kHz to 100 mHz in some experiments).

Impedance spectra were analyzed using ZView 3.3d software (Scribner Associates, Inc.). Equivalent circuit fitting (described in Section 2.2.2.5, above) was performed with the data-modulus weighting method, with a careful indication of initial fit values until a satisfactory fit was obtained. Calculated values and fit results were exported and plotted in Origin.

### 2.3.2.2. Chronocoulometry measurements

Chronocoulometry was used to determine the charge density,  $\sigma_M$ , at the electrode surface by measuring the difference between the charge density at a potential  $E_i$  and  $E_{des}$ , where the bilayer is adsorbed to, or desorbed from the electrode surface, respectively. First, the Au(111) electrode was held at a base potential,  $E_b$ , of -100 mV for 120 s. Then, the potential was switched to a potential of interest,  $E_i$ , and then held for 120 s. Next, the desorption potential,  $E_{des}$ , equal to -950 mV, was applied for 0.15 s. The current transient of this step corresponds to the desorption of the film and recharging of the interface. By integration of this current transient, the difference between  $\sigma_i$  and  $\sigma_{des}$  is obtained.<sup>210</sup> The absolute charge densities for bare Au(111) electrodes were calculated using the potential of zero charge,  $E_{pzc}$ , determined independently to be 215 mV vs. Ag|AgCl.<sup>211</sup>

## 2.3.3. PM-IRRAS measurements

### 2.3.3.1. PM-IRRAS experiment

The CaF<sub>2</sub> prism was rinsed with water, then methanol several times, and then pat dried with a KimWipe tissue. Next, it was placed in a UV ozone chamber, frosted side down, for 20 min. The spectroelectrochemical cell and electrodes were cleaned and prepared as described previously in Sections 2.1.2 and 2.1.3 (above). The angle of incidence was adjusted according to calculations for the selected region. The position of the empty spectroelectrochemical cell

was adjusted to obtain a maximal signal. The background signal was acquired in air, and the spectroelectrochemical cell was then carefully filled with 0.1 M NaF in D<sub>2</sub>O. The Au(111) electrode was moved towards the prism until the best signal was obtained. The cell was again readjusted to maximize the signal. Then, the gap thickness was measured, as described in Section 2.2.3.3 above. Once the gap was optimal, the detector was filled with liquid nitrogen. Moreover, the TOM box and the spectroelectrochemical cell were purged for 6 h using the CO<sub>2</sub>- and H<sub>2</sub>O-free air. The background spectrum was acquired with the PEM turned off. To run the actual experiment, the PEM is turned on, and the output signal is checked. The PEM gain should be set to a value that gives the best average and difference signal intensity, but the difference signal should remain smaller than the average. The “macro” file is run. The “macro” file is a home-written script algorithm that coordinates spectrometer and potentiostat running simultaneously. First, the initial potential of the WE is set, and then a series of potentials is applied, as programmed in a “macro” file. For the BacSp222 study, this file was programmed to start at -0.2 V vs. Ag|AgCl and then increase to 0.3 V with a 0.1-V potential step. Then, the spectra were acquired from -0.3 V to -0.8 V with a -0.1-V potential step. The spectra are acquired with the 4-cm<sup>-1</sup> resolution and 6000 scans per the potential applied. The acquisition is carried out at least overnight, and liquid nitrogen is refilled every 10 h. When spectra are recorded with the 4 cm<sup>-1</sup> resolution, the data points are computed by every 2 cm<sup>-1</sup>. The bands are plotted by interpolation between these points; therefore, the band position can be determined with the 0.5-cm<sup>-1</sup> accuracy.<sup>212</sup>



## CHAPTER 3: Results and discussion

The research undertaken during my Ph.D. studies resulted in four projects. Herein, I present findings regarding the activity nature of membrane-active species such as bacteriocin BacSp222, peptide LL-37, and organic aerosol compounds - nitrophenols - towards a model cell membrane supported on a solid substrate. First, I describe the results of studies on mechanical characteristics of a single DMPC bilayer in the ripple phase supported on mica. Then, I discuss orientational and conformational changes induced in the DMPC bilayer by the BacSp222. Next, there is an evaluation of interactions of toxic nitrophenols with a multi-component bilayer mimicking a lung cell membrane. Finally, I discuss the activity of the only human cathelicidin peptide, LL-37, towards a microbial-like model membrane.

### 3.1. Nanomechanical characterization of a DMPC single bilayer in a ripple phase

The present work was undertaken to extend the knowledge of the physical properties of the DMPC bilayer in the ripple phase under physiological conditions. Thorough understanding and control over the phospholipid bilayer formation and its characteristics seem crucial regarding establishing the nature of membrane-active species mechanism of activity. The DMPC bilayer properties are thoroughly studied as DMPC phospholipids often constitute the main component of model biological membranes. Still, the properties and behavior of a ripple phase are not that well explored, especially in the case of a single bilayer.

#### 3.1.1. Phospholipid bilayer and its phase transitions

Model cell membranes are frequently made with zwitterionic 1,2-dimyristoyl-*sn*-glycero-3-phosphocholine (DMPC), a PC phospholipids representative, one of the main components of the eukaryotic cell membranes. The physical state of the DMPC supported bilayer can be changed with the temperature<sup>213</sup> or potential applied.<sup>116</sup> At a low temperature, i.e., below the main transition temperature ( $T_{m \text{ DMPC}} \approx 24^\circ\text{C}$ ), phospholipid molecules are in a gel phase,  $L_\beta$ , characterized by acyl chains being ordered and fully extended with the maximum tilt with respect to the normal of the plane of the phospholipid bilayer.<sup>213</sup> At  $T_m$ , a transition to a less ordered liquid-crystalline phase,  $L_\alpha$ , occurs.<sup>214</sup> Above  $T_m$ , phospholipid acyl chains melt, forming a liquid-like conformation.<sup>213</sup>

The lamellar gel and fluid phases are the most frequently studied lipid phases because they are biologically relevant. In these phases, the phospholipid bilayer surface is flat. However, at the intermediate temperature, i.e., between pre-transition temperature,  $T_p$  ( $T_{p\text{ DMPC}} \approx 14^\circ\text{C}$ ), and  $T_m$ , the ripple phase,  $P_\beta$ , is formed. The ripple phase surface is corrugated, in contrast to the gel and fluid phase. In general, a typical periodicity of the corrugations is 12-16 nm, so-called stable ripple phase, or double those values, named metastable ripple phase,<sup>215, 216</sup> also referred to as asymmetric and symmetric ripples, respectively.<sup>217</sup> Importantly, the thermal history of the sample, as well as its hydration, influence its stability and thus modulate the periodicity.<sup>75, 218, 219</sup> In the stable ripple phase, the acyl chains are tilted, while in the metastable ripple phase, the acyl chains are oriented vertically to the plane of the phospholipid membrane.<sup>220</sup> Interestingly, so far, the ripple phase has been only observed for a multibilayer phospholipid system supported on a solid substrate.<sup>221</sup> For the single phospholipid bilayer, the ripple structure formation is precluded because of lateral stress from the solid substrate.<sup>222</sup> But the presence of tris(hydroxymethyl)aminomethane (Tris) in a buffer solution induced the ripple phase formation in a single 1,2-dipentadecanoyl-*sn*-glycero-3-phosphatidylcholine bilayer.<sup>223</sup> So far, the mechanism of these structures' formation has not been fully elucidated. However, it has been proposed that periodic behavior resulting in ripple formation might arise from competitive interactions within the sample – the coexistence of phospholipids with different acyl chain conformations.

The different physical states of phospholipid molecules can affect the physiological functions of all biological membranes when exposed to various external factors. For instance, phospholipase  $A_2$  exhibited higher activity toward a DMPC supported membrane in the ripple phase than in the gel phase.<sup>224</sup> However, the explanation of the relationship between the physical state of the cell membrane and its influence on the living cells functioning under natural conditions remains a great challenge.<sup>225</sup>

### 3.1.2. Ripple phase in a single DMPC bilayer

The DMPC bilayer was deposited on a mica surface by the LB/LS in this study. After deposition, it was stored at  $4^\circ\text{C}$  overnight in a buffer solution, either containing Tris or not. Then, it was brought back to  $21^\circ\text{C}$ , and then, after 1-h stabilization, it was imaged with the AFM. The PF-QNM AFM topography images were acquired in the same buffer in which the sample was stored, i.e., (a) 20 mM Tris, 150 mM NaCl, 5 mM EDTA buffer, pH = 7.6 or (b) 10 mM HEPES, 150mM NaCl, 5 mM  $\text{CaCl}_2$ , pH = 7.4 (Figure 3.1-1a and 1b, respectively). Their cross-sectional profiles are compared in Figure 3.1-1c.

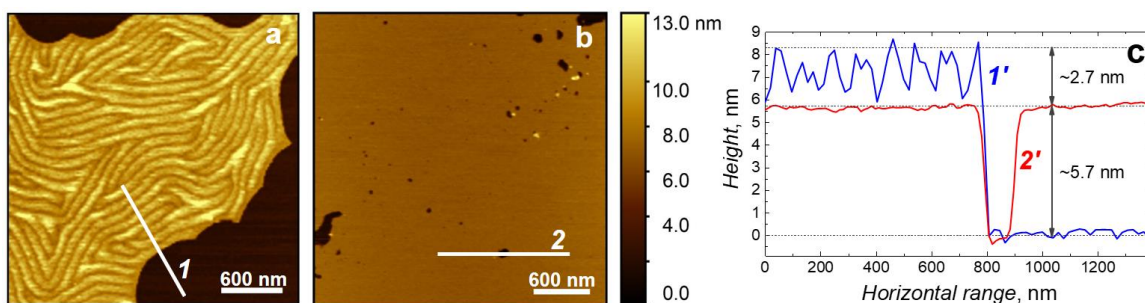
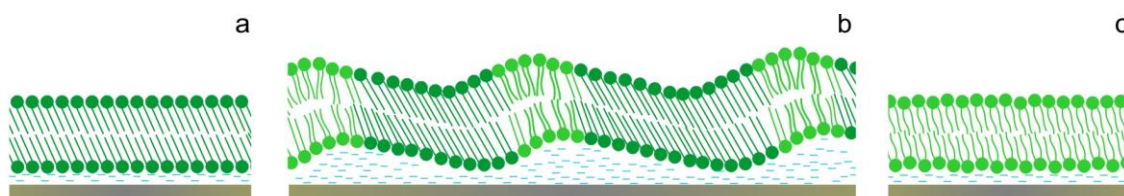


Figure 3.1-1. The  $3 \times 3 \mu\text{m}^2$  AFM topography images of the DMPC single bilayer supported on mica, acquired at 21 °C in a buffer solution (a) with and (b) without Tris component, pH = 7.6 and 7.4, respectively. (c) The cross-sectional profiles were taken along the straight lines displayed in Panels a and b.

The DMPC single bilayer topography (Figure 3.1-1a) exhibited features characteristic of the ripple phase<sup>226</sup> (Scheme 3.1-1b), i.e., the presence of corrugations arranged in a manner typical for this phase and characteristic temperature treatment. Periodic ripples are well distinguishable on the entire bilayer surface. Profile 1 in Figure 3.1-1c is the bilayer cross-sectional profile in the ripple phase taken along Line 1 shown in Figure 3.1-1a. The profile includes a part of uncovered mica used to determine the bilayer thickness, which was determined to be a ~6-nm thick layer, called the bottom layer, with the ripples rising to ~9.0 nm, thus resulting in a ~3-nm amplitude thickness changes (Profile 1 in Figure 3.1-1c). Figure 3.1-1b shows an AFM topography image of the DMPC bilayer deposited and pre-treated according to the same procedure used for the DMPC bilayer shown in Figure 3.1-1a in the absence of the Tris component of the buffer solution. The surface of the bilayer is smooth and featureless, only marked with commonly occurring defects. The average thickness of this smooth bilayer, determined from the edge of the bilayer defects (Profile 2 in Figure 3.1-1c), was  $5.9 \pm 0.1$  nm. This value coincides with the thickness of the bottom layer of the bilayer in the ripple phase (Profile 1 in Figure 3.1-1c). The obtained result confirms that the DMPC single bilayer supported on a solid substrate in the ripple phase is inhibited, but the presence of the Tris induces the ripple phase formation.<sup>222, 223</sup>



Scheme 3.1-1. A schematic representation of a phospholipid bilayer structure in (a) gel, (b) ripple, and (c) liquid phase. The bilayer is deposited on a solid substrate, and a thin water layer separates them. Changes in observed thickness result from rearrangement of the phospholipids and the presence of corrugations.

A closer look at the topographic features reveals that the ripple phase organizes in variously shaped domains. In these domains, highly ordered and long parallel stripes predominate (Figure 3.1-2a and 2b). These stripes bend with a predominant angle of 120 or 60° suggesting the hexagonal packing of the DMPC molecules within the bilayer.<sup>218</sup> In some domains, ordered spirally self-closed structures in the triangle shape are formed (arrows in Figure 3.1-2a). Sharp boundaries between domains are visible, and the stripes within the domains do not cross each other. Moreover, ripples do not lose their order at domain boundaries and at the edge of the bilayer, where the stripes remain parallel or perpendicular to the edge. Well-defined and ordered ripples with unchanged arrangement may suggest high stability of the DMPC bilayer in the presence of Tris. In general, the observed ripple structure is similar to that observed for multibilayer phospholipid films supported on a solid substrate.<sup>220</sup>

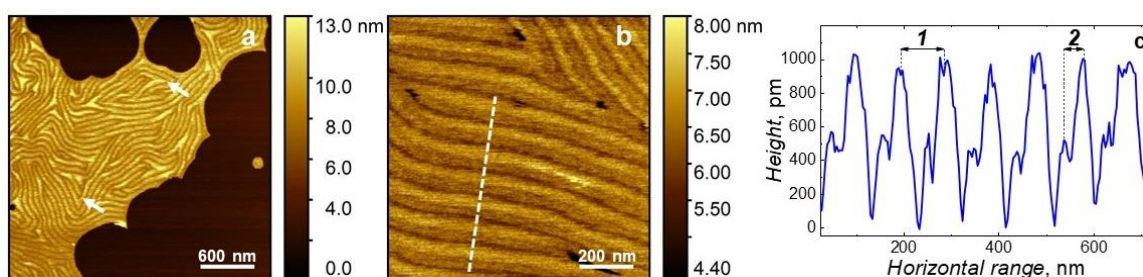


Figure 3.1-2. (a)  $5 \times 5 \mu\text{m}^2$  and (b)  $1 \times 1 \mu\text{m}^2$  AFM image of DMPC bilayer acquired at 21 °C in 20 mM Tris, 150 mM NaCl, 5 mM EDTA buffer, pH = 7.6. (c) Cross-sectional profile taken along the straight line displayed in Panel b.

A higher magnification AFM image was acquired for qualitative characterization of the ripples structure (Figure 3.1-2b). Figure 3.1-2c shows the cross-section profile taken along the line indicated in Figure 3.1-2b. Observed corrugations form long asymmetric ripples composed of two stripes of different heights. Such structures were observed regardless of the direction of the AFM scanning. The distance between the ripples is  $96.0 \pm 7.8 \text{ nm}$  (Figure 3.1-2c, dimension 1) with an average amplitude of  $0.97 \pm 0.03 \text{ nm}$ , while the two stripes within the same ripple are spaced  $41.0 \pm 3.0 \text{ nm}$  apart (Figure 3.1-2c, dimension 2). The observed amplitude of ripples varied amongst different samples. However, they remained within the  $\sim 1$  up to  $\sim 5 \text{ nm}$  amplitude range. Similar structures but of much smaller periodicity were observed for the supported 1,2-dipentadecanoyl-*sn*-glycero-3-phosphocholine single bilayer in the presence of the Tris component.<sup>223</sup> The ripple amplitude strongly depends on the temperature and the periodicity of the ripple itself.<sup>220</sup> Different ripples' amplitude values can be found in the literature depending on the temperature and measurement technique. For instance, STM studies showed that the amplitude of the asymmetric (stable) ripple phase in DMPC lipid bilayers was 2.4 and 1.1 nm at 23 °C and 20°C, respectively.<sup>227</sup> X-ray diffraction

studies showed that the ripple amplitude is 1.0 nm at 23.6 °C for fully hydrated DMPC in a stable ripple phase,<sup>228</sup> while for meta-stable phase, it varies from 1.9<sup>226, 229</sup> to 8.0 nm at 18 °C.<sup>230</sup> These discrepancies in amplitude values may result from the fact that values reported in the literature relate to multi-bilayer systems, while our research concerns a single bilayer. Ripple phase of higher periodicity, up to 100 nm, were reported for multilamellar structures, which correspond to values observed in our system.<sup>231, 232</sup> A few large ripple structures, of a wavelength of ~60 nm and amplitude of ~10 nm, were observed for supported double DMPC<sup>221</sup> and DPPC<sup>220</sup> bilayer system. Results presented herein suggest that indeed “macro” ripple structure in a single bilayer system supported on the mica was observed in this study.

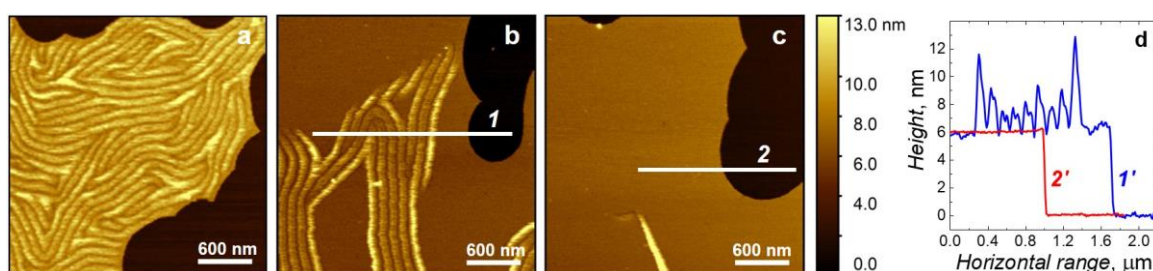


Figure 3.1-3. The AFM topography images of the DMPC single bilayer acquired at (a) 115, (b) 285, and (c) 378 min of continuous scanning at 21 °C in 20 mM Tris, 150 mM NaCl, 5 mM EDTA buffer, pH = 7.6. (d) Cross-sectional height profiles were taken along the lines indicated in Panels b and c.

Figure 3.1-3 shows the AFM topography images of the supported DMPC single bilayer recorded at different times during continuous scanning. The bilayer has been observed for 8 h since the sample had been moved from 4 °C to 21 °C ( $t_0 = 0$ ). The bilayer shown in Figure 3.1-3 was recorded at different timespans since  $t_0$ . Initially, the whole surface of the bilayer was covered with ripples. Then, rippled structures gradually disappeared, transforming into a smooth bilayer of  $6.1 \pm 0.1$  nm height (Figure 3.1-3c). For comparison, the relaxation time of the DPPC supported double bilayer from the ripple phase to the gel phase took over 10 h at ~23 °C.<sup>221</sup> The presence of two coexisting domains of different heights and topography, as indicated in Figure 3.1-3b, clearly indicates that the sample was undergoing a phase transition at that moment.<sup>233</sup> The ripples forming the boundary between the ripple structure and the smooth bilayer are higher than the ripples in between (Profile 1 in Figure 3.1-3d). The height of the boundary and internal ripples was  $4.7 \pm 0.3$  and  $2.1 \pm 0.4$  nm, respectively. The coexistence of ripples of different heights with clearly higher corrugations at the phase boundary may indicate strong stresses present in the layer, which over time relax, leading to the disappearance of corrugations. After ~400 min of imaging, most of the ripples within the

scanned area vanished, and the bilayer height remained unchanged (Profile 2 in Figure 3.1-3d). The height of the smooth bilayer presented in Figure 3.1-3c is very close to the height of the bilayer shown in Figure 3.1-1b. That indicates that the ripple phase observed at 21 °C for the supported DMPC single bilayer in the presence of the Tris component is metastable.

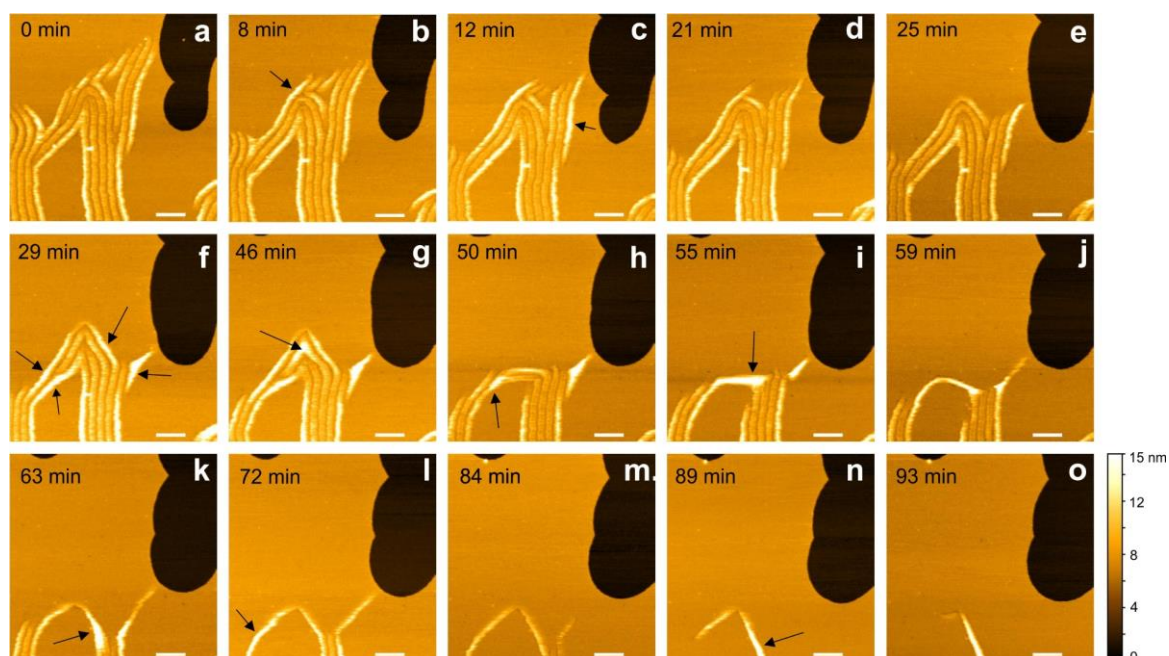


Figure 3.1-4. AFM topography images of the DMPC bilayer deposited on mica acquired at different timespans during continuous scanning at 21 °C in 20 mM Tris, 150 mM NaCl, 5 mM EDTA buffer, pH = 7.6. Arrows indicate areas of increased height and lateral size, suggesting sites of phase transitions. All images are  $3 \times 3 \mu\text{m}^2$  in size and 0 to 15.5 nm in  $z$ -scale. The scale bar corresponds to a 400-nm distance.

A detailed process of ripples vanishing was captured as a sequence of images presented in Figure 3.1-4. Images were recorded between 285 and 378 min since  $t_0$ , giving a  $\sim 90$ -min observation timespan. The time needed to record a single AFM image was  $\sim 4$  min. Thus, changes in bilayer topography are shown every  $\sim 4$  min or its multiplicity. If no significant changes were captured, the image was skipped. Noticeably, when ripples were vanishing, in a manner of being shortened in length, one of the nearby ripples increased in height and lateral size, which is visible as brighter areas marked with arrows in Figure 3.1-4. This behavior suggests that those might be sites of phase transitions. Interestingly, like those between Figure 3.1-4 Panels g and h or j and k, the most pronounced changes occurred in a relatively short timescale of single image acquisition. This behavior presumably suggests that some transitions are manifested as abrupt or step changes rather than gradual vanishing.

### 3.1.3. Nanomechanical mapping of a single DMPC bilayer in a ripple phase

The mechanism of the ripple phase formation is not entirely understood. Factors such as hydration of the bilayer and the orientation and conformation of phospholipid molecules may play a considerable role in forming this phase. The indentation force measurement on a lipid bilayer fingerprints the specific lipid bilayer state.<sup>67</sup> Therefore, to better understand the ripple morphology, the sample was herein characterized nanomechanically. To explain whether the observed changes in topography are accompanied by changes in the bilayer local mechanical properties, Young's modulus was mapped (Figure 3.1-5b) simultaneously with topography (Figure 3.1-5a). The Young's modulus map was determined based on F-D curves acquired at the constant indentation force of 200 pN. The obtained results show that nanomechanical changes observed on the bilayer surface correlated with the ripple structure present in the topography images. The dark brown and orange/red areas, visible on the topography and modulus map, correspond to uncovered mica.

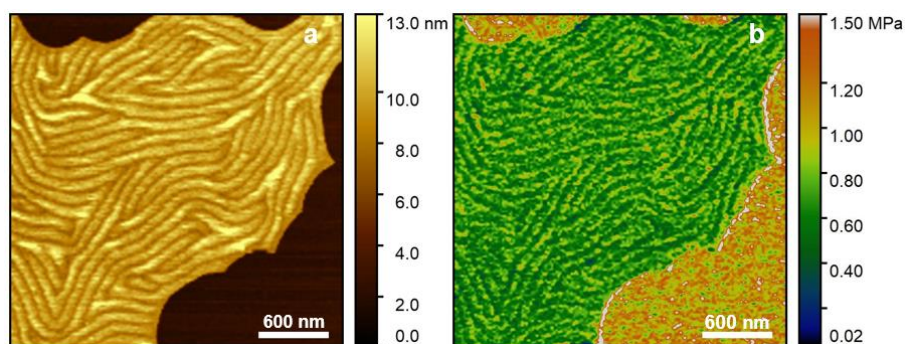


Figure 3.1-5. AFM maps of the (a) topography and (b) corresponding Young's modulus of the DMPC single bilayer deposited on mica. The bilayer was imaged at 21 °C in 20 mM Tris, 150 mM NaCl, 5 mM EDTA buffer, pH = 7.6.

Another area of the macro-rippled structure of the DMPC single bilayer acquired at higher magnification, and corresponding Young's modulus, are shown in Figure 3.1-6a and 6b, respectively. Figure 3.1-6c shows cross-sectional profiles of the topography (solid red curve) and Young's modulus (dotted green curve) taken along the straight lines displayed in Panels a and b, respectively. Young's modulus profile is  $\pi/2$  out of phase to the height profile. Notably, Young's modulus for a lower stripe is higher than that for a higher stripe of the same ripple. The observed changes in nanomechanical properties under the constant indentation force indicate the nonlinearity or inhomogeneity of the sample under stress applied.<sup>234</sup>

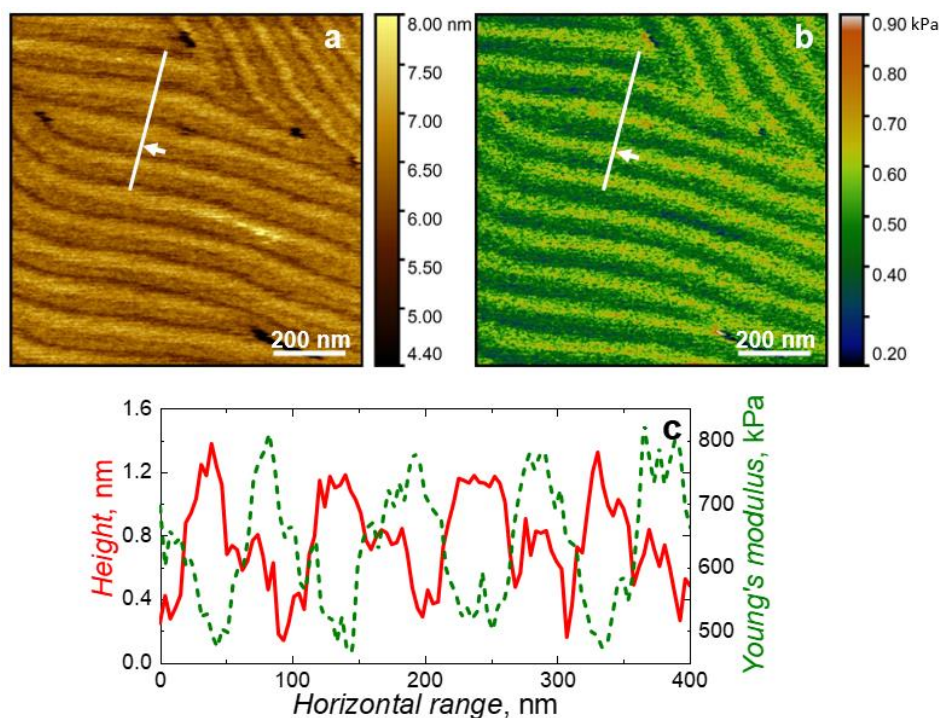


Figure 3.1-6. (a) Topography and (b) Young's modulus map of a DMPC single bilayer deposited on mica. (c) Corresponding cross-sectional profiles of the topography (solid red curve) and Young's modulus (dashed green curve) from Panels a and b, respectively. Imaging was performed at 21 °C in 20 mM Tris, 150 mM NaCl, 5 mM EDTA buffer, pH = 7.6.

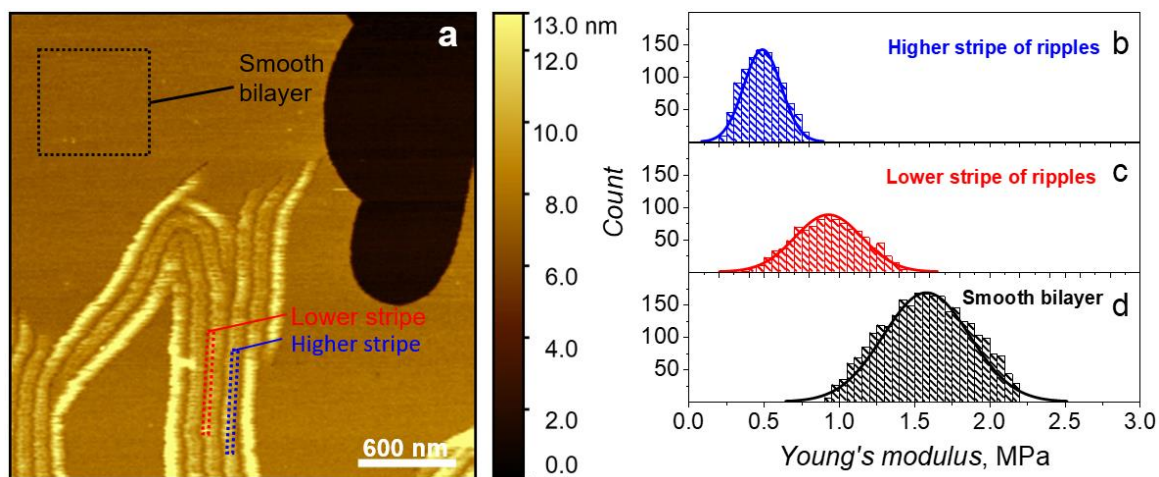


Figure 3.1-7. (a) The AFM topography image and (b, c, d) Young's modulus histograms calculated for the (b) higher and (c) lower stripe of the ripples as well as (d) smooth bilayer schematically indicated as rectangles on the AFM topography image. The Young's modulus was calculated by analyzing ~10 000 F-D curves acquired during the AFM imaging.

The next step was a detailed quantitative analysis of Young's modulus maps. F-D curves in the number of ~10 000 were acquired for analysis from both the higher and lower stripe areas and the smooth area of the same bilayer (Figure 3.1-7a). For the loading of 200 pN, the

AFM tip indentation was less than 20% of the DMPC bilayer thickness to avoid the contribution of the underlying mica substrate.<sup>72, 235</sup> However, additional control calculations were performed, taking into account the solid substrate effect.

Figure 3.1-8 shows the AFM topography image and corresponding Young's modulus map determined without (Figure 3.1-8b) and with (Figure 3.1-8c) the finite sample thickness correction. In both cases, the average Young's modulus, calculated for the higher stripe, is lower than that calculated for the lower stripe of the ripple. That is, in the case of no substrate correction, the modulus is  $491 \pm 95$  (higher stripe) and  $929 \pm 195$  kPa (lower stripe), while after substrate correction, it is  $319 \pm 105$  and  $587 \pm 200$  kPa, respectively. An average Young's modulus stayed equal to  $1032 \pm 246$  and  $1580 \pm 260$  kPa with and without the substrate correction, respectively, for a smooth bilayer (Figure 3.1-7b - 7d and Figure 3.1-8d - 8f). After considering the substrate influence, Young's modulus was reduced by 35, 37, and 35% for the higher and lower stripes of the ripples, and a smooth bilayer, respectively.

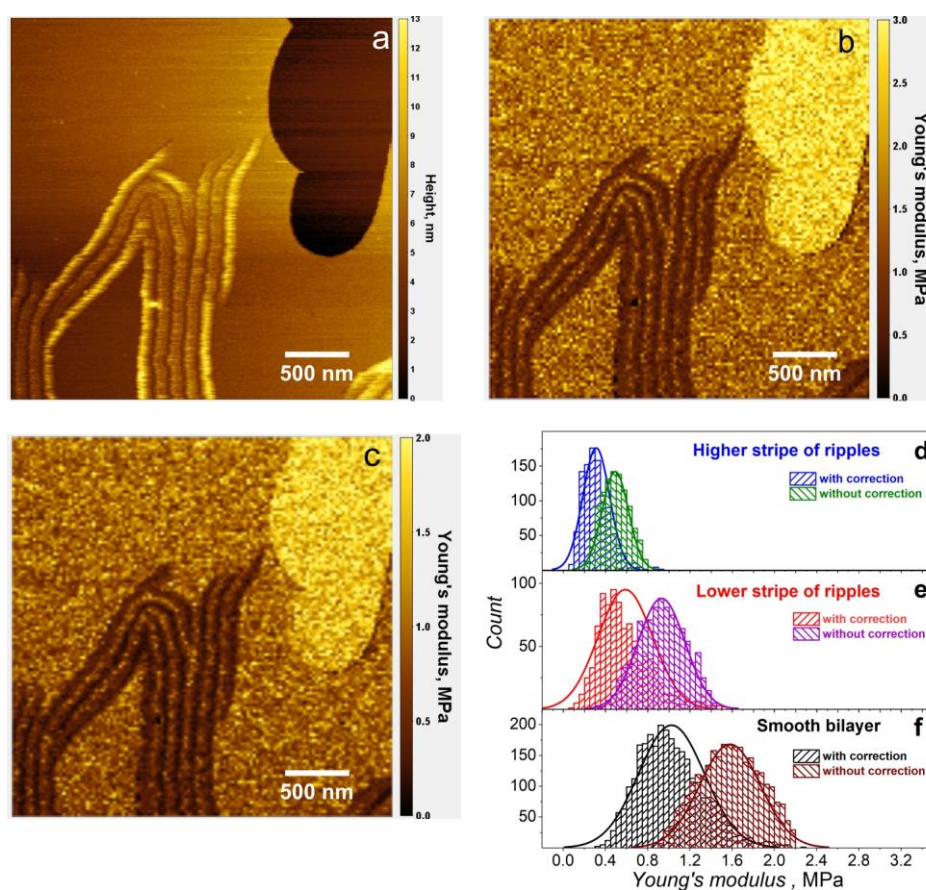


Figure 3.1-8. (a) The AFM topography image and (b, c) Young's modulus map of the DMPC single bilayer deposited on mica determined (b) without and (c) with solid substrate correction. (d, e, f) Young's modulus histograms, corresponding to Young's modulus map shown in Panel c, calculated for the (d) higher and (e) lower stripes of the ripples as well as (f) smooth bilayer.

The nanomechanical analysis showed that the characteristic corrugations are visible on Young's modulus maps without and with the substrate correction. Similarly, the magnitudes of Young's modulus changes determined for the higher and lower stripes of the ripples were comparable before and after the substrate correction. Therefore, one can conclude that the periodic changes of Young's modulus are not simply an artifact of variations in bilayer height. Another critical issue is the contact area of the AFM probe with the surface, which can vary when the AFM tip is located on the ripple top or slope, influencing the measurements of mechanical properties. However, a direct consequence of this reason would be a value of Young's modulus determined for smooth bilayer between values measured for lower and higher stripes of the ripples, which is not the observed case (Figure 3.1-7). Therefore, it can be concluded that the most likely reason for the observed modulation in mechanical properties is the coexistence of different phospholipid bilayer phases within ripples.

A higher Young's modulus characterizes the phospholipid bilayer in the gel than in the fluid phase.<sup>72</sup> The present observations indicate that the state of phospholipids forming the higher stripe of ripples resembles the fluid-like phase, while those at the lower stripe of the ripples can be considered a gel-like phase. Moreover, based on the electron density maps calculated from the X-ray diffraction data, theoretical analysis was performed to establish the conformation and orientation of the phospholipid acyl chains in the ripple phase.<sup>229, 236</sup> It was shown that the organization of acyl chains for the DMPC multilayer system is alternated in the ripple phase, characterized by asymmetric ripple geometry. For the longer side of the ripple, the chains are arranged as in the gel phase and tilted by 18°, while for a shorter side of the ripple, the chains resemble a liquid phase arrangement.<sup>226, 229</sup> This inference can be supported by another model that combines a pre-transition and main transition as if both were associated with the chain-melting process, not only the main transition.<sup>237</sup> Thus, the ripple formation during the pre-transition would also involve chain melting. That, in turn, would be observed as the coexistence of both gel- and fluid-like phospholipid conformations. In particular, the formation of fluid line defects would lead to a local bending of the membrane, which was experimentally observed as ripples.

Moreover, during pre-transition, a *gauche* conformation appears in the lipid acyl chains,<sup>238</sup> which supports the coexistence of both gel- and fluid-like phospholipid domains. The steric inter-monolayer interactions and geometric constraints lead to the formation of periodic ripple of the membrane. Consequently, the nature of these constraints is expected to influence the composition and arrangement of lipid phase domains, as such that they are most energetically favorable. Therefore, it is expected to observe different compositions of gel and liquid

phase domains. The presented results support this conclusion and provide additional information about periodically changed local nanomechanical properties of the DMPC single bilayer supported on mica.

### **3.1.4. Conclusions**

The Tris component triggered ripple phase formation in a DMPC single bilayer in the present study. Changes in topography were accompanied by the local changes in Young's modulus. Furthermore, the nanomechanical properties were distributed unevenly, i.e., the higher stripes were characterized by Young's modulus lower than that determined for lower stripes of the ripples. That indicates that the ripple phase is composed of phospholipid molecules of periodically changed orientation and conformation characteristic for the fluid-like and gel-like state of DMPC.

## 3.2. Orientational and conformational studies of BacSp222 activity towards a DMPC bilayer

The PM-IRRAS and chronocoulometry were applied to reveal the secondary structure, orientation, and mechanism of activity of a recently discovered bacteriocin peptide BacSp222 under electrochemical conditions.<sup>239</sup> Herein, the bacteriocin was investigated in a model DMPC bilayer. The influence of BacSp222 on conformation and orientation of DMPC phospholipids acyl chains was determined. Moreover, AFM imaging was used to show the influence of BacSp222 activity on DMPC bilayer topography.

### 3.2.1. Bacteriocin BacSp222

BacSp222 is a linear 50-amino-acid peptide, 5922 g mol<sup>-1</sup>, cationic, N-terminally formylated, of the following sequence: MAGLLRFLLSKGRALYNWAKSHVKGKVEWLKSGATYEQIKEWIEN-ALGWR, rich in tryptophan and lysine residues. Tryptophan residues are considered involved in the AMP-membrane interactions, and lysine contributes to strong antimicrobial activity and reduced hemotoxicity. BacSp222 is a representative of the bacteriocin group of antimicrobial peptides. Bacteriocins are toxins produced by bacteria to inhibit the growth of similar bacterial strains in their native environment. Therefore, they gained interest as AMPs in the search for alternatives to traditional antibiotics.<sup>240</sup> BacSp222 is produced by *Staphylococcus pseudintermedius* strain 222, a pathogen isolated from dog skin lesions.<sup>183</sup> It is multifunctional and acts as a bacteriocin, toxin, virulence factor, and immunomodulatory factor. Figure 3.2-1 shows the lowest-energy structure of BacSp222 as calculated based on NMR experiments in solution.<sup>241</sup> BacSp222 has a globular, rigid four-helix bundle structure, with helices separated by short turns. The amino-acid sequence of BacSp222 seems to remain unique in terms of similarities to other known peptides, but the four-helix bundle structure resembles other bacteriocins, such as aureocin A53, lacticin Q, enterocin 7A, and 7B. They all share similar physicochemical properties, so perhaps also similar antimicrobial functionalities, e.g., lacticin Q was reported to form toroidal pores in biological membranes.<sup>242</sup>

The surface of BacSp222 viewed from the N-terminal side (Figure 3.2-1a, 2c, 2e) shows that hydrophobic residues are exposed to the solvent, and almost the whole surface is positively charged. On the other hand, the C-terminal side (Figure 3.2-1b, 1d, 1f) is mostly hydrophilic and neutral, with some negatively charged residues. As a result, the N-terminal part is anticipated to interact with the negatively charged bacterial cell membranes. Moreover, spatial separation of hydrophilic and hydrophobic sites enhances the possibility of the pore formation mechanism of BacSp222 activity.

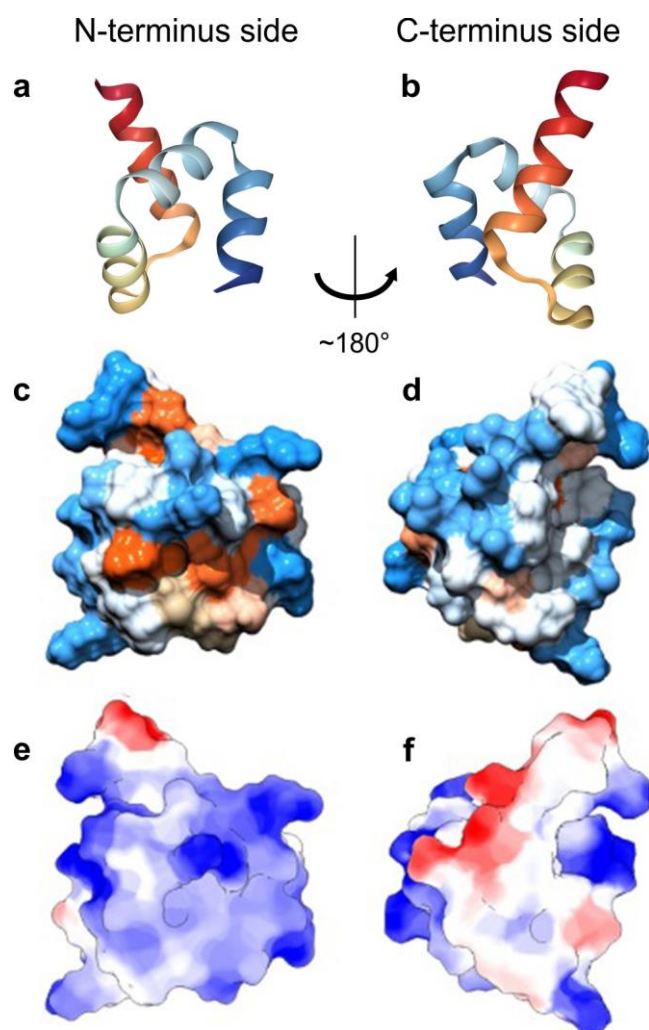


Figure 3.2-1. The structure of BacSp222, shown as (a, b) a ribbon diagram, color-coded from N-terminus (blue) to C-terminus (red). (c, d) Surfaces are marked blue for the most hydrophilic, through white to orange for the most hydrophobic. (e, f) Coulombic potential generated in Chimera for pH = 5.0. Positively charged surfaces are colored blue, through white to red for negatively charged. BacSp222 structures can be found in the PDB under accession code 5LWC. Adapted from Ref.<sup>241</sup>

### 3.2.2. Electrochemical properties of the DMPC bilayer in the presence of BacSp222

Chronocoulometry was employed to examine the charge density of the DMPC and DMPC/BacSp222 membrane, deposited on Au(111). The metal|electrolyte interface is considered a capacitor upon applied potential. The charge stored at the interface is associated with the electric field acting on the adsorbed phospholipid bilayer. In the potential range of  $-400$  to  $400$  mV vs. Ag|AgCl, where the bilayer is adsorbed at the metal surface, the electric field of  $-1.0 \times 10^8$  to  $2.0 \times 10^7$  V m<sup>-1</sup> is acting on the bilayer.<sup>83</sup> This field corresponds to that found in biological membranes.<sup>103</sup> Figure 3.2-2 shows charge density plots of the bare Au(111) electrode and the Au(111) electrode coated with DMPC and DMPC/BacSp222 (9:1

lipid-to-peptide molar ratio). The bottom abscissa plots the electrode potential vs. the reference electrode, while the top abscissa plots values of  $E - E_{pzc}$ , which is a measure of a potential drop across the membrane, equivalent of the transmembrane potential.<sup>60</sup> The absolute charge densities for bare Au(111) were calculated using the potential of zero charge,  $E_{pzc}$ , determined independently to be 215 mV vs. Ag|AgCl.<sup>211</sup>

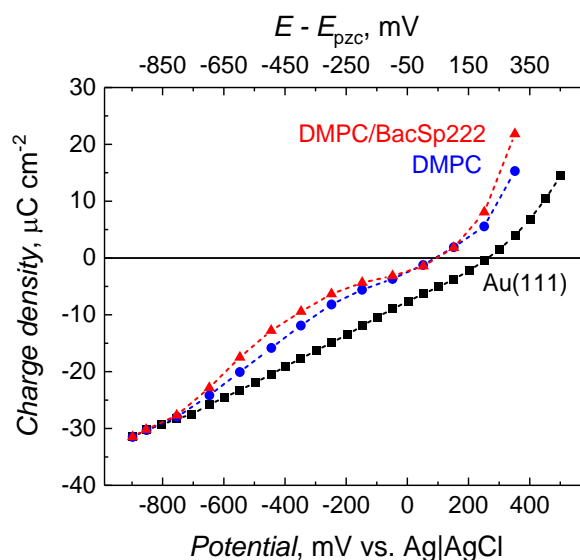


Figure 3.2-2. Charge density curves for the bare Au(111) electrode (black) and the Au(111) electrode coated with DMPC (blue) and DMPC/BacSp222 (9:1 molar ratio) (red) in a 0.1 M  $\text{KClO}_4$  supporting electrolyte solution. The bottom abscissa plots the potential applied to the Au(111) electrode vs. the reference electrode. The top abscissa plots values of  $(E - E_{pzc})$ , which is a measure of the potential drop across the membrane, equivalent of the transmembrane potential.

Chronocoulometry measurements determine potential-dependent properties of the bilayer and the effect of peptide insertion into the membrane. By scanning the potential from  $E_{pzc}$  toward a negative or positive direction, the gold|electrolyte interface is charged negatively or positively, respectively. The capacitance of the metal|electrolyte interface decreases upon absorption of organic molecules.<sup>243</sup> Thus, after DMPC and DMPC/BacSp222 adsorption, the charge density at the gold|electrolyte interface decreased. In the potential range of  $-700$  to  $-200$  mV vs. Ag|AgCl, which corresponds to transmembrane potentials between  $-750$  to  $-150$  mV, less charge is stored at the interface in the presence of BacSp222. Therefore, the bilayer has fewer defects, or it is thicker in the presence of the peptide.

The potential-induced changes in the charge density of the gold|electrolyte interface were correlated with the orientational and conformational changes of the DMPC phospholipid molecules.<sup>210</sup> The charge density of Au(111)|DMPC and Au(111)|DMPC/BacSp222 changes slowly from  $-10$  to  $5 \mu\text{C cm}^{-2}$ , which is in the potential range of  $-300$  to  $200$  mV vs. Ag|AgCl (transmembrane potential of  $-350$  to  $150$  mV). The charge density change is faster

for both more negative and more positive potentials, suggesting de-wetting of the bilayers.<sup>244</sup> Below  $-700$  mV, the charge density curves of the DMPC and DMPC/BacSp222 merge with the curve corresponding to the bare Au(111) electrode. That indicates that both bilayers are detached from the electrode surface. Such behavior of the phospholipid bilayers was previously studied by chronocoulometry,<sup>109</sup> elastic light scattering,<sup>245</sup> and neutron reflectivity.<sup>244</sup> The DMPC bilayer desorbs at negative potentials but remains in the 1-nm proximity to the electrode surface. Then, the gap formed between the bilayer and the electrode is filled with the electrolyte solution.

The presence of molecules with dipole moment components oriented in the direction normal to the electrode surface influences the surface potential. As a result, the  $E_{pzc}$  shifts by  $-160$  mV after adsorption of the molecular film on the Au(111) electrode. The shift is comparable to the dipole potential measured in vesicles.<sup>246</sup> The lipids in contact with the metal were hydrated, as demonstrated by neutron reflectivity<sup>243</sup> and ATR-IR spectroscopy.<sup>43</sup> Therefore, the measured dipole potential originates from the difference between the hydration states of the polar regions of the bilayer two leaflets.

There is no significant difference in  $E_{pzc}$  for the bilayer of the DMPC and DMPC/BacSp222, even though the BacSp222 is a positively charged peptide. So, it should influence the bilayer, charging it positively upon insertion and shifting  $E_{pzc}$  towards positive potentials. The result suggests that the isoelectric point (pI) of BacSp222 equals the pH of 0.1 M KClO<sub>4</sub>, being 6.0.

### **3.2.3. Conformational and orientational changes of the DMPC bilayer in the presence of BacSp222**

The tilt angle of the deuterated DMPC molecules, DMPC-d<sub>54</sub>, in the presence of BacSp222 was determined by analyzing the characteristic features of the IR spectra in the C–D stretching region, i.e., between 2300 and 2000 cm<sup>-1</sup>. DMPC-d<sub>54</sub> was used to avoid overlapping with C–H stretching vibration bands originating from BacSp222.

Figure 3.2-3 shows the PM-IRRAS spectra of the C–D stretching region of the DMPC-d<sub>54</sub> acyl chains in the absence and presence of BacSp222, acquired at a series of potentials from 200 to  $-800$  mV vs. Ag|AgCl. Table 3-1 shows the conditions applied to obtain the PM-IRRAS data. The spectra of randomly oriented molecules were calculated based on transmission spectra of DMPC-d<sub>54</sub> and DMPC-d<sub>54</sub>/BacSp222 (9:1 molar ratio) in D<sub>2</sub>O.

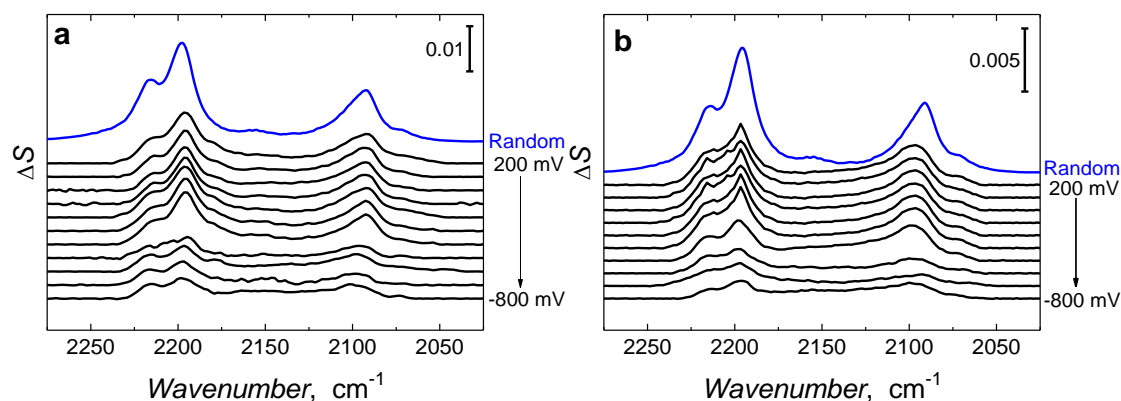


Figure 3.2-3. PM-IRRAS spectra in the C-D stretching region corresponding to (a) DMPC-d<sub>54</sub> and (b) DMPC-d<sub>54</sub>/BacSp222 (9:1 molar ratio), for potentials from 200 to -800 mV. The spectra simulated for randomly oriented DMPC-d<sub>54</sub> and DMPC-d<sub>54</sub>/BacSp222 molecules are marked in blue.

Table 3-1. The conditions used to acquire PM-IRRA spectra in the indicated spectral regions for the DMPC-d<sub>54</sub>/BacSp222 membrane.

Spectral Region	Electrolyte Solution	Angle of incidence, °	Thin cavity thickness, μm
Amide I	D <sub>2</sub> O	60	5.4
C-D stretching	H <sub>2</sub> O	60	5.0

Quantitative spectra analysis requires band deconvolution. An example of band deconvolution for randomly oriented DMPC-d<sub>54</sub>/BacSp222 molecules and experimental spectra of DMPC-d<sub>54</sub>/BacSp222 bilayer measured at 0 V is shown in Figure 3.2-4. As a result of band deconvolution, band center positions were assigned to be 2196 and 2096 cm<sup>-1</sup> for the asymmetric,  $\nu_{as}(\text{CD}_2)$ , and symmetric,  $\nu_s(\text{CD}_2)$ , methylene stretching, respectively, which is in agreement with previous studies.<sup>108</sup> Other bands, corresponding to the CD<sub>3</sub> asymmetric,  $\nu_{as}(\text{CD}_3)$ , and symmetric,  $\nu_s(\text{CD}_3)$ , stretching appeared at 2214 and 2115 cm<sup>-1</sup>, respectively. The two bands at 2069 and 2152 cm<sup>-1</sup> correspond to the Fermi resonances of the bending modes of CD<sub>3</sub> and CD<sub>2</sub>.<sup>247</sup>

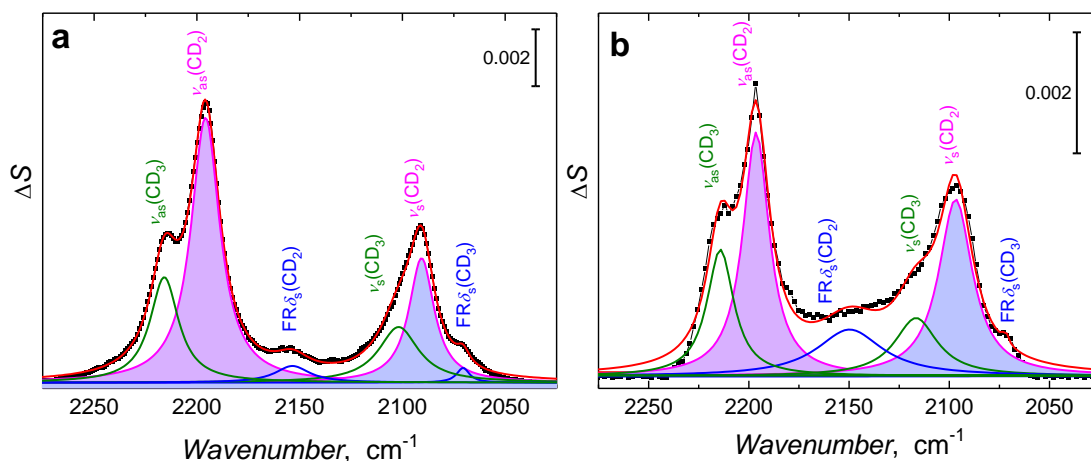


Figure 3.2-4. Spectra deconvolution by Lorentzian fit of the (a) simulated spectra of randomly oriented DMPC-d<sub>54</sub>/BacSp222 molecules and (b) experimental spectra of DMPC-d<sub>54</sub>/BacSp222 bilayer measured at 0 V. The deconvoluted spectra are marked as black squares, and the cumulative result of deconvolution is marked as a red curve.

The methylene (or deuterated methylene) stretching vibrations,  $\nu(\text{CH}_2)$ , provide information about the conformational order of the lipid acyl chains. The frequencies of symmetric and antisymmetric  $\text{CH}_2$  stretching vibrations of non-deuterated lipids increase from 2849 and 2917  $\text{cm}^{-1}$  to 2853 and 2923  $\text{cm}^{-1}$ , respectively, upon phase transition from the ordered gel to the disordered liquid-crystalline phase.<sup>104</sup>

Figure 3.2-5 shows peak center positions for the  $\nu_{\text{as}}(\text{CD}_2)$  and  $\nu_{\text{s}}(\text{CD}_2)$  vibrations determined at each potential, with 0.5  $\text{cm}^{-1}$  accuracy, in the presence and absence of BacSp222. No significant shift was observed for the  $\nu_{\text{as}}(\text{CD}_2)$  peak position, which average is equal to 2196  $\text{cm}^{-1}$  in the whole potential range. For an all-*trans* conformation, the  $\nu_{\text{as}}(\text{CD}_2)$  position was determined to be 2191  $\text{cm}^{-1}$ .<sup>248</sup> Therefore, the  $\nu_{\text{as}}(\text{CD}_2)$  peak position shift towards higher wavenumber suggests that acyl chains for the DMPC-d<sub>54</sub> sample are partially melted and contain *gauche* conformations (groups, in this case, carbon atoms, separated by a torsion angle of approximately 60°, Figure 3.2-5b and 5c).

In the absence of BacSp222, the  $\nu_{\text{s}}(\text{CD}_2)$  peak positions are constant and equal to 2092  $\text{cm}^{-1}$  in the potential range of -400 to 300 mV. For potentials below -400 mV, a 4- $\text{cm}^{-1}$  shift occurs toward higher frequencies (a blue shift). For an all-*trans* conformation, the  $\nu_{\text{s}}(\text{CD}_2)$  position was determined to be 2088  $\text{cm}^{-1}$ .<sup>248</sup> A blue shift in the  $\nu_{\text{s}}(\text{CD}_2)$  band position for the DMPC-d<sub>54</sub> sample suggests the change of the acyl chains conformation from the all-*trans* to partially melted containing *gauche* conformation. The number of *gauche* conformations further increase at potentials more negative than -400 mV and after BacSp222 adsorption. Changes in the band position are followed by band broadening, which is characteristic of the phospholipid bilayer phase transition from gel to liquid crystalline.<sup>249</sup> In the pres-

ence of BacSp222, the  $\nu_s(\text{CD}_2)$  band position is approximately  $2096\text{ cm}^{-1}$  and remains constant in the whole potential range. Below  $-600\text{ mV}$ , the band position is the same as in the absence of BacSp222.

The interaction of BacSp222 with the bilayer increases the disordering of the acyl chains,<sup>250</sup> similarly, as for gramicidin A, alamethicin, and bacteriorhodopsin interacting with the DMPC- $\text{d}_{54}$  bilayer,<sup>248</sup> as well as amyloid  $\beta$  influencing brain-like fBLM.<sup>57</sup> A bilayer with more mobile phospholipids is expected to have fewer defects and be more compact under such conditions. PM-IRRAS results correspond well with those chronocoulometric, which showed that the presence of BacSp222 decreased the charge density of the interface.

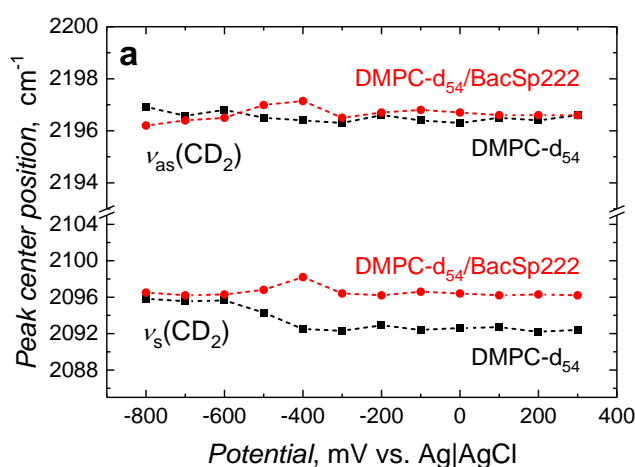


Figure 3.2-5. (a) Peak center position vs. the potential for the (top)  $\nu_{as}(\text{CD}_2)$  and (bottom)  $\nu_s(\text{CD}_2)$  in the BacSp222 (●) presence and (■) absence.

The DMPC- $\text{d}_{54}$  orientational changes were quantitatively analyzed by determining tilt angles using the procedure described in Section 2.2.3.9 above. Calculating the tilt angle of lipid acyl chains assumes an all-*trans* conformation, which occurred not to be the case. As peak position analysis showed, phospholipids are partially melted, containing *gauche* conformations. Therefore, only the average angle between the electrode surface normal and the  $\text{CD}_2$  moieties plane normal can be calculated. The obtained values are the average tilt of the *trans* fragments of the acyl chains and are treated as a measure of the tilt changes, not the exact or absolute value. Figure 3.2-6 shows the change in the tilt angle of DMPC- $\text{d}_{54}$  acyl chains with potential in the absence and presence of BacSp222. Both cases follow the same pattern where the tilt angle is constant at potentials between 300 and  $-400\text{ mV}$  and is decreased below  $-400\text{ mV}$ . Constant tilt angle in the broad potential range indicates that there is little or no effect of electrostriction on the lipid molecules, which is consistent with the previous discussion of the impact of electrostriction on the orientation of lipid bilayer supported on the metal electrode.<sup>83</sup> From 300 to  $-400\text{ mV}$ , the average tilt angle is  $37^\circ$  and  $23^\circ$  in the absence and

presence of BacSp222, respectively. For potentials more negative than  $-400$  mV, the tilt angle decreased for both samples and remained lower in the case of DMPC- $d_{54}$  without BacSp222.

Adsorption of BacSp222 influences both conformation and orientation of the DMPC- $d_{54}$  phospholipids by increasing the content of *gauche* conformations and increasing the average tilt angle of the DMPC- $d_{54}$  acyl chains.

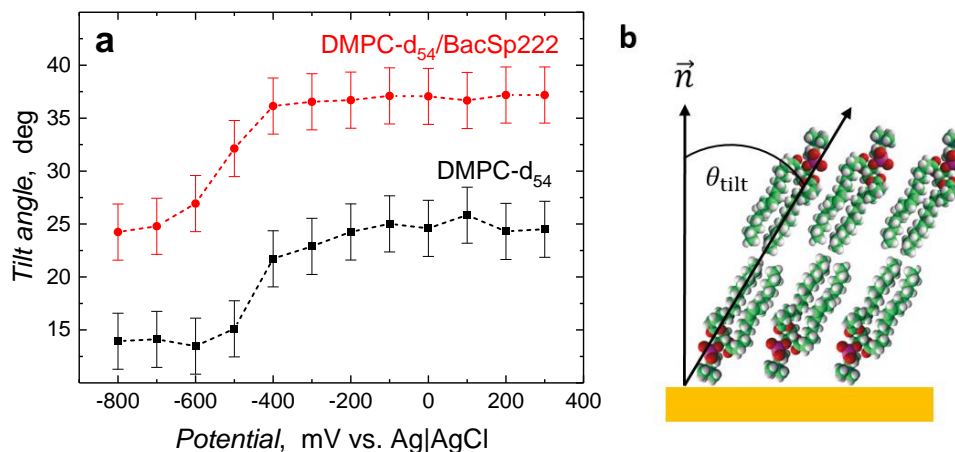


Figure 3.2-6. The average tilt angle of the *trans* fragment of the phospholipid acyl chains vs. the potential for DMPC- $d_{54}$  in the BacSp222 (●) presence and (■) absence.

### 3.2.4. Change of orientation and secondary structure of BacSp222 in the presence of the DMPC bilayer in the electric field

The orientation and secondary structure of BacSp222 in the DMPC- $d_{54}$  presence under electrochemical conditions were further evaluated by analyzing the amide I region. The amide I band is assigned to C=O stretching vibrations, which constitute  $\sim 80\%$  of the vibrations within the bands  $1700$  and  $1600$   $\text{cm}^{-1}$ .<sup>251, 252</sup> Amide I is mainly used to evaluate the polypeptide or protein secondary structure. For complex peptide molecules comprising  $\alpha$ -helices,  $\beta$ -sheets,  $\beta$ -turns, or disordered structures, the amide I band requires deconvolution to reveal sub-bands characteristic positions.<sup>252</sup>

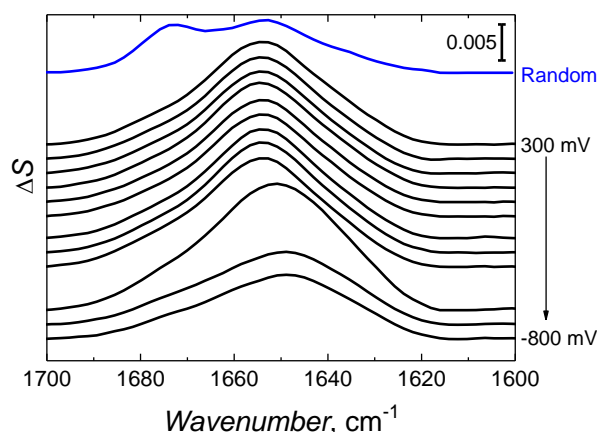


Figure 3.2-7. PM-IRRRA spectra in the amide I region corresponding to the BacSp222 C=O stretching vibrations at selected potentials from 300 to -800 mV vs. Ag|AgCl. The spectrum simulated for randomly oriented BacSp222 molecules is marked in blue.

Figure 3.2-7 shows the PM-IRRRA spectra in the amide I region corresponding to the BacSp222 C=O stretching vibrations recorded for potentials from 300 to -800 mV, every 100 mV. Table 3-1 shows the conditions applied to obtain the PM-IRRAS data. The BacSp222 is incorporated into the DMPC-d<sub>54</sub> bilayer, but the IR band in Figure 3.2-7 originates from BacSp222 only, as it was previously shown that DMPC-d<sub>54</sub> is not absorbing IR photons in the 1700 – 1600 cm<sup>-1</sup> region.<sup>105</sup>

The intensities of the experimental bands are much higher than that for the simulated spectrum of randomly oriented BacSp222 molecules. In the random BacSp222 spectrum, two peaks arise at 1673 and 1654 cm<sup>-1</sup>, respectively corresponding to  $\beta$ -turn and  $\alpha$ -helical secondary structures. In the experimental PM-IRRAS spectra for the DMPC-d<sub>54</sub> /BacSp222, the peak intensity at 1673 cm<sup>-1</sup>, corresponding to  $\beta$ -turn structure, is very weak. The intensities of the experimental spectra do not change significantly in the potential range of 300 to -500 mV. However, below -600 mV, the intensity of the amide I band is significantly lower, and its shape changes. Chronocoulometric measurements have shown that the bilayer is detached from the electrode surface at such negative potentials (Figure 3.2-2). Therefore, the SD method and FSD can be applied to address changes in the orientation and conformation of BacSp222 at changing potential.

The positions of the amide I sub-bands were additionally determined by the SD method and FSD of the spectra, revealing bands at 1635, 1645, and 1674 cm<sup>-1</sup> for BacSp222 molecules in random orientation, characteristic of the  $\beta$ -sheet,  $\alpha$ -helix, and  $\beta$ -turn structures, respectively<sup>253-257</sup> (Figure 3.2-8). Corresponding bands FWHM values were determined to be 22.5, 16.9, and 15.9 cm<sup>-1</sup>, respectively. The integrated band intensity was used to determine that the BacSp222 molecules in random orientation are mostly  $\alpha$ -helical (58%), with the  $\beta$ -turn

(32%) and  $\beta$ -sheet (10%) structures also present. Similar values were obtained for BacSp222 in solution studied by circular dichroism (CD).<sup>183</sup>

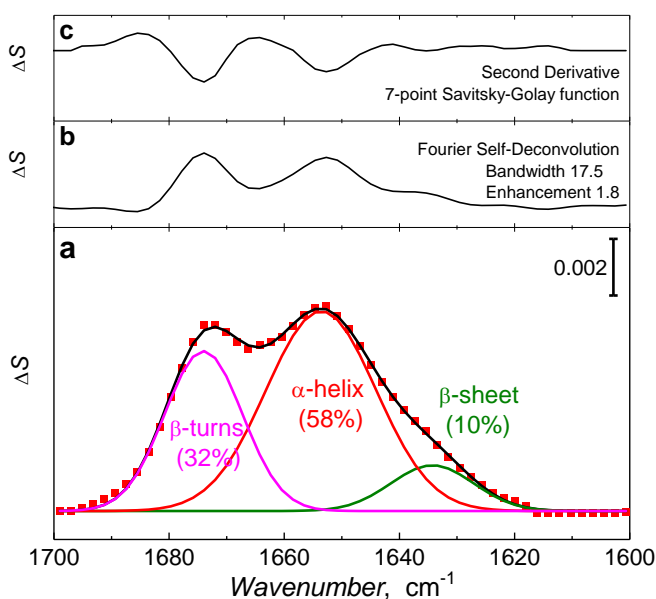


Figure 3.2-8. (a) Deconvolution of the amide I band of the randomly oriented BacSp222 molecules. The positions of sub-bands were determined using (b) the Fourier self-deconvolution and (c) the second-derivative method.

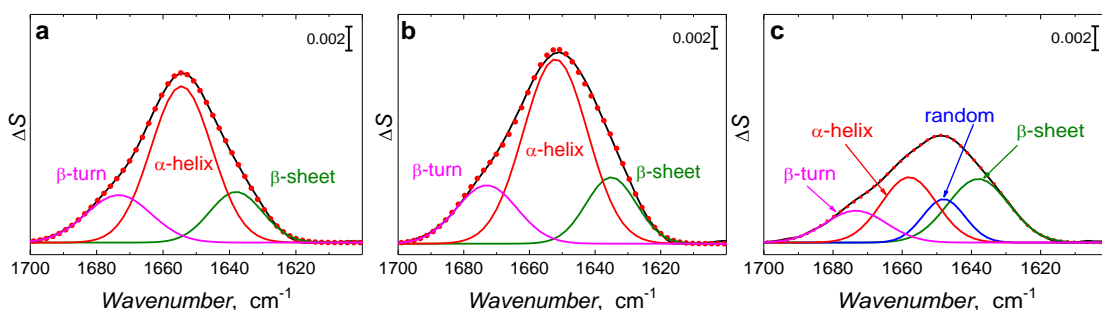


Figure 3.2-9. Deconvolution of the amide I band of the BacSp222 incorporated in the DMPC bilayer recorded at the potential of (a) 100 mV, (b) -600 mV, and (c) -800 mV vs. Ag|AgCl. The black curve is the experimental spectra. The red dotted curve is the cumulative result of band deconvolution.

The same procedure was performed for spectra acquired at different potentials. Figure 3.2-9 shows deconvolution of spectra acquired at potentials of 100 mV, -600 mV, and -800 mV. Amide I band changes when adsorbed molecules are exposed to different potentials. In the potential range of 200 to -500 mV, differences are subtle. The dominant band is at  $1654\text{ cm}^{-1}$  with an FWHM of  $21\text{--}23\text{ cm}^{-1}$ . Two other bands at  $1635$  and  $1678\text{ cm}^{-1}$  with FWHM of  $19$  and  $22\text{ cm}^{-1}$  are much less pronounced. The potential decrease causes a decrease in the  $\alpha$ -helix band intensity accompanied by the appearance of a new band at  $1649\text{ cm}^{-1}$

(FWHM  $14\text{ cm}^{-1}$ ). This new band position is characteristic of a random structure,<sup>251</sup> suggesting the potential-induced unfolding of the BacSp222 at potentials below  $-600\text{ mV}$ . The SD and FSD analysis of the amide I band revealed that BacSp222 undergoes potential-induced conformational changes.

The  $\alpha$ -helical part of the peptide is responsible for its insertion into the phospholipid bilayer. Therefore, the  $\alpha$ -helix band was used to determine BacSp222 orientational changes upon insertion into the DMPC- $d_{54}$  membrane. Figure 3.2-10 and Table 3-2 show the calculated tilt angle between the  $\alpha$ -helix transition dipole moment and surface normal as a function of applied potential. Four  $\alpha$ -helices were recognized in the BacSp222 secondary structure by the NMR spectroscopy in aqueous solution.<sup>241</sup> However, that was in the absence of lipids and thus, the exact orientation and alignment of each of four  $\alpha$ -helix for BacSp222 in the presence of a phospholipid bilayer is unknown. The PM-IRRAS provides band intensities which contain information on the averaged orientation and alignment of transition dipole moments of all  $\alpha$ -helices.

The average tilt angle of the transition dipole moment of  $\alpha$ -helices equals  $\sim 39^\circ$  and remains unchanged in the potential range of  $300$  to  $-600\text{ mV}$ . At lower potentials, where the bilayer is detached from the electrode, the angle increases to  $61^\circ$ . The potential dependence of the BacSp222 tilt angle reveals that low potentials induce substantial changes in orientation of the  $\alpha$ -helix, which correspond to conformational unfolding to a random structure.

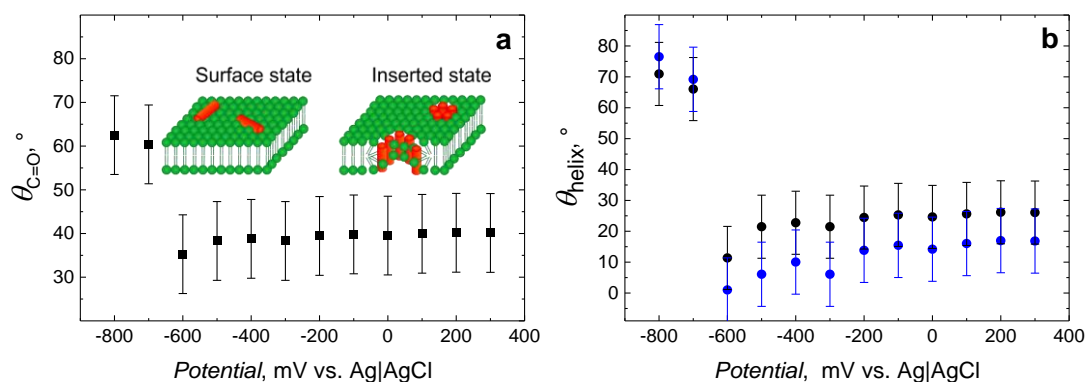


Figure 3.2-10. The average tilt angle of (a) the transition dipole moments ( $\theta_{C=O}$ ) and (b) the major axis of the  $\alpha$ -helical components ( $\theta_{helix}$ ) of BacSp222 as a function of the electrode potential vs. Ag|AgCl. The tilt angle of  $\alpha$ -helices was calculated for reference angles of ( $\bullet$ )  $34^\circ$  and ( $\bullet$ )  $38^\circ$ .

The average tilt angle of  $\alpha$ -helices long axes vs. transition moment of the amide I vibration (reference angle) was calculated to be between  $34^\circ$  and  $38^\circ$ .<sup>203, 204, 258, 259</sup> The corresponding tilt angle of  $\alpha$ -helices was determined according to the procedure described in Section 2.2.3.9 above. Table 3-2 and Figure 3.2-10 show the average tilt angles of the BacSp222  $\alpha$ -helix calculated for reference angles of  $34^\circ$  and  $38^\circ$ . The low tilt angle, between  $24^\circ$  and  $12^\circ$ , of

the  $\alpha$ -helix indicates that BacSp222 remains inserted in the bilayer in the potential range of 300 to -600 mV. At potentials below -600 mV, the orientation of  $\alpha$ -helix changes dramatically and equals 70-77° at -800 mV. Thus, the change in  $\alpha$ -helix orientation, from perpendicular to parallel, against the membrane surface normal, may be described as an inserted state and surface state, with transition potential between -600 and -700 mV.

Table 3-2. The calculated values of the order parameter ( $S$ ), the tilt angle ( $\theta_{\text{tilt}}$ ) of transition dipole moment vs. electrode surface normal, and tilt angle ( $\theta_{\text{helix}}$ ) of the  $\alpha$ -helix long axis vs. transition moment of the amide I vibration (reference angle,  $\theta_{\text{ref}}$ ), at each applied potential.

Potential, mV vs. Ag AgCl	$\theta_{\text{tilt}}, ^\circ$	$S_{\text{C=O}}$	$S_{\text{helix}}$		$\theta_{\text{helix}}, ^\circ$	
			$\theta_{\text{ref}} = 34^\circ$	$\theta_{\text{ref}} = 38^\circ$	$\theta_{\text{ref}} = 34^\circ$	$\theta_{\text{ref}} = 38^\circ$
300	40.12	0.38	0.71	0.87	26.1	16.8
200	40.16	0.38	0.71	0.87	26.1	17.0
100	39.93	0.38	0.72	0.88	25.6	16.0
0	39.52	0.39	0.74	0.91	24.6	14.2
-100	39.79	0.39	0.73	0.89	25.3	15.4
-200	39.45	0.39	0.74	0.91	24.4	13.8
-300	38.29	0.42	0.80	0.98	21.5	6.1
-400	38.77	0.41	0.78	0.95	22.8	10.0
-500	38.29	0.42	0.80	0.98	21.5	6.1
-600	38.00	0.43	0.81	0.99	20.1	3.2
-700	60.40	-0.13	-0.25	-0.31	66.0	69.2
-800	62.51	-0.18	-0.34	-0.42	70.9	76.5

### 3.2.4.1. ATR-IR study of the BacSp222 orientation in a dehydrated DMPC multibilayer

The results obtained show that BacSp222 molecules interact with the DMPC-d<sub>54</sub> bilayer by inserting its  $\alpha$ -helical part nearly parallel to the membrane surface normal, under exposure to a static electric field. The peptide orientation undergoes a transition from inserted to surface state when the bilayer is detached from the metal surface at sufficiently negative potentials. At these potentials, the bilayer is lifted from the metal surface, de-wetting of the elec-

trode occurs. That means that the water spacer between the electrode and bilayer is thickened, and most importantly, the bilayer becomes dehydrated, as shown by the SEIRAS experiments.<sup>43</sup>

The ATR-IR spectroscopy measurements were herein performed to determine the orientation of the BacSp222 molecules in a dry DMPC multibilayer.<sup>239</sup> The ATR-IR spectroscopy results confirmed that BacSp222 is mainly  $\alpha$ -helical, with  $\beta$ -sheets and  $\beta$ -turns also present. The order parameter of  $\alpha$ -helices was calculated to be negative ( $-0.17$ ), which is associated with BacSp222 molecules' orientation parallel to the membrane surface.<sup>260</sup>

The calculated average tilt angle of the DMPC phospholipids comprising multibilayer film was  $\sim 62^\circ$ . The PM-IRRAS data showed that the BacSp222  $\alpha$ -helix is almost parallel to the membrane surface normal (inserted state) for the fully hydrated DMPC- $d_{54}$  bilayer, in the potential range of 300 to  $-600$  mV. As shown by PM-IRRAS and ATR-IR spectroscopy for a dehydrated bilayer, BacSp222 changes orientation from parallel to perpendicular to the membrane surface normal (surface state). Therefore, the hydration level of the bilayer influences the orientation of the BacSp222 molecules. Interestingly, the effect of hydration was also studied by ATR-IR spectroscopy for melittin in hydrated multibilayer system,<sup>260</sup> and the results showed that the melittin  $\alpha$ -helix is perpendicular to the membrane surface normal, which is contrary to present findings for BacSp222. Thus, the mechanism of membrane activity of melittin and BacSp222 is different.

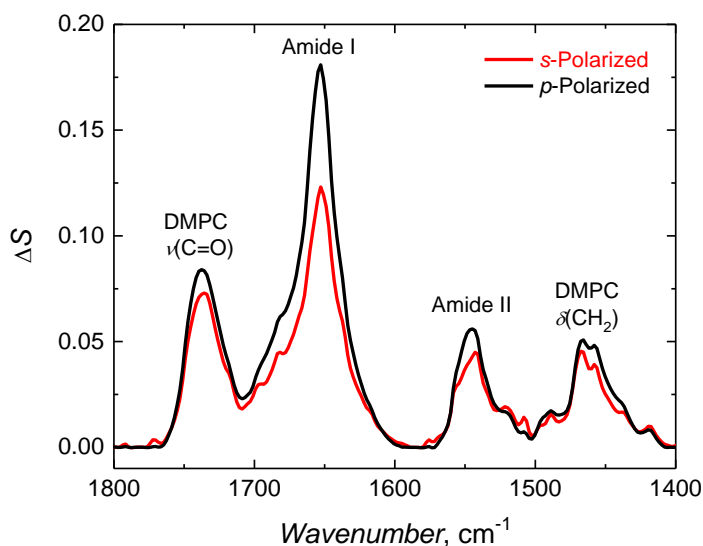


Figure 3.2-11. Polarized ATR-IR spectra of the dry multibilayer DMPC/BacSp222 film acquired in collaboration with Michael Grossutti and Prof. Jacek Lipkowski. Bands characteristic for amide I and amide II vibrations of BacSp222 and two bands associated with the C=O stretching and C-H bending of DMPC are visible.

### 3.2.5. AFM imaging of the DMPC bilayer disruption upon BacSp222 activity

A DMPC bilayer was deposited on mica and imaged in a 150 mM NaCl, 10 mM HEPES, 5 mM CaCl<sub>2</sub> buffer (pH = 7.4) to reveal topographical changes occurring in the bilayer upon BacSp222 activity. Two peptide concentrations were examined, i.e., those of the 90:1 and 10:1 lipid-to-peptide molar ratios. For that, peptides were added to a freshly prepared SUVs solution and then vortexed before deposition. Figure 3.2-12a shows a DMPC bilayer in the absence of membrane-disrupting bacteriocin. DMPC bilayer thickness was estimated to be  $4.53 \pm 0.19$  nm (profile 1 in Figure 3.2-12b). Figure 3.2-12c-12h shows DMPC/BacSp222 bilayer images exhibiting significant damages compared to the intact bilayer. Thinned bilayer area (Figure 3.2-12c, left side) with visible holes distributed among the surface is neighboring a severely disrupted bilayer area (Figure 3.2-12c, right side), further shown in Panel d. The average grain size in Figure 3.2-12d is approximately 12 nm, and bilayer thickness is  $3.44 \pm 0.43$  nm (Profile 2 in Figure 3.2-12b). There are no areas with the bilayer remaining smooth at higher bacteriocin concentrations (Figure 3.2-12e–12h). The BacSp222 activity completely alters the bilayer. In Figure 3.2-12e and 12f, pore-like structures are visible. Ob-long, fiber-like structures, tens of nanometers long (Figure 3.2-12g), and globular structures protruding 1.5-2 nm above the surface (Figure 3.2-12h) are present in a different sample area.

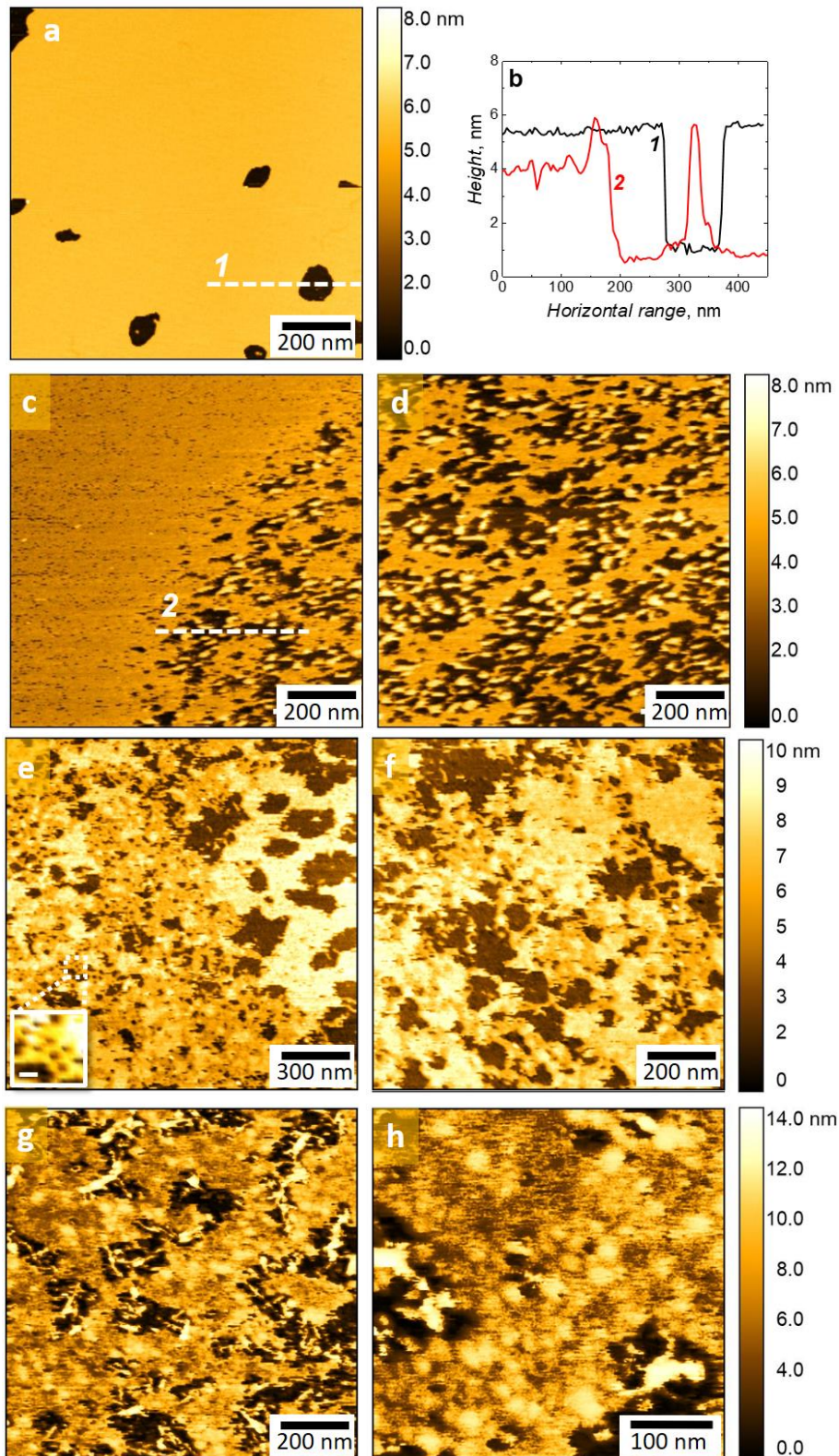


Figure 3.2-12. The AFM images of a DMPC bilayer deposited on mica, (a) in the absence and (c – h) in the presence of BacSp222. (b) Cross-sectional profiles of (curve 1) DMPC and (curve 2) DMPC/BacSp222, as shown on images a and c. Three samples of DMPC/BacSp222 bilayer deposited on mica are shown, at concentrations of (c, d) 90:1 lipid-to-peptide molar ratio, and (e – h) 10:1 lipid-to-peptide molar ratio. Inset in Panel e shows an enlarged and processed area of possible pores cluster, with the scale bar indicating a 20-nm distance.

### 3.2.6. Conclusions

The results showed that the BacSp222 structure in solution is ordered, being mainly  $\alpha$ -helical (58%) with  $\beta$ -turns (32%) and  $\beta$ -sheets (10%) also present. The structure does not change significantly after adsorption to the phospholipid bilayer. This finding is interesting because usually, the majority of  $\alpha$ -helical peptides are disordered in the bulk solution and only fold into helix at initial interaction with the bilayer.<sup>261</sup>

The discussed research showed that BacSp222 interacts with the DMPC bilayer by changing the orientation and conformation of phospholipid acyl chains. These chains become less tilted with respect to the membrane surface normal and undergo chain melting transition in the presence of BacSp222. The BacSp222 molecules undergo a potential-driven change of orientation against the bilayer surface. The molecule is inserted into the bilayer at an average angle below  $30^\circ$  against the membrane surface normal in a wide potential range. At potentials more negative than  $-600$  mV, the peptide becomes surface-oriented. That is accompanied by the gradual unfolding of BacSp222 at such negative potentials. PM-IRRAS and ATR-IR spectroscopy experiments showed that the hydration level of the DMPC bilayer influences the secondary structure and orientation of BacSp222 molecules in the bilayer. Peptides are unable to insert into a dehydrated multibilayer system and remain in a surface state.

AFM imaging revealed extensive damage induced by the BacSp222 adsorption. Even though the potential was not applied to the mica-supported bilayer, the areas exhibiting pore-like structures, as well as surface aggregates, were found. The visualization of the BacSp222-affected membrane leaves no doubt on the disruptive activity of the peptide.

As described above, the orientation of the BacSp222, together with the decrease in the tilt of phospholipid acyl chains, suggests pore formation. Initially, a pore formation via the barrel-stave model was proposed because of the relatively low tilt angle of the BacSp222 against the surface normal. However, BacSp222 is water-soluble, and moreover, further studies of the BacSp222 structure<sup>241</sup> instead indicate that, due to the four-helix bundle structure, the BacSp222 molecules may only partially insert into the bilayer and then induce further changes in the phospholipid molecules. Interestingly, bacteriocins are known to mainly act through membrane-bound mediators or receptors, e.g., nisin binding to Lipid II, so that they are selective towards specific bacteria species.<sup>11</sup> Findings presented herein show that for synthetically obtained BacSp222, this specificity might not be upheld, which would comply with the postulated broad-spectrum activity.<sup>183</sup>

### 3.3. Toxicity of selected airborne nitrophenols on a model lung-like lipid membrane

#### 3.3.1. Nitrophenols – environmental pollutants and screening of their toxicity effects

Nitrated phenols are toxic components of atmospheric aerosol particles. The pollutants enter the atmosphere through biomass,<sup>262</sup> wood, fuel,<sup>263</sup> and coal combustion.<sup>264</sup> They are also found in industrial chemical wastes, including pesticides, insecticides, pharmaceuticals, dyes, plasticizers,<sup>265</sup> and wood preservatives.<sup>266</sup> Trace amounts of nitrophenols were identified in airborne fine particulate matter<sup>267</sup> and atmospheric waters,<sup>268, 269</sup> which is regarded as a threat to living organisms.

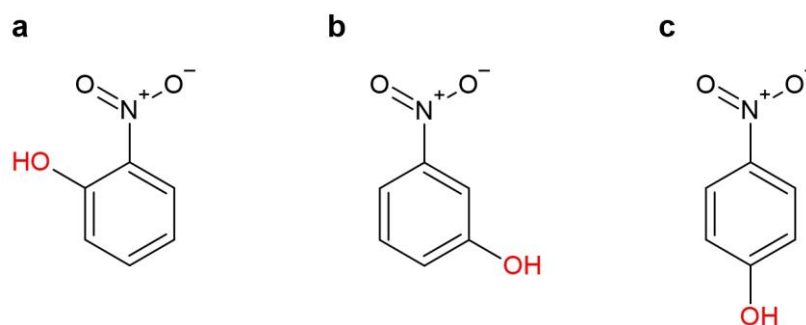
Nitrophenols are harmful to plants.<sup>270</sup> 2-Nitrophenol and 4-nitrophenol are listed as priority hazardous environmental pollutants,<sup>271</sup> inducing genotoxic effects with respiratory implications.<sup>272</sup> In general, biomass, fuel, and coal-burning emissions correlate with asthma, allergy, bronchitis, and other pulmonary diseases in areas impacted by smog.<sup>273</sup> It is agreed that emissions of nitroaromatics need to be regulated. Some governments and authorities are trying to conduct screening of potentially toxic or genotoxic chemicals. Various methodologies have been reported to study the toxicological effects of environmental pollutants on human cells, where BEAS-2B and A549 cell lines were established as widely used in vitro cell models to study the impact of wood burning, exhaust and diesel emission, and biomass combustion products in the fine particulate matter.<sup>274</sup> Various model cell lines are applied to study the effects of environmental pollutants on human health, but scientists are also trying to screen the toxicological effects in an even more efficient way, which constraints the use of in vivo models. Nevertheless, the mechanism of cell functioning disruption by exposure to nitrophenols is yet unknown.

The initial presumption was that the nitrophenols cross the cell membrane and target intracellular components. The question remains, whether (and how) nitrophenols interact with the cell membrane or not. This study aims to determine if nitrophenols interact with the model phospholipid bilayer and, therefore, if the applied method is suitable to screen the toxicity of nitrophenols. The MW of the studied nitrophenols is 139.11 g mol<sup>-1</sup>, comparable to the MW of the single amino acid (average amino acid MW  $\approx$  110 g mol<sup>-1</sup>). For this reason, it is uncertain if any effect of the nitrophenols will be recognized. For comparison, the MW of the AMPs is usually 1100-5500 g mol<sup>-1</sup>, i.e., 10-50 times higher. Even though no such interactions as described for AMPs are expected, herein, it is proposed just to compare the properties of

a phospholipid bilayer in the absence and presence of nitrophenols and seek for symptoms of membrane-disrupting or properties-changing effects.

### 3.3.1.1. Preparation of nitrophenols mixture

In the present study, 2-nitrophenol, 3-nitrophenol (ReagentPlus™, 99%), and 4-nitrophenol (Sigma-Aldrich) were used as components of toxic aerosol particles (Scheme 3.3-1). First, all nitrophenols were dissolved in a double-distilled Milli-Q water (resistivity of 18.2 MΩ cm at 25 °C). Next, the mixture of 2-nitrophenol, 3-nitrophenol, and 4-nitrophenol was prepared at a concentration range between 0.01 to 200 μg mL<sup>-1</sup>, which is much below the solubility limits for these compounds, except one sample of 2 mg mL<sup>-1</sup> prepared, which, however, is within the upper limit of solubility.<sup>275, 276</sup> The dissolved nitrophenols were then boiled in the water bath at 100 °C for 2-3 min before cooling down at room temperature. Finally, an equimolar mixture of three nitrophenols was prepared from the original stock solution and used in the microscopic and electrochemical measurements and cellular exposure studies referred to as the nitrophenols mixture.



Scheme 3.3-1. Structural formulas of relevant biomass and fuel-burning aerosol components used in the present study. (a) 2-Nitrophenol, (b) 3-nitrophenol, and (c) 4-nitrophenol.

The CV and EIS electrochemical techniques and AFM imaging, previously applied to study peptide-lipid interactions, were harnessed to screen the toxicity of airborne nitrophenols towards lung-like model membranes. The CV and EIS responses exhibit characteristic features in case of defect formation in a model membrane.<sup>121, 196</sup> Therefore, the combination of CV and EIS with direct AFM visualization is a powerful tool to screen the toxicity effect of a given compound, providing the answer to whether it is a membrane-disrupting agent or not. Additionally, the cytotoxic effect of the nitrophenols mixture was studied on the following cell lines: BEAS-2B (immortalized bronchial epithelial cells) and A549 (cancerous alveolar epithelial cells), with the use of the phase-contrast microscopy (PCM).<sup>277</sup>

### 3.3.1.2. Model lung-like lipid membrane

Model membrane mimics eukaryotic cell membrane by adequate selection of phospholipids. Therefore, a multicomponent bilayer was used with phospholipids characteristic for a lung cell. BEAS-2B and A549 cell lines represent bronchial epithelium (BECs) obtained from the autopsy of non-cancerous individuals and immortalized by SV-40 viral transcript and the adenocarcinomic human alveolar basal epithelium (A549) explanted from cancerous patients, respectively. It was not intended at this stage of research to differentiate between the two for model membrane preparation. The BECs and A549 cells are mainly composed of ~60-80% phosphatidylcholines (PC) and ~7-15% phosphatidylglycerol (PG) (16:0-18:1).<sup>278</sup> Among PCs in human lungs, 1,2-dimyristoyl-*sn*-glycero-3-phosphocholine, DMPC(14:0-14:0), 1-palmitoyl-2-oleoyl-*sn*-glycero-3-phosphocholine, POPC (16:0-18:1), and 1,2-dipalmitoyl-*sn*-glycero-3-phosphocholine, DPPC (16:0-16:0), are most abundant.<sup>279</sup> Therefore, the lung-like model membrane used in the present study comprises a DMPC, DPPC, and POPC mixture, called the 3×PC membrane. A single-phospholipid membrane composed of DMPC was used as a reference model membrane to reveal whether the nitrophenols exhibit or not any affinity towards specific lipids.

### 3.3.2. Cytotoxic activity of the nitrophenols mixture towards BEAS-2B and A549 epithelial cells

Nitrophenols mixture induced a decreased cellular viability and inhibited growth at 0.1 mg mL<sup>-1</sup> after 24-h exposure in both BEAS-2B and A549 cell lines (Figure 3.3-1). In addition, cellular shapes changed to round, indicating cytoplasm and cell membrane damage. An increased concentration of 0.2 mg mL<sup>-1</sup> number of cells decreased, and cell disruption occurred more frequently. After 48-h exposure, the number of disrupted cells increased. In the case of BEAS-2B cells, the disappearance of the viable cells was even more pronounced. Thus, exposure to nitrophenols induced cell death in both “normal” and cancerous cells in a time- and concentration-dependent manner. This effect was more pronounced for “normal” BEAS-2B cells. The detailed mechanism of epithelial cell disruption is not resolved. The cellular shape change and cell detachment indicate cell death through cell membrane damage in the presence of the nitrophenols mixture.

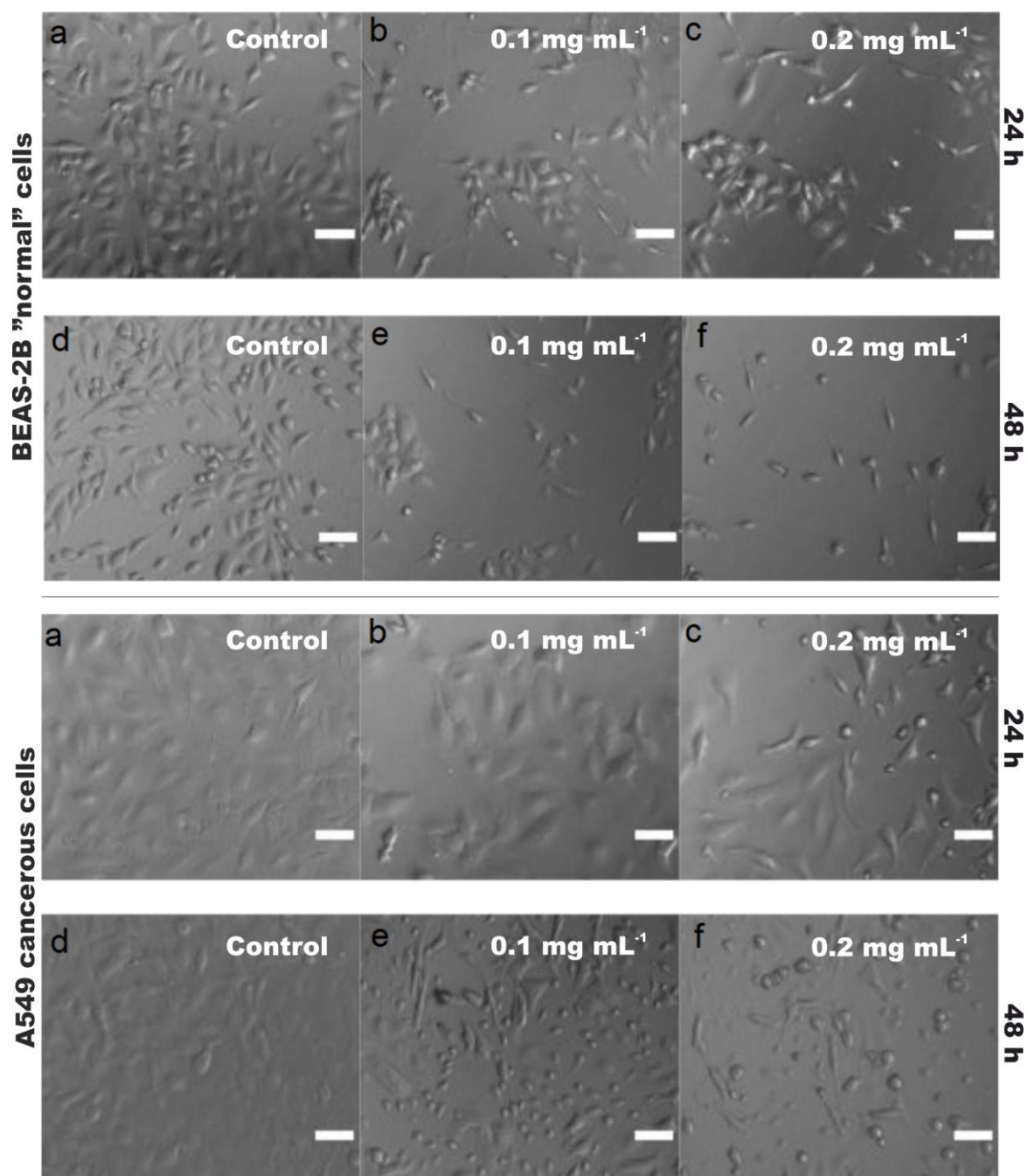


Figure 3.3-1. Phase-contrast optical microscopy images of (top) BEAS-2B and (bottom) A549 cell lines incubated for (a-c) 24 h and (d-f) 48 h in the (a and d) 0  $\mu\text{g mL}^{-1}$  (control cells), (b and e) 0.1  $\text{mg mL}^{-1}$ , (c and f) 0.2  $\text{mg mL}^{-1}$  nitrophenols mixture solution. Images scale bars refer to 50  $\mu\text{m}$  distance. Images were acquired in collaboration with M.Sc. Faria Khan and Prof. Rafał Szmigielski.

### 3.3.3. Electrochemical study of defect formation in a model membrane

The CV experiments, using an Au(111)| $\beta$ -Tg electrode coated with the model membrane, were performed before and after exposure to the nitrophenols mixture (Figure 3.3-2). The examined electrode was coated with either the DMPC or 3 $\times$ PC bilayer. In the potential range between  $-400$  mV and  $100$  mV vs. SCE, CV curves exhibit capacitive behavior (a rectangular-like shape with no current peaks). Apparently, no faradaic reactions occur in this potential range, and the electrode can be characterized by the charging and discharging of the electric double layer at the electrode|solution interface.<sup>198</sup> Additionally, the absence of a current peak in the CV curves indicates that nitrophenols are electroinactive in this potential range. In the case of the 3 $\times$ PC membrane (Figure 3.3-2a), the presence of nitrophenols increased the current density in the whole potential range, which corresponds to the increase in electrode capacitance, most likely, indicating membrane damage. Upon this damage, defects uncover the submembrane region, allowing for enhanced ion flux to the metal electrode. No pronounced differences were observed for the DMPC bilayer (Figure 3.3-2b) after incubation in the mixed nitrophenols solution. The difference in the CV response for the 3 $\times$ PC and DMPC membrane suggests an increased activity of nitrophenols toward the model membrane representing the bronchial epithelium.

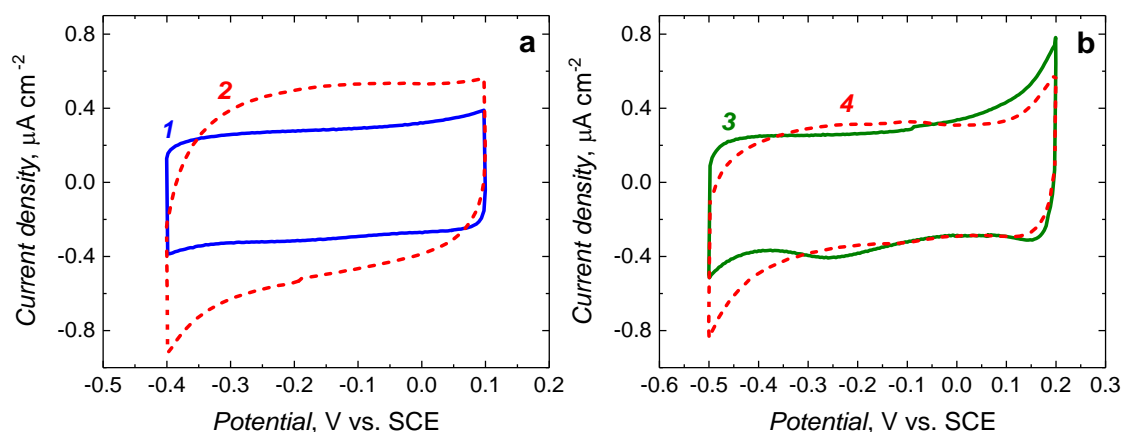


Figure 3.3-2. Cyclic voltammetry curves for the (a) 3 $\times$ PC and (b) DMPC model membranes, deposited on Au(111)| $\beta$ -Tg electrode, before (curve 1 and 3, solid) and after (curve 2 and 4, dashed red) 20-h incubation in the  $200\text{-}\mu\text{g mL}^{-1}$  mixed nitrophenols  $0.01$  M PBS solution. The scan rate was  $20$  mV  $\text{s}^{-1}$ .

The EIS measurements were carried out to determine the cause of capacity change, whether it resulted from destructive nitrophenols activity or dielectric changes within the bilayer because of nitrophenols adsorption. Spectra were acquired under conditions the same as those for the CV measurements.

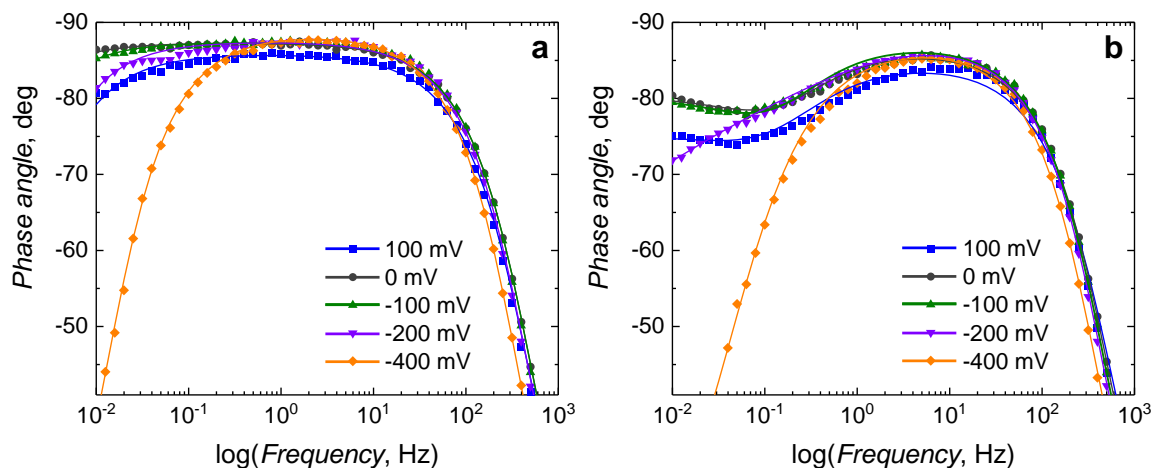


Figure 3.3-3. The phase angle of impedance vs. frequency curves for the 3×PC membrane, deposited on the Au(111)|β-Tg electrode, (a) before and (b) after 20-h incubation in the 200- $\mu\text{g mL}^{-1}$  nitrophenols mixture in 0.01 M PBS (pH = 7.4). Symbols and curves of the same colors represent experimental data and fitting the equivalent electrical circuits, respectively.

Figure 3.3-3a shows phase angle vs. frequency curves for the 3×PC membrane. The phase angle of the intact 3×PC membrane remained constant after reaching a value of  $86 \pm 2^\circ$  below 10 Hz, for potential applied from 100 to  $-300$  mV, indicating that the membrane capacitance mainly controls the impedance (Section 2.2.2.3, above). After incubation in the mixed nitrophenols solution, a minimum in the phase angle spectra appeared (Figure 3.3-3b). This minimum is a characteristic feature indicating transmembrane defect formation.<sup>196</sup> It is also interpreted as an indication of ionophore properties of some membrane-active molecules.<sup>52, 122</sup> The minimum is relatively shallow and shifted from  $f_{\text{min}} = 63$  mHz at  $-100$  mV and 0 mV to  $f_{\text{min}} = 50$  mHz at 100 mV. It indicates a decrease in defect density<sup>121, 197</sup> at more negative potentials and, therefore, a possible potential-dependent change in nitrophenols behavior. It is suggested that such a high value of the minimum on the phase angle vs.  $\log f$  plot may indicate the heterogeneous distribution of defects in the bilayer,<sup>280</sup> which would comply with the multicomponent bilayer architecture. At more negative potentials, the minimum is not seen in the examined frequency range. Presumably, below  $-200$  mV, the minimum is shifted to lower frequencies out of the measurement range, or the electroporation starts dominating. A significant drop in the phase angle at frequencies  $< 1$  Hz at  $-400$  mV is associated with electroporation and electro-dewetting of the membrane.<sup>41, 43, 244</sup> Moreover, as electroporation occurs at negative potentials, i.e., below  $-100$  mV, the impedance of ion transport through the pores may dominate the EIS spectra and exhibit a decrease in the phase angle at frequencies below 0.1 Hz.<sup>52, 124</sup> That could be the case of the spectra recorded at  $-200$  mV. At these potentials, the measurement or fitting can be restricted to frequencies above 0.1 Hz to minimize the contribution of the ion transport through the pores to the measured impedance. However, in the current case, the differences in fit were negligible.

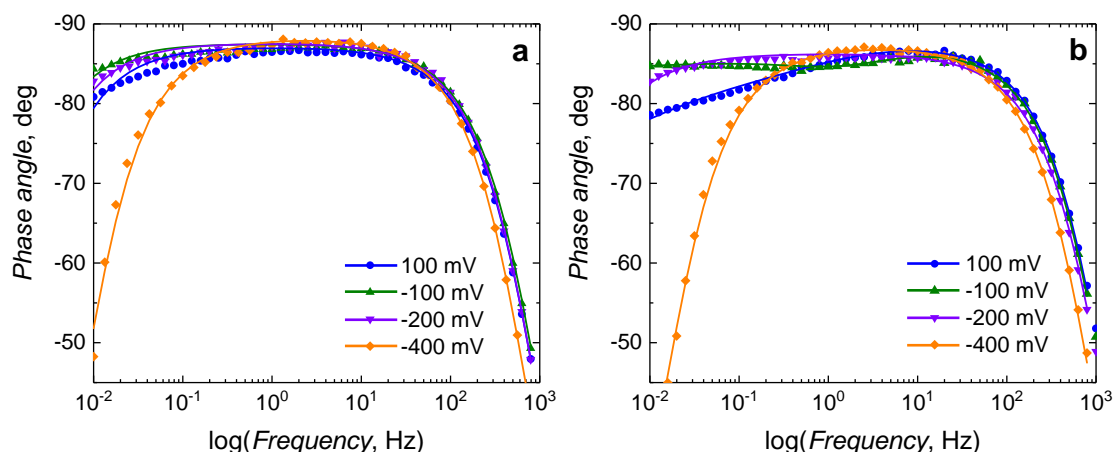


Figure 3.3-4. The phase angle of impedance vs. frequency curves for the DMPC membrane, deposited on the Au(111)| $\beta$ -Tg electrode (a) before and (b) after 20-h incubation in the 200- $\mu\text{g mL}^{-1}$  nitrophenols mixture in 0.01 M PBS (pH = 7.4). Symbols and curves of the same colors represent experimental data and fitting the equivalent electrical circuits, respectively.

Figure 3.3-4a shows the phase angle vs. frequency curves for the DMPC bilayer before the nitrophenols activity. Both the phase angle spectra and CV curves for the DMPC and 3 $\times$ PC bilayer before nitrophenol action are comparable, indicating that both membranes were initially of similar quality. The phase angle of the intact DMPC bilayer remained constant after reaching  $86 \pm 2^\circ$  below 10 Hz, for potential applied from 100 to  $-300$  mV. For potentials below  $-400$  mV, the effect of membrane electroporation preceding electro-dewetting (lifting of the bilayer) dominated, as explained above. After incubation of the DMPC bilayer in the nitrophenols mixture, no characteristic minimum was observed in the spectra within the examined frequency range (Figure 3.3-4b). EIS results agree with the CV results, indicating non-destructive interaction between nitrophenols and DMPC phospholipids.

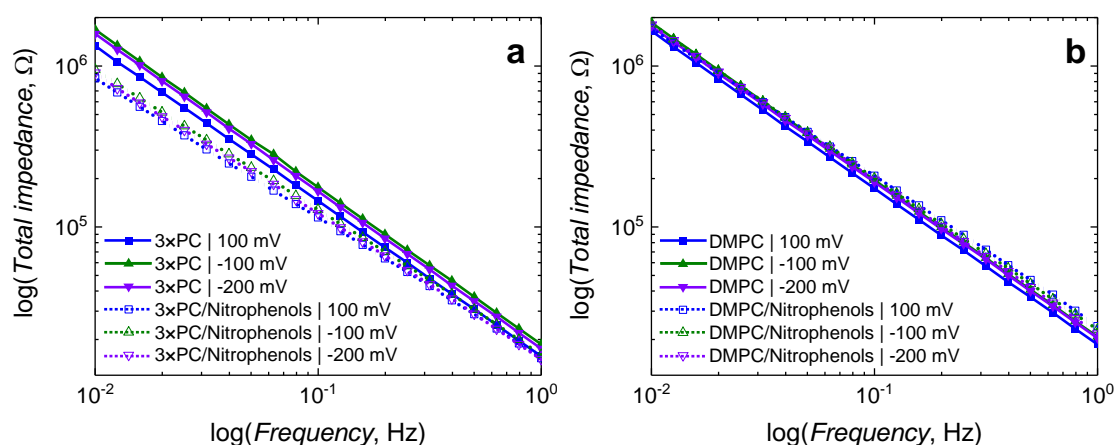


Figure 3.3-5. The modulus of impedance vs. frequency curves for the (a) 3 $\times$ PC and (b) DMPC membrane, deposited on the Au(111)| $\beta$ -Tg electrode, before (solid curves) and after (dashed curves) 20-h incubation in the 200- $\mu\text{g mL}^{-1}$  nitrophenols mixture in 0.01 M PBS (pH = 7.4). Symbols and curves of the same colors represent experimental data and results of fitting the equivalent electrical circuits, respectively.

The feature characteristic for the membrane defects formation was, as expected, also observed in the modulus of impedance vs. frequency spectra. For the 3×PC membrane, a “kink” or deviation from linearity is observed at  $\sim 0.1$  Hz after incubation in the nitrophenols mixture (Figure 3.3-5a). Such an effect is not observed for the DMPC membrane (Figure 3.3-5b).

The EIS spectra were analyzed using equivalent electrical circuits, as described in Section 2.2.2.4 above. The resulting membrane capacitance ( $Q_m$ ) and defect resistance ( $R_{def}$ ) values are presented in Figure 3.3-6 and Figure 3.3-7 for the 3×PC and DMPC membranes, respectively. Corresponding values of all electrical elements are provided in Table 3-3 and Table 3-4. For the intact 3×PC membrane, the  $\alpha$  coefficient values for  $Q_m$  were close to 1.0, allowing interpreting the  $Q_m$  as an equivalent to the membrane capacitance.<sup>114, 121</sup> The  $R_{def}$  value at  $E \approx 0$  V is above  $50 \text{ M}\Omega \text{ cm}^2$ , which shows significant insulating properties of the fBLM. For the intact 3×PC and DMPC bilayers,  $CPE_{sp}$  and  $\alpha_{sp}$  values were close to zero, and exhibited very high standard deviation values. Therefore, these parameters turned out to be non-physical and negligible in the EEC fitting and are not included in the model (Figure 2.2-4c), as discussed in Section 2.2.2.5. After incubating in the nitrophenols mixture, the  $Q_m$  and  $R_{def}$  values for the 3×PC membrane increased and decreased by 13% and 96%, respectively, in the whole potential range. This behavior is related to the increased ion flux through the bilayer because of defect formation, similarly to other reports.<sup>57, 124</sup>

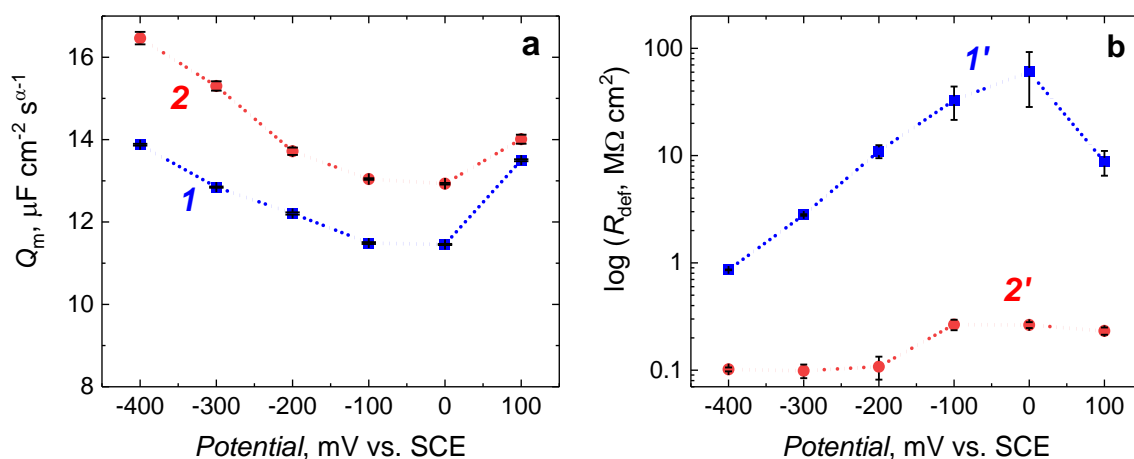


Figure 3.3-6. Membrane (a) capacitance and (b) resistance calculated for the 3×PC bilayer before (curves 1 and 1', blue) and after (curves 2 and 2', red) 20-h incubation in the  $200\text{-}\mu\text{g mL}^{-1}$  nitrophenols mixture in  $0.01 \text{ M PBS}$  ( $\text{pH} = 7.4$ ).

Table 3-3. Values of the equivalent electrical circuit elements for the 3×PC bilayer.  $R_s$  and  $R_{def}$  are resistances of a supporting electrolyte solution and membrane defects, respectively;  $Q_m$  and  $Q_{sp}$  are constant phase elements of a membrane and a spacer, respectively;  $\alpha_m$  and  $\alpha_{sp}$  are constant-phase-element dimensionless parameters.

Sample	Potential mV vs. SCE	$Q_m$ $\mu\text{F cm}^{-2} \text{s}^{\alpha-1}$	$\alpha_m$	$R_{def}$ $\text{M}\Omega \text{ cm}^2$	$Q_{sp}$ $\mu\text{F cm}^{-2} \text{s}^{\alpha-1}$	$\alpha_{sp}$
3×PC	100	13.50 ± 0.02	0.954 ± 0.001	8.77 ± 2.28	-	-
	0	11.45 ± 0.01	0.970 ± 0.001	60.43 ± 32.06	-	-
	-100	11.49 ± 0.02	0.971 ± 0.001	32.79 ± 11.26	-	-
	-200	12.21 ± 0.03	0.972 ± 0.001	10.99 ± 1.53	-	-
	-300	12.85 ± 0.02	0.983 ± 0.001	2.80 ± 0.05	-	-
	-400	13.88 ± 0.02	0.983 ± 0.001	0.86 ± 0.01	-	-
3×PC/Nitrophenols	100	14.01 ± 0.11	0.940 ± 0.001	0.23 ± 0.02	5.48 ± 0.13	0.75 ± 0.01
	0	12.93 ± 0.02	0.964 ± 0.001	0.26 ± 0.02	3.84 ± 0.08	0.79 ± 0.01
	-100	13.04 ± 0.02	0.969 ± 0.001	0.27 ± 0.03	4.40 ± 0.07	0.79 ± 0.01
	-200	13.72 ± 0.09	0.971 ± 0.001	0.11 ± 0.03	3.42 ± 0.08	0.59 ± 0.01
	-300	15.30 ± 0.11	0.965 ± 0.001	0.10 ± 0.01	3.34 ± 0.12	0.22 ± 0.01
	-400	16.46 ± 0.15	0.968 ± 0.001	0.10 ± 0.01	11.58 ± 0.41	0.20 ± 0.01

After the DMPC bilayer incubation in the nitrophenols mixture, both  $Q_m$  and  $R_{def}$  values decreased in the whole potential range (Figure 3.3-7). The data scale is kept the same as that in Figure 3.3-6 to highlight differences in nitrophenols mixture interaction with the DMPC and 3×PC bilayer. The decrease in the DMPC capacitance by 13% is followed by the resistance decrease by 96% on average, compared to the initial values (Table 3-4). Presumably, the decrease in capacitance originates from nitrophenols adsorption on the bilayer surface and interaction with the DMPC molecules, resulting in the change of dielectric properties and (or) thickness of the bilayer and not the defect formation. This behavior contrasts with that for the 3×PC bilayer, in which the nitrophenols induced the defect formation and transmembrane ion flux.

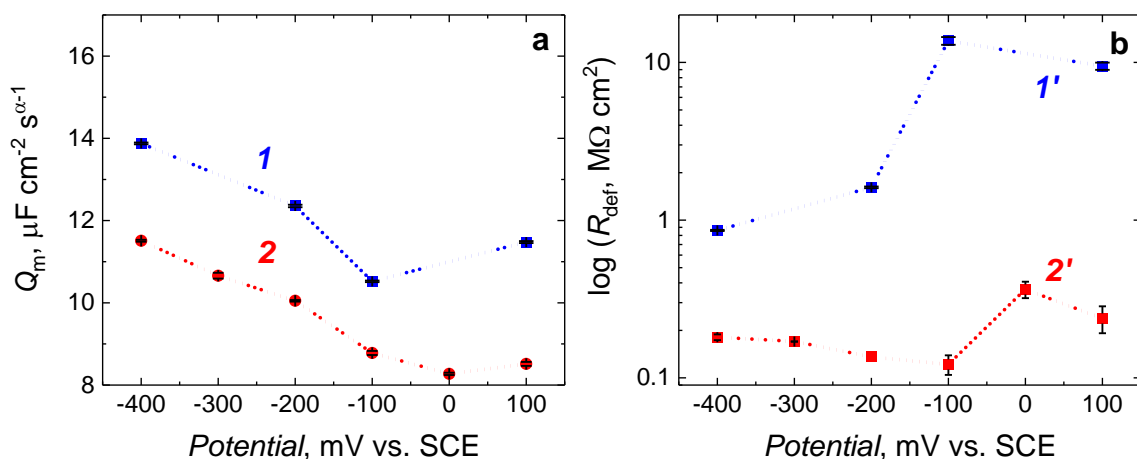


Figure 3.3-7. Membrane (a) capacitance and (b) resistance calculated for the DMPC bilayer before (curves 1 and 1', blue) and after (curves 2 and 2', red) 20-h incubation in the 200- $\mu\text{g mL}^{-1}$  nitrophenols mixture in the 0.01 M PBS solution. The inset shows enlarged values of resistance for the DMPC bilayer after incubation in the nitrophenols mixture solution.

Table 3-4. Values of the equivalent electrical circuit components for the DMPC bilayer.  $R_s$  and  $R_{\text{def}}$  are resistances of a supporting electrolyte solution and a membrane defects, respectively;  $Q_m$  and  $Q_{\text{sp}}$  are constant phase elements of a membrane and a spacer, respectively;  $\alpha_m$  and  $\alpha_{\text{sp}}$  are constant-phase-element dimensionless parameters.

Sample	$E$ , mV vs. SCE	$Q_m$ $\mu\text{F cm}^{-2} \text{s}^{\alpha-1}$	$\alpha_m$	$R_{\text{def}}$ $\text{M}\Omega \text{ cm}^2$	$Q_{\text{sp}}$ $\mu\text{F cm}^{-2} \text{s}^{\alpha-1}$	$\alpha_{\text{sp}}$
DMPC	100	$11.48 \pm 0.02$	$0.967 \pm 0.001$	$9.5 \pm 0.5$	-	-
	-100	$10.24 \pm 0.02$	$0.972 \pm 0.001$	$20.2 \pm 1.5$	-	-
	-200	$10.52 \pm 0.02$	$0.973 \pm 0.001$	$13.7 \pm 0.8$	-	-
	-400	$12.36 \pm 0.03$	$0.981 \pm 0.001$	$1.61 \pm 0.02$	-	-
DMPC/Nitrophenols	100	$8.51 \pm 0.05$	$0.972 \pm 0.001$	$0.24 \pm 0.05$	$1.32 \pm 0.04$	$0.62 \pm 0.01$
	0	$8.27 \pm 0.03$	$0.973 \pm 0.001$	$0.36 \pm 0.04$	$0.92 \pm 0.03$	$0.77 \pm 0.01$
	-100	$8.78 \pm 0.05$	$0.969 \pm 0.001$	$0.12 \pm 0.02$	$1.10 \pm 0.05$	$0.81 \pm 0.01$
	-200	$10.05 \pm 0.02$	$0.959 \pm 0.001$	$0.14 \pm 0.01$	$0.06 \pm 0.01$	$0.09 \pm 0.05$
	-300	$10.68 \pm 0.02$	$0.963 \pm 0.001$	$0.17 \pm 0.01$	$0.29 \pm 0.01$	$6.1 \times 10^{-9} \pm 0.004$
	-400	$11.56 \pm 0.03$	$0.968 \pm 0.001$	$0.18 \pm 0.01$	$1.40 \pm 0.02$	$1.2 \times 10^{-9} \pm 0.001$

### 3.3.4. Phospholipids rearrangement and model membrane disintegration upon nitrophenols activity

The intact 3×PC bilayer (Figure 3.3-8a and Figure 3.3-9a) exhibits domains of different heights indicating phase separation of phospholipids. The multicomponent 3×PC bilayer consists of phospholipids of different acyl chains lengths and transition temperatures,<sup>281</sup> which is 24 °C, 41 °C, and -2 °C for DMPC, DPPC, and POPC, respectively.<sup>182, 282</sup> The thickness of the 3×PC bilayer was  $6.0 \pm 0.2$  nm for the thicker domains, with  $0.9 \pm 0.1$ -nm average height difference between the thicker and thinner domains. This discrepancy in domain thickness results from different lengths of acyl chains of the phospholipids used and the different phase states of the phospholipids at 21 °C. Under these conditions, DMPC and DPPC phospholipids are in a gel phase, while POPC is in the liquid phase. Therefore, taking default lengths of phospholipid acyl chains (number of carbon atoms in a phospholipid acyl chain), one may conclude that the DPPC and POPC most likely constitute the thicker domain, as shown in the AFM images, while the thinner domain is comprised of DMPC. However, bilayer thickness also depends on phospholipids acyl chains tilt angle, but those were not determined in this study.

Figure 3.3-8 shows AFM images of the 3×PC bilayer before and after incubation in the  $2 \text{ mg mL}^{-1}$  nitrophenols mixture in 0.01 M PBS. The mixture concentration was tenfold higher than that found in the atmosphere.<sup>283-285</sup> After 1-h incubation, the 3×PC bilayer entirely disintegrated (Figure 3.3-8b), with only small bilayer patches left, scattered all around the mica surface. These bilayer patches, being  $\sim 4.9 \pm 0.7$  nm thick, were thinner than the intact bilayer. Thus, the majority of phospholipids were removed from the mica surface.

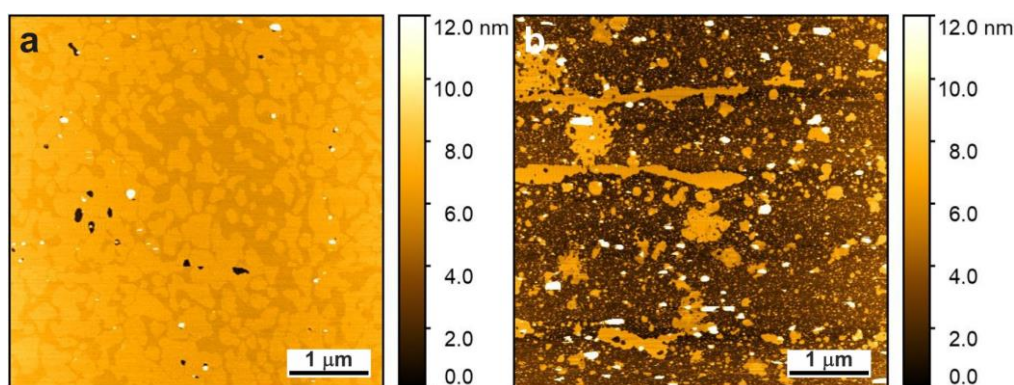


Figure 3.3-8. AFM images of the 3×PC bilayer deposited on mica, acquired in Milli-Q water (a) before and (b) after 1-h incubation in the  $2 \text{ mg mL}^{-1}$  nitrophenols mixture in 0.01 M PBS (pH = 7.4).

The 3×PC bilayer was then examined in the presence of nitrophenols at an environmentally relevant concentration of 200  $\mu\text{g mL}^{-1}$ . After the initial 15-min interaction, the membrane undergoes rapid rearrangements (Figure 3.3-9b and 8c). The phospholipid domains, previously well pronounced (Figure 3.3-9a and 8e), disappeared. Instead, the image was blurred, confirming rapid reorganization and or conformational changes of phospholipid molecules. Similar behavior was observed for various membrane-active peptides.[48](#), [80](#), [133](#), [286](#) Presumably, phospholipid mobility or liquidity changes were induced because numerous stroke-like artifacts are visible. Individual pore-like structures are visible during the first hour of imaging in the presence of nitrophenols. The AFM tip was able to reach down to approximately 1-nm depth into the pore-like defect structures. The average defect diameter was estimated to be  $12 \pm 4$  nm. After 18-h incubation, the AFM image was clear again, and some domains reappeared. The thickness of the bilayer decreased to  $4.8 \pm 0.3$  nm and  $5.5 \pm 0.3$  nm for the thinner and thicker domain. The thinner domain was prevalent (Figure 3.3-9f). Interestingly, after 24-h incubation, the bilayer thickness decreased to  $3.5 \pm 0.1$  nm, and, again, no areas with visible domain separation were found (Figure 3.3-9g). Additionally, areas of uncovered mica surface increased. This behavior suggests selective interaction between nitrophenols mixture and phospholipids, presumably with POPC because of a significant decrease in bilayer thickness. However, the mechanism of phospholipid extraction remains to be elucidated.

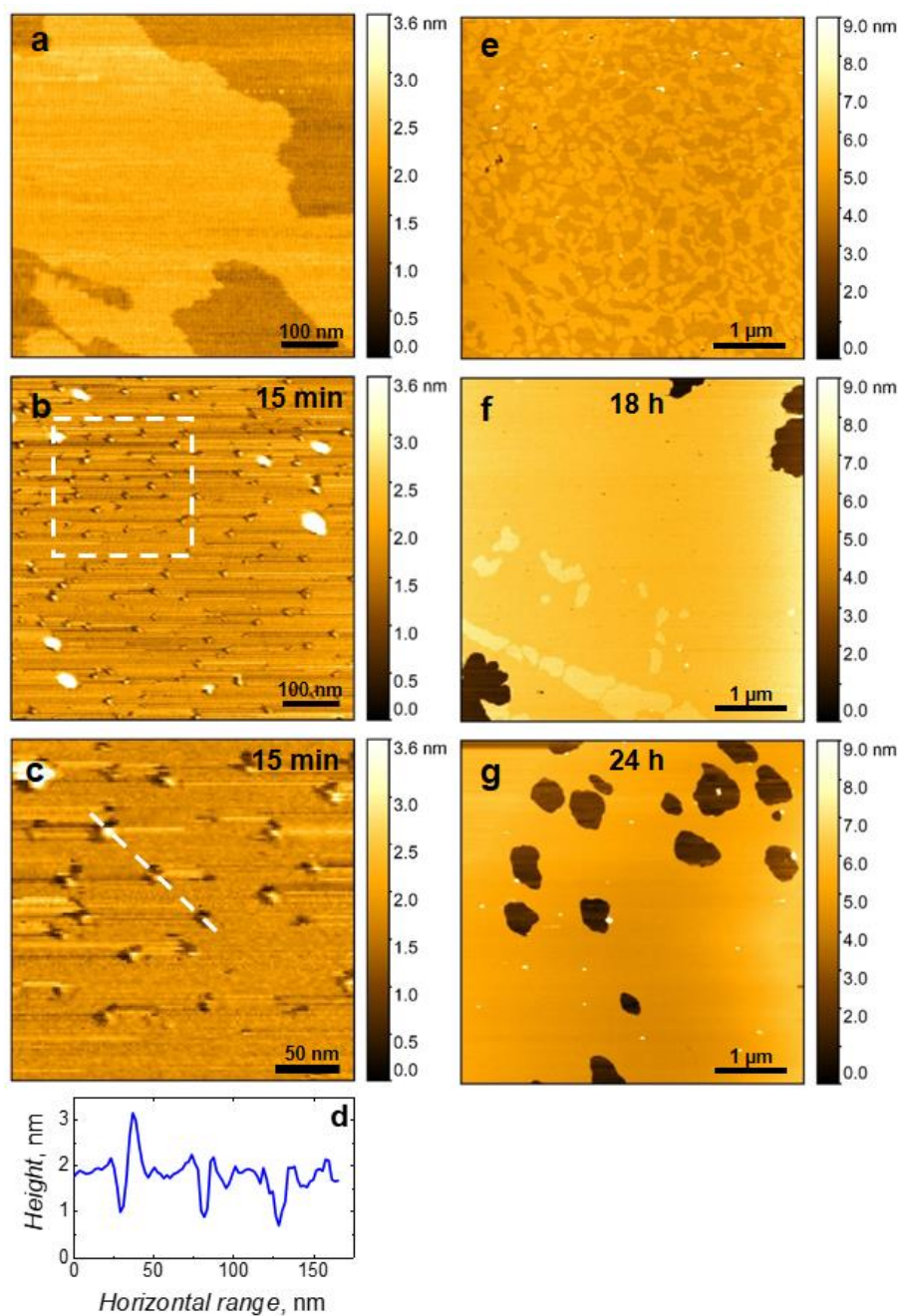


Figure 3.3-9. AFM images of the 3×PC bilayer deposited on mica, acquired in Milli-Q water (a, e) before and after incubation in the 200- $\mu\text{g mL}^{-1}$  nitrophenols mixture solution for (b, c) 15 min, (f) 18 h, and (g) 24 h. All images are of the same sample; Panel g was captured in a different sample area. Image (c) shows an enlarged area marked in Panel b, and graph (d) shows the cross-sectional height profile taken along the line indicated in Panel c.

Moreover, a single-component DMPC bilayer behavior in the presence of nitrophenols was examined. Figure 3.3-10 shows AFM images and corresponding Young's modulus maps of the DMPC bilayer before and after 1-h incubation in the 200- $\mu\text{g mL}^{-1}$  nitrophenols mixture in 0.01 M PBS (pH = 7.4). The intact DMPC bilayer exhibited a smooth surface with a minimal number of defects. Its thickness was estimated to be  $4.22 \pm 0.20$  nm by fitting a step profile

to the bilayer edge (Figure 3.3-10c). After incubation in the nitrophenols mixture, no defects were found within the scanned area. Interestingly, Young's modulus decreased by  $\sim 60\%$ , i.e., from  $32 \pm 12$  MPa ( $R^2 = 0.981$ ) to  $13 \pm 11$  MPa ( $R^2 = 0.969$ ) in the absence and presence of nitrophenols, respectively (Figure 3.3-10f). Both modulus maps were obtained at a Peak Force of 120 pN.

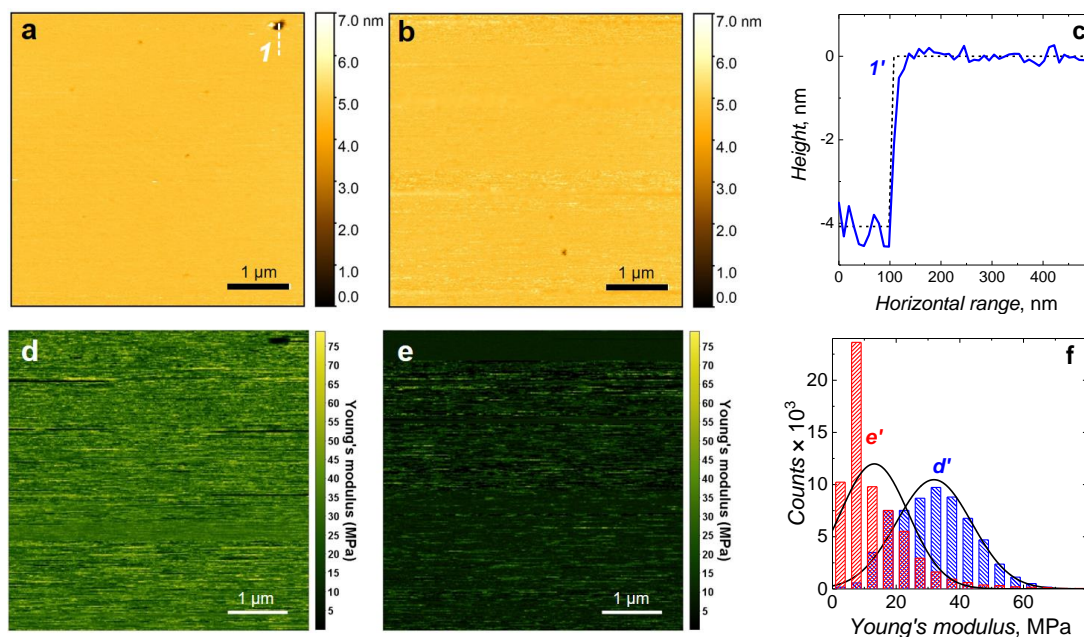


Figure 3.3-10. AFM images of (a, b) topography and (d, e) corresponding Young's modulus maps of the DMPC bilayer deposited on mica, acquired in Milli-Q water, (a, d) before and (b, e) after 1-h incubation in the  $200\text{-}\mu\text{g mL}^{-1}$  nitrophenol mixture in 0.01 M PBS (pH = 7.4). (c) Cross-sectional height profile and edge fit (dashed curve), and (f) Young's modulus histograms of the DMPC bilayer before (curve  $d'$ , blue) and after (curve  $e'$ , red) incubation in the nitrophenols mixture.

After 24-h incubation in the nitrophenols mixture, the DMPC bilayer thickness slightly increased, from  $4.43 \pm 0.55$  nm to  $4.76 \pm 0.20$  nm (curve  $1'$  vs. curve  $2'$  in Figure 3.3-11c). Notably, the DMPC bilayer thickness measurement might not be precise because of the low number of defects and small sizes of these defects. However, given that the DMPC is in a gel phase at  $21^\circ\text{C}$  and keeping in mind EIS results showing changes in the bilayer capacitance and resistance, one can conclude that the nitrophenols interact with the DMPC bilayer by loosening its structure by inserting into the bilayer interior. As a result, Young's modulus of the bilayer decreased (Figure 3.3-10f), followed by a slight thickness increase. However, no further damage was induced within the DMPC membrane (Figure 3.3-11).

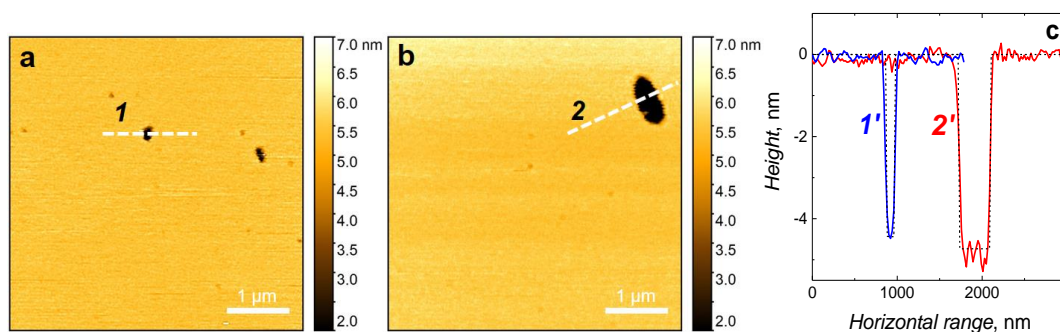


Figure 3.3-11. The AFM topography images of the DMPC bilayer deposited on mica (a) before and (b) 24 h after DMPC incubation in  $200 \mu\text{g mL}^{-1}$  nitrophenols mixture in 0.01 M PBS (pH = 7.4). (c) Cross-sectional height profiles, taken along the lines indicated in Panels a and b and corresponding edge fits (dashed curves).

The DMPC bilayer was not immediately disrupted, as was the case for the higher nitrophenols concentration ( $2 \text{ mg mL}^{-1}$ ). The nitrophenols mixture activity is, most likely, concentration-dependent. Furthermore, the results suggest that nitrophenols may not disintegrate the membrane at lower concentrations but pass through it, changing its properties. This behavior would imply that nitrophenols can penetrate the biological cell and react with its interior components. Results for the DMPC bilayer showed that the bilayer is not destroyed at  $200 \mu\text{g mL}^{-1}$  nitrophenols mixture concentration. However, its properties are changed. This observation supports conclusions for nitrophenols' interaction with the  $3\times\text{PC}$  bilayer, where only a part of the phospholipids seems to be affected by the nitrophenols. The occurrence of transient pore-like defects was observed in a short time after nitrophenols mixture injection.

### 3.3.5. Conclusions

Both results on cell lines and model membranes suggest that nitrophenols interact with the biological membrane. For the lower concentration ( $200 \mu\text{g mL}^{-1}$ ), the nitrophenols activity caused minor topographic changes in the DMPC bilayer, resembling compacting and phospholipid chain melting, while the  $3\times\text{PC}$  membrane clearly disintegrated. These results correspond well with the EIS and CV results. Apparently, airborne nitrophenols induce substantial changes in cell membranes, facilitating these pollutants to penetrate lung cells and bring about the development of various diseases.

## **3.4. Interaction of LL-37 human cathelicidin peptide with model microbial-like lipid membrane**

### **3.4.1. LL-37 cathelicidin peptide**

The object of this research project is LL-37 human cathelicidin, which was introduced in detail in Section 1.6 above. As already discussed, the literature does not indicate a single mechanism of the LL-37 membrane attack.<sup>7</sup> Therefore, the present study is focused on details of the membrane disruption mechanism.

It is widely agreed that the composition and physicochemical properties of the model membrane impact the LL-37 activity and influence the results of the peptide/lipid interaction studies.<sup>136, 165, 168-170</sup>

A multicomponent model bilayer was applied to study the interactions between the LL-37 peptide and a model membrane because it resembles biological membrane heterogeneity in terms of lipid composition and lateral structuration into specialized compartments or domains.<sup>91</sup> The model membrane comprised neutral/zwitterionic PC and acidic/negatively charged PG phospholipids of three different acyl chains lengths (saturated DMPC/DMPG (14:0) and DPPC/DPPG (16:0), and unsaturated POPC/POPG (16:0-18:1)). The PC/PG phospholipids were chosen, which both possess cylindrical molecular shape, have similar packing density, and do not form H-bonds,<sup>169</sup> to limit the number of factors differentiating the applied six-component phospholipid mixture. Therefore, the phospholipids comprising microbial-like model membrane applied in this study differed in terms of acyl chain lengths (and, therefore, phospholipids phase), acyl chain saturation, and headgroup charge. It was deposited on a hydrophilic mica surface or gold electrode modified with a hydrophilic monolayer of 1-thio- $\beta$ -D-glucose that serves as a water-rich spacer promoting phospholipids mobility and protecting the peptide from denaturation in contact with the metal substrate. The system was studied in either 10 mM PBS (pH = 7.4) or Milli-Q water after incubation in 2 mM CaCl<sub>2</sub>.

### **3.4.2. Electrochemical study of defects formation in a model membrane**

A model microbial-like membrane, composed of DMPC/DMPG, POPC/POPG, and DPPC/DPPG, each mixed at the 3:2 molar ratio, and combined in an equimolar mixture, named the 3×PC/3×PG membrane, was deposited on the Au(111) single-crystal electrode modified with a  $\beta$ -Tg self-assembled monolayer for the electrochemical study.

Figure 3.4-1a shows the phase angle vs. frequency plots for the 3×PC/3×PG membrane deposited on the Au(111)|β-Tg electrode in the absence of LL-37. Let us consider the behavior of this angle, starting with high frequency. After reaching the value of  $-80^\circ$  at 10 Hz, we can see that the phase angle does not change in the lower frequency range at potentials  $E > -300$  mV vs. SCE, which is characteristic of capacitive systems.<sup>121</sup> For  $E \leq -300$  mV vs. SCE, the phase angle significantly decreases at low frequencies indicating the 3×PC/3×PG membrane electroporation and electro-dewetting (lifting of the bilayer).<sup>41, 43, 287</sup>

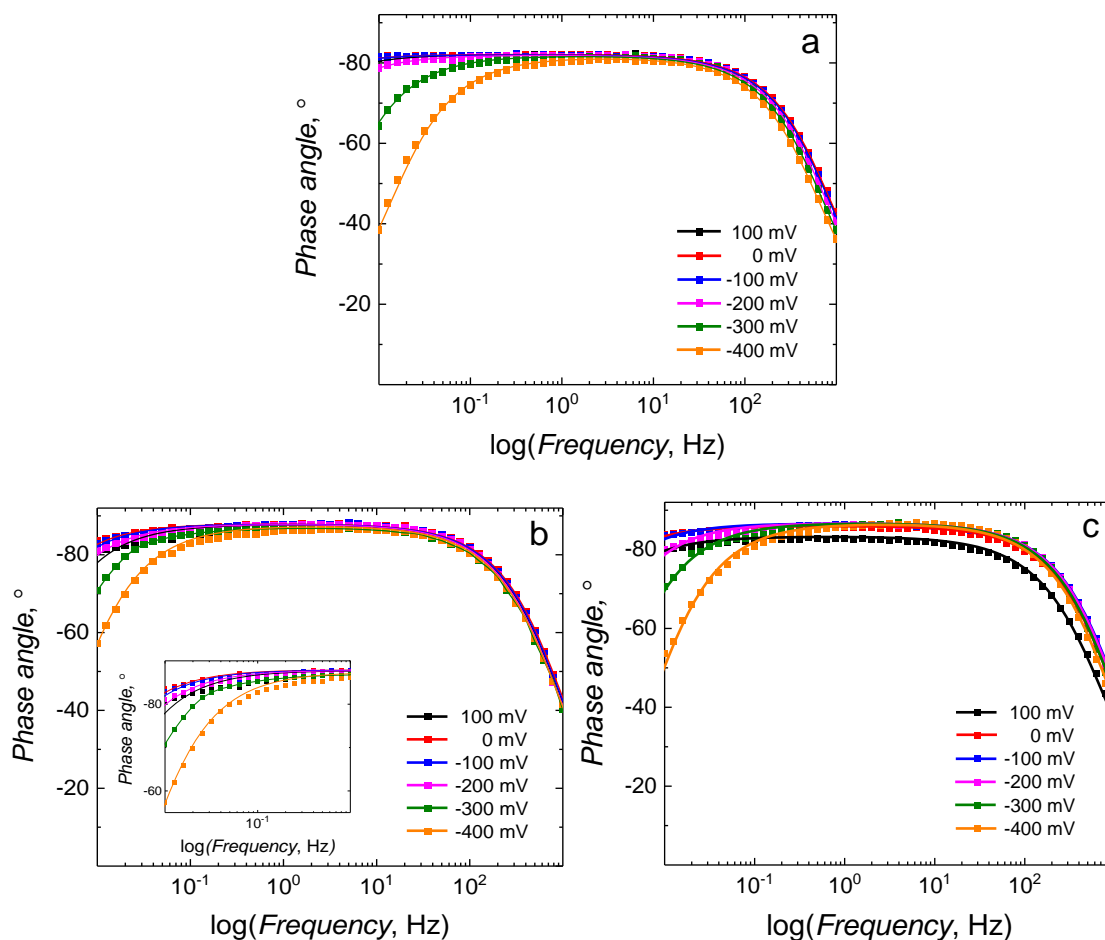


Figure 3.4-1. The phase angle as a function of frequency curves for the Au(111)|β-Tg|3×PC/3×PG membrane (a) in the absence and the presence of LL-37 at the (b) 1:500 and (c) 1:60 peptide-to-lipid molar ratio at different potentials in 10 mM PBS (pH = 7.4). Symbols and curves of the same colors represent experimental data and results of fitting the equivalent electrical circuits, respectively. Inset in Panel b shows the low-frequency range of the phase angle changes with frequency, magnified.

The presence of LL-37 at the 1:500 peptide-to-lipid molar ratio causes visible changes in the phase angle in the potential range of 100 to  $-200$  mV vs. SCE (Figure 3.4-1b). Similar behavior was observed for the higher LL-37 concentration (Figure 3.4-1c). In the LL-37 presence, the phase angle reaches  $\sim -87^\circ$  at 10 Hz, which is higher than for the membrane without

LL-37 discussed above. The phase angle is low for sub-Hertz frequencies, indicating the formation of defects in the membrane.<sup>121, 196</sup> All these changes in the phase angle suggest that LL-37 noticeably perturbs the bilayer structure. However, very subtle to none differences are visible in the impedance vs. frequency plot shown in Figure 3.4-2.

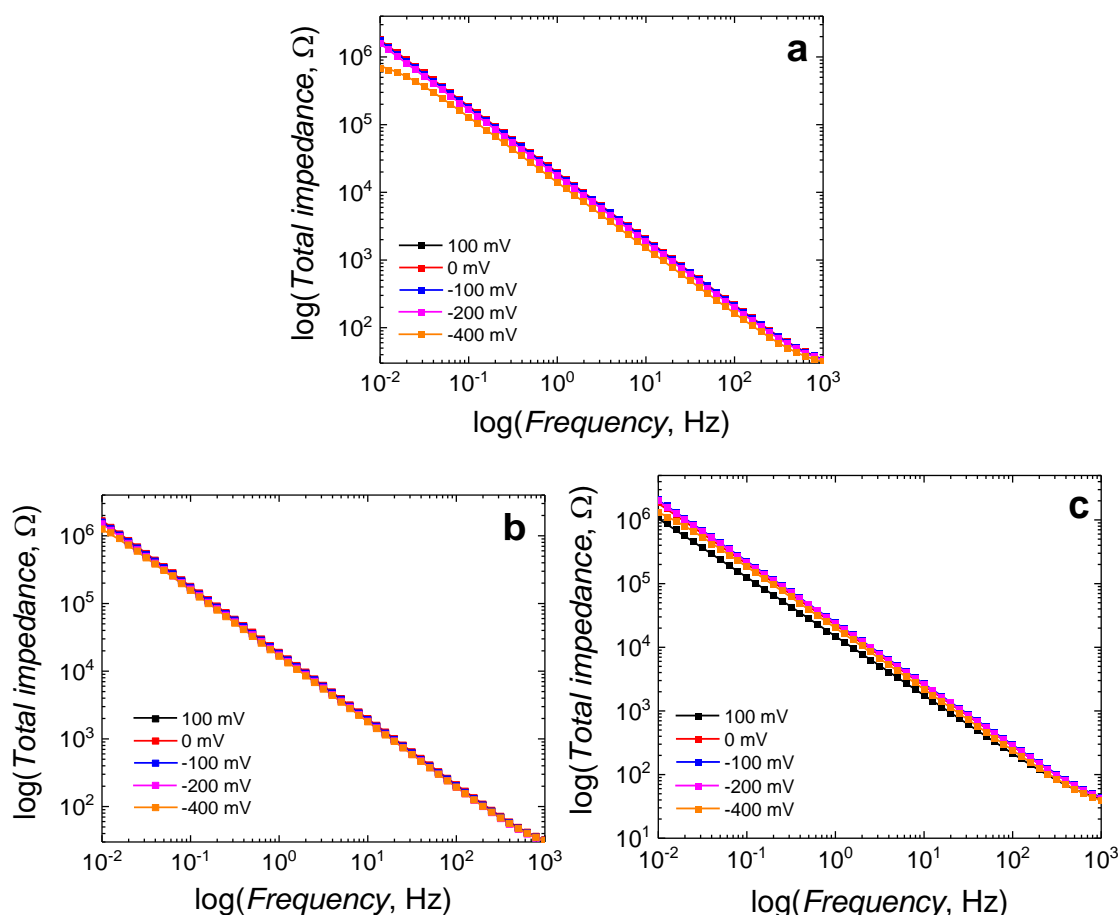


Figure 3.4-2. The modulus of impedance vs. frequency curves for the Au(111)| $\beta$ -Tgl/3 $\times$ PC/3 $\times$ PG model microbial membrane (a) in the absence and presence of the LL-37 at the (b) 1:500 and (c) 1:60 peptide-to-lipid molar ratio, at different potentials in 10 mM PBS (pH = 7.4). Symbols and curves of the same colors represent experimental data and results of fitting the equivalent electrical circuits, respectively.

Below  $-300$  mV vs. SCE, the 3 $\times$ PC/3 $\times$ PG membrane electroporation and electro-dewetting<sup>41, 43, 244</sup> dominate, manifested by a significant decrease in the phase angle below  $\sim 60^\circ$ . Interestingly, smaller changes of the phase angle are observed in the presence of LL-37 than in its absence ( $60^\circ$  vs.  $40^\circ$ , respectively). Thus, a defect-free membrane seems more prone to electroporation than a membrane previously disturbed by the peptides' toxic activity.

Changes in the 3 $\times$ PC/3 $\times$ PG membrane properties upon interaction with LL-37 were quantitatively described by changes in its capacitance and changes in the resistance of the

resulting defects. The values of these parameters in a function of the potential applied to the electrode were determined by fitting an equivalent electrical circuit (EEC) to the experimental data shown in Figure 3.4-1 and Figure 3.4-2.

Figure 3.4-3 shows curves of the change in  $R_{\text{def}}$  and  $Q_m$  as a function of applied potential. The numerical values of the fit are shown in Table 3-5. In the absence of LL-37, the  $R_{\text{def}}$  value (curve 1 in Figure 3.4-3a) is significantly higher than that in the LL-37 presence (curves 2 and 3 in Figure 3.4-3a) for potentials  $E \geq -200$  mV. In this potential range, the 3×PC/3×PG membrane in the absence of LL-37 is a good insulator with very few defects. The membrane is lifted from the electrode surface at lower potentials, leading to lower membrane insulating properties, reflected by decreased resistance. The LL-37 presence at the 1:500 (curve 2) and 1:60 (curve 3) peptide-to-lipid molar ratio significantly decreases  $R_{\text{def}}$  because of the defects forming in the membrane. This high decrease in the  $R_{\text{def}}$  value indicates a significant change in the 3×PC/3×PG membrane insulating properties, showing that LL-37 interacts with the membrane and alters its structure. Surprisingly, the higher the LL-37 concentration, the lower is the  $R_{\text{def}}$  drop. This behavior is further discussed in the AFM results section (Section 3.4.3).

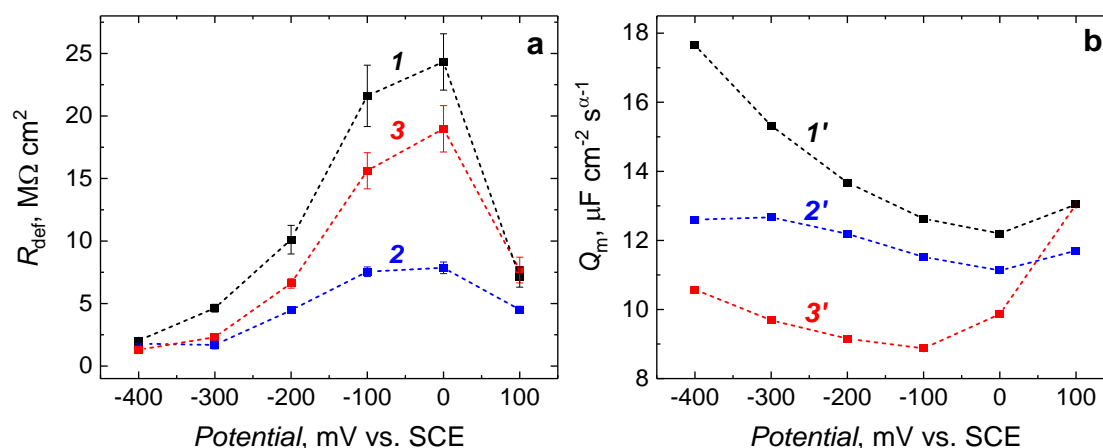


Figure 3.4-3. (a) Defects resistance ( $R_{\text{def}}$ ) and (b) membrane capacitance ( $Q_m$ ) calculated at different potentials for the Au(111)| $\beta$ -Tg|3×PC/3×PG membrane in the absence (curve 1 and 1') and in the presence of LL-37 (curves 2 and 2' as well as 3 and 3'). Curves 2 and 2', and 3 and 3' refer to the 1:500 and 1:60 peptide-to-lipid molar ratio, respectively.

The LL-37 presence at the 1:500 peptide-to-lipid molar ratio slightly changes the 3×PC/3×PG membrane capacitance (curve 2' in Figure 3.4-3b). In contrast, for a higher LL-37 concentration, a capacitance drop is more significant (curve 3' in Figure 3.4-3b). Capacitance is defined by the  $\epsilon/d$  ratio, where  $\epsilon$  is electric permittivity and  $d$  is the membrane thickness. Therefore, the 3×PC/3×PG membrane capacitance changes suggest that LL-37 interacts with the membrane by altering its structure, affecting electric permittivity and thickness. Thinning

of the bilayer and the formation of quasi-interdigitated phase in the LL-37 presence have already been reported for the DPPC/DPPG.<sup>169</sup> In some studies, undefined defects described as transient lesions causing transmembrane current fluctuations were found.<sup>165</sup> LL-37 oligomerizes in solution. It adsorbs on the membrane surface in the form of monomers or oligomers.<sup>174</sup> Particularly, it preserves an oligomeric form if adsorbed on zwitterionic phospholipids (e.g., PC) but dissociates into monomers if adsorbed on negatively charged phospholipids (e.g., PG).<sup>164, 174</sup> Therefore, both forms are expected to be present in the 3×PC/3×PG membrane. Adsorption of the LL-37 oligomers and monomers and their interactions with lipid headgroups would explain changes in the membrane capacitance.

Table 3-5. Values calculated for each component of the equivalent electrical circuit applied to model the 3×PC/3×PG bilayer in the absence and presence of LL-37.

Sample	$E$ , mV vs. SCE	$Q_m$ , $\mu\text{F cm}^{-2} \text{s}^{\alpha-1}$	$\alpha_m$	$R_{\text{def}}$ , $\text{M}\Omega \text{ cm}^2$	$Q_{\text{sp}}$ , $\mu\text{F cm}^{-2} \text{s}^{\alpha-1}$	$\alpha_{\text{sp}}$
3×PC/3×PG	100	13.04 ± 0.03	0.971 ± 0.001	7.12 ± 0.81	0.89 ± 0.19	0.51 ± 0.14
	0	12.20 ± 0.02	0.975 ± 0.001	24.32 ± 6.25	0.36 ± 0.09	0.80 ± 0.09
	-100	12.63 ± 0.02	0.976 ± 0.001	21.61 ± 2.46	0.51 ± 0.11	0.78 ± 0.07
	-200	13.68 ± 0.03	0.975 ± 0.001	10.11 ± 1.15	1.20 ± 0.56	0.77 ± 0.17
	-300	15.32 ± 0.05	0.972 ± 0.001	4.63 ± 0.31	2.52 ± 0.74	0.64 ± 0.11
	-400	17.65 ± 0.06	0.969 ± 0.001	2.03 ± 0.06	15.81 ± 4.99	0.70 ± 0.11
3×PC/3×PG + LL-37 (100:1)	100	11.70 ± 0.02	0.977 ± 0.001	4.51 ± 0.28	1.00 ± 0.08	0.48 ± 0.03
	0	11.13 ± 0.01	0.979 ± 0.001	7.86 ± 0.46	0.64 ± 0.04	0.58 ± 0.06
	-100	11.52 ± 0.01	0.979 ± 0.001	7.54 ± 0.38	0.99 ± 0.07	0.64 ± 0.06
	-200	12.19 ± 0.02	0.978 ± 0.001	4.45 ± 0.21	0.79 ± 0.09	0.45 ± 0.04
	-300	12.67 ± 0.03	0.967 ± 0.001	1.69 ± 0.31	1.87 ± 0.10	0.42 ± 0.18
	-400	12.60 ± 0.04	0.971 ± 0.001	1.79 ± 0.04	14.61 ± 3.11	0.38 ± 0.01
3×PC/3×PG + LL-37 (10:1)	100	13.04 ± 0.03	0.971 ± 0.001	7.68 ± 1.03	0.51 ± 0.15	0.02 ± 0.14
	0	9.86 ± 0.02	0.953 ± 0.001	18.97 ± 6.85	0.16 ± 0.07	0.24 ± 0.10
	-100	8.87 ± 0.01	0.963 ± 0.001	15.62 ± 1.45	0.24 ± 0.04	0.23 ± 0.10
	-200	9.13 ± 0.01	0.964 ± 0.001	6.61 ± 0.38	0.63 ± 0.09	0.25 ± 0.05
	-300	9.69 ± 0.02	0.965 ± 0.001	2.31 ± 0.11	2.92 ± 0.55	0.33 ± 0.09
	-400	10.58 ± 0.03	0.967 ± 0.001	1.30 ± 0.04	5.25 ± 0.41	0.34 ± 0.06

### 3.4.3. AFM imaging of model membrane disintegration upon LL-37 activity

A high-resolution AFM imaging was applied to unravel the LL-37 influence on the 3×PC/3×PG membrane deposited on mica by the SUVs deposition. The intact 3×PC/3×PG membrane comprises smooth phospholipid domains of  $5.71 \pm 0.06$ ,  $4.07 \pm 0.07$ , and  $3.38 \pm 0.04$  nm height (domain 1, 2, and 3, respectively, in Figure 3.4-4a and 4d). Taking into account the transition temperature and the acyl chains lengths of the individual phospholipids, one can assume that the domain 1, 2, and 3 corresponds to POPC/POPG (fluid phase), DPPC/DPPG (gel phase), and DMPC/DMPG (gel phase) phospholipids, respectively.<sup>182, 282</sup> Figure 3.4-4b and 4c show the AFM images of the membrane deposited from the solution containing the 3×PC/3×PG SUVs, in the LL-37 presence at the peptide-to-lipid molar ratio of 1:500 and 1:60, respectively.

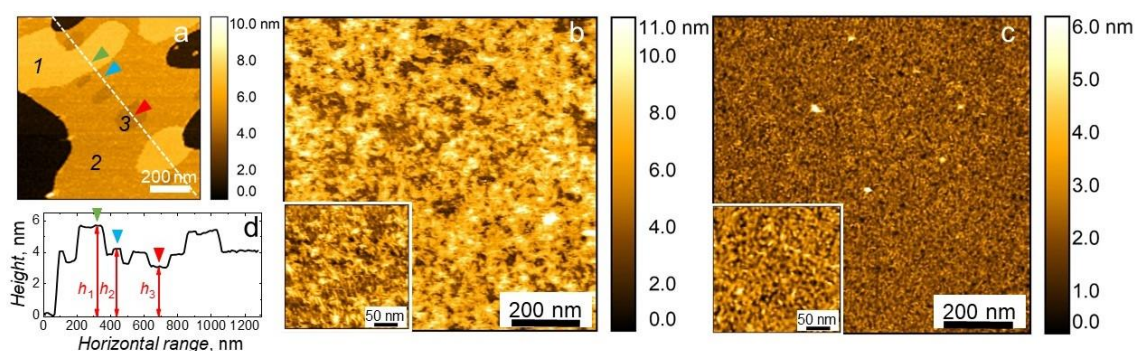


Figure 3.4-4. The AFM images of the 3×PC/3×PG membrane deposited on mica, in the LL-37 (a) absence and (b, c) presence, at (b) 1:500 and (c) 1:60 peptide-to-lipid molar ratio. Insets in Panels b and c show higher resolution images exhibiting the membrane morphology in more detail. (d) Corresponding cross-sectional profile along the dashed line in Panel a. Measured heights indicated in panel (d) are  $h_1 \approx 5.71$  nm,  $h_2 \approx 4.07$  nm, and  $h_3 \approx 3.38$  nm.

The presence of LL-37 significantly perturbed the 3×PC/3×PG membrane. The domains, visible in the membrane in the LL-37 absence, disappear in the LL-37 presence, and the membrane structure is destroyed (perforated). This result explains the change in the EIS phase angle at low frequencies, characteristic of the defects formation in the membrane (Figure 3.4-1b and 1c). For the low LL-37 concentration (Figure 3.4-4b), elongated grains or fibril-like structures are distinguished, while for the high LL-37 concentration (Figure 3.4-4c), a grain-like homogenous structure dominates. In both cases, defects are seen in the membrane. Moreover, the membrane shown in Figure 3.4-4c is more compact than that shown in Figure 3.4-4b. These results clarify why the  $R_{def}$  decreases more for the lower than higher LL-37 concentration (Figure 3.4-3a).

Force spectroscopy was applied to determine the thickness and mechanical properties of the 3×PC/3×PG membrane deposited on mica both in the absence and presence of LL-37.

The resulting F-D curves exhibit a discontinuity or a "jump". The width and breakthrough force at which the jump occurs provide information about the thickness and mechanical properties of the membrane. Figure 3.4-5a shows exemplary F-D curves in the LL-37 absence and presence (curves 1 and 2, respectively). Two jumps in the F-D curve are visible for the intact 3×PC/3×PG membrane, most likely, corresponding to the two leaflets of the membrane. That is caused by different forces acting upon the inner and outer leaflet, together with the presence of the Ca<sup>2+</sup> ions that might be trapped between the inner leaflet and solid substrate after bilayer deposition but removed from the outer leaflet during flushing of the membrane after deposition (imaging is performed in Milli-Q water). In contrast, only one jump of a much lower breakthrough force is observed for the 3×PC/3×PG membrane deposited on mica in the LL-37 presence at the 1:60 peptide-to-lipid molar ratio (curve 2 in Figure 3.4-5a). Importantly, no jump in the F-D curves for the 3×PC/3×PG membrane was observed in the presence of LL-37 at the 1:500 peptide-to-lipid molar ratio, suggesting that the membrane in Figure 3.4-4b does not form a compact layer. Figure 3.4-5(b, c, e) and Figure 3.4-5(d, f) show respective histograms of the breakthrough force and jump width for the 3×PC/3×PG membrane in the LL-37 absence and presence.

For the intact 3×PC/3×PG membrane, the breakthrough force distribution is bimodal with maxima at  $619 \pm 151$  and  $1113 \pm 177$  pN for the first jump and corresponding  $1402 \pm 445$  and  $1942 \pm 487$  pN for the second jump (Figure 3.4-5b and 5c). Similar behavior was observed for DMPC/egg-PC bilayers, resulting from the coexistence of phospholipids in the gel and liquid phases.<sup>55</sup> The AFM images confirm the presence of domains resulting from the membrane composed of different phospholipids (Figure 3.4-4a and Figure 3.4-6a). However, the breakthrough force distributions for the second jump are much broader, which can be explained by a strong influence of the substrate for the lower leaflet of the membrane.

The presented results show that the LL-37 activity decreases both the average jump width and the breakthrough force, indicating deposition of a thinner and softer membrane which is in line with the EIS results showing a decrease in the 3×PC/3×PG coated electrode capacitance because of the LL-37 treatment (Figure 3.4-3b).

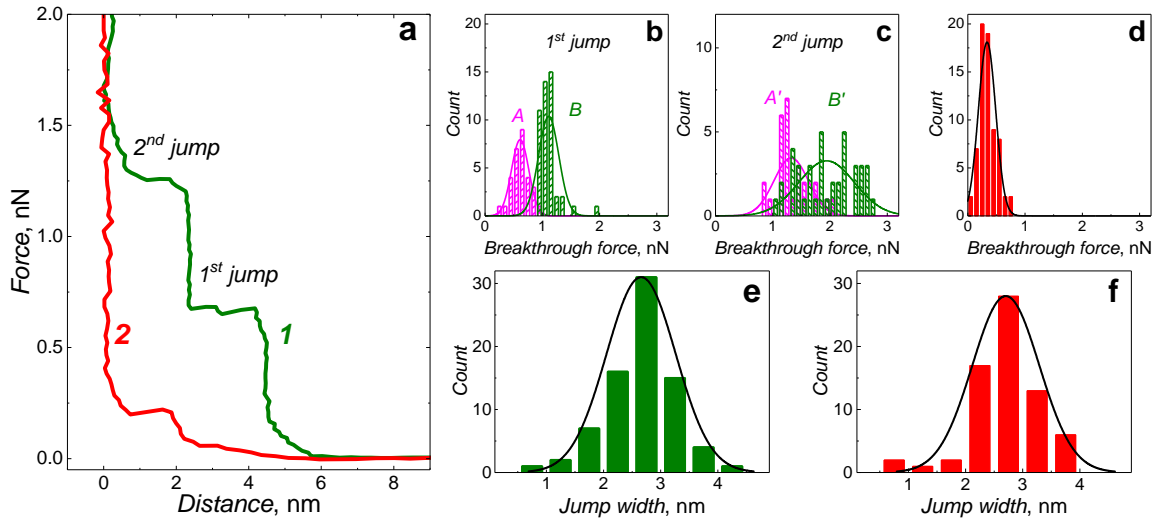


Figure 3.4-5. (a) Exemplary force-distance curves for the 3×PC/3×PG membrane in the LL-37 absence (curve 1) and presence (curve 2). (b-f) Histograms of the jump width and breakthrough forces of the F-D curves acquired for the 3×PC/3×PG membrane deposited on mica in the LL-37 (b, c, e) absence and (d, f) presence at the 1:60 peptide-to-lipid molar ratio. For the intact bilayer, breakthrough force distributions are bimodal as shown in Panels b, the 1<sup>st</sup> jump (A and B distribution), and c, the 2<sup>nd</sup> jump (A' and B' distributions).

Based on the jump widths and the breakthrough forces, the elastic deformation,  $\delta$ , and membrane thickness were roughly determined utilizing Eq. 3.4.3-1 derived from the Hertzian model.<sup>55, 288</sup>

$$\delta = \left( \frac{9F^2}{16RE^{*2}} \right)^{\frac{1}{3}} \quad 3.4.3-1$$

$F$  is the average breakthrough force in the above equation,  $R$  is the tip end radius, and  $E^*$  is the effective compression modulus determined from Young's modulus of a bilayer in a liquid crystalline state ( $66 \times 10^6 \text{ N m}^{-2}$ ).<sup>55, 209, 289</sup> Noticeably, this approach is instead a rough estimation suitable for comparative purposes only since the 3×PC/3×PG membrane is comprised of phospholipids of different phases, and the compression modulus used in the calculation may not be precise for the 3×PC/3×PG lipid mixture.

For the intact 3×PC/3×PG membrane, the elastic deformation was calculated as a sum of the first and second jump deformations and equaled to  $1.02 \pm 0.27$  and  $1.34 \pm 0.32$  nm for the A and B breakthrough force distribution, respectively, which corresponds to corrected bilayer thickness of  $3.94 \pm 0.79$  and  $3.82 \pm 0.71$  nm, respectively. For the 3×PC/3×PG membrane in the presence of LL-37 at the 1:60 peptide-to-lipid molar ratio, the elastic deformation is  $0.26 \pm 0.08$  nm, which is lower than that for the intact membrane, and the resulting corrected layer thickness is  $2.97 \pm 0.59$  nm. The values are summarized in Table 3-6. The calculated values are not the same as those determined through cross-sectional AFM profiles

because the applied effective compression modulus value is an estimation and is for the liquid crystalline phase.

Table 3-6. An average breakthrough force, jump width, elastic deformation, and corrected layer thickness for the 3×PC/3×PG membrane in the LL-37 absence and presence, calculated based on the averaged F-D curves-derived parameters. *A* and *A'*, and *B* and *B'* denote the breakthrough force distributions shown in Figure 3.4-5b and 5c.

Sample	Breakthrough force, pN	Jump width, nm	Elastic deformation, nm	Layer corrected thickness, nm
3×PC/3×PG ( <i>1<sup>st</sup> + 2<sup>nd</sup> jump</i> )	( <i>A</i> ) 619 ± 151 ( <i>A'</i> ) 1402 ± 445	2.92 ± 0.66	1.02 ± 0.27	3.94 ± 0.79
3×PC/3×PG ( <i>1<sup>st</sup> + 2<sup>nd</sup> jump</i> )	( <i>B</i> ) 1113 ± 177 ( <i>B'</i> ) 1942 ± 486	2.48 ± 0.50	1.34 ± 0.32	3.82 ± 0.71
3×PC/3×PG+ LL-37 (10:1 <i>m/m</i> )	338 ± 152	2.71 ± 0.59	0.26 ± 0.08	2.97 ± 0.59

Differences in the obtained EIS and AFM results for low and high LL-37 concentrations may arise from the increase in toxicity of LL-37 with the increase in its concentration. That is, at the 1:100 peptide-to-lipid ratio, LL-37 interacts with the SUVs to form lipid-peptide complexes leading to vesicle disruption, which occurs in the solution. As a result, lipid-peptide complexes are deposited on the mica in the form of a disordered layer with the structure shown in Figure 3.4-4b. For a higher LL-37 concentration, the complex formation is presumably more efficient, leading to the SUVs disruption and formation of smaller and more uniform globular objects. These objects, if adsorbed, then form a more compact layer shown in Figure 3.4-4c. LL-37 forms peptide-lipid complexes *in vivo*.<sup>171</sup> Oligomerization and then fibril-like structures formation by LL-37 dimers in the presence of lipids was confirmed by electron microscopy, using lipid vesicles (DOPC/DOPG, 3:7, at the 1:250 peptide-to-lipid molar ratio) incubated with gold-labeled S37C mutant peptides.<sup>171</sup> When LL-37 adsorbs on the membrane surface, it can polymerize and selectively extract bacterial lipids, destabilizing the membrane. Two lipid molecules per one monomeric LL-37 molecule can be extracted from a membrane.<sup>171</sup> The presence of fiber-like structures (Figure 3.4-4b) may trigger a local increase of the peptide concentration. As a result, the lipids extraction occurs from the membrane,<sup>181</sup> supporting the LL-37 mechanism of action that involves forming cytotoxic oligomers in the presence of negatively charged phospholipids (SOPC/POPG, 4:1 and 3:2)<sup>178</sup> or saturated phospholipids (DMPC/DMPG, 4:1).<sup>138</sup>

The membrane was first deposited on mica, and then LL-37 was added to the AFM cell to visualize *in situ* the interaction of LL-37 with the 3×PC/3×PG membrane. Figure 3.4-6

shows the AFM images, recorded at the same spot, for the 3×PC/3×PG membrane before (Figure 3.4-6a) and after (Figure 3.4-6b and 6c) injection of 1 μg of LL-37 into the AFM cell, which corresponds to the 1:500 peptide-to-lipid molar ratio. The 3×PC/3×PG membrane shown in Figure 3.4-6a consists of smooth and defect-free domains, similar to the membrane shown in Figure 3.4-4a. Dark areas represent the bare mica that was not covered by the bilayer.

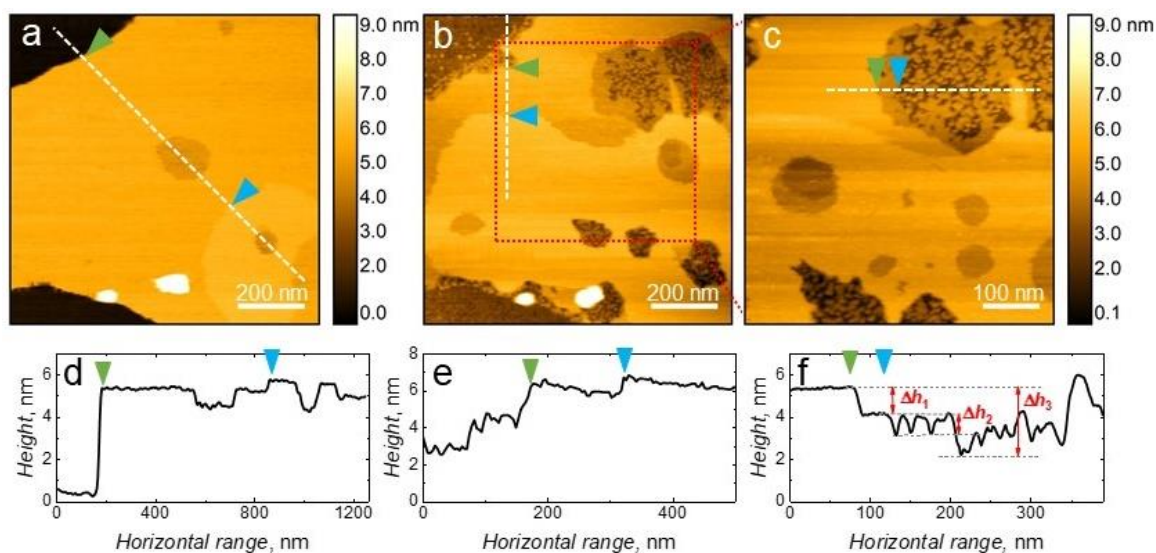


Figure 3.4-6. The AFM images of the 3×PC/3×PG membrane deposited on mica, (a) before and (b) 15 min, and (c) 65 min after 1-μg LL-37 injection into the AFM cell, which corresponds to the 1:500 peptide-to-lipid molar ratio. Corresponding cross-sectional profiles along dashed lines in the image (a), (b), and (c) are shown in (d), (e), and (f), respectively. Measured height differences indicated in panel (f) are  $\Delta h_1 \approx 1.3$  nm,  $\Delta h_2 \approx 1.0$  nm, and  $\Delta h_3 \approx 3.0$  nm.

At 15 min after the LL-37 addition, the AFM image changed significantly (Figure 3.4-6b). The mean surface roughness (calculated for 0.3 μm<sup>2</sup> area) of bare mica increased from 126 to 320 pm in the absence and presence of LL-37, respectively. In addition, an even more significant increase in the mean surface roughness, from 212 to 745 pm, was observed for the membrane within all three domains. That confirms observations regarding the LL-37 adsorption on the membrane surface (in a monomeric and or oligomeric form<sup>164, 174</sup>) and resulting changes in membrane morphology.

Three distinctive features are visible in the 3×PC/3×PG membrane after the LL-37 addition. First, within the same imaging spot, proportions of individual domains areas are changed compared to the intact membrane. It may result from selective interaction of LL-37 with phospholipids, changing domains size in the membrane. Second, all the membrane edges are broken so that their thickness becomes similar to that of the inner leaflet of the phospholipid membrane (i.e., membrane thinning occurs). Third, the membrane shows areas with visible globular objects with a diameter of 4.6 to 18.3 nm. These objects are relatively well separated and locally form discontinuous films close to the edges of the membrane.

At 65 min after the LL-37 addition, the membrane topography did not change significantly (Figure 3.4-6c). However, more areas appeared thinner, indicating that the membrane disruption proceeded. Figure 3.4-6f shows a cross-sectional profile taken along a severely disrupted area of the bilayer. It suggests that either the outer phospholipid leaflet is removed from the membrane first, followed by the changes in the inner leaflet, or a major bilayer thinning because of the presence of LL-37, occurs. The thinning effect, unraveled in the present work by EIS and AFM, might be explained as a major bilayer thinning or formation of a quasi-interdigitated bilayer phase for the fluid or gel phase, respectively, similarly as for the bilayer of DPPC/DPPG binary lipid mixture.<sup>169</sup>

The presence of the globular structures may indicate that LL-37 interacts with the 3×PC/3×PG membrane by the peptide-lipid complexes formation, in accord with the previous studies.<sup>138, 171</sup> These studies show that the LL-37 interacts with the microbial-like model membrane supported on mica by the peptide-lipid complex formation similar to the “carpet” dissolution process, and extraction of the lipids from the lipid matrix, which appears to prefer the bilayer edges or defects (Figure 3.4-6b and 6c). However, all these changes differ from those shown in Figure 3.4-4. Importantly, conditions of LL-37 interaction with phospholipids were not the same in each experiment. The difference in the observed changes can, most likely, be attributed to the presence of the solid substrate, which might constrain phospholipid fluidity and mobility. Moreover, the limited access of LL-37 to phospholipids is expected when the bilayer is adsorbed on the substrate surface (access only to the upper leaflet). Therefore, in the case shown in Figure 3.4-4, a mechanism in which LL-37 first interacts with phospholipid vesicles in solution, and then the modified parts of the film are deposited on the substrate seems more likely.

It was previously revealed by external reflection FTIR spectroscopy and NR experiments at the air-water interface<sup>172</sup> that the peptide insertion is favored at the locations of the saturated lipid tails, such as DPPG. Pore formation was found in bilayers composed of unsaturated phospholipids (DOPC/DOPG, 4:1), while membrane modulation by fibril-like peptide-lipid “superstructures” was found in bilayers comprised of saturated phospholipids (DMPC/DMPG, 4:1 and 3:2) at LL-37 concentrations between 1 to 20 μM.<sup>138</sup> Our AFM results suggest that in a multicomponent bilayer mixture of saturated and unsaturated phospholipids of different acyl chain lengths, detergent-like effect via a so-called “carpet” model dominates over pore-formation.

### 3.4.4. Changes in orientation and conformation of the phospholipid acyl chains in the presence of LL-37

The above discussed EIS and AFM results show that LL-37 strongly interacts with the 3×PC/3×PG membrane, leading to the disappearance of phospholipid domains and dramatic changes in the membrane morphology. However, the results of these measurements do not account for the effect of LL-37 on the orientation and conformation of the phospholipid molecules in the membrane. Therefore, PM-IRRAS under electrochemical conditions was herein utilized, which allowed determining potential-dependent changes in molecular orientation and conformation inside the membrane.<sup>103</sup>

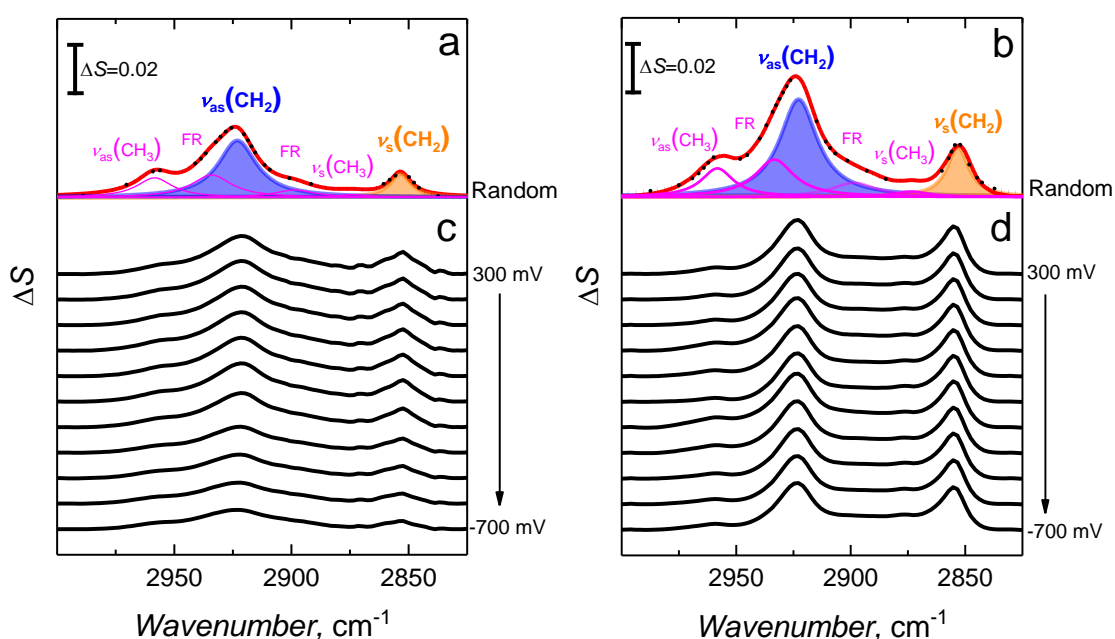


Figure 3.4-7. (a) and (b) PM-IRRAS spectra for the C–H stretching region of the 3×PC/3×PG acyl chains, in the absence and presence of LL-37 at the 1:500 peptide-to-lipid molar ratio, respectively, for selected potentials vs. Ag|AgCl in 0.1 M NaF in D<sub>2</sub>O. Corresponding spectra for randomly oriented molecules that mimic experimental conditions are shown in Panel c and d, respectively. They were calculated using the optical constants of cell materials.

Figure 3.4-7a and 7b show the PM-IRRAS spectra of the C–H stretching region of the 3×PC/3×PG membrane in the absence and presence of LL-37 at the peptide-to-lipid molar ratio of 1:500, respectively. The spectra were acquired at selected potentials, as shown. This spectral region allows determining conformational and orientational changes of the phospholipids in the 3×PC/3×PG membrane induced by membrane-active peptides. Each spectrum was deconvoluted into individual bands of symmetric and asymmetric stretches of the CH<sub>2</sub> and CH<sub>3</sub> moieties. Examples of deconvolution are presented in Figure 3.4-7a-7b. This

figure shows simulated spectra that mimic the studied system assuming a random orientation of the molecules in the LL-37 absence and presence, respectively. These spectra were calculated from optical constants (Figure 3.4-8) of the cell materials (including membrane). Table 3-7 lists all parameters used for the C–H stretching spectra simulation.

Table 3-7. Summary of the conditions used to obtain the PM-IRRA spectra for the 3×PC/3×PG bilayer supported on an Au(111)|β-Tg electrode in the absence and presence of LL-37 in the C–H stretching region.

Bilayer	Electrolyte solution composition	Angle of incidence, °	Thin cavity thickness, μm
3×PC/3×PG	0.1 M NaF in D <sub>2</sub> O	59	4.8
3×PC/3×PG + LL-37	0.1 M NaF in D <sub>2</sub> O	57	2.2

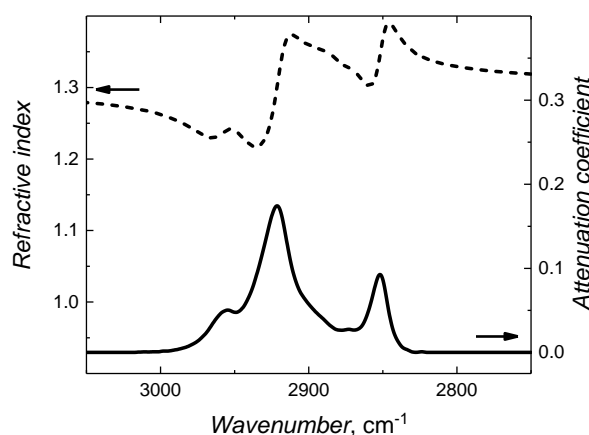


Figure 3.4-8. The optical constants for the C–H stretching region, determined from 3×PC/3×PG vesicles in D<sub>2</sub>O. The dashed curve indicates a refractive index, and the solid curve indicates an attenuation coefficient.

Of particular importance for our discussion is the symmetric CH<sub>2</sub> band ( $\nu_s(\text{CH}_2)$ ), a very sensitive indicator of conformational and orientational changes of acyl chains. Figure 3.4-9a and 9b show the changes of the  $\nu_s(\text{CH}_2)$  band position and FWHM as the function of potential for both experiments done in the LL-37 absence and presence.

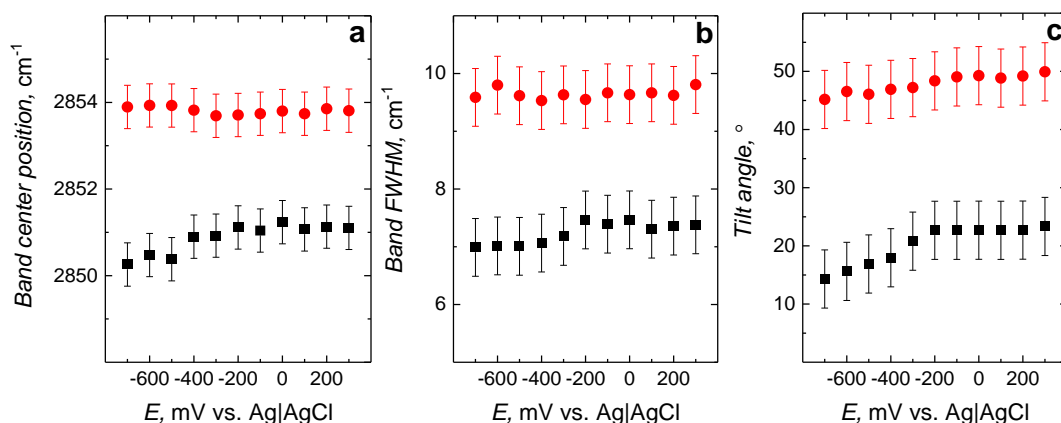


Figure 3.4-9. Changes in the (a)  $\nu_s(\text{CH}_2)$  band center position, (b)  $\nu_s(\text{CH}_2)$  band FWHM, and (c) lipid acyl chains average tilt angle (with respect to membrane normal) as a function of potential for the 3 $\times$ PC/3 $\times$ PG bilayer deposited on the Au(111)| $\beta$ -Tg electrode, in the (■) LL-37 absence and (●) presence, in the 0.1 M NaF in D<sub>2</sub>O solution.

The presence of LL-37 causes the  $\nu_s(\text{CH}_2)$  band to shift towards a higher wavenumber (Figure 3.4-9a) and to broaden (Figure 3.4-9b). Additionally, without the LL-37, the  $\nu_s(\text{CH}_2)$  band position shifts towards lower wavenumbers and narrows at potentials less than  $-200$  mV. In the presence of the LL-37, this behavior is not observed. The increase in the wavenumber and the broadening of the  $\nu_s(\text{CH}_2)$  band indicates a change in the conformation of the acyl chains from all-*trans* to increasingly more *gauche*. Therefore, it can be inferred that the interaction of LL-37 with the 3 $\times$ PC/3 $\times$ PG membrane causes conformational disordering of the all-*trans* acyl chains. These results are in good agreement with the behavior observed by AFM (Figure 3.4-4), i.e., without LL-37, the model membrane has no defects and clearly visible domains of different phospholipid compositions. The presence of LL-37 causes the complete disappearance of the separated domains and phospholipid disordering, resulting in acyl chain-melting phase transition.

The  $\nu_s(\text{CH}_2)$  and  $\nu_{as}(\text{CH}_2)$  bands were used to determine the changes in phospholipid orientation as a function of potential for the 3 $\times$ PC/3 $\times$ PG membranes without and with LL-37 (Figure 3.4-9c). Details on the procedure for the average tilt angle determination of the *trans* fragments of phospholipid acyl chains relative to the normal to the membrane plane can be found in Section 2.2.3.9 above. The arrangement of phospholipids in the membrane without LL-37 is typical of the Au(111)-supported bilayer. That is, in the potential range of 300 to  $-200$  mV, the *trans* fragments of phospholipid acyl chains are slightly tilted against the membrane normal. The tilt angle in this potential range is  $\sim 24^\circ$  and remains unchanged. The corresponding order parameter equals  $\sim 0.89$  (Table 3-8).

Table 3-8. Order parameters of the lipid acyl chain and corresponding tilt angles for the 3×PC/3×PG bilayer in the absence and presence of LL-37.

Potential, mV	Order parameter		Tilt angle, °	
	Without LL-37	With LL-37	Without LL-37	With LL-37
300	0.87	0.43	23	50
200	0.86	0.43	23	49
100	0.91	0.43	23	49
0	0.91	0.41	23	49
-100	0.90	0.44	23	49
-200	0.89	0.46	23	48
-300	0.91	0.41	23	47
-400	0.92	0.43	18	47
-500	0.94	0.45	17	46
-600	0.96	0.47	16	47
-700	0.98	0.48	14	45

The order parameter close to unity is characteristic of the closely packed lipid acyl chains. Below -200 mV, the tilt angle decreases due to the electro-dewetting and further lifting the bilayer from the electrode surface. This phenomenon is associated with the shift towards lower wavenumbers and narrowing the  $\nu_s(\text{CH}_2)$  band (Figure 3.4-9a and 9b). The presence of LL-37 significantly changes the value of the acyl chains tilt angle, which remains constant for the potentials  $\geq -200$  mV and equals to  $\sim 49^\circ$ , and then it slightly decreases to  $\sim 47^\circ$  for lower potentials (Figure 3.4-9). Such a significant change in the tilt angle, from  $\sim 24^\circ$  to  $\sim 49^\circ$ , indicates substantial reorganization in the phospholipid bilayer due to interaction with LL-37. This interaction is typical of antimicrobial peptides whose mechanism of action is described by the "carpet" model. Furthermore, an increase in the tilt angle of the molecules impacts the bilayer thickness, as was confirmed by direct AFM observations, and may explain a decrease in the membrane capacitance measured by EIS (Figure 3.4-3b). A decrease in capacitance and thickness implies a significant increase in the membrane electric permittivity. As a result of LL-37 activity, the order parameter decreases to an average value of 0.44, indicating an increase in disorder of the acyl chains. The closer the order parameter is to 0, the more disordered is the lipid film.

Our results show that the average tilt angle of acyl chains in the presence of LL-37 approaches  $55^\circ$ , which is characteristic of completely disordered molecules. This finding excludes the possibility of the formation of the barrel and toroidal pores. Instead, it indicates that LL-37 interacts with the 3×PC/3×PG membranes based on the "carpet" mechanism. According to this mechanism, the lipid molecules undergo significant reorientation leading to the dramatic increase in the tilt of their acyl chains.

### **3.4.5. Conclusions**

Studies of the AMPs' mechanism of activity towards biological membranes require the use of simplified models. However, this use may often lead to inconclusive results, as many of the AMPs exhibit different activity mechanisms towards membranes of different compositions and physicochemical properties. In biological systems, the variety of phospholipids comprising the membrane is much greater than in the simplified models. Here, the mechanism of the LL-37 peptide activity towards the multicomponent membrane model was studied. Based on the results, it can be concluded that the model membrane with 2:1 saturated to unsaturated lipids of different lengths is severely disrupted, and the "carpet" membrane dissolution dominates the disruption process. Furthermore, the EIS, AFM, and PM IRRAS results strongly support the membrane disruption through a non-pore, "carpet" mechanism followed by a detergent-like activity step involving fiber-like peptide-lipid interactions.

## CHAPTER 4: Research summary and future prospective

Planar lipid bilayers are a valuable platform for studying the activity of membrane-active molecules. In the present study, surface-sensitive techniques were applied to evaluate the physicochemical properties of bilayer lipid membranes in the presence of membrane-active molecules.

Mechanical properties of a single phospholipid bilayer in a ripple phase triggered by the presence of Tris were investigated, showing that the ripples are comprised of alternately arranged phospholipids in liquid and gel phases. To the best of my knowledge, this is the first time when ripple phase was nanomechanically characterized by atomic force microscopy.

Recently isolated BacSp222 bacteriocin and human cathelicidin LL-37 antimicrobial peptides interactions with multicomponent bilayer lipid membranes were investigated herein. BacSp222 was studied in a DMPC bilayer and LL-37 in a microbial-like model membrane.

When approaching orientational and conformational studies of BacSp222, little has been known about this peptide. This peptide was only recently isolated and known to be a bacteriocin type of peptide, presumably exhibiting a broad spectrum of activity. A supported DMPC bilayer, which is the most straightforward model membrane was used. BacSp222 exhibited a membrane-disrupting effect, suggesting highly non-specific peptide-lipid interaction, different from what is usually assigned for bacteriocins. BacSp222 exhibited potential-dependent behavior, being inserted into the bilayer at an average angle of  $30^\circ$  and then, below  $-600$  mV vs. Ag|AgCl, was surface-oriented.

Experimental results on the LL-37 mechanism of activity found in many studies seem contradictory. The present research was conducted with the assumption that pore formation is most expected for  $\alpha$ -helical, amphipathic LL-37. However, experiments refused to prove any signs of this behavior. Instead, a non-pore “carpet” model was proposed. The model membrane (2:1 saturated to unsaturated lipids) was severely disrupted up to a stage where the bilayer lost its cohesion. The average tilt angles of phospholipid acyl chains were close to that of entirely disordered molecules and the presence of LL-37 induced phospholipids chain melting.

EIS provides very characteristic spectra for well-defined transmembrane pores, especially if these would distribute homogeneously. The same applies to the AFM imaging – if there are any stable pore structures, like in barrel or toroidal pore models, they could be visualized. Instead, defects were imaged, sometimes called transient pores, i.e., not-well structurally defined local loss of lipid material. Therefore, my impression from reviewing available literature

was that the term “pore” might sometimes have been used misleadingly, not referring to a well-defined transmembrane peptide assembly but instead to a local loss in lipid material.

Surface-sensitive biophysical techniques were applied to evaluate the toxic activity of selected nitrophenols on model lung-like bilayer lipid membrane. Nitrophenols caused severe changes in a multicomponent bilayer, inducing defect formation and ion flux through the membrane. The research showed that nitrophenols interact with the membrane in a way that facilitates their insertion and, presumably, penetration through the membrane into the cell interior, which causes cell damage and promotes the development of various lung diseases.

Results presented in this thesis brought new insights into physicochemical changes induced in various membrane models by membrane-active molecules. Still, further research may be conducted to answer the following questions.

1. The mechanical response of the rippled bilayer surface was herein investigated with the greatest care to apply sufficient corrections which exclude the possibility of the substrate influence on the mechanical properties. However, the applied model may not be adequate to account for the particular geometry of the ripples and underlying water reservoir. Therefore, would the development of a finite thickness correction model accounting for that geometry and the presence of a water layer of different thicknesses underneath the bilayer change the interpretation of the bilayer's nano-mechanical response?
2. Bacteriocins are a group of AMPs that often interact with bacterial membranes via specific anchoring partners, e.g., nisin is binding to membranes via Lipid II. Even though BacSp222 exhibited possible non-selectivity towards membrane composition, would the BacSp222 activity be modulated by the presence of Lipid II or other membrane components?
3. There are many other components of air pollution of similar origin and presumably inducing similar effects as nitrophenols, including 4-nitrocatechol, 4-nitroguaiacol, 3-nitrosalicylic acid, pinic acid, pinonic acid, and 3-methyl-1,2,3-butanetricarboxylic acid. Do these pollutants exhibit pieces of evidence of destructive interaction with lipid bilayer membranes?
4. AMPs act differently in the presence of various phospholipids. What is the mechanism of LL-37 activity in membranes of different compositions, including phosphatidylserines and cardiolipins? Moreover, the orientation of LL-37 molecules was only investigated in this study by AFM. Thus what is the orientation of these molecules in the bilayer lipid membrane determined by PM-IRRAS?

## References

1. CDC. Antibiotic resistance threats in the United States, 2019. Atlanta, GA: U.S. Department of Health and Human Services, CDC; 2019
2. World Health Organization. Antibiotic resistance. 2020; Available from: <https://www.who.int>.
3. Last, N.B. et al., A common landscape for membrane-active peptides, *Protein Sci.*, 22, 2013, 870-882.
4. Zasloff, M., Antimicrobial peptides of multicellular organisms, *Nature*, 415, 2002, 389-395.
5. Jenssen, H. et al., Peptide antimicrobial agents, *Clin. Microbiol. Rev.*, 19, 2006, 491-511.
6. Bechinger, B. and Lohner, K., Detergent-like actions of linear amphipathic cationic antimicrobial peptides, *Biochim. Biophys. Acta Biomembr.*, 1758, 2006, 1529-1539.
7. Hancock, R.E.W., Cationic peptides: effectors in innate immunity and novel antimicrobials, *Lancet. Infect. Dis.*, 1, 2001, 156-164.
8. Haney, E.F. and Hancock, R.E.W., Peptide design for antimicrobial and immunomodulatory applications, *Peptide Sci.*, 100, 2013, 572-583.
9. Hancock, R.E.W. and Sahl, H.G., Antimicrobial and host-defense peptides as new anti-infective therapeutic strategies, *Nat. Biotechnol.*, 24, 2006, 1551-1557.
10. Thomas, S. et al., CAMP: a useful resource for research on antimicrobial peptides, *Nucleic Acids Res.*, 38, 2010, D774-80.
11. Shai, Y., Mode of action of membrane active antimicrobial peptides, *Biopolymers*, 66, 2002, 236-248.
12. Magana, M. et al., The value of antimicrobial peptides in the age of resistance, *Lancet Infect. Dis.*, 20, 2020, e216-e230.
13. Hale, J.D. and Hancock, R.E., Alternative mechanisms of action of cationic antimicrobial peptides on bacteria, *Expert Rev. Anti-Infect. Ther.*, 5, 2007, 951-959.
14. Nguyen, L.T. et al., The expanding scope of antimicrobial peptide structures and their modes of action, *Trends Biotechnol.*, 29, 2011, 464-472.
15. Wang, Z. and Wang, G., APD: The Antimicrobial Peptide Database, *Nucleic Acids Res.*, 32, 2004, D590-2.
16. Pirtskhalava, M. et al., DBAASP v.2: an enhanced database of structure and antimicrobial/cytotoxic activity of natural and synthetic peptides, *Nucleic Acids Res.*, 44, 2016, D1104-D1112.
17. Kang, X. et al., DRAMP 2.0, an updated data repository of antimicrobial peptides, *Sci. Data*, 6, 2019.

18. Ye, G. et al., LAMP2: a major update of the database linking antimicrobial peptides, *Database*, 2020, 2020.
19. Teixeira, V. et al., Role of lipids in the interaction of antimicrobial peptides with membranes, *Prog. Lipid Res.*, 51, 2012, 149-177.
20. Epanand, R.M. and Epanand, R.F., Bacterial membrane lipids in the action of antimicrobial agents, *J. Pep. Sci.*, 17, 2011, 298-305.
21. Su, Z. et al., Electrode-supported biomimetic membranes: An electrochemical and surface science approach for characterizing biological cell membranes, *Curr. Opin. Electrochem.*, 12, 2018, 60-72.
22. Gorter, E. and Grendel, F., On bimolecular layers of lipoids on the chromocytes of the blood, *J. Exp. Med.*, 41, 1925, 439-443.
23. Singer, S.J. and Nicolson, G.L., The Fluid Mosaic Model of the Structure of Cell Membranes, *Science*, 175, 1972, 720-731.
24. Nicolson, G.L., The Fluid—Mosaic Model of Membrane Structure: Still relevant to understanding the structure, function and dynamics of biological membranes after more than 40 years, *Biochim. Biophys. Acta Biomembr.*, 1838, 2014, 1451-1466.
25. Vereb, G. et al., Dynamic, yet structured: The cell membrane three decades after the Singer–Nicolson model, *Proc. Natl. Acad. Sci. U.S.A.*, 100, 2003, 8053-8058.
26. Simons, K. and Toomre, D., Lipid rafts and signal transduction, *Nat. Rev. Mol. Cell Biol.*, 1, 2000, 31-39.
27. Hianik, T., Biological Membranes and Membrane Mimics, in *Bioelectrochemistry*, P.N. Bartlett, Editor. 2008, John Wiley & Sons, Ltd. p. 87-156.
28. Vanderkooi, G. and Green, D.E., Biological Membrane Structure, I. The Protein Crystal Model for Membranes, *Proc. Natl. Acad. Sci. U. S. A.*, 66, 1970, 615-621.
29. Huang, Y.B. et al., Alpha-helical cationic antimicrobial peptides: relationships of structure and function, *Protein Cell*, 1, 2010, 143-152.
30. Sackmann, E., Chapter 1 Biological membranes architecture and function, in *Handbook of Biological Physics*, R. Lipowsky and E. Sackmann, Editors. 1995, North-Holland. p. 1-63.
31. Mueller, P. et al., Reconstitution of Cell Membrane Structure in vitro and its Transformation into an Excitable System, *Nature*, 194, 1962, 979-980.
32. Bangham, A.D. et al., Diffusion of univalent ions across the lamellae of swollen phospholipids, *J. Mol. Biol.*, 13, 1965, 238-IN27.
33. McConnell, H.M. et al., Supported planar membranes in studies of cell-cell recognition in the immune system, *Biochim. Biophys. Acta*, 864, 1986, 95-106.
34. Czogalla, A. et al., Validity and applicability of membrane model systems for studying interactions of peripheral membrane proteins with lipids, *Biochim. Biophys. Acta Mol. Cell Biol. Lipids*, 1841, 2014, 1049-1059.

35. Koynova, R. and Tenchov, B., Phase Transitions and Phase Behavior of Lipids, in Encyclopedia of Biophysics, G.C.K. Roberts, Editor. 2013, Springer Berlin Heidelberg: Berlin, Heidelberg. p. 1841-1854.
36. Simons, K. and Ikonen, E., Functional rafts in cell membranes, *Nature*, 387, 1997, 569-72.
37. Volinsky, R. et al., Investigations of antimicrobial peptides in planar film systems, *Biochim. Biophys. Acta Biomembr.*, 1758, 2006, 1393-1407.
38. Sackmann, E., Supported membranes: scientific and practical applications, *Science*, 271, 1996, 43-48.
39. Castellana, E.T. and Cremer, P.S., Solid supported lipid bilayers: From biophysical studies to sensor design, *Surf. Sci. Rep.*, 61, 2006, 429-444.
40. Knoll, W. et al., Tethered bimolecular lipid membranes—A novel model membrane platform, *Electrochim. Acta*, 53, 2008, 6680-6689.
41. Lipkowski, J., Biomimetic membrane supported at a metal electrode surface: a molecular view, in Advances in Planar Lipid Bilayers and Liposomes, A. Iglič and C.V. Kulkarni, Editors. 2014, Academic Press. p. 1-49.
42. Lipkowski, J., Biomimetics: a new research opportunity for surface electrochemistry, *J. Solid State Electrochem.*, 2020.
43. Uchida, T. et al., SEIRAS studies of water structure at the gold electrode surface in the presence of supported lipid bilayer, *J. Electroanal. Chem.*, 716, 2014, 112-119.
44. Penkauskas, T. and Preta, G., Biological applications of tethered bilayer lipid membranes, *Biochimie*, 157, 2019, 131-141.
45. Sinner, E.K. and Knoll, W., Functional tethered membranes, *Curr. Opin. Chem. Biol.*, 5, 2001, 705-711.
46. Munro, J.C. and Frank, C.W., Adsorption of disulfide-modified polyacrylamides to gold and silver surfaces as cushions for polymer-supported lipid bilayers, *Polymer*, 44, 2003, 6335-6344.
47. Ruiz, M., Detailed diagram of lipid bilayer cell membrane. 2017, Wikimedia Commons.
48. Kycia, A.H. et al., Atomic force microscopy studies of a floating-bilayer lipid membrane on an Au(111) surface modified with a hydrophilic monolayer, *Langmuir*, 27, 2011, 10867-10877.
49. Kycia, A.H. et al., Electrochemical and STM Studies of 1-Thio- $\beta$ -D-glucose Self-Assembled on an Au(111) Electrode Surface, *Langmuir*, 27, 2011, 13383-13389.
50. Su, Z. et al., Water Structure in the Submembrane Region of a Floating Lipid Bilayer: The Effect of an Ion Channel Formation and the Channel Blocker, *Langmuir*, 36, 2020, 409-418.
51. Smith, S.R. et al., Characterization of a Self-Assembled Monolayer of 1-Thio- $\beta$ -d-Glucose with Electrochemical Surface Enhanced Raman Spectroscopy Using a Nanoparticle Modified Gold Electrode, *Langmuir*, 31, 2015, 10076-10086.

52. Su, Z.F. et al., Ionophore properties of valinomycin in the model bilayer lipid membrane 1. Selectivity towards a cation, *J. Solid State Electrochem.*, 24, 2020, 3125-3134.
53. Su, Z. et al., Ion transport mechanism in gramicidin A channels formed in floating bilayer lipid membranes supported on gold electrodes, *Electrochim. Acta*, 375, 2021, 137892.
54. Abbasi, F. et al., Direct visualization of alamethicin ion pores formed in a floating phospholipid membrane supported on a gold electrode surface, *Electrochim. Acta*, 267, 2018, 195-205.
55. Abbasi, F. et al., Pore forming properties of alamethicin in negatively charged floating bilayer lipid membranes supported on gold electrodes, *Langmuir*, 34, 2018, 13754-13765.
56. Su, Z. et al., In situ electrochemical and PM-IRRAS studies of colicin E1 ion channels in the floating bilayer lipid membrane, *Langmuir*, 35, 2019, 8452-8459.
57. Mrdenovic, D. et al., Alzheimer's disease-related amyloid  $\beta$  peptide causes structural disordering of lipids and changes the electric properties of a floating bilayer lipid membrane, *Nanoscale Adv.*, 2020.
58. Mrdenovic, D. et al., Inhibition of Amyloid  $\beta$ -Induced Lipid Membrane Permeation and Amyloid  $\beta$  Aggregation by K162, *ACS Chem. Neurosci.*, 2021.
59. Bard, A.J., *Electrochemical dictionary*. 2008: Springer.
60. Kycia, A.H. et al., In Situ PM-IRRAS Studies of Biomimetic Membranes Supported at Gold Electrode Surfaces, in *Vibrational Spectroscopy at Electrified Interfaces*. 2013, John Wiley & Sons, Inc. p. 345-417.
61. Tsong, T.Y. and Astumian, R.D., Electroconformational Coupling: How Membrane-Bound ATPase Transduces Energy from Dynamic Electric Fields, *Annu. Rev. Physiol.*, 50, 1988, 273-290.
62. Clarke, R.J., The dipole potential of phospholipid membranes and methods for its detection, *Adv. Colloid Interface Sci.*, 89-90, 2001, 263-281.
63. Huang, W. and Levitt, D.G., Theoretical calculation of the dielectric constant of a bilayer membrane, *Biophys. J.*, 17, 1977, 111-128.
64. Su, Z. et al., Measurements of the Potentials of Zero Free Charge and Zero Total Charge for 1-thio- $\beta$ -D-glucose and DPTL Modified Au(111) Surface in Different Electrolyte Solutions, *Z. Phys. Chem.*, 226, 2012, 995.
65. Garcia-Manyes, S. et al., Effect of Ion-Binding and Chemical Phospholipid Structure on the Nanomechanics of Lipid Bilayers Studied by Force Spectroscopy, *Biophys. J.*, 89, 2005, 1812-1826.
66. Garcia-Manyes, S. et al., Effect of Temperature on the Nanomechanics of Lipid Bilayers Studied by Force Spectroscopy, *Biophys. J.*, 89, 2005, 4261-4274.
67. Garcia-Manyes, S. et al., Nanomechanics of lipid bilayers: heads or tails?, *J. Am. Chem. Soc.*, 132, 2010, 12874-12886.

68. Butt, H.-J. et al., Force measurements with the atomic force microscope: Technique, interpretation and applications, *Surf. Sci. Rep.*, 59, 2005, 1-152.
69. Butt, H.-J. and Franz, V., Rupture of molecular thin films observed in atomic force microscopy. I. Theory, *Phys. Rev. E*, 66, 2002, 031601.
70. Melcrová, A. et al., Concurrent Compression of Phospholipid Membranes by Calcium and Cholesterol, *Langmuir*, 35, 2019, 11358-11368.
71. Garcia-Manyes, S. et al., Effect of pH and ionic strength on phospholipid nanomechanics and on deposition process onto hydrophilic surfaces measured by AFM, *Electrochim. Acta*, 51, 2006, 5029-5036.
72. Picas, L. et al., Direct Measurement of the Mechanical Properties of Lipid Phases in Supported Bilayers, *Biophys. J.*, 102, 2012, L01-L03.
73. Dimitriadis, E.K. et al., Issues concerning the measurement of elastic properties at microscopic scales with the AFM, *Biophys. J.*, 82, 2002, 56a-56a.
74. Dimitriadis, E.K. et al., Determination of elastic moduli of thin layers of soft material using the atomic force microscope, *Biophys. J.*, 82, 2002, 2798-2810.
75. Koynova, R. and Caffrey, M., Phases and phase transitions of the phosphatidylcholines, *Biochim. Biophys. Acta Rev. Biomembr.*, 1376, 1998, 91-145.
76. Levine, Y.K. et al., Multilayer of phospholipid bimolecular leaflets, *Nature*, 220, 1968, 577-578.
77. Tamm, L.K. and McConnell, H.M., Supported phospholipid bilayers., *Biophys. J.*, 47, 1985, 105-113.
78. Mitchell, M.L. and Dluhy, R.A., In situ FT-IR investigation of phospholipid monolayer phase transitions at the air-water interface, *J. Am. Chem. Soc.*, 110, 1988, 712-718.
79. Nullmeier, M. et al., Interaction of siglec protein with glycolipids in a lipid bilayer deposited on a gold electrode surface, *J. Electroanal. Chem.*, 649, 2010, 177-188.
80. Juhaniwicz-Dębińska, J. et al., Diverse effect of cationic lipopeptide on negatively charged and neutral lipid bilayers supported on gold electrodes, *Electrochim. Acta*, 298, 2019, 735-744.
81. Garcia-Araez, N. et al., Layer-by-Layer PM-IRRAS Characterization of DMPC Bilayers Deposited on an Au(111) Electrode Surface, *Langmuir*, 22, 2006, 10365-10371.
82. Barenholz, Y. et al., A simple method for the preparation of homogeneous phospholipid vesicles, *Biochemistry*, 16, 1977, 2806-2810.
83. Zawisza, I. et al., Potential-driven structural changes in Langmuir-Blodgett DMPC bilayers determined by in situ spectroelectrochemical PM IRRAS, *Langmuir*, 23, 2007, 5180-5194.
84. Reviakine, I. and Brisson, A., Formation of supported phospholipid bilayers from unilamellar vesicles investigated by atomic force microscopy, *Langmuir*, 16, 2000, 1806-1815.

85. Richter, R.P. et al., Formation of Solid-Supported Lipid Bilayers: An Integrated View, *Langmuir*, 22, 2006, 3497-3505.
86. Weirich, K.L. et al., Bilayer Edges Catalyze Supported Lipid Bilayer Formation, *Biophys. J.*, 98, 2010, 85-92.
87. Richter, R.P. and Brisson, A.R., Following the formation of supported lipid bilayers on mica: a study combining AFM, QCM-D, and ellipsometry, *Biophys. J.*, 88, 2005, 3422-3433.
88. Åkesson, A. et al., Composition and structure of mixed phospholipid supported bilayers formed by POPC and DPPC, *Soft Matter*, 8, 2012, 5658-5665.
89. Reimhult, E. et al., A Multitechnique Study of Liposome Adsorption on Au and Lipid Bilayer Formation on SiO<sub>2</sub>, *Langmuir*, 22, 2006, 3313-3319.
90. Pawłowski, J. et al., Mechanism of lipid vesicles spreading and bilayer formation on an Au(111) surface, *Langmuir*, 31, 2015, 11012-11019.
91. Steinem, C. and Janshoff, A., Multicomponent membranes on solid substrates: Interfaces for protein binding, *Curr. Opin. Colloid Interface Sci.*, 15, 2010, 479-488.
92. Kelley, E.G. et al., Scaling relationships for the elastic moduli and viscosity of mixed lipid membranes, *Proc. Natl. Acad. Sci. U. S. A.*, 117, 2020, 23365-23373.
93. Kučerka, N. et al., Fluid phase lipid areas and bilayer thicknesses of commonly used phosphatidylcholines as a function of temperature, *Biochim. Biophys. Acta*, 1808, 2011, 2761-71.
94. Kučerka, N. et al., Structural Significance of Lipid Diversity as Studied by Small Angle Neutron and X-ray Scattering, *Membranes*, 5, 2015, 454-472.
95. Nagle, J.F. and Tristram-Nagle, S., Structure of lipid bilayers, *Biochim. Biophys. Acta Rev. Biomembr.*, 1469, 2000, 159-195.
96. Sochacki, K.A. et al., Real-time attack on single Escherichia coli cells by the human antimicrobial peptide LL-37, *Proc. Natl. Acad. Sci. U. S. A.*, 108, 2011, E77-E81.
97. Van Der Kraan, M.I.A. et al., Ultrastructural effects of antimicrobial peptides from bovine lactoferrin on the membranes of Candida albicans and Escherichia coli, *Peptides*, 26, 2005, 1537-1542.
98. Epand, R.M. and Epand, R.F., Liposomes as Models for Antimicrobial Peptides, in *Meth. Enzymol.* 2003, Academic Press. p. 124-133.
99. Bechinger, B. and Salnikov, E.S., The membrane interactions of antimicrobial peptides revealed by solid-state NMR spectroscopy, *Chem. Phys. Lipids*, 165, 2012, 282-301.
100. Tristram-Nagle, S., Use of X-Ray and Neutron Scattering Methods with Volume Measurements to Determine Lipid Bilayer Structure and Number of Water Molecules/Lipid. 2015, Springer International Publishing. p. 17-43.
101. Pabst, G. et al., Applications of neutron and X-ray scattering to the study of biologically relevant model membranes, *Chem. Phys. Lipids*, 163, 2010, 460-479.

102. Nagle, J.F. et al., Structure of gel phase DPPC determined by X-ray diffraction, *Chem. Phys. Lipids*, 218, 2019, 168-177.
103. Brand, I., Application of Infrared Spectroscopy for Structural Analysis of Planar Lipid Bilayers under Electrochemical Control, in *Advances in Planar Lipid Bilayers and Liposomes*. 2013. p. 21-62.
104. Tamm, L.K. and Tatulian, S.A., Infrared Spectroscopy of Proteins and Peptides in Lipid Bilayers, *Q. Rev. Biophys.*, 30, 1997, 365-429.
105. Zamlynny, V. and Lipkowski, J., Quantitative SNIFTIRS and PM-IRRAS of organic molecules at electrode surfaces, in *Diffraction and Spectroscopic Methods in Electrochemistry*, R.C. Alkire, et al., Editors. 2006, WILEY-VCH Verlag GmbH & Co. KGaA, Weinheim, Germany. p. 315-376.
106. Bin, X. and Lipkowski, J., Electrochemical and PM-IRRAS studies of the effect of cholesterol on the properties of the headgroup region of a DMPC bilayer supported at an Au(111) electrode, *J. Phys. Chem. B*, 110, 2006, 26430-26441.
107. Bin, X. et al., Electrochemical and PM-IRRAS studies of the effect of the static electric field on the structure of the DMPC bilayer supported at an Au(111) electrode surface, *Langmuir*, 21, 2005, 330-347.
108. Brosseau, C.L. et al., Electrochemical and PM-IRRAS a Glycolipid-Containing Biomimetic Membrane Prepared Using Langmuir-Blodgett/Langmuir-Schaefer Deposition, *Langmuir*, 24, 2008, 13058-13067.
109. Horswell, S.L. et al., Electrochemical and PM-IRRAS studies of potential controlled transformations of phospholipid layers on Au(111) electrodes, *Faraday Discuss.*, 121, 2002, 405-422.
110. Matyszewska, D. et al., PM-IRRAS Studies of DMPC Bilayers Supported on Au(111) Electrodes Modified with Hydrophilic Monolayers of Thioglucose, *Langmuir*, 32, 2016, 1791-1798.
111. Hillman, A.R. et al., Structure and dynamics of phospholipid bilayer films under electrochemical control, *Faraday Discuss.*, 145, 2010, 357-379.
112. Zaborowska, M. et al., Structural modifications of lipid membranes exposed to statins – Langmuir monolayer and PM-IRRAS study, *J. Mol. Liq.*, 2020, 113570.
113. Su, Z. et al., In situ electrochemical and PM-IRRAS studies of alamethicin ion channel formation in model phospholipid bilayers, *J. Electroanal. Chem.*, 819, 2018, 251-259.
114. Su, Z. et al., EIS and PM-IRRAS studies of alamethicin ion channels in a tethered lipid bilayer, *J. Electroanal. Chem.*, 812, 2018, 213-220.
115. Leitch, J.J. et al., Electrochemical and PM-IRRAS Characterization of Cholera Toxin Binding at a Model Biological Membrane, *Langmuir*, 29, 2013, 965-976.
116. Lipkowski, J., Building biomimetic membrane at a gold electrode surface, *Phys. Chem. Chem. Phys.*, 12, 2010, 13874-13887.

117. Su, Z. et al., Gramicidin A ion channel formation in model phospholipid bilayers tethered to gold (111) electrode surfaces, *Electrochim. Acta*, 243, 2017, 364-373.
118. Steinem, C. et al., Impedance analysis of ion transport through gramicidin channels incorporated in solid supported lipid bilayers, *Bioelectrochem. Bioenerg.*, 42, 1997, 213-220.
119. Steinem, C. et al., Impedance analysis of supported lipid bilayer membranes: a scrutiny of different preparation techniques, *Biochim. Biophys. Acta Biomembr.*, 1279, 1996, 169-180.
120. Valincius, G. et al., Electrochemical impedance spectroscopy of tethered bilayer membranes, *Langmuir*, 28, 2012, 977-990.
121. Valincius, G. and Mickevicius, M., Tethered phospholipid bilayer membranes: an interpretation of the electrochemical impedance response, in *Advances in Planar Lipid Bilayers and Liposomes*, A. Iglič, C.V. Kulkarni, and M. Rappolt, Editors. 2015, Academic Press. p. 27-61.
122. Su, Z. et al., How Valinomycin Ionophores Enter and Transport K<sup>+</sup> across Model Lipid Bilayer Membranes, *Langmuir*, 35, 2019, 16935-16943.
123. Juhaniwicz-Dębińska, J. et al., Physicochemical Characterization of Daptomycin Interaction with Negatively Charged Lipid Membranes, *Langmuir*, 36, 2020, 5324-5335.
124. Su, Z. et al., Role of transmembrane potential and defects on the permeabilization of lipid bilayers by alamethicin, an ion-channel-forming peptide, *Langmuir*, 34, 2018, 6249-6260.
125. Su, Z. et al., Mechanisms of alamethicin ion channel inhibition by amiloride in zwitterionic tethered lipid bilayers, *J. Electroanal. Chem.*, 848, 2019.
126. Vockenroth, I.K. et al., Stable insulating tethered bilayer lipid membranes, *Biointerphases*, 3, 2008, FA68-FA73.
127. Leitch, J. et al., In Situ PM-IRRAS Studies of an Archaea Analogue Thiolipid Assembled on a Au(111) Electrode Surface, *Langmuir*, 25, 2009, 10354-10363.
128. Juhaniwicz, J. et al., Interaction of Cecropin B with Zwitterionic and Negatively Charged Lipid Bilayers Immobilized at Gold Electrode Surface, *Electrochim. Acta*, 204, 2016, 206-217.
129. Sek, S. et al., Molecular Resolution Imaging of an Antibiotic Peptide in a Lipid Matrix, *J. Am. Chem. Soc.*, 131, 2009, 6439-6444.
130. Pieta, P. et al., Direct visualization of the alamethicin pore formed in a planar phospholipid matrix, *Proc. Natl. Acad. Sci. U. S. A.*, 109, 2012, 21223-21227.
131. Heath, G.R. et al., Visualization of diffusion limited antimicrobial peptide attack on supported lipid membranes, *Soft Matter*, 14, 2018, 6146-6154.
132. Hammond, K. et al., Atomic force microscopy to elucidate how peptides disrupt membranes, *Biochim. Biophys. Acta Biomembr.*, 1863, 2021, 183447.
133. Juhaniwicz-Dębińska, J. et al., Lipopeptide-induced changes in permeability of solid supported bilayers composed of bacterial membrane lipids, *J. Electroanal. Chem.*, 812, 2018, 227-234.

134. Juhaniwicz, J. and Sek, S., Interaction of Melittin with Negatively Charged Lipid Bilayers Supported on Gold Electrodes, *Electrochim. Acta*, 197, 2016, 336-343.
135. Smetanin, M. et al., Molecular resolution visualization of a pore formed by trichogin, an antimicrobial peptide, in a phospholipid matrix, *Biochim. Biophys. Acta Biomembr.*, 1838, 2014, 3130-3136.
136. Durr, U.H. et al., LL-37, the only human member of the cathelicidin family of antimicrobial peptides, *Biochim. Biophys. Acta*, 1758, 2006, 1408-25.
137. Johansson, J. et al., Conformation-dependent antibacterial activity of the naturally occurring human peptide LL-37, *J. Biol. Chem.*, 273, 1998, 3718-3724.
138. Shahmiri, M. et al., Membrane Core-Specific Antimicrobial Action of Cathelicidin LL-37 Peptide Switches Between Pore and Nanofibre Formation, *Sci. Rep.*, 6, 2016, 38184.
139. Wang, G., Structures of Human Host Defense Cathelicidin LL-37 and Its Smallest Antimicrobial Peptide KR-12 in Lipid Micelles, *J. Biol. Chem.*, 283, 2008, 32637-32643.
140. Burton, M.F. and Steel, P.G., The chemistry and biology of LL-37, *Nat. Prod. Rep.*, 26, 2009, 1572-1584.
141. Agerberth, B. et al., FALL-39, a putative human peptide antibiotic, is cysteine-free and expressed in bone marrow and testis, *Proc. Natl. Acad. Sci. U. S. A.*, 92, 1995, 195-199.
142. Cowland, J.B. et al., hCAP-18, a cathelin/pro-bactenecin-like protein of human neutrophil specific granules, *FEBS Letters*, 368, 1995, 173-176.
143. Larrick, J.W. et al., Complementary DNA sequence of rabbit CAP18—A unique lipopolysaccharide binding protein, *Biochem. Biophys. Res. Comm.*, 179, 1991, 170-175.
144. Méndez-Samperio, P., The human cathelicidin hCAP18/LL-37: A multifunctional peptide involved in mycobacterial infections, *Peptides*, 31, 2010, 1791-1798.
145. Travis, S.M. et al., Bactericidal Activity of Mammalian Cathelicidin-Derived Peptides, *Infect. Immun.*, 68, 2000, 2748-2755.
146. Barns, K.J. and Weisshaar, J.C., Real-time attack of LL-37 on single *Bacillus subtilis* cells, *Biochim. Biophys. Acta Biomembr.*, 1828, 2013, 1511-1520.
147. Smeianov, V. et al., Activity of cecropin P1 and FA-LL-37 against urogenital microflora, *Microb. Infect.*, 2, 2000, 773-777.
148. Scheenstra, M.R. et al., Cathelicidins PMAP-36, LL-37 and CATH-2 are similar peptides with different modes of action, *Sci. Rep.*, 9, 2019, 4780.
149. Okumura, K. et al., C-terminal domain of human CAP18 antimicrobial peptide induces apoptosis in oral squamous cell carcinoma SAS-H1 cells, *Cancer Lett.*, 212, 2004, 185-194.
150. Tripathi, S. et al., Antiviral Activity of the Human Cathelicidin, LL-37, and Derived Peptides on Seasonal and Pandemic Influenza A Viruses, *PLOS ONE*, 10, 2015, e0124706.
151. Currie, S.M. et al., The Human Cathelicidin LL-37 Has Antiviral Activity against Respiratory Syncytial Virus, *PLOS ONE*, 8, 2013, e73659.

152. Vandamme, D. et al., A comprehensive summary of LL-37, the factotum human cathelicidin peptide, *Cell. Immunol.*, 280, 2012, 22-35.
153. López-García, B. et al., Anti-Fungal Activity of Cathelicidins and their Potential Role in *Candida albicans* Skin Infection, *J. Invest. Dermatol.*, 125, 2005, 108-115.
154. Scott, M.G. et al., The Human Antimicrobial Peptide LL-37 Is a Multifunctional Modulator of Innate Immune Responses, *J. Immunol.*, 169, 2002, 3883-3891.
155. Rosenfeld, Y. et al., Endotoxin (Lipopolysaccharide) Neutralization by Innate Immunity Host-Defense Peptides, *J. Biol. Chem.*, 281, 2006, 1636-1643.
156. Mishra, B. and Wang, G., Titanium surfaces immobilized with the major antimicrobial fragment FK-16 of human cathelicidin LL-37 are potent against multiple antibiotic-resistant bacteria, *Biofouling*, 33, 2017, 544-555.
157. Neshani, A. et al., LL-37: Review of antimicrobial profile against sensitive and antibiotic-resistant human bacterial pathogens, *Gene Rep.*, 17, 2019, 100519.
158. Agier, J. et al., Cathelicidin impact on inflammatory cells, *Cent. Eur. J. Immunol.*, 2, 2015, 225-235.
159. Hemshekhar, M. et al., Immunomodulatory Functions of the Human Cathelicidin LL-37 (aa 13–31)-Derived Peptides are Associated with Predicted  $\alpha$ -Helical Propensity and Hydrophobic Index, *Biomolecules*, 9, 2019, 501.
160. Sigurdardottir, S.L. et al., The anti-microbial peptide LL-37 modulates immune responses in the palatine tonsils where it is exclusively expressed by neutrophils and a subset of dendritic cells, *Clin. Immunol.*, 142, 2012, 139-149.
161. Kahlenberg, J.M. and Kaplan, M.J., Little Peptide, Big Effects: The Role of LL-37 in Inflammation and Autoimmune Disease, *J. Immunol.*, 191, 2013, 4895-4901.
162. Bucki, R. et al., Antibacterial Activities of Rhodamine B-Conjugated Gelsolin-Derived Peptides Compared to Those of the Antimicrobial Peptides Cathelicidin LL37, Magainin II, and Melittin, *Antimicrob. Agents Chemother.*, 48, 2004, 1526.
163. Thwaite, J.E. et al., Proteolytic Degradation of Human Antimicrobial Peptide LL-37 by *Bacillus anthracis* May Contribute to Virulence, *Antimicrob. Agents Chemother.*, 50, 2006, 2316.
164. Xhindoli, D. et al., The human cathelicidin LL-37 — A pore-forming antibacterial peptide and host-cell modulator, *Biochim. Biophys. Acta Biomembr.*, 1858, 2016, 546-566.
165. Gutschmann, T. et al., Interaction of CAP18-Derived Peptides with Membranes Made from Endotoxins or Phospholipids, *Biophys. J.*, 80, 2001, 2935-2945.
166. Schneider, V.A.F. et al., Imaging the antimicrobial mechanism(s) of cathelicidin-2, *Sci. Rep.*, 6, 2016, 32948.
167. Nordström, R. et al., Membrane interactions of antimicrobial peptide-loaded microgels, *J. Colloid Int. Sci.*, 562, 2020, 322-332.

168. Lohner, K. and Blondelle, S.E., Molecular Mechanisms of Membrane Perturbation by Antimicrobial Peptides and the Use of Biophysical Studies in the Design of Novel Peptide Antibiotics, *Comb. Chem. High Throughput Screen.*, 8, 2005, 241-256.
169. Sevcsik, E. et al., Interaction of LL-37 with Model Membrane Systems of Different Complexity: Influence of the Lipid Matrix, *Biophys. J.*, 94, 2008, 4688-4699.
170. Strömstedt, A.A. et al., Interaction between amphiphilic peptides and phospholipid membranes, *Curr. Opin. Colloid Interface Sci.*, 15, 2010, 467-478.
171. Sancho-Vaello, E. et al., Structural remodeling and oligomerization of human cathelicidin on membranes suggest fibril-like structures as active species, *Sci. Rep.*, 7, 2017, 15371.
172. Ciumac, D. et al., Influence of Acyl Chain Saturation on the Membrane-Binding Activity of a Short Antimicrobial Peptide, *ACS Omega*, 2, 2017, 7482-7492.
173. Henzler Wildman, K.A. et al., Mechanism of Lipid Bilayer Disruption by the Human Antimicrobial Peptide, LL-37, *Biochemistry*, 42, 2003, 6545-6558.
174. Oren, Z. et al., Structure and organization of the human antimicrobial peptide LL-37 in phospholipid membranes: relevance to the molecular basis for its non-cell-selective activity, *Biochem. J.*, 341 ( Pt 3), 1999, 501-513.
175. Lee, C.-C. et al., Transmembrane Pores Formed by Human Antimicrobial Peptide LL-37, *Biophys. J.*, 100, 2011, 1688-1696.
176. de Miguel Catalina, A. et al., The C-Terminal VPRTES Tail of LL-37 Influences the Mode of Attachment to a Lipid Bilayer and Antimicrobial Activity, *Biochemistry*, 58, 2019, 2447-2462.
177. Zsila, F. et al., Disorder-to-helix conformational conversion of the human immunomodulatory peptide LL-37 induced by antiinflammatory drugs, food dyes and some metabolites, *Int. J. Biol. Macromol.*, 129, 2019, 50-60.
178. Sood, R. et al., Binding of LL-37 to model biomembranes: Insight into target vs host cell recognition, *Biochim. Biophys. Acta Biomembr.*, 1778, 2008, 983-996.
179. Gál, M. et al., Electrochemical and AFM study of the interaction of recombinant human cathelicidin LL-37 with various supported bilayer lipid membranes, *J. Electroanal. Chem.*, 821, 2018, 40-46.
180. Morgera, F. et al., Primate cathelicidin orthologues display different structures and membrane interactions, *Biochem. J.*, 417, 2009, 727-735.
181. Sancho-Vaello, E. et al., The structure of the antimicrobial human cathelicidin LL-37 shows oligomerization and channel formation in the presence of membrane mimics, *Sci. Rep.*, 10, 2020, 17356.
182. Silvius, J.R., Thermotropic phase transitions of pure lipids in model membranes and their modifications by membrane proteins, in *Lipid-protein interactions*. 1982, John Wiley & Sons, Inc.: New York.
183. Wladyka, B. et al., A Peptide Factor Secreted by *Staphylococcus pseudintermedius* Exhibits Properties of both Bacteriocins and Virulence Factors, *Sci. Rep.*, 5, 2015, 14569.

184. Engelsmann, K. et al., Underpotential deposition of lead on polycrystalline and single-crystal gold surfaces, *J. Electroanal. Chem.*, 114, 1980, 1-24.
185. Clavilier, J., Flame-Annealing and Cleaning Technique, in *Interfacial Electrochemistry*, A. Wieckowski, Editor. 1999, Marcel Dekker, Inc.: New York, Basel. p. 231-248.
186. Dakkouri, A.S. and Kolb, D.M., Reconstruction of Gold Surfaces, in *Interfacial Electrochemistry*, A. Wieckowski, Editor. 1999, Marcel Dekker, Inc.: New York, Basel. p. 151-174.
187. Shi, Z. and Lipkowski, J., Chloride adsorption at the Au(111) electrode surface, *J. Electroanal. Chem.*, 403, 1996, 225-239.
188. Su, Z. et al., Electrochemical and PM-IRRAS studies of floating lipid bilayers assembled at the Au(111) electrode pre-modified with a hydrophilic monolayer, *J. Electroanal. Chem.*, 688, 2013, 76-85.
189. Rideau, E. et al., Liposomes and polymersomes: a comparative review towards cell mimicking, *Chem. Soc. Rev.*, 47, 2018, 8572-8610.
190. Enders, O. et al., Structural Calorimetry of Main Transition of Supported DMPC Bilayers by Temperature-Controlled AFM, *Biophys. J.*, 87, 2004, 2522-2531.
191. Peak Force QNM. User Guide, 2011.
192. Pittenger, B. et al. Toward Quantitative Nanomechanical Measurements on Live Cells with PeakForce QNM. 2013.
193. Gramse, G. et al., Nanoscale Measurement of the Dielectric Constant of Supported Lipid Bilayers in Aqueous Solutions with Electrostatic Force Microscopy, *Biophys. J.*, 104, 2013, 1257-1262.
194. Brett, C.M.A. and Brett, A.M.O., *Electrochemistry: Principles, Methods, and Applications*. 1993, United States: Oxford University Press. 444.
195. Frumkin, A.N. et al., Potentials of Zero Charge, in *Comprehensive Treatise of Electrochemistry: The Double Layer*, J.O.M. Bockris, B.E. Conway, and E. Yeager, Editors. 1980, Springer US: Boston, MA. p. 221-289.
196. Kwak, K.J. et al., Formation and finite element analysis of tethered bilayer lipid structures, *Langmuir*, 26, 2010, 18199-18208.
197. Raila, T. et al., Electrochemical impedance of randomly distributed defects in tethered phospholipid bilayers: Finite element analysis, *Electrochim. Acta*, 299, 2019, 863-874.
198. Bard, A.J. and Faulkner, L.R., *Electrochemical methods. Fundamentals and applications*. 2nd ed. 2001: Wiley.
199. Brand, I., *Application of Polarization Modulation Infrared Reflection Absorption Spectroscopy in Electrochemistry*. Monographs in Electrochemistry, ed. F. Scholz. 2020: Springer Nature Switzerland AG. 122.

200. Zamlynyy, V., Electrochemical and Spectroscopic Studies of Pyridine Surfactants at the Gold-Electrolyte Interface. 2002, University of Guelph, Guelph, Ontario, Canada
201. Moskovits, M., Surface selection rules, *J. Chem. Phys.*, 77, 1982, 4408-4416.
202. Umemura, J. et al., Quantitative evaluation of molecular orientation in thin Langmuir-Blodgett films by FT-IR transmission and reflection-absorption spectroscopy, *J. Phys. Chem.*, 94, 1990, 62-67.
203. Okamura, E. et al., Molecular Orientation in Thin Langmuir-Blodgett Films of Dipalmitoylphosphatidylcholine as Studied by FTIR Transmission and Reflection-Absorption Spectroscopy, *Can. J. Chem.*, 69, 1991, 1691-1694.
204. Marsh, D. et al., Orientation of the Infrared Transition Moments for an Alpha-Helix, *Biophys. J.*, 78, 2000, 2499-2510.
205. Stella, L. et al., Alamethicin Interaction with Lipid Membranes: A Spectroscopic Study on Synthetic Analogues, *Chem. Biodiversity*, 4, 2007, 1299-1312.
206. Hutter, J.L. and Bechhoefer, J., Calibration of atomic-force microscope tips, *Rev. Sci. Instrum.*, 64, 1993, 1868-1873.
207. Lévy, R. and Maaloum, M., Measuring the spring constant of atomic force microscope cantilevers: thermal fluctuations and other methods, *Nanotechnology*, 13, 2002, 33-37.
208. Hermanowicz, P. et al., AtomicJ: An open source software for analysis of force curves, *Rev. Sci. Instrum.*, 85, 2014, 063703.
209. Jadidi, T. et al., Poisson's Ratio and Young's Modulus of Lipid Bilayers in Different Phases, *Front. Bioeng. Biotechnol.*, 2, 2014.
210. Zawisza, I. et al., Electrochemical and Photon Polarization Modulation Infrared Reflection Absorption Spectroscopy Study of the Electric Field Driven Transformations of a Phospholipid Bilayer Supported at a Gold Electrode Surface, *Biophys. J.*, 85, 2003, 4055-4075.
211. Laredo, T. et al., Measurement of the Charge Number Per Adsorbed Molecule and Packing Densities of Self-Assembled Long-Chain Monolayers of Thiols, *Langmuir*, 23, 2007, 6205-6211.
212. Griffith, P.R. and de Haseth, J.E., Fourier Transform Infrared Spectrometry. 1986, New York: John Wiley and Sons.
213. Janiak, M.J. et al., Nature of thermal pre-transition of synthetic phospholipids - dimyristoyllecithin and dipalmitoyllecithin, *Biochemistry*, 15, 1976, 4575-4580.
214. Evans, E. and Kwok, R., Mechanical calorimetry of large dimyristoylphosphatidylcholine vesicles in the phase transition region, *Biochemistry*, 21, 1982, 4874-4879.
215. Luna, E.J. and McConnell, H.M., Intermediate monoclinic phase of phosphatidylcholines, *Biochim. Biophys. Acta*, 466, 1977, 381-392.
216. Bernchou, U. et al., Correlation between the ripple phase and stripe domains in membranes, *Biochim. Biophys. Acta Biomembr.*, 1808, 2011, 2849-2858.

217. Katsaras, J. et al., Clarification of the ripple phase of lecithin bilayers using fully hydrated, aligned samples, *Phys. Rev. E*, 61, 2000, 5668-5677.
218. Zasadzinski, J.A.N., Effect of stereoconfiguration on ripple phases ( $P_{\beta}$ ) of dipalmitoylphosphatidylcholine, *Biochim. Biophys. Acta*, 946, 1988, 235-243.
219. Sengupta, K. et al., Novel structural features of the ripple phase of phospholipids, *Europhys. Lett.*, 49, 2000, 722-728.
220. Kaasgaard, T. et al., Temperature-controlled structure and kinetics of ripple phases in one- and two-component supported lipid bilayers, *Biophys. J.*, 85, 2003, 350-360.
221. Fang, Y. and Yang, J., Role of the bilayer-bilayer interaction on the ripple structure of supported bilayers in solution, *J. Phys. Chem.*, 100, 1996, 15614-15619.
222. Johnson, S.J. et al., Structure of an adsorbed dimyristoylphosphatidylcholine bilayer measured with specular reflection of neutrons, *Biophys. J.*, 59, 1991, 289-294.
223. Mou, J.X. et al., Tris(hydroxymethyl)aminomethane ( $C_4H_{11}NO_3$ ) induced a ripple phase in supported unilamellar phospholipid bilayers, *Biochemistry*, 33, 1994, 4439-4443.
224. Leidy, C. et al., Evolution of a rippled membrane during phospholipase A(2) hydrolysis studied by time-resolved AFM, *Biophys. J.*, 87, 2004, 408-418.
225. van Meer, G. et al., Membrane lipids: where they are and how they behave, *Nat. Rev. Mol. Cell Biol.*, 9, 2008, 112-124.
226. Akabori, K. and Nagle, J.F., Structure of the DMPC lipid bilayer ripple phase, *Soft Matter*, 11, 2015, 918-926.
227. Woodward, J.T. and Zasadzinski, J.A., Amplitude, wave form, and temperature dependence of bilayer ripples in the  $P_{\beta}$  phase, *Phys. Rev. E*, 53, 1996, R3044-R3047.
228. Pabst, G. et al., Structure and fluctuations of phosphatidylcholines in the vicinity of the main phase transition, *Phys. Rev. E*, 70, 2004, 021908.
229. Sun, W.J. et al., Structure of the ripple phase in lecithin bilayers, *Proc. Natl. Acad. Sci. U. S. A.*, 93, 1996, 7008-7012.
230. Krbecek, R. et al., Three dimensional microscopic surface profiles of membranes reconstructed from freeze etching electron micrographs, *Biochim. Biophys. Acta Biomembr.*, 554, 1979, 1-22.
231. Brown, R.E. et al., Macro-ripple phase formation in bilayers composed of galactosylceramide and phosphatidylcholine, *Biophys. J.*, 68, 1995, 1396-1405.
232. Meyer, H.W. et al., Macroripple-structures induced by different branched-chain phosphatidylcholines in bilayers of dipalmitoylphosphatidylcholine, *Chem. Phys. Lipids*, 82, 1996, 179-189.
233. Alessandrini, A. et al., What do we really measure in AFM punch-through experiments on supported lipid bilayers?, *Soft Matter*, 7, 2011, 7054-7064.

234. Dokukin, M.E. and Sokolov, I., On the measurements of rigidity modulus of soft materials in nanoindentation experiments at small depth, *Macromolecules*, 45, 2012, 4277-4288.
235. Dieluweit, S. et al., Mechanical properties of bare and protein-coated giant unilamellar phospholipid vesicles. A comparative study of micropipet aspiration and atomic force microscopy, *Langmuir*, 26, 2010, 11041-11049.
236. Wack, D.C. and Webb, W.W., Synchrotron X-ray study of the modulated lamellar phase  $P_{\beta}$  in the lecithin-water system, *Phys. Rev. A*, 40, 1989, 2712-2730.
237. Heimburg, T., A model for the lipid pretransition: coupling of ripple formation with the chain-melting transition, *Biophys. J.*, 78, 2000, 1154-1165.
238. Meyer, H.W., Pretransition-ripples in bilayers of dipalmitoylphosphatidylcholine: undulation or periodic segments? A freeze-fracture study, *Biochim. Biophys. Acta Lipid Lipid Met.*, 1302, 1996, 138-144.
239. Pieta, P. et al., Physicochemical Studies on Orientation and Conformation of a New Bacteriocin BacSp222 in a Planar Phospholipid Bilayer, *Langmuir*, 32, 2016, 5653-5662.
240. Cotter, P.D. et al., Bacteriocins — a viable alternative to antibiotics?, *Nat. Rev. Microbiol.*, 11, 2013, 95-105.
241. Nowakowski, M. et al., Spatial attributes of the four-helix bundle group of bacteriocins – The high-resolution structure of BacSp222 in solution, *Int. J. Biol. Macromol.*, 107, 2018, 2715-2724.
242. Yoneyama, F. et al., Effect of a Negatively Charged Lipid on Membrane-Lacticin Q Interaction and Resulting Pore Formation, *Biosci. Biotech. Bioch.*, 74, 2010, 218-221.
243. Damaskin, B.B. et al., Adsorption of Organic Compounds on Electrodes. 1971, New York: Plenum Press.
244. Burgess, I. et al., Electric field-driven transformations of a supported model biological membrane - an electrochemical and neutron reflectivity study, *Biophys. J.*, 86, 2004, 1763-76.
245. Bizzotto, D. et al., Amphiphilic and ionic surfactants at electrode surfaces, in *Interfacial Electrochemistry: Theory, Experiment and Applications.*, A. Wieckowski and M. Dekker, Editors. 1999: New York. p. 405-426.
246. Gross, E. et al., Dual-Wavelength Ratiometric Fluorescence Measurement of the Membrane Dipole Potential, *Biophys. J.*, 67, 1994, 208-216.
247. Liang, C.Y. and Lytton, M.R., Infrared Spectra of Crystalline and Stereoregular Polymers, *J. Polym. Sci.*, 61, 1962, S45-S48.
248. Lee, D.C. et al., A Difference Infrared Spectroscopic Study of Gramicidin A, Alamethicin, and Bacteriorhodopsin in Perdeuterated Dimyristoylphosphatidylcholine, *Biochim. Biophys. Acta*, 769, 1984, 49-56.
249. Pare, C. et al., Differential Scanning Calorimetry and H-2 Nuclear Magnetic Resonance and Fourier Transform Infrared Spectroscopy Studies of the Effects of Transmembrane Ex-Helical Peptides on the Organization of Phosphatidylcholine Bilayers, *Biochim. Biophys. Acta Biomembr.*, 1511, 2001, 60-73.

250. Sikorska, E. et al., Membrane Structure and Interactions of Peptide Hormones with Model Lipid Bilayers, *Biochim. Biophys. Acta Biomembr.*, 1818, 2012, 2982-2993.
251. Kong, J. and Yu, S., Fourier Transform Infrared Spectroscopic Analysis of Protein Secondary Structures, *Acta Biochim. Biophys. Sinica*, 39, 2007, 549-559.
252. Surewicz, W.K. et al., Determination of Protein Secondary Structure by Fourier Transform Infrared Spectroscopy: A Critical Assessment, *Biochemistry*, 32, 1993, 389-394.
253. Byler, D.M. and Susi, H., Examination of the Secondary Structure of Proteins by Deconvolved FTIR Spectra, *Biopolymers*, 25, 1986, 469-487.
254. Goormaghtigh, E. et al., Evaluation of the Information Content in Infrared Spectra for Protein Secondary Structure Determination, *Biophys. J.*, 90, 2006, 2946-2957.
255. Goormaghtigh, E. et al., Secondary Structure and Orientation of the Amphipathic Peptide GALA in Lipid Structures. An Infrared-Spectroscopic Approach, *Eur. J. Biochem.*, 195, 1991, 421-429.
256. Goormaghtigh, E. et al., Secondary Structure of the Membrane-Bound Form of the Pore-Forming Domain of Colicin A. An Attenuated Total-Reflection Polarized Fourier-Transform Infrared Spectroscopy Study, *Eur. J. Biochem.*, 202, 1991, 1299-1305.
257. Surewicz, W.K. and Mantsch, H.H., New Insight into Protein Secondary Structure from Resolution-Enhanced Infrared Spectra, *Biochim. Biophys. Acta*, 952, 1988, 115-130.
258. Miyazawa, T. and Blout, E.R., The Infrared Spectra of Polypeptides in Various Conformations: Amide I and II Bands, *J. Am. Chem. Soc.*, 83, 1961, 712-719.
259. Tsubio, M., Infrared Dichroism and Molecular Conformation of  $\alpha$ -Form Poly- $\gamma$ -Benzyl-L-Glutamate, *J. Polym. Sci.*, 59, 1962, 139-153.
260. Frey, S. and Tamm, L.K., Orientation of Melittin in Phospholipid Bilayers. A Polarized Attenuated Total Reflection Infrared Study, *Biophys. J.*, 60, 1991, 922-930.
261. Mak, P. et al., Effect of Antimicrobial Apomyoglobin 56-131 Peptide on Liposomes and Planar Lipid Bilayer Membrane, *Int. J. Antimicrob. Agents*, 17, 2001, 137-142.
262. Harrison, M.A.J. et al., Nitrated phenols in the atmosphere: a review, *Atmos. Environ.*, 39, 2005, 231-248.
263. Inomata, S. et al., 4-Nitrophenol, 1-nitropyrene, and 9-nitroanthracene emissions in exhaust particles from diesel vehicles with different exhaust gas treatments, *Atmos. Environ.*, 110, 2015, 93.
264. Li, M. et al., Nitrated phenols and the phenolic precursors in the atmosphere in urban Jinan, China, *Sci. Total Environ.*, 714, 2020, 136760.
265. Hartter, D.R., The use and importance of nitroaromatic chemicals in the chemical industry, in *Toxicity of Nitroaromatic Compounds. 1985: Chemical Industry*, Institute of Toxicology, Washington DC. p. 1-14.

266. Goi, A. and Trapido, M., Comparison of advanced oxidation processes for the destruction of 2, 4-dinitrophenol, in Proc. Estonian Acad. Sci. Chem. 2001: Estonia. p. 5-17.
267. Kitanovski, Z. et al., Composition and mass size distribution of nitrated and oxygenated aromatic compounds in ambient particulate matter from southern and central Europe – implications for the origin, *Atmos. Chem. Phys.*, 20, 2020, 2471-2487.
268. Schummer, C. et al., Analysis of phenols and nitrophenols in rainwater collected simultaneously on an urban and rural site in east of France, *Sci. Total Environ.*, 407, 2009, 5637-43.
269. Rudziński, K.J. and Szmigielski, R., Aqueous reactions of sulfate radical-anions with nitrophenols in atmospheric context, *Atmosphere*, 10, 2019, 795.
270. Rippen, G. et al., Do airborne nitrophenols contribute to forest decline?, *Environ. Technol. Lett.*, 8, 1987, 475-482.
271. An, Y.F. et al., The 3-methyl-4-nitrophenol (PNMC) compromises airway epithelial barrier function, *Toxicology*, 395, 2018, 9-14.
272. Purohit, V. and Basu, A.K., Mutagenicity of nitroaromatic compounds, *Chem. Res. Toxicol.*, 13, 2000, 673-92.
273. Bølling, A.K. et al., Health effects of residential wood smoke particles: the importance of combustion conditions and physicochemical particle properties, *Part. Fibre Toxicol.*, 6, 2009, 29.
274. Raudoniute, J. et al., Pro-inflammatory effects of extracted urban fine particulate matter on human bronchial epithelial cells BEAS-2B, *Environ. Sci. Pollut. Res.*, 25, 2018, 32277-32291.
275. Verschueren, K., Handbook of Environmental Data on Organic Chemicals. 4th ed. 2001, New York: John Wiley & Sons. 1634.
276. Yalkowsky, S.H. et al., Handbook of Aqueous Solubility Data. 2nd ed. 2010, Boca Raton, FL: CRC Press.
277. Majewska, M. et al., Toxicity of selected airborne nitrophenols on eukaryotic cell membrane models, *Chemosphere*, 266, 2021, 128996.
278. Zemski Berry, K.A. et al., Lipidomic characterization and localization of phospholipids in the human lung *J. Lipid Res.*, 58, 2017, 926-933.
279. Kyle, J.E. et al., Cell type-resolved human lung lipidome reveals cellular cooperation in lung function, *Sci. Rep.*, 8, 2018, 13455.
280. Valincius, G. et al., Electrochemical Impedance Spectroscopy of Tethered Bilayer Membranes: An Effect of Heterogeneous Distribution of Defects in Membranes, *Electrochim. Acta*, 222, 2016, 904-913.
281. Feigenson, G.W., Phase diagrams and lipid domains in multicomponent lipid bilayer mixtures, *Biochim. Biophys. Acta*, 1788, 2009, 47-52.

282. Avanti Polar Lipids. Phase transition temperatures for glycerophospholipids. [cited 2020 23 Jul]; Available from: <https://avantilipids.com/tech-support/physical-properties/phase-transition-temps>.
283. Kahnt, A. et al., One-year study of nitro-organic compounds and their relation to wood burning in PM10 aerosol from a rural site in Belgium, *Atmos. Environ.*, 81, 2013, 561-568.
284. Wang, Y. et al., The formation of nitro-aromatic compounds under high NO<sub>x</sub> and anthropogenic VOC conditions in urban Beijing, China, *Atmos. Chem. Phys.*, 19, 2019, 7649-7665.
285. Wang, X. et al., Emissions of fine particulate nitrated phenols from the burning of five common types of biomass, *Environ. Pollut.*, 230, 2017, 405-412.
286. Juhaniwicz, J. and Sek, S., Atomic force microscopy and electrochemical studies of melittin action on lipid bilayers supported on gold electrodes, *Electrochim. Acta*, 162, 2015, 53-61.
287. Juhaniwicz-Dębińska, J. et al., Effect of Interfacial Water on the Nanomechanical Properties of Negatively Charged Floating Bilayers Supported on Gold Electrodes, *Langmuir*, 35, 2019, 9422-9429.
288. Dufrene, Y.F. et al., Characterization of the physical properties of model biomembranes at the nanometer scale with the atomic force microscope, *Faraday Discuss.*, 111, 1999, 79-94.
289. Needham, D. and Evans, E., Structure and Mechanical-Properties of Giant Lipid (DMPC) Vesicle Bilayers from 20-Degrees-C Below to 10-Degrees-C above the Liquid-Crystal Crystalline Phase-Transition at 24-Degrees-C, *Biochemistry*, 27, 1988, 8261-8269.

